

## Report Information

**Name:** Leslie Bromberg

**Organization:** Massachusetts Institute of Technology

**Email:** [brom@psfc.mit.edu](mailto:brom@psfc.mit.edu)

**Distribution:** Approved for public release; distribution is unlimited.

### Contract Information

Contract Number: N00014-14-1-0272

Contract Title: Superconductor armature winding for high performance electrical machines

Program Officer: Dr. H. Scott Coombe

CO-PI Information: Prof. J. Kirtley, MIT; Prof. J. Brisson, MIT

### Abstract

The impact of the use of high/medium temperature superconductors for applications to generators was investigated in an all-superconducting machine. Superconductor armature windings in electrical machines bring many design challenges that need to be addressed en route to becoming a potentially viable solution for a modern rotating equipment. Foremost amongst the challenges are the cryogenic environment and the need to address the excessive ac losses. We used an integrated design to investigate the major technological issues that must be simultaneously satisfied for successful implementation of a robust, high power density, high efficiency superconducting generator. Thus, for example, the interaction between the superconducting cable design, ac losses in the SC, cable current/voltage/insulation, and cooling will be integrated in models were used to evaluate the “sweet” spots with regard to overall system configuration.

The purpose of this program was not to design a specific machine, but rather to investigate through system design, modeling and component tests the issues confronting SC generators. These issues compromise the conductor selection, superconductor and cable performance, cryostat configuration and cooling choice, cable support and superconductor strains and stresses, and cable insulation/breakdown/partial discharge. The last issues are particularly relevant to the armature, as the ac losses in the SC require intimate contact with a coolant (for example, gaseous helium), which has rather poor dielectric strength. During the first phase of the program, we plan to build models to investigate several configurations of the generator and determine the sensitivity of performance to key design system parameters. We evaluated the cryogenic loads, the electrical efficiency, generator torque and power, and the impact on the weight, size and signature of the generator.

We have focused during this phase on the design, modeling and evaluations of multiple generator designs. The issues described above were investigated, to highlight potential obstacles to implementation. We used a wound-field synchronous generator design successfully tested by TWMC for evaluation of the technologies proposed in the program. The machine is designed for operation at power frequency of 117 Hz, which should help address the issues of ac losses. Based on their design and manufacturing database, TWMC has codes which permit this design to be parametrically scaled to alternate operating conditions, for example to investigate higher speed operation. The use of parametric scaling relations facilitates the development of a road map that would result in a fast, low cost route to system optimization. The system code was developed through a collaboration between MIT (PSFC/EE), TWMC, Dr. Philippe Masson of the University of Houston and Dr. Swarn Kalsi. The objective functions were weight, size, efficiency and/or cost.

The system code was calibrated with a Navy generator. The rated parameters of the baseline machine

are 14 MW, 7000 rpm, synchronous generator built for a turbine generator application. Although we will use a specific generator built and tested by TWMC as a baseline design for this investigation, the approach will remain applicable to a broad spectrum of machines. Cryostat topologies, operating temperature and coolant choice, superconductor type and cable design was modeled, included in the system code and investigated parametrically to develop a road map that would result in a fast, low cost route to implementation.

Once the low-hanging fruits was identified, and the critical items identified, limited testing took place, mostly in the second year of this program. Superconductors and cables, cryogenics, cooling fluids, ac losses in small calorimeters at MIT was evaluated experimentally, both in order to benchmark the codes as well as to provide insight in potential issues with the technology being investigated.

## **Superconductor armature winding for high performance electrical machines**

Grant number: N00014-14-1-0272

Prepared by

L. Bromberg (PI), P.C. Michael, J. Voccio, S. Hahn, J. Kirtley,  
J.V. Minervini, J. Brisson, S. Hensley, C. Galea, J. Lin, E. Vargas and C. Schaefer  
Massachusetts Institute of Technology

E. Chen and H. Karmaker  
TECO-Westinghouse

Philippe Masson  
Consultant

Swarn Kalsi  
Consultant

Final report  
December 5, 2016

**DISTRIBUTION STATEMENT. Approved for public release; distribution is unlimited.**

**Distribution:**

Donald J. Hoffman  
Office of Naval Research  
875 North Randolph Street  
Arlington, VA 22203-1995  
Email: DONALD.HOFFMAN@NAVY.MIL

Naval Research Laboratory  
reports@library.nrl.navy.mil

Eric Garfield  
Office of Naval Research  
495 Summer Street, Room 627  
Boston, MA 02210-2109  
Email: garfiee@onr.navy.mil  
(His contact information has changed slightly since this award was issued)

Defense Technical Information Center  
TR@dtic.mil

Jacob Kephart, Ph.D.  
Applied Superconductivity Team Lead  
Naval Surface Warfare Center Philadelphia Division  
Machinery Research, Logistics and Ship Integrity Department  
Machinery Research and Silencing Division  
Energy Conversion R&D Branch, Code 325  
Ph: 215-897-8474  
Cell: 267-582-0974  
Fax: 215-897-8380  
jacob.kephart@navy.mil

H. Scott Coombe, Ph.D., P.E.  
Program Officer, Code 331  
Office of Naval Research  
875 N Randolph St, Rm 267  
Arlington, VA 22203 USA  
Office: (703) 696-1291  
Cell: (703) 965-3371  
NIPR: harold.coombe@navy.mil

## Contents

EXECUTIVE SUMMARY .....	8
1. Baseline Design and Objectives .....	13
2. Generator topologies for fully superconducting machines .....	15
2.1 Radial flux machines .....	15
2.2 Rapid scanning of configuration.....	21
2.3 Axial flux machines.....	22
2.4 Toroidal stators .....	23
2.5 Switched Reluctance Machines (SRM).....	29
2.6 AC Homopolar Machines .....	33
2.6.1 With ReBCO in Armature and Field Windings.....	35
2.6.2 Magnetic Analysis .....	41
2.6.3 Effect of Armature Magnetic Field on the Excitation Coil.....	45
2.6.4 Summary of ReBCO Machine .....	46
2.6.5 MgB2 in the rotor and armature windings .....	50
Comparison among machines without SC in the rotor.....	54
2.7 Machine Configurations Optimization and Comparison.....	55
2.8 References .....	59
3. Weight reduction by iron elimination.....	60
3.1 Solid shield. .....	60
3.2 Litz-wire shield. .....	61
3.3 Radial flux machines with electrically conducting shield .....	63
3.3 References .....	64
4. Investigation of local field modification to control AC losses .....	65
4.1 Magnetic elements .....	65
4.2 Electrically conducting elements .....	67
5. Stator Winding and Assembly .....	71
5.1 Superconductor Manufacturing Method .....	71
5.2 Number of Legs per Slot.....	71
5.3 Coil Manufacturing.....	72
5.3.1 Random Wound Coil .....	72
5.3.2 Form Wound Coil .....	73
5.4 Stator Assembly .....	76
5.4.1 Radial Saddle Coil Stator Assembly.....	76
5.4.2 Racetrack Coil.....	77
5.4.3 Toroidal Coil .....	78
5.4.4 AC Homopolar Stator .....	79
5.5 Joints .....	81
5.4 Conclusion.....	81
6. Superconductor Options .....	82
6.1 High Temperature Superconductor Selection.....	82
6.2 Bi-2212 .....	83
6.3 Strain Effects .....	85
6.4 AC Losses.....	86
6.4.1 AC loss calculations for YBCO.....	87

6.4.2 AC loss calculations for MgB <sub>2</sub> (233 Hz operation) .....	91
6.4.3 AC losses in CICC for toroidal Stators.....	93
6.5 Experimental losses in MgB <sub>2</sub> CICC topologies .....	96
6.5.1 Sample preparation .....	96
6.5.2 Heat treatment .....	98
6.5.3. Critical current characterization of the MgB <sub>2</sub> strands and triplets .....	100
6.5.4. Estimation of zero field, 20K critical current.....	101
6.6 Summary .....	109
6.7 References .....	109
7. Cable Design.....	111
7.1 MgB <sub>2</sub> Cable-in-Conduit Conductor .....	111
7.2 Conductor Overview .....	112
7.2.1 Technology demonstration .....	114
7.3 Prototype sample fabrication .....	115
7.3.1 Triplet cabling .....	115
7.3.2. Jacket compaction trials.....	116
7.3.3 Second-stage cabling .....	119
7.3.4 Cable draw-through and compaction .....	120
7.3.5 Thermohydraulic Considerations .....	121
7.4 Two-layer CORC .....	121
7.5 References .....	123
8. Quench detection and protection for MgB <sub>2</sub> .....	125
8.1 Hot spot temperature rise .....	125
8.2 Added copper strands .....	128
8.3 Solid cryogen stabilized MgB <sub>2</sub> cable.....	129
8.3.1 Thermal model during steady operation .....	130
8.3.2 Transient Analysis .....	131
8.3.4 Conclusions .....	133
8.4 Quench detection using co-wound voltage tap in MgB <sub>2</sub> CICC.....	133
8.4.1 Axial current effect .....	134
8.4.2 Transverse field effect .....	136
8.5 YBCO-based thermal sensor.....	136
8.5.1 stripline quench detector .....	138
8.6 Indirect cooling with gaseous helium .....	140
8.6.1 Foams.....	141
8.6.2 Adhesive.....	141
8.6.3 Electrochemically attaching foams to fins .....	144
8.6.4 3D printing of heat exchangers and foams .....	146
8.6.5 Alternative means for open-cell, porous materials .....	150
8.7 References .....	151
9 Cryogenic design .....	153
9.1 Single cryostat.....	153
9.2 Separate cryostats.....	154
9.3 Individual cryostats surrounding individual stator windings. .....	154
9.4 Cryostat Summary .....	155
9.5 Refrigeration and Refrigerator Issues .....	155
9.5.1 Overall Cryogenic Loads/Summary .....	156

9.5.2 Coolants .....	156
9.5.3 Cryogenic Loads due to Leads.....	157
9.5.4 Radiation.....	159
9.5.5 Convection in the Cryostat.....	160
9.6 Refrigerator .....	161
9.7 Specific Cryocoolers .....	163
9.8 Development of ship-cryogenic system.....	164
9.9 References .....	164

# EXECUTIVE SUMMARY

The use of superconducting motors for armatures of rotating machinery, and in particular, generator, is challenging. The challenges are due to the AC losses in the superconductor, which requires sophisticated coolant topologies and require refrigerators, with their inefficiency, size/weight and reliability issues. In addition, the shapes of the coils are complex, and impose manufacturability issues, especially for MgB2.

We built a team that included experts in superconductivity, cryogenics, rotating machinery, and manufacturing.

We have performed an investigation of the issues, quantified them, and proposed potential solutions. This report describes design approach, assumptions and results for a wide range of machines. It should be noted that these designs are essentially first pass and are not optimum in any sense.

Initially we did a broad exploration of generator topologies, to see how they compare with respect to some metrics (size, weight, efficiency, manufacturability). We have then addressed some of the obstacles that were identified in the broad study, quantifying the issues and proposing potential solutions. We have then reoptimized the most promising approaches.

## *Topology considerations*

We investigated the following topologies

- salient pole
- iron teeth and no-iron
- axial flux machines
- with back-iron and without (eddy current shields)
- SuperSat
- switch reluctance generators
- AC Homopolar
- Toroidal (Gramme ring) generators

We built simple 2D physics-based models for the different topologies and did self-consistent analysis of the different configurations. We compared the results with the baseline and looked at the options and rated the machines. Because of the AC losses, it was clear that a small number of poles (in a SC armature) was attractive.

We then investigated the issues of the machines, described in the following.

## *Investigation of local field modification to control ac losses*

We investigate both the use of magnetic shielding and electrical shielding materials for minimization of the AC losses. In the case of YBCO, we tried to both reduce the magnetic field, and also make it parallel to the tapes, to minimize the losses in the superconductor.

We found that the magnetic field was only partially successful for changing the field direction next to the tapes. Iron teeth decreased the field at the superconductor, but placing magnetic material with the sole purpose of aligning the field with the tapes was of limited value. In addition, this approach does not work with the self field.

The electrical shielding (by placing conductor paths to reduce or eliminate the external magnetic field was also of limited value. It was possible to shield the field, but with substantial AC losses in the conducting shield. The conducting shield can be at room temperature. Even then, the losses were substantial to impact the efficiency of the generator (~1%) and were high, making them difficult to remove. For the generator that met the NAVY requirements, the losses were over 1000 W/m.

### *Cryogenic design*

We investigated generator topologies to avoid the need for a rotating seal. Although the geometry of the cryostat was substantially simplified, the prime mover would have to transmit the forces through a dielectric cryostat.

We also developed models for the cryogenic system (size, cost and weight, as a function of cooling power and temperature). We also developed means for direct cooling of the superconductor (for MgB2) and indirect cooling of YBCO, using helium gas.

### *Modeling of generators*

We built 2D models for the generators. We used that model when comparing the different generator topologies and superconductor type (MgB2, Bi2212 and YBCO). The model calculated self-consistently the AC losses. We looked at the cable manufacturing. For MgB2 we developed a Cable in Conduit Conductor (CICC), and for YBCO we considered stacked and Roebel cables. We looked at the manufacturability of the coils, in particular due to the strain sensitivity of reacted MgB2 strands.

Bi2212 does not offer substantially advantages over MgB2, and we did not investigate it as thoroughly as MgB2 or YBCO.

We looked at operating temperature of the coolant. (20K, with liquid hydrogen and gaseous helium, 35 K and 50 K with gaseous helium, and 65 K, with liquid nitrogen and gaseous helium. 20 K was adequate for MgB2, and 35 – 50 K was optimal for YBCO, due to the improved performance of the SC.

We also looked at the impact of some of the designs for minimization of the electromagnetic signature. We developed electrically conducting shields with low loss using Litz wire approaches.

### *Cable designs*

Cable manufacturing using HTS is in early stages. For YBCO, stacked cables, partially aligned with the predominant magnetic field, twisted at the end, was chosen. CORC required substantially higher superconductor (both because of the helical winding pattern of the tapes, as well because the tapes see

all the magnetic field, as it is not possible to align the tapes with the predominant magnetic field.

For MgB<sub>2</sub> cables, we investigated Cable-in-conduit conductor (CICC). The strands were placed in a gap between two tubes, with the coolant flowing through the inner tube. In order to immobilize the strands of the cable (there will be large Lorenz forces in the superconductor cables) we investigate the use of a frozen filler. Because of the nature of the winding (2 stages of cabling), we settled for wind and react.

We tested the cables by building one with 18 triplets, as part of component verification/testing. We also measured the AC losses in the triplets, using HyperTech low-loss, small filaments strands (15 microns). The strands provided by Hypertech has small diameter (0.3 mm), resulting in low current per strand. Losses in strands substantially higher than expected, due probably to highly conducting Nb sheath around the MgB<sub>2</sub> filaments (the measured losses were coupling or eddy current losses), with small hysteresis losses. Improved manufacturing may reduce the AC losses further.

### *Cryostat designs*

We developed concepts with and without rotating cryogenic couplers, with non-sliding seals. In order to transmit the torque from the prime mover, we needed to transfer the load across the cryostat. We analyzed magnetic couplers, which turned out to be feasible but large/heavy.

One of the motivations of investigating the switch reluctance and AC homopolar topologies was that there were no rotating seals. The SC armature and rotor are stationary. However, the frequency of operation had to increase, resulting in higher AC losses (in the armature).

### *System optimization*

After performing the analysis, we used the codes to optimize a generator. We used two topologies, the salient pole and the gramme ring (toroidal stator). The results indicated that the approach may be attractive for NAVY applications. However, the costs of superconductor (about 300k\$, at 2016 YBCO prices) and the cost/size of the cryocoolers (about 500k\$) makes the implementation of these concepts challenging.

Further weight reduction could be obtained by using a toroidal stator concept with a resistive shield, without back iron. Most of the weight of the machine is in the backiron.

For machines with a superconducting rotor, both MgB<sub>2</sub> and YBCO offer potentially attractive designs.

For MgB<sub>2</sub>:

#### AC Losses

- MgB<sub>2</sub> cable ~500-2000 kW @ 20 K
  - 10 micron fil., 1cm twist pitch, 1e-6 Wm matrix res.
  - Efficiency > 99% (COP – 90 W/W)
- Specific torque
  - 3-5 Nm/kg is over 5 times better than conventional machines in this power/speed range

For YBCO:

AC Losses

3 mm wide tapes would lead to ~3-5 kW @ 50 K

Efficiency >99 % (COP – 20 W/W)

Specific torque

3-5 Nm/kg is over 5 times better than conventional machines in this power/speed range

Note that the specific torque for conventional PM water cooled generators is ~ 0.6 Nm/kg. Gramme stator configuration could potentially be a viable option for MgB2 and YBCO

The following conclusions are from the investigation of the machines that do not have superconductor in the rotor are:

- SRM generators is determined to be too heavy, large and inefficient and does not satisfy ONR requirements
- ACHP with copper armature and MgB2 field winding meets all ONR requirements; its mass exceeds the ONR requirement merely by 700 kg.
- ACHP with MgB2 windings meets all requirements except the mass, which is 1,800 kg more than the requirement. The machine alone is 7,700 kg but the system mass exceeds the ONR requirements due to the mass of cooling system.
- Only the ACHP with ReBCO windings met all requirements.

### *Technology Gaps*

Means of reducing further the AC losses in both YBCO and MgB2 would improve the performance of all machines. There are substantial programs for addressing this need. Some of this work (such as the striation of the YBCO tapes and the high resistance matrix for MgB2) should be encouraged.

There is a need to develop means to remove the relative large AC losses in the armature winding superconductor. Different superconductor may require different means, either direct or indirect cooling.

Refrigerators also need to improve. Conventional refrigerators have shown relatively slow progress. TurboBrayton refrigerators offer the potential for efficiency, compact and light weight approaches. There should be continued development of components and systems for this type of refrigerator.

There is need for improving and/or demonstration the manufacture of the assembly, from initial cabling to coil winding. MgB2, in particular, is very sensitive to strain after reacting, but it may be necessary to finish the winding process after heat treatment.

Quench detection is critical. We tried to develop mean for detecting the generation of a normal zone. Because of the high thermal capacity, normal zone propagation is slow, and the resulting voltages are small. Coupled with a very noisy environment makes quench detection critical.

All key parameters for MgB2 and ReBCO machines are a strong function of superconductor

characteristics; such as critical current, operating temperature and AC losses. A better estimate of these characteristics could impact their attractiveness with respect to the specified ORN requirements. Further improvement can also improve the attractiveness of the concepts.

## 1. BASELINE DESIGN AND OBJECTIVES

We started by investigated conventional approaches with radial flux machines. We are comparing with a baseline that the NAVY uses, and is in the Philadelphia Navy Yard. The machine parameters are 14 MW, operating at 7000 rpm and weighing about 18 tones. The torque of the machine is 20 kNm. Figure 1.1 shows the baseline machine. [Calfo]

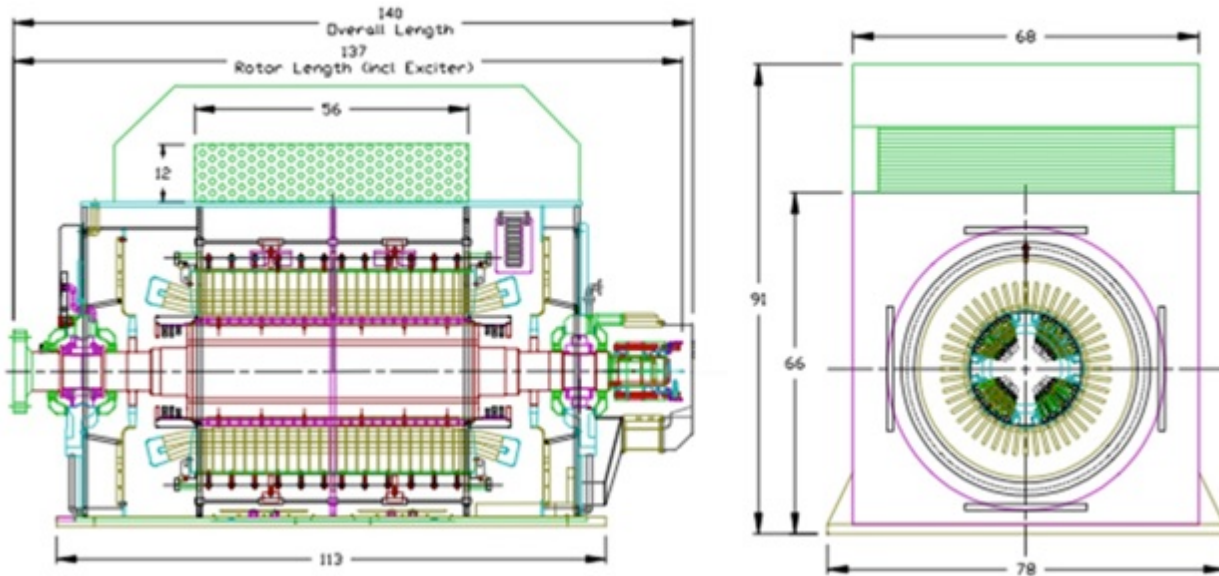


Figure 1.1 Baseline machine design

The impact of the use of high/medium temperature superconductors for applications to the armature winding of generators has been investigated in an all-superconducting machine. Superconductor armature windings in electrical machines bring many design challenges that need to be addressed en route to becoming a potentially viable solution for a modern rotating equipment. Foremost amongst the challenges are the cryogenic environment and the need to address the excessive ac losses. We have used an integrated design to investigate the major technological issues that must be simultaneously satisfied for successful implementation of a robust, high power density, high efficiency superconducting generator. Thus, for example, the interaction between the superconducting cable design, ac losses in the SC, cable current/voltage/insulation, and cooling will be integrated in models that will be used to evaluate the “sweet” spots with regard to overall system configuration.

The purpose of this program was not to design a specific machine, but rather to investigate through system design, modeling and component tests the issues confronting SC generators. These issues compromise the conductor selection, superconductor and cable performance, cryostat configuration and cooling choice, cable support and superconductor strains and stresses, and cable insulation/breakdown/partial discharge. The last issues are particularly relevant to the armature, as the ac losses in the SC require intimate contact with a coolant (for example, gaseous helium), which has rather poor dielectric strength. We built models of several generator configurations. We evaluated the cryogenic loads, the electrical efficiency, generator torque and power, and see the impact on the weight, size and signature of the generator.

A system code was developed through a collaboration between MIT (PSFC/EE), TWMC and Dr. Philippe Masson of the University of Houston. The objective functions to be optimized are weight, size and/or cost.

## 2. GENERATOR TOPOLOGIES FOR FULLY SUPERCONDUCTING MACHINES

We have investigated several topologies to generate the data needed for the rest of the program. We have investigated radial and axial machines, the number of poles. In particular, we have investigated the radial machine with toroidal stators (Gramme ring), the switch reluctance and AC homopolar topologies.

We have looked at two specific topologies that do not require cryogenic coupling. Key objective of this part of the effort is to investigate concepts requiring no superconducting windings on the rotor in order to avoid difficulties with coolant transfer to high speed rotor. Two general concepts, with potential for meeting these objectives were selected; Switched Reluctance Machine (SRM) and AC Homopolar (AHP). The cryostats in these machines are stationary, substantially decreasing the complexity of the machine.

### 2.1 RADIAL FLUX MACHINES

For comparison purposes we assume a MGB2 stator. We have also investigated YBCO and Bi2212 (described below). We are using filaments that are 30 microns, although we will present further down results with machines with 10 micron filaments, being developed by HyperTech under both Navy and NASA funding. We have actually tested the performance of HyperTech strands, triplets and cables, described in Section 7)

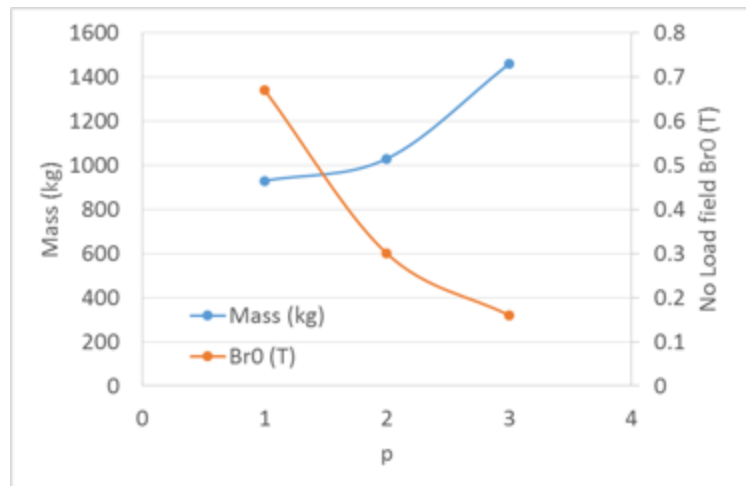


Figure 2.1 Mass and no-load magnetic field as a function of the periodicity of the machine.

We assume that the refrigerator has an efficiency of 20% of Carnot, and the superconductor is at 20 K. The fraction of critical of the current at field and temperature is 40%. The machine goal is 98% efficiency, including the AC loads, the cryocooler power requirement to remove the cryogenic loads (which include current leads, radiation and convection losses in the cryostats).

We have determined that the optimal performance is achieved with 2-pole machines. Operating with increased number of poles increases slightly the total weight (including the refrigerator), but decreases the magnetic field., Figure 2.1 shows the tradeoffs, where p in the half the number of poles.

The weight of the machine is dominated by the iron. For the machine with p=1 in Figure 2.1, the

superconductor weight is about 1/5 the weight of the iron. Thus, if we could eliminate the iron, it may be possible to substantially reduce the weight of the system.

Figure 2.2 shows a direct comparison between an iron based machine and a resistive shield machine (in section 3 we describe means of implements resistive, image-current shields). Unfortunately, the flux lines are much more perpendicular to stator winding with magnetic shield (resulting in better use of the field made by the rotor), and as a consequence, the torque is reduced and more radial forces are applied on stator winding.

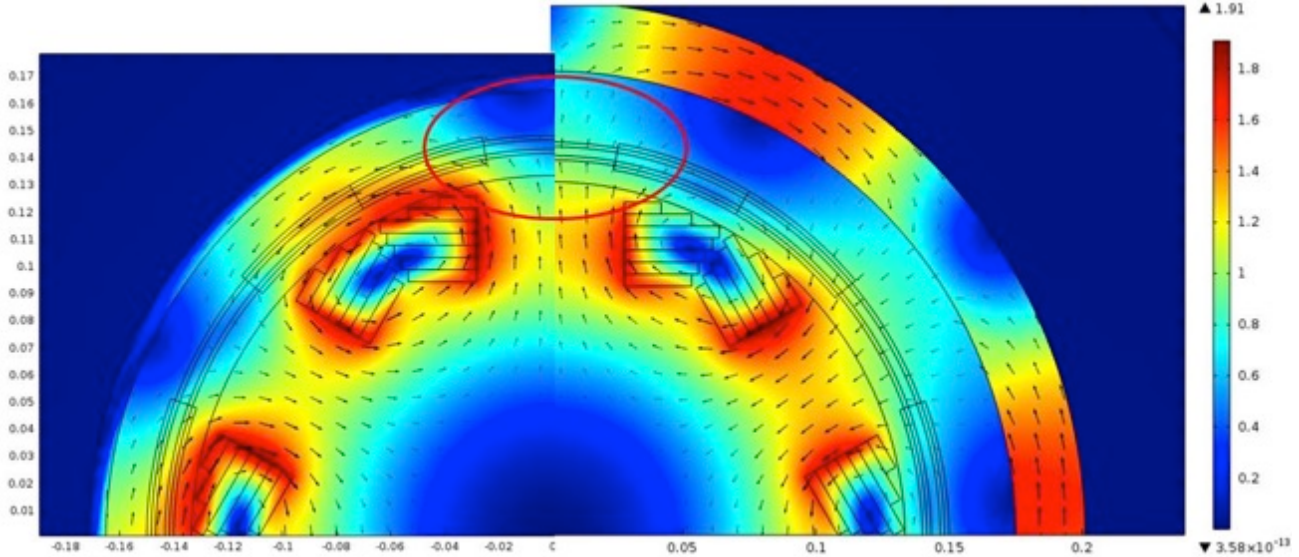


Figure 2.2 Comparison between iron-shield (left) and resistive shield (right).

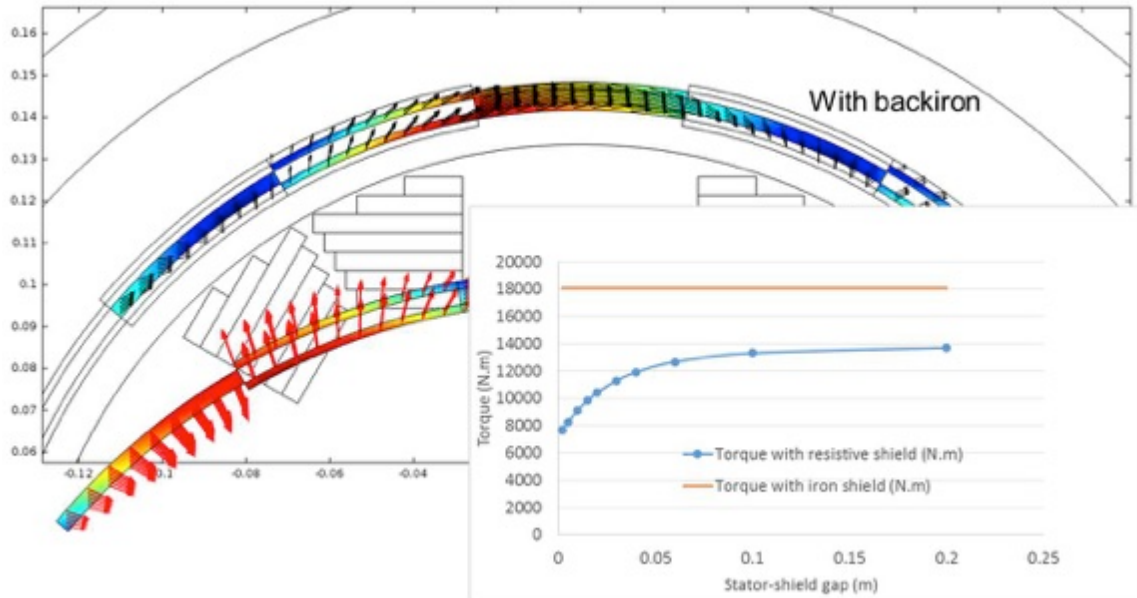


Figure 2.3 Comparison between back-iron machine (top) and resistive shield (Bottom).

Figure 2.3 shows the loads resulting in the winding for the two configurations. The loads for the resistive machine are much more radial (radial loads do not result in useful torque). In comparison, the machine with the back-iron shows loads that are mostly azimuthal. It is desirable to have the flux lines cross the stator winding as radially as possible. The less efficient use of the available flux, and the

increased amperage of the rotor winding because of increased reluctance of the machine, is a consequence of the removal of the iron from the stator winding (which is a result of the desire to decrease the machine weight).

We have made a comparison between six configurations, for machines with 20 kNm and 2 layer stator winding. The machines considered are:

- Iron shield
  - Iron teeth
  - No iron teeth
- Resistive shield
  - Single rotor winding
    - Iron teeth
    - No iron teeth
  - Double rotor winding
    - Iron teeth
    - No iron teeth

The results are illustrated in Figures 2.4-3.9. The removal of the back-iron makes the field go in the azimuthal direction, decreasing the efficiency of the coupling to the stator, as indicated above. Placing iron teeth in the case of resistive shield further exacerbates the problem with the field being “shorted out” by the iron teeth.

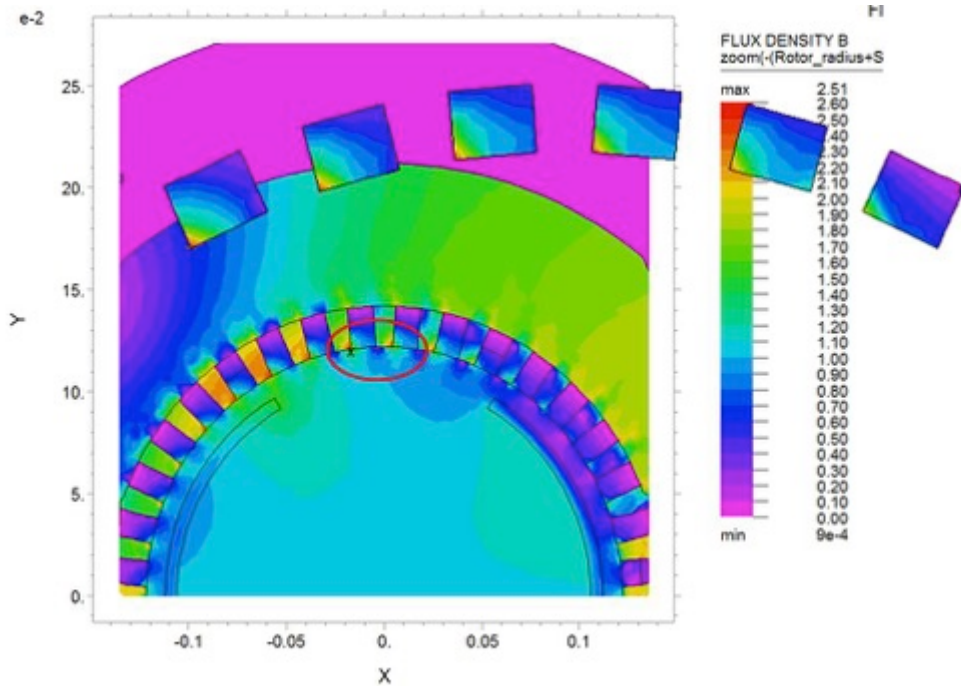


Figure 2.4. Flux density for a design with iron shield and iron teeth.

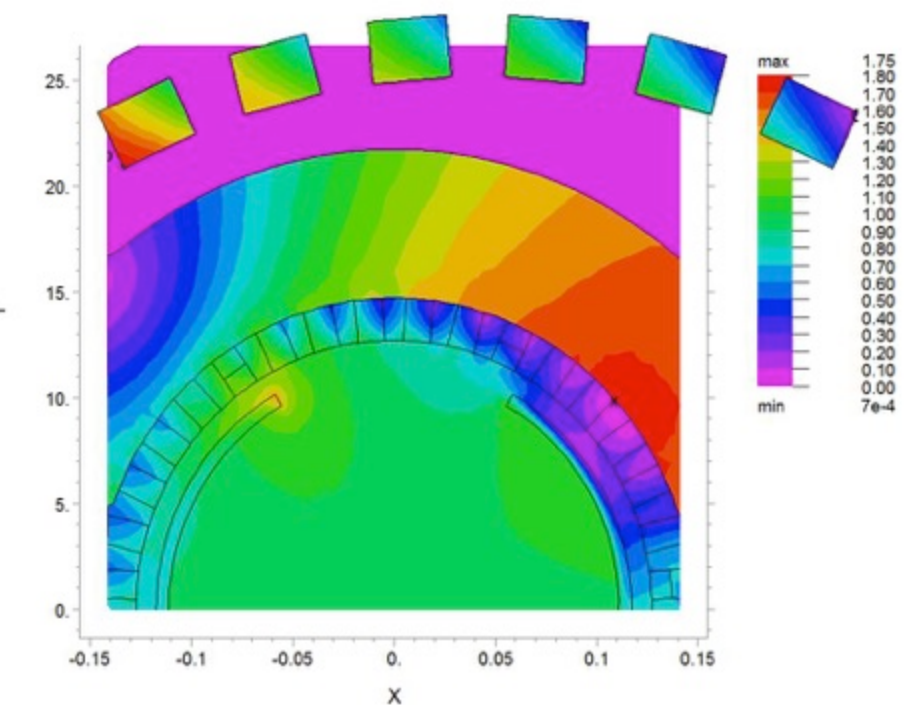


Figure 2.5. Flux density for a design with iron shield and no iron teeth.

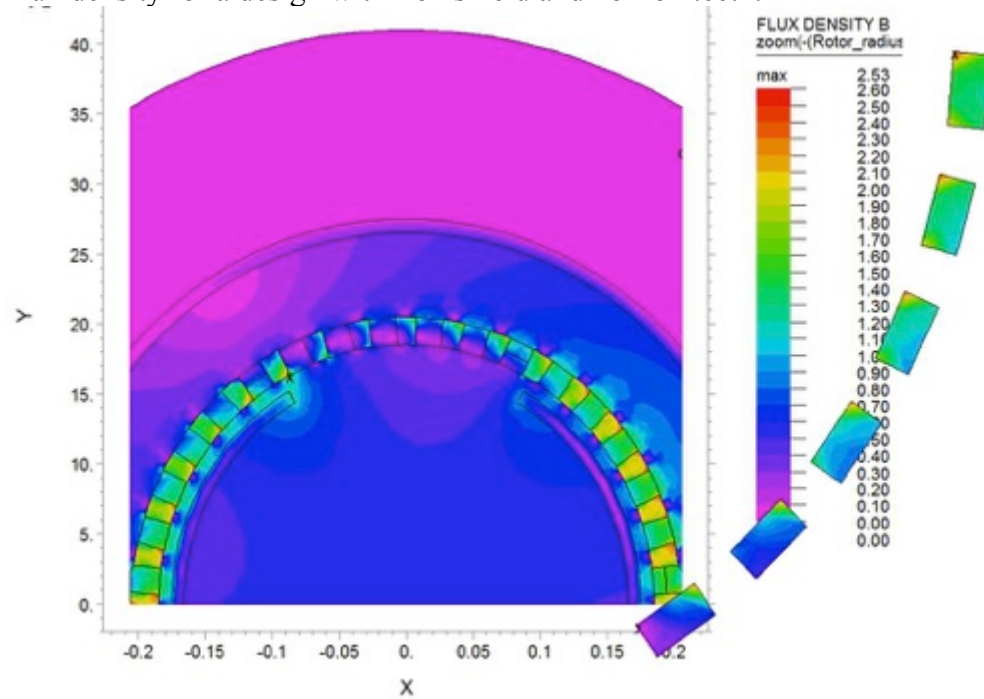


Figure 2.6. Flux density for a design with resistive shield and iron teeth.

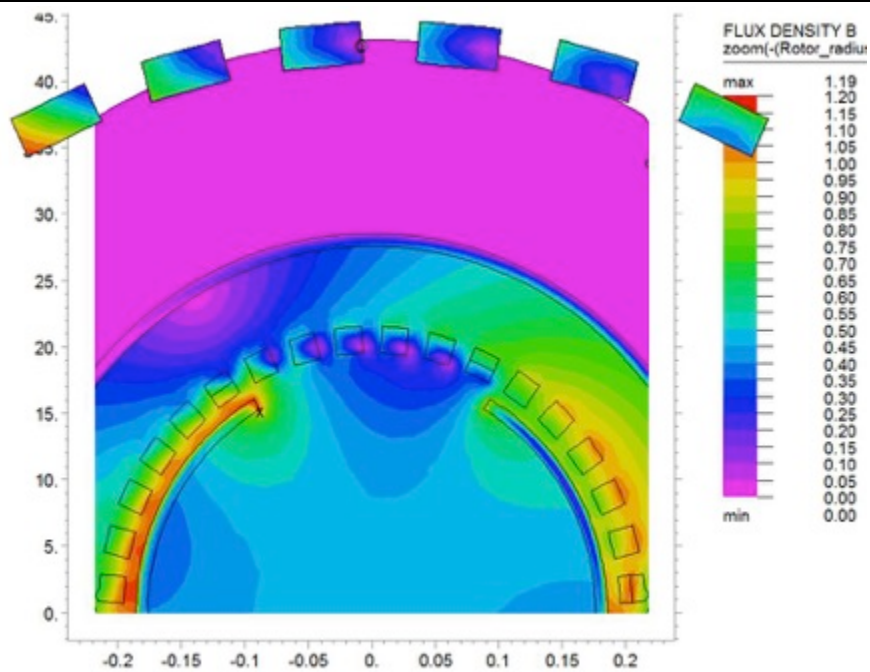


Figure 2.7. Flux density for a design with resistive shield and no iron teeth.

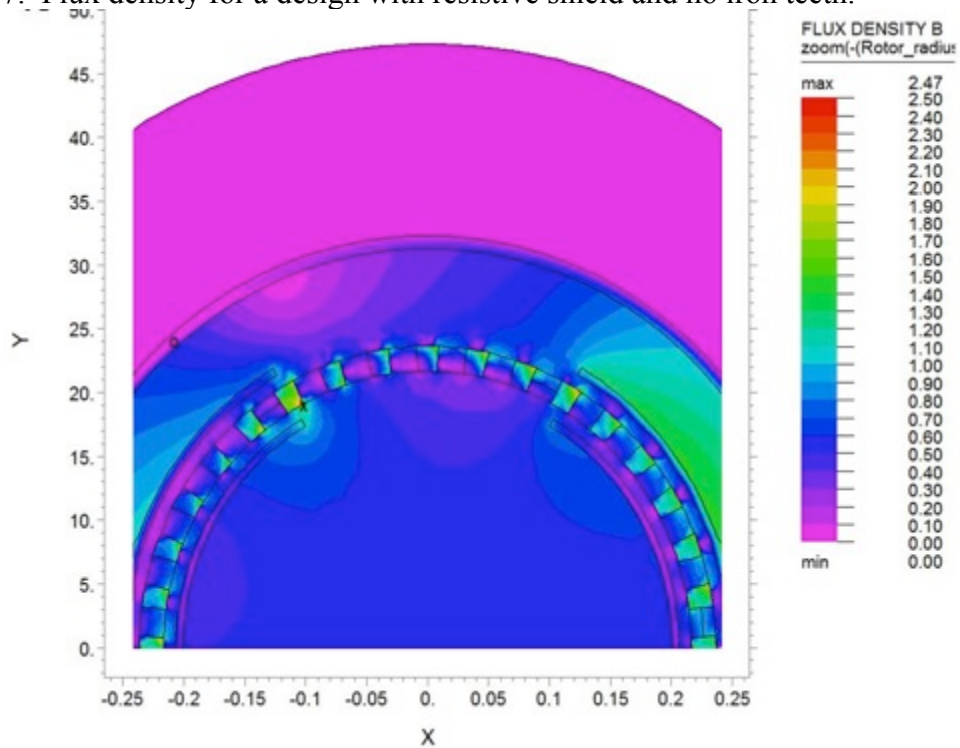


Figure 2.8. Flux density for a design with double rotor, resistive shield and iron teeth.

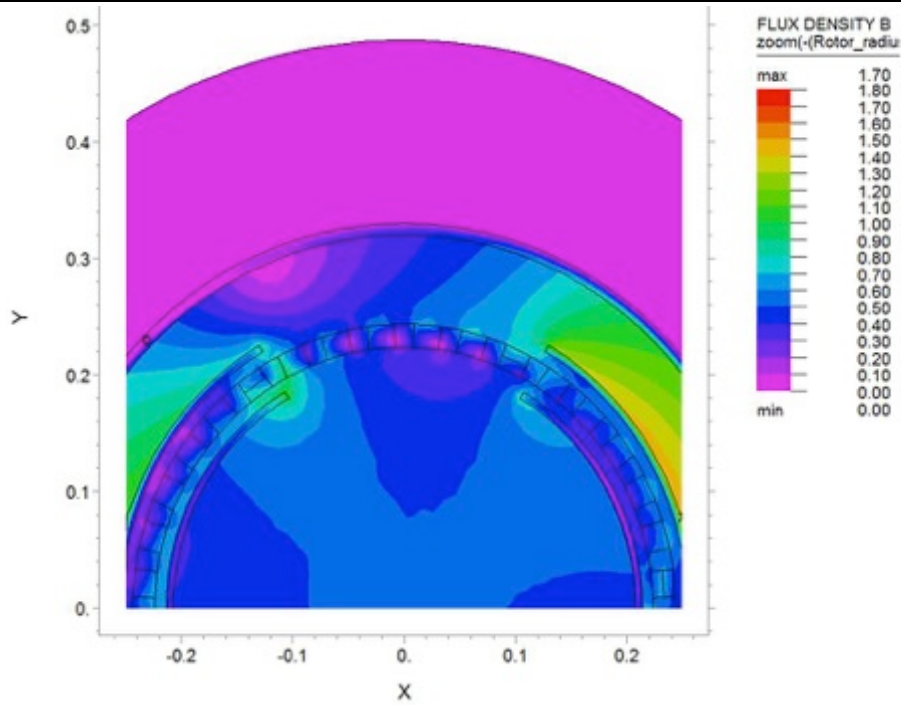


Figure 2.9. Flux density for a design with double rotor, resistive shield and no iron teeth.

Table 2.1 shows a summary of the comparison between these 6 radial flux machines. Mass comprises only the active material over the active length and it is shown only for comparison purpose. It is not clear how the optimal machine can be derived. The losses are high, as a consequence of using the large diameter filaments, but the table is mostly to compare, relatively, the advantages of the machines. The lighter machine is the single rotor machine, without iron teeth, but this results in substantially higher AC losses than some of the other designs. The machine with the highest AC losses is the one with backiron and teeth, which is somewhat surprising. This machine design basically replaces the conventional stator conductor winding with superconductor.

We tried to investigate the double rotor as a means to increase the directionality of the field, making it radial in the region of the stator (which is between the double rotor). The lighter machine is the double rotor without teeth.

The machine with the lowest losses is the design with a single rotor, iron shield, but no iron teeth. In this case, the AC losses are about 3 kW.

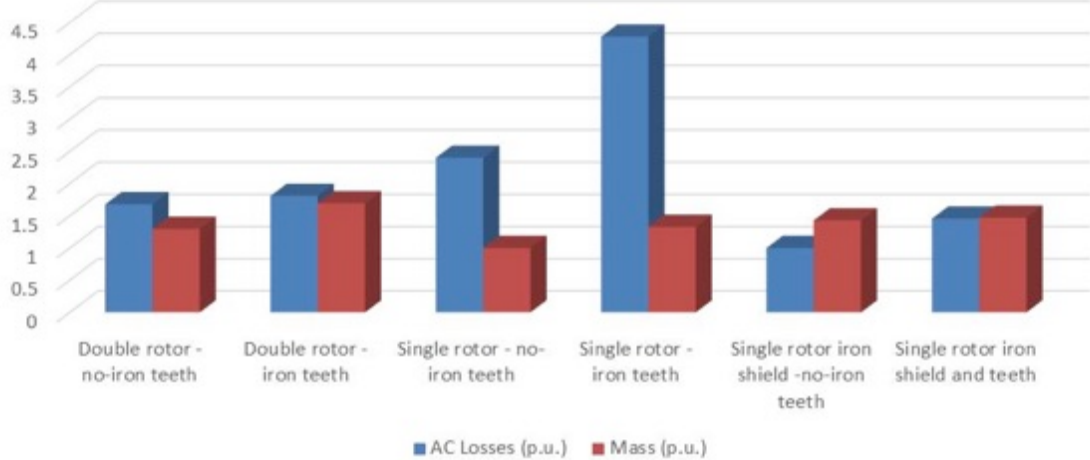


Figure 2.10 Mass (relative) and AC loss (relative) for the six superconducting stator configurations.

## 2.2 RAPID SCANNING OF CONFIGURATION.

Because of the large wide space to be investigated, we have used an approach where the parameters of the designs are changed over a given range, and the designs, if feasible, are compared.

We have used the approach with radial flux machines. 6 machines are considered: the HTS conventional machine (with HTS rotor only), machines with HTS stators (but with two filling fraction, 0.25 and 0.5), a machine with a cold iron shield, and a machine with no backiron. The results are shown in Figure 2.11. The weight of the machines as a function of the amount of conductor required indicate that there is a tradeoff between machine weight and amount of HTS. The lighter machine corresponds to that with no backiron. We have yet to reproduce the results of the no-backiron case with the more detailed model.

Figure 2.12 shows a comparison of the weights and the corresponding refrigerator to remove the AC losses. The figure indicates that machines with superconducting stators may be marginally better than HTS designs with conventional stator, but may be dominated by the weight of the cryocooler at 20 K. Conventional refrigerators are used (using the models described in section 9). Lighter refrigerators could have a large impact on the results, as indicated in section 9. In particular, highly efficient, lightweight Reverse Turbo Brayton systems look highly attractive and would profoundly change the conclusions derived from Figure 2.12

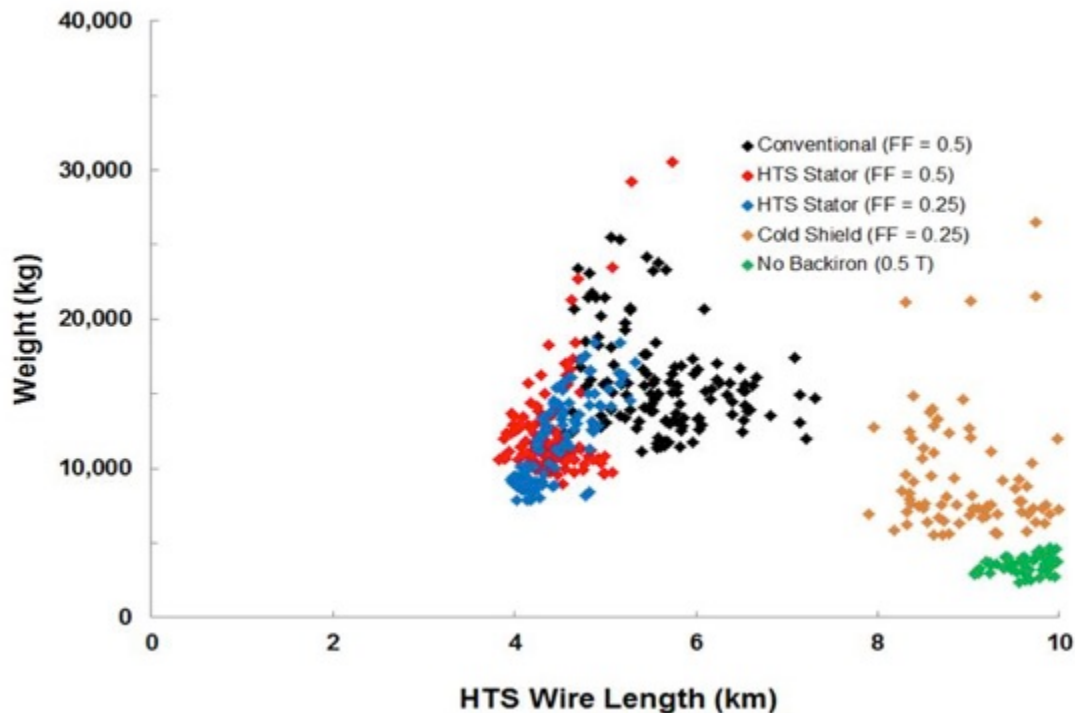


Figure 2.11. Optimization runs showing HTS baseline case and showed pathway to lower weight cases for SC stators.

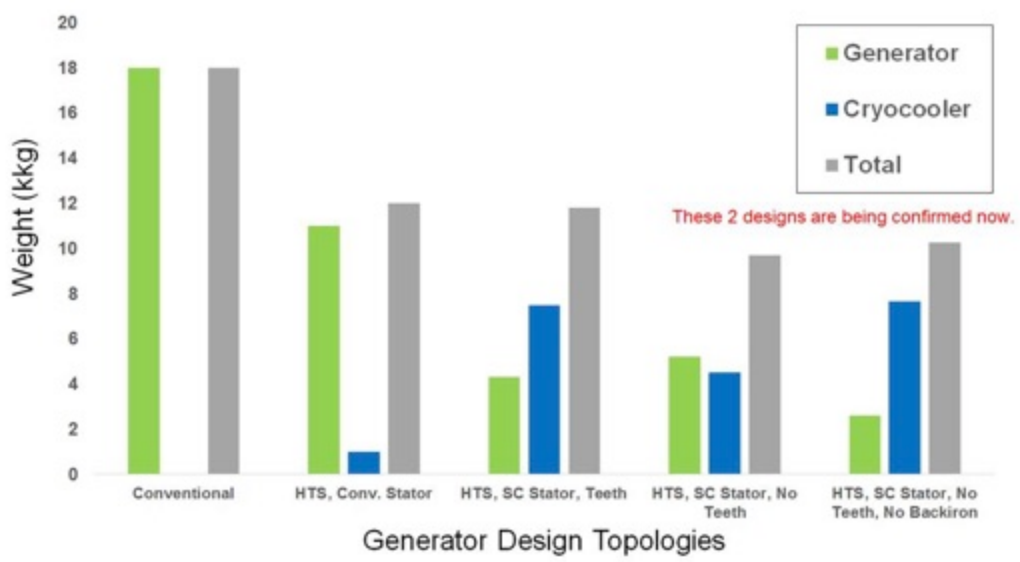


Figure 2.12. Weights of the generator and the refrigerators for the different topologies included in Figure 2.11.

## 2.3 AXIAL FLUX MACHINES

We have investigated axial flux machines. They tend to be more compact than radial flux machines, compared to radial flux machines. The coil geometry is also a lot simpler than conventional stator

windings, as described in section 5. The windings can be in the form of deformed racetrack forms, with either simple common cryostats or individual cryostat around each winding.

Figure 2.13 shows a conceptual design of an axial flux machine. The figure illustrates one with one rotor and two stator windings. The coil windings are in “pancake” type designs. For the Navy applications, the size limitations are more severe in the axial direction, rather than in the diameter. The reason is that the prime mover is a turbine that is of diameter substantially larger than the generator, and the generator is in the “shade” of the prime mover. However, the axial direction extend the power system size, and thus, limiting the length of the generator substantially decreases the footprint of the system.

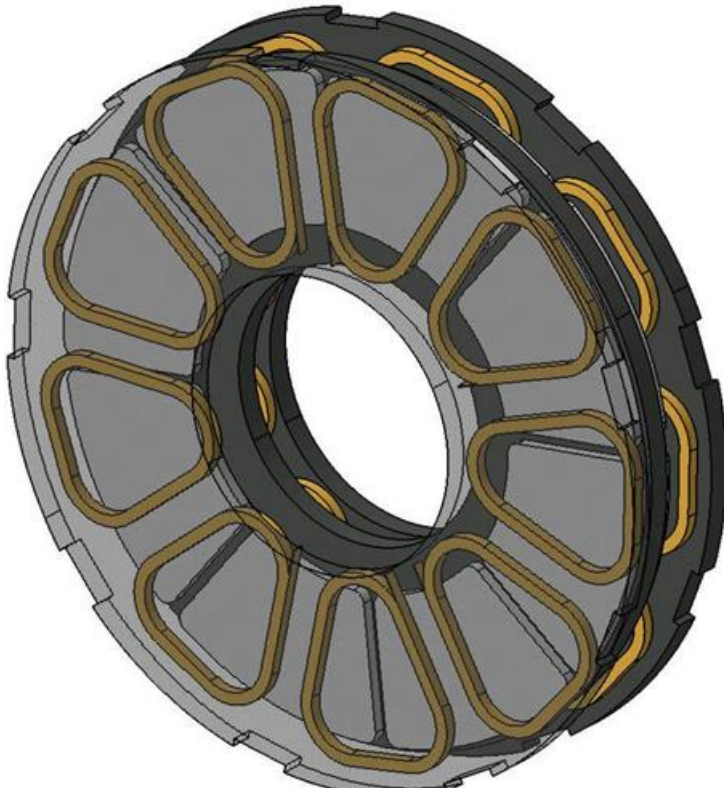


Figure 2.13 Example of axial flux generator with 2 stators and 1 rotor design

For high power applications, multiple rotors are required, increasing the complexity of the design. The reason for the high power limitation has to do with the required size, and in particular, the radial build. For high power, the large diameters at high speed yields very high surface speeds. The surface speed limit the material choice, due to large centrifugal loads (due to acceleration and density of the structure) and the associated stresses. For stainless steel the rotational speed is limited to about 200 m/s, while for aluminum, it is 300 m/s (mostly due to the lower density). The limitation, at 7000 rpm, is about 0.5 diameter for stainless steel, and about 0.8 m diameter for aluminum 1061. Thus, axial flux machines are not of interest for high power, high speeds applications, such as the Navy machine that we are investigating.

## 2.4 TOROIDAL STATORS

We have investigated toroidal stator configurations. As discussed in section 5, racetracks coils are very attractive from a manufacturing point of view, with coils that could easily be made from

conductors that are reacted after winding (in the case of MgB<sub>2</sub>), or wound after react (as in the case of the 2<sup>nd</sup> generation coated conductor or Bisco 2212).

The geometry offers some additional advantages, especially if the racetracks are oriented in the radial direction. In this section we describe that configuration. The alternative configuration is of interest to machines that have a high pole number, or in the case of low pole number, several of the windings of the same phase are placed next to each other. That configuration results in larger amount of superconductor exposed to the magnetic field (increasing AC losses) and decreased coupling (because the flux in-between racetrack windings does not generate EMF).

As a consequence, we have only concentrated on the radially oriented windings, as illustrated in Figure 2.14. Thus configuration have several advantages:

- High flux coupling: The windings capture all the flux that is accumulated in the stator iron)
- Lower exposure of the superconductor to varying magnetic fields: Only the windings near the stator see large stator fields, while the outer layer of windings only sees the self-generated AC fields.
- Ease of manufacturing:
  - racetrack coils are easily made from many superconductors
  - each coil could be placed in a separate cryostat.

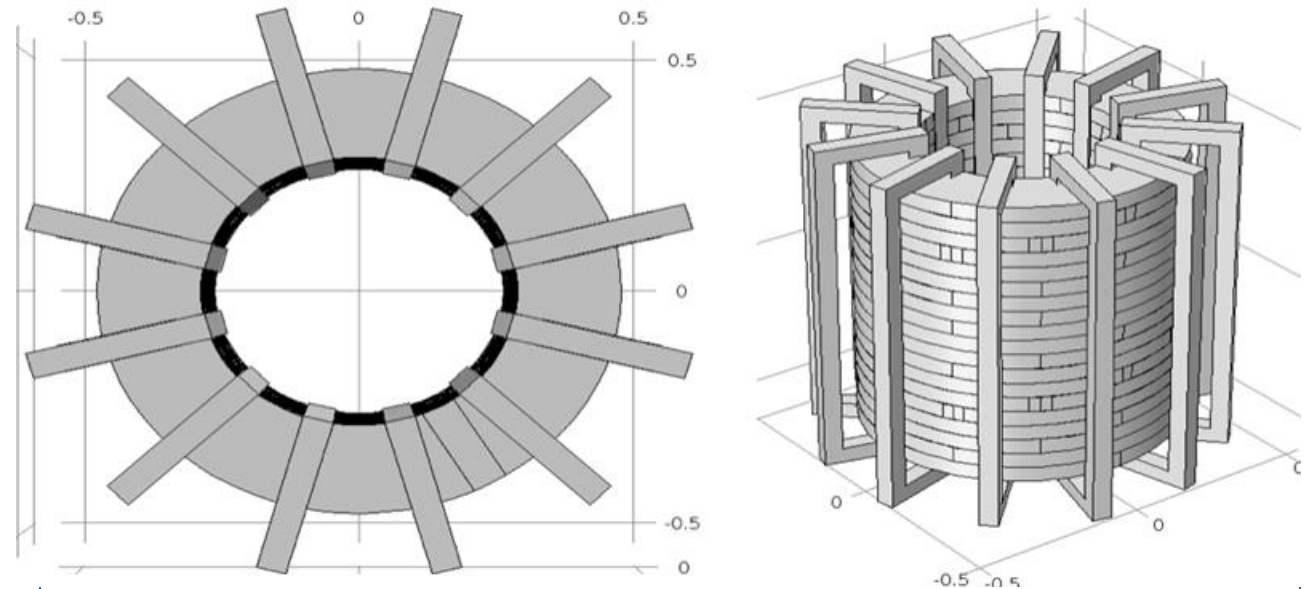


Figure 2.14 Top and side view of a toroidal winding generator.

There are problems with manufacturing of the toroidal stator (the need to have the stator winding encircle the stator iron). We discuss several means to manufacture the stator in section 3.3.3.

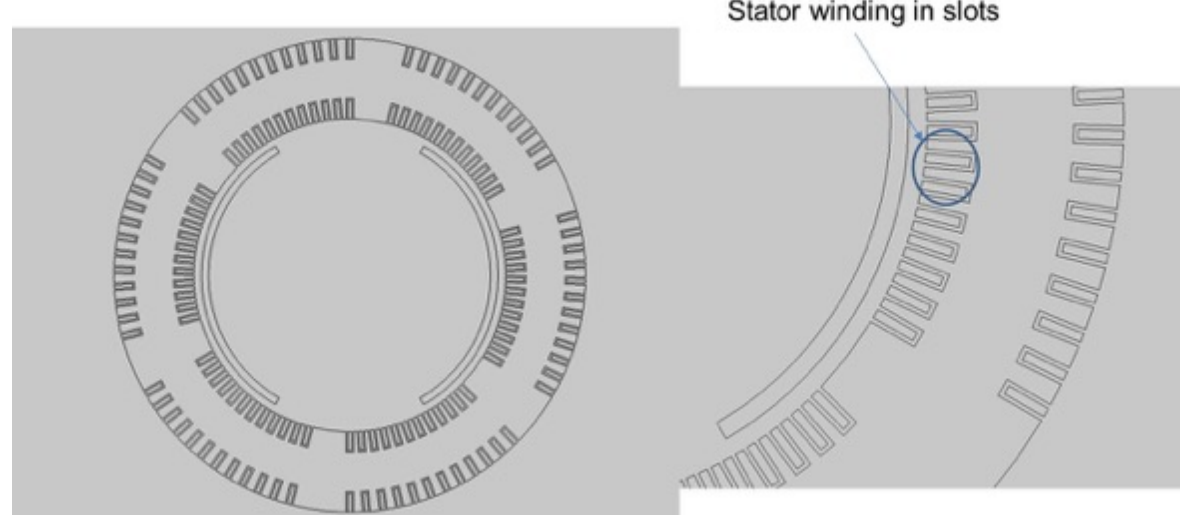


Figure 2.16 Ring stator machine (slots) geometry

Figure 2.15 shows the diagram for the model used to calculate the performance of the toroidal stator machine. Figure 2.15 shows both inner and outer legs of the toroidal windings inserted in the iron. It is likely that for manufacturability, the outer leg of the toroidal winding should not be in the winding, in order to allow for placement of segments of the stator iron in the bore of the toroidal windings. The methods of construction are described in Section 3.

With this configuration, as well with others, it is possible to have designs where the magnetic field is dominated by the rotor or by the stator. Figure 2.17 shows the results of toroidal winding (with the outer leg removed from the stator iron, as described above) for both stator and rotor dominated fields. In the case of the stator dominated field, the field in the rotor changed substantially when the stator is energized that when it is not, and can increase or decrease in intensity. However, the field in the rotor, under steady conditions, does not change in time, as the rotor is precessing at the same speed at the field in the stator coils, and thus, it is constant). In the case of rotor dominated, shown in Figure 2.17(b), the field in the rotor does not change substantially when the stator is activated. We intend to optimize the design and determine which of the two cases results in the lighter machine.

We use the cable design described in Section 7, with 81 superconducting strands surrounding a 3 mm tube that carries the coolant. We assume two such cables per slot, with 72 slots around the machine. The geometry is shown in Figure 2.18.

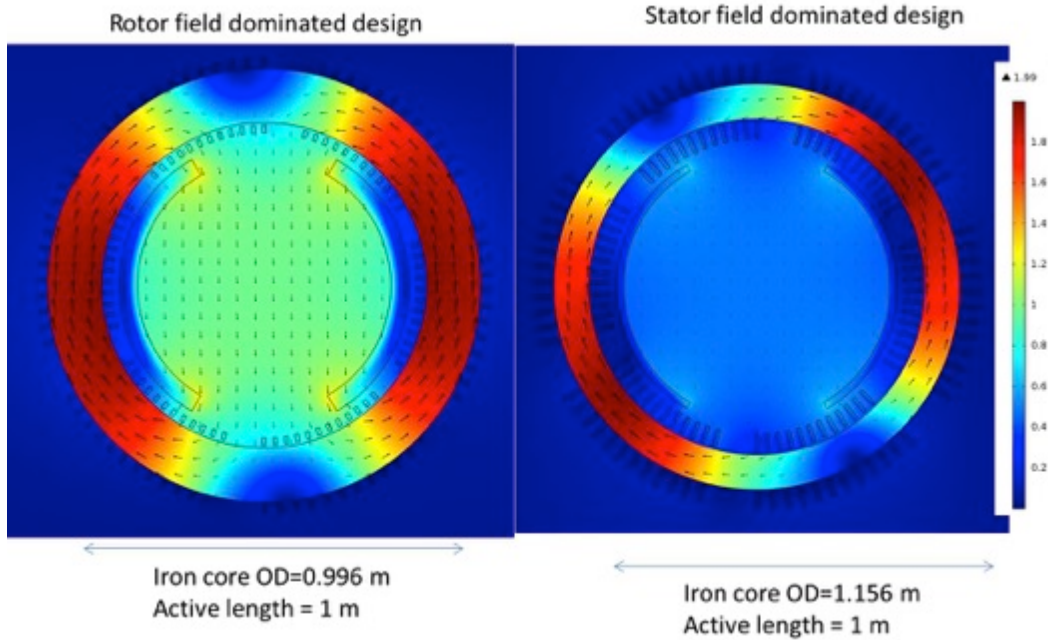


Figure 2.17 Possible designs for toroidal machines, at 10 MW and 7000 rpm.

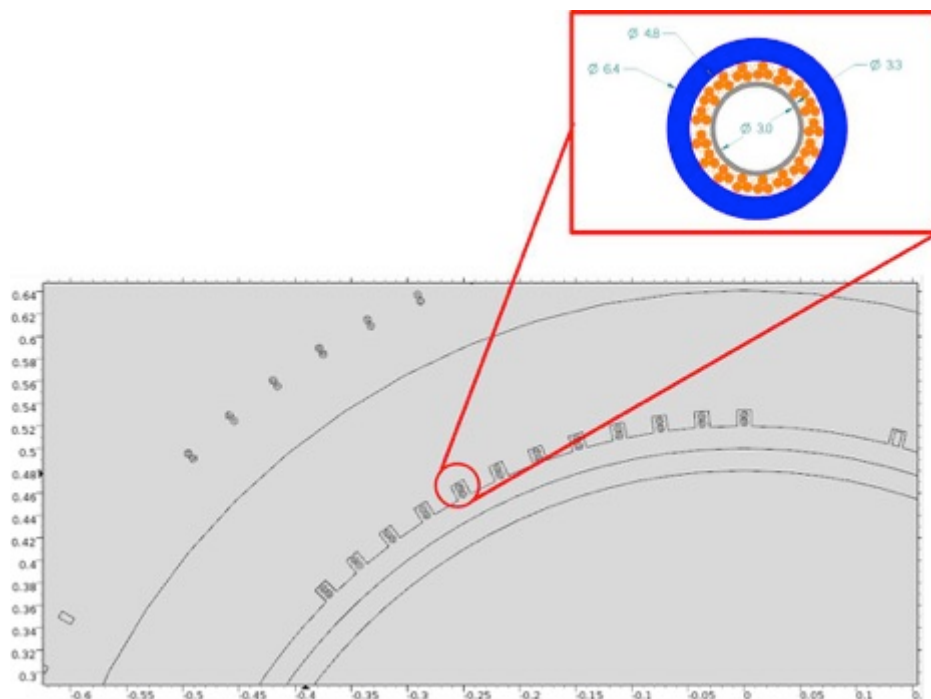


Figure 2.18 2 CICC cables per slot, only inner leg of toroidal stator winding in the slot.

Typical field profiles, for a design that satisfies the requirement of 14 MW at 7000 rpm, is shown in Figure 2.19. Note that the outer leg is removed from the iron. Also, that the field is effectively trapped in the stator iron, and that each coil can intercept all of the field accumulated in the iron during the cycle, increasing the coupling. Also, there is very small fields in the outer leg of the machine, decreasing substantially the AC losses in the superconductor.

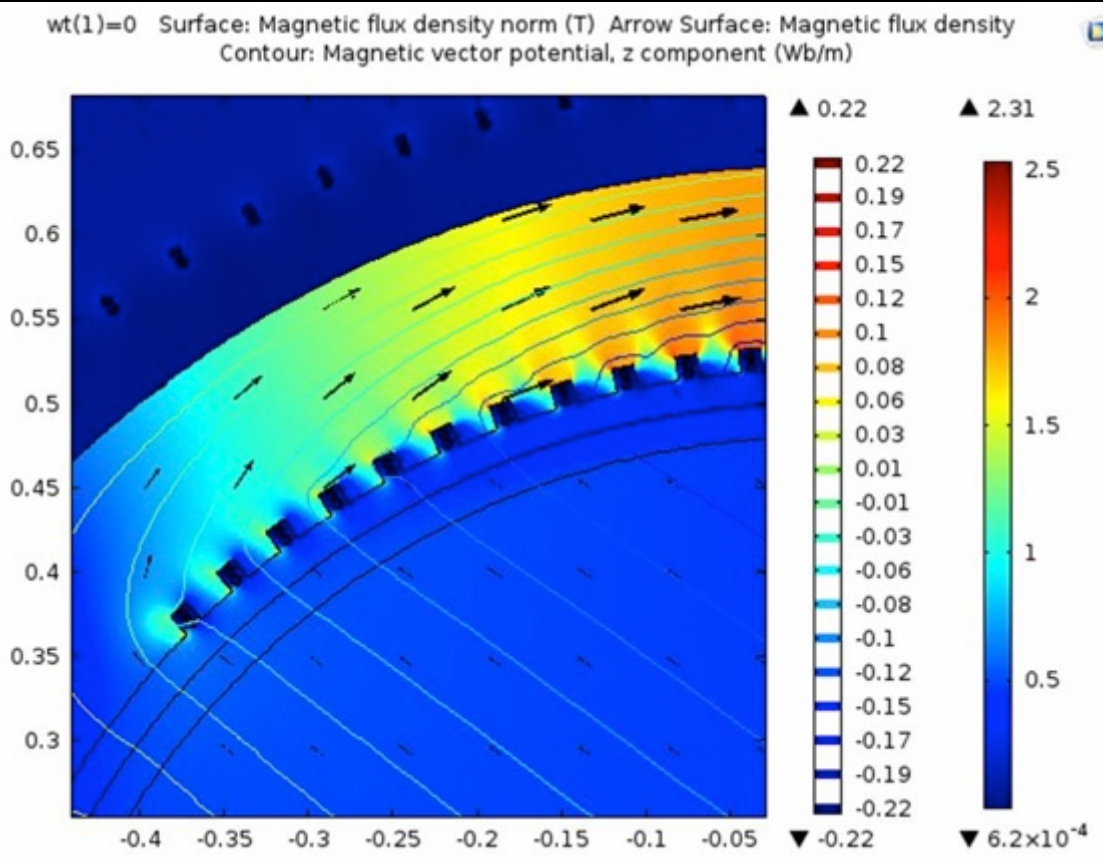


Figure 2.19 Field on the iron and field lines for the toroidal winding case.

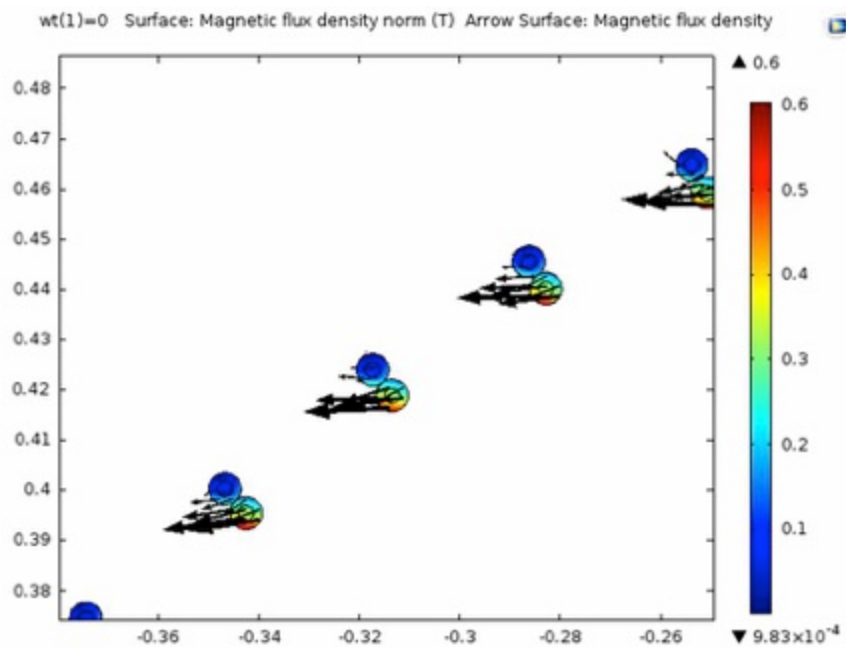


Figure 2.20 Field amplitude and direction at the highest field position along the inner leg of the stator winding.

The field on the inner winding of the toroidal stator is shown in Figure 2.20. There are very limited sections of the winding that have substantial fields, on the order of 0.5 T. Most of the winding experiences a field that is comparable to the self field, about 0.2 T. Not captured in Figure 2.20 is the fact that the field does not rotate around the conductor, but is about in the same direction, but changing amplitude and sign. The lack of rotation of the field has substantial consequences for the AC losses, decreasing them substantially.

The field and the field direction in the outer winding is shown in Figure 2.21, indicating that the self field is about 0.1-0.2 T. In this case the direction of the field rotates around the conductor, as should be the case for self-field.

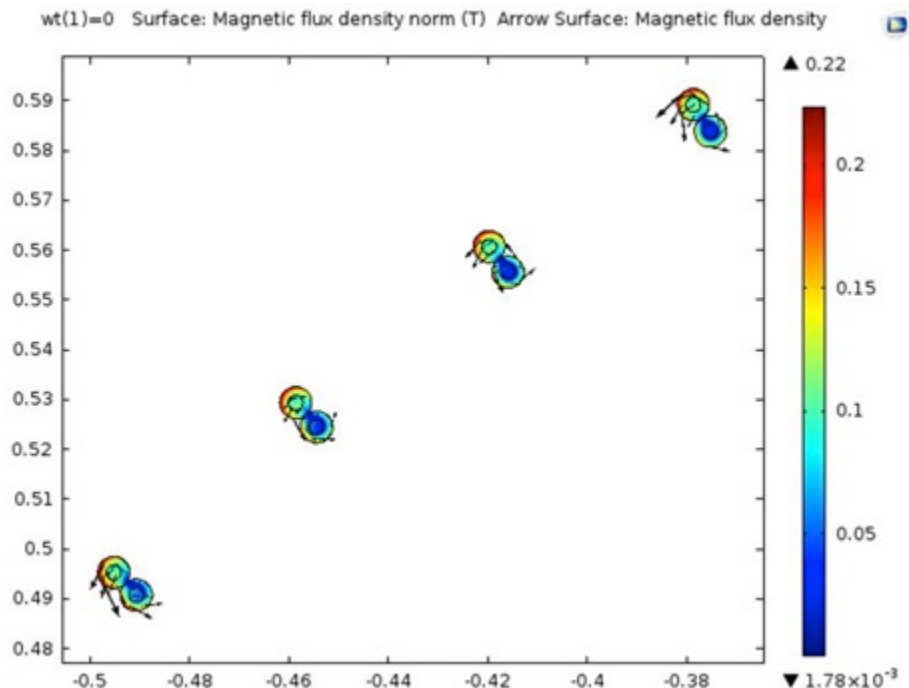


Figure 2.21 Field amplitude and direction at the highest field position along the outer leg of the stator winding.

The results are summarized in Table 2.2. The assumption on the cable design and the strands are provided in the Table. The change in field amplitude is assumed to be about 0.25T. with only a small rotating component. The field in outer leg is assumed to be 0.06 T, with a 50% rotating component. The losses in the winding about 660 W. This is small number for such a large machine, allowing substantial improvements in total machine efficiency (to over 99%).

The weight of the machine is dominated by the iron (about 86% of the total weight of the machine, with the rotor being about 6% and the cable about 1%). The mass of the machine is about 2.8 tons, with a specific torque of about 7 Nm/kg and a specific power of about 5 kW/kg. It should be noted that these numbers do not include the refrigerator. Using the results from Section 8.7, the weight of 2 refrigerators is about 2.4 tons, decreasing the specific power of the system to about 2.5 kW/kg. The goal in the middle term set up by the Navy is over 2 kW/kg, so this machine already surpasses the goal set up in that document by the NAVY. [Kuseian]

Table 2.2 Illustrative design of toroidal winding machine

MgB2 cable					
Jc	8000 A/mm <sup>2</sup>				
Filament OD	10 $\mu\text{m}$				
Twist pitch	10 mm				
Matrix res.	140 n $\Omega$ .m				
Nb filaments	5000/cable				
Ic cable	3140				
I/Ic	0.65				
In slots					
$\Delta B$	0.25 T				
Rot Field	20 %				
Top sections					
$\Delta B$	0.06 T				
Rot Field	50 %				
AC losses					
Magnetization + current	400 W		93 W		493 W
Eddy current	20 W		1.5 W		21.5 W
Coupling	125 W		7.5 W		132.5 W
Matrix Mag.	20 W		2 W		22 W
Total	560 W		104 W		664 W

machines. A machine with 4 poles on rotor and 6 poles on stator was selected for evaluation (Fig. 2.22). MgB2 windings operating at 20K were selected for the stator. As shown in the figures, 2 stator coils are energized at a time. Key dimensions and design results are summarized below:

Number of poles on rotor	4
Number of poles on stator	6
Nominal speed	7000 RPM
Stator coils	MgB2
Stator coil operating temp.	20 K
Radius to foot of rotor poles	250 mm
Rotor pole width	320 mm
Rotor pole height	160 mm
Air gap length	3 mm
Stator inside radius	163 mm
Radius to bottom of stator poles	672 mm
Outside radius of stator yoke	870 mm
Axial length	3500 mm

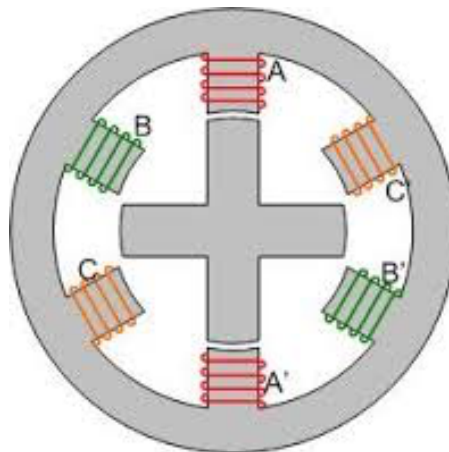


Figure 2.22: Selected SRM configuration for study

Vanadium Permedur core material was selected for both rotor and stator laminations. The air gap between rotor and stator was selected a 3 mm, which is quite aggressive for such a large diameter machines. 2-D flux plots were created for calculating phase inductance for two positions; 1) rotor and stator poles are aligned, and 2) rotor and stator poles are completely unaligned. Figure 2.23 shows variation of inductance as a function of phase excitation. At low saturation level, ratio between aligned and unaligned position was 10.3 but at high saturation levels it dropped to 1.08.

Figure 2.24 shows variation of flux/pole as a function of excitation for the two positions. The upper curve (solid line) shows flux as a function of excitation when poles are aligned. The lower curve (dotted line) is for the case when poles are misaligned. In general, the machine output is proportional to the area between the two curves. In most designs, SRM are designed to operate at an excitation level just above the knee of the upper curve. As shown in the figures, maximum output of this machine will be proportional to area enclosed between the two curves. This was the design point selected for the current study.

Figure 2.25 shows power generated as a function of stator current. The relationship is nearly linear but losses are a strong function of pole stator current and frequency. Listed below are some key mechanical features of the SRM that make this concept unattractive;

- Tip speed of rotor for the selected rotor radius is 349 m/s, which is too high for magnetic hardened steel with an allowable operating stress of 33 ksi. The rotor radius needs to be reduced to 714 mm (28 in) for staying within the allowable stress limit
- Rotor mechanical dimensions (rotor diameter of 952 mm (37.5 in) and axial length of 3500 mm (138 in)) exceed the ONR guidelines
- Expected machine mass (~ 22 kkg) is higher than a conventional machine and also exceeds the ONR guidelines.

Core loss density at 1.5W/kg at  $\sim 2T$  and 60 Hz, increases to  $1.5*(467/60)2 = 91$  kW/kg. This translates to 2MW of core loss. It will be extremely challenging to remove these losses.

All these factors make this machine unsuitable for ONR intended applications.

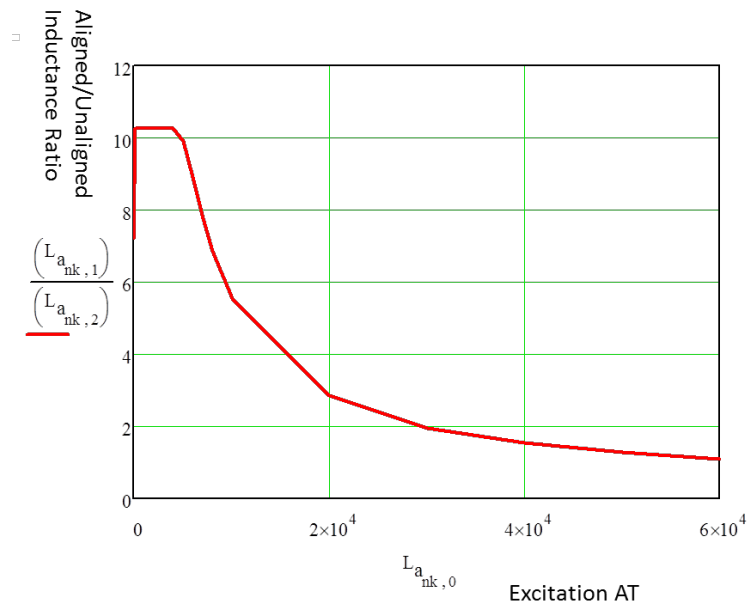


Figure 2.23: Variation of inductance in aligned and unaligned stator and rotor poles as a function of stator and rotor poles

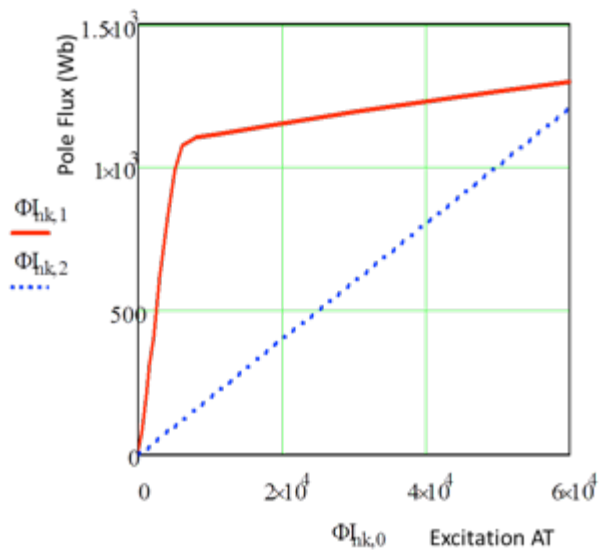


Figure 2.24: Flux per pole as a function of excitation for the aligned and unaligned position of poles

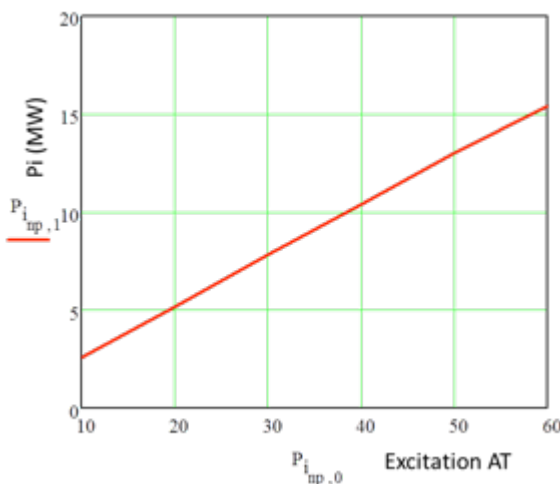


Figure 2.25: Power generated as a function of excitation

Superconducting (MgB2) coil design details are summarized below:

- Stator coils are sized on the basis of a 3 strand cable; each strand being 0.83 mm diameter
- Maximum field experienced by a MgB2 coil  $\sim 0.23\text{T}$  at excitation of 60,000 ampere-turns (AT)
- The cable is operated at 60% of  $I_c = 1735\text{A}$ ; critical current ( $I_c$ ) being 2890 A at 20K
- Each coil has 35 turns, which could be accommodated in a single layer winding
- Length of cable needed for each coil is 276 m; or total length of strands is 830 m

AC losses in MgB2 coils are listed below:

- Hysteresis losses in MgB2 strands/phase (each phase includes 2 coils) = 2960 W
- Thermal conduction through current leads = 340 W
- Thermal heat load through cryostat = 80 W
- Total heat load for each stator/phase = 3380 W

- Compressor power needed to remove these losses = 1.5 MW
- Core loss is also on the order of 2 MW

Total compressor power only to cool one phase is 3.5 MW, which is excessive for a 14MW machine – thus making this concept INFEASIBLE.

In summary, features making SRM unattractive for the ONR specified application are listed below:

- The SRM design exceeds ONR guidelines in mass by 83% and axial length by ~ 22%.
- Refrigeration power 3.5kW leads to a system efficiency of 95% which is lower than ONR specified target of 98%
- Additionally SRM being inherently acoustically more noisy would make them less desirable for ONR Applications

Because of all above stated unattractive features of SRM, it was not studied further.

## 2.6 AC HOMOPOLAR MACHINES

AC Homopolar machines are commonly employed in various industries. These machines are suitable for high speed applications as they have no windings on the rotor. Some of the Pros and Cons of AC Homopolar (AHP) machines are listed below.

Pros:

- a) Solid rotor body without any winding – simplifies design
- b) Synchronous machine with superconducting 3-phase winding
- c) Both field and armature superconducting windings are stationary – enabling simpler cryostat and easier cooling
- d) Employs single layer armature winding for ease of construction and higher power density
- e) Higher air gap magnetic field than conventional machines

Cons:

- a) Best designed AC Homopolar has power density  $\frac{1}{2}$  of heteropolar machines
- b) Rotor operation under partial vacuum desired for reducing windage loss

General Electric [Sivasubramaniam] built such a machine for the US Air Force employing superconducting field winding and conventional air gap winding made of fine strand copper Litz wire. In this program, we investigated two options, one with REBCO and the second one with MgB2.

The overall machine configuration is shown in Fig. 2.26. The rotor is made of solid magnetic iron with 2 salient poles on each end. The poles on ends are displaced by 90 degrees as shown in the figure.

This configuration results in an equivalent 4-pole configuration as viewed from the stator. The armature employs 3-phase, 4-pole winding configuration shown in the figure. Such a winding made of copper Litz wire was built by AMSC [Kalsi] for a 4-pole, 1800 RPM synchronous motor. The excitation field winding constitutes a single circular coil placed outside of the armature winding.

Laminated iron core on the stator encloses both armature and field windings.

The iron core laminations are arranged in 2 different fashions. On each end, laminations are stacked radially to let field lines enter each lamination through its edge. The middle section of the iron core has laminations wound like a spring using the rotor axis as the reference. The flux lines enter and

leave these laminations also through their edges. Thus the flux lines never experience broad side of laminations. It should be noted that 3 part lamination could be combined into a single lamination at the risk of trapping the field coil, which would not be accessible without taking the whole core apart.

The flux travel pattern is shown in Fig. 2.27 and is explained below:

- 1) From rotor pole, the field travels across air gap (x direction) and enters into the stator
- 2) The field travels in the lamination (in plane)
- 3) The field crosses into lamination stacked radially and starts travelling azimuthally (y direction)
- 4) The field continues to travel azimuthally
- 5) The field starts travelling axially (z direction) into lamination stacked circumferentially
- 6) The field travels in the lamination (in plane)
- 7) The field travels across the air gap into the rotor pole
- 8) The field returns back to position 1 through the solid rotor core

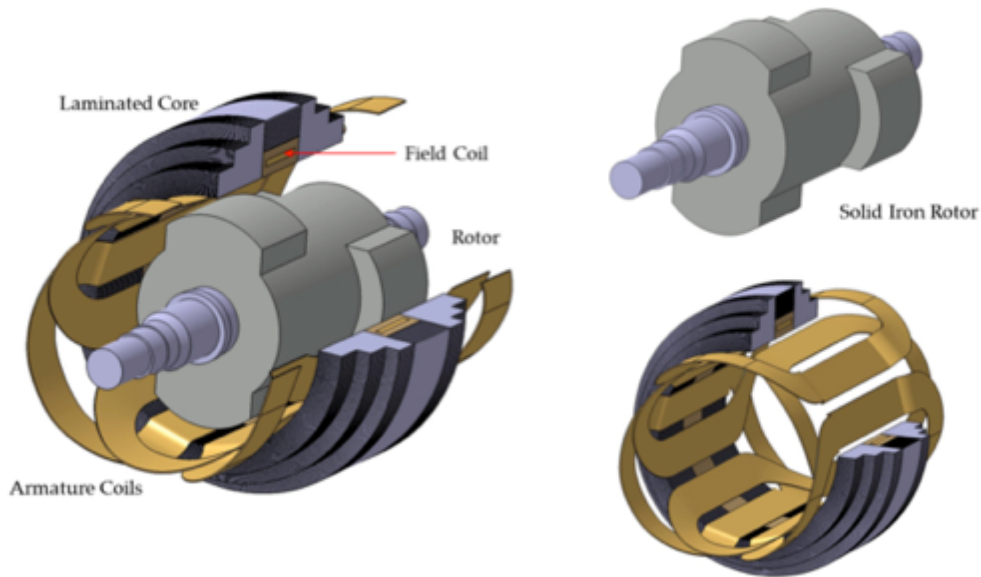


Fig. 2.26: Overall Homopolar machine configuration showing rotor, armature and field windings and laminated magnetic core

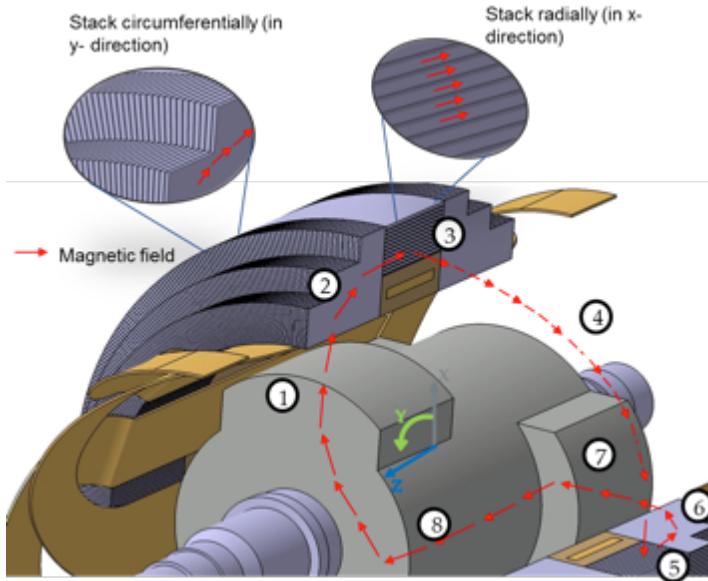


Fig. 2.26: Arrangement of machine components showing iron lamination pattern details and direction of flux travel

### 2.6.1 WITH REBCO IN ARMATURE AND FIELD WINDINGS

The magnetic cross-section of the machine is shown in Fig. 2.28 – all dimensions are in mm. The limiting factor for determining machine dimensions is the surface stress experience at the rotor pole tips. Rotor is made of hardened steel with yield and ultimate stresses of 50 ksi and 100 ksi, respectively. Allowable stress is taken as minimum of  $2/3 \times \text{yield}$  or  $1/3 \times \text{ultimate stress}$ . On this basis, allowable rotor tip speed is 262 m/s. In the current machine design, the selected pole tip radius is 340 mm – which corresponds to a tip speed of 250 m/s, which is close to the allowable tip speed calculated above. An air-gap length of 5 mm is chosen as a reasonable practical clearance between the stator and rotor. Rest of the dimensions are selected iteratively (but manually) to generate required power. Two highlighted areas are for the ReBCO windings; larger area represents armature coils and the smaller area is the excitation field winding. Radial thickness of each winding area is 42 mm, which consists of 12 mm thickness for the ReBCo coils and 15 mm of each side of the coil for the aerogel thermal insulation. The rotor is constructed from solid magnetic steel and has 80 mm tall pole bodies. Each pole axial length is 250 mm. The field winding has an axial length of 200 mm and has a mean radius of 467 mm. These dimensions represent the best guesses and they are not optimal in any sense. The stator employs laminated iron core. This study has assumed JNEX-Core (Model 10 JNEX900, 0.10 mm thickness) as the core material in order to reduce AC losses due to magnetic field of 233 Hz. Analysis in (Appendix A) shows that the core losses are only a small fraction of total losses. Possibility of using another material could be evaluated during machine optimization design study in the future.

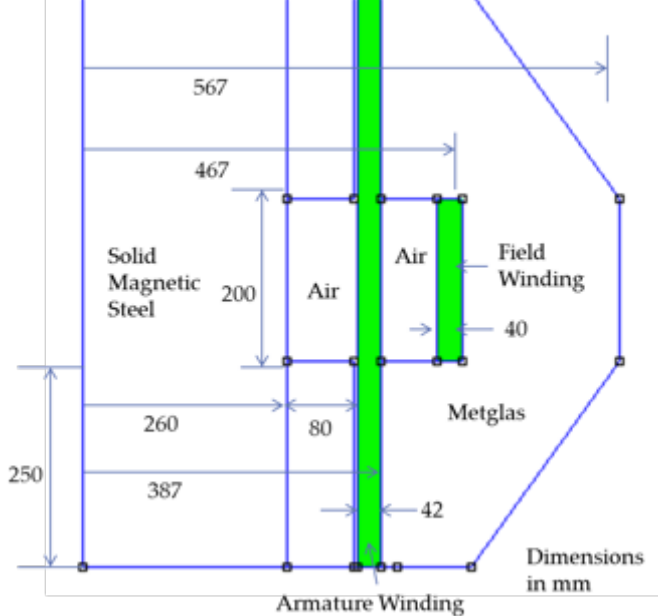


Fig. 2.28: Cross-section showing dimensions for various components of the machine

An air gap armature winding arrangement used by AMSC for their 5,000 HP motor is shown in Fig. 2.29. These coils were built with copper Litz cable. This study assumes that similar coils could also be built with ReBCO Roebel or MgB<sub>2</sub> cables. Fig. 2.30 shows superconducting armature winding concept envision for the current machine. All coils are epoxy impregnated to create a monolithic structure capable of supporting the loads other than the main torque, which needs to be transmitted to the back iron.

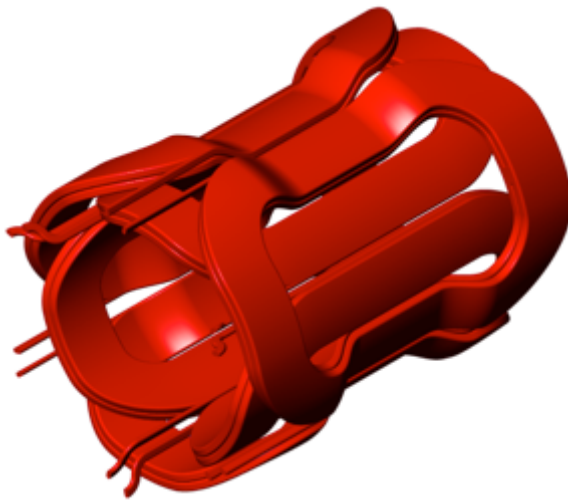


Fig. 2.29: A single layer airgap winding concept employed in an AMSC 5,000 HP motor [Kalsi]



Fig. 2.30: Superconducting single layer winding concept proposed for the current machine

Fig. 2.31 shows radial magnetic field that links with Phase A coils and its harmonic content calculated with a 2-D FEA code. All harmonics are odd and their magnitude is small and acceptable – on the basis of criterion applied in conventional machines. However, to be precise their contribution to AC losses could be estimated if necessary.

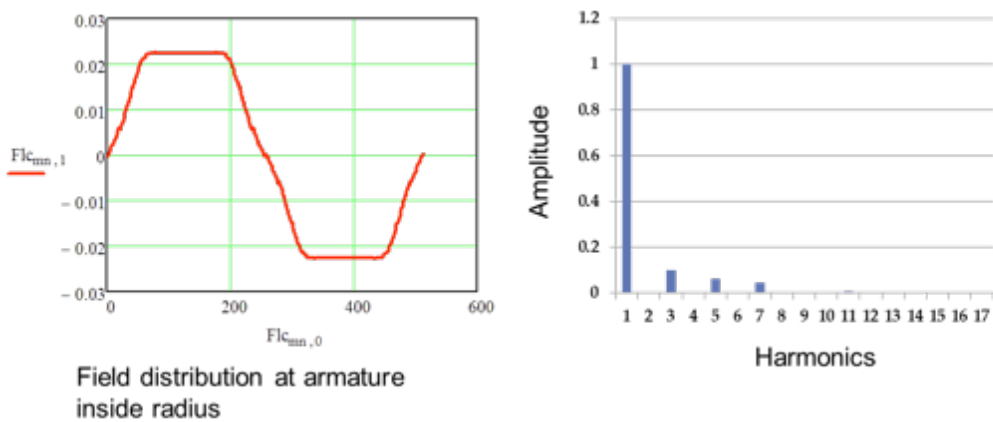


Fig. 2.31: Radial field distribution at Phase-A coils (open-circuit) and its harmonic content

The machine configuration shown in Fig. 2.26 is totally enclosed in a 50 mm thick cylinder located at the outside radius of the stator core. Fig. 2.32 shows the cryostat outside of the iron. Both ends of this cylinder are capped with 50 mm thick plates. The whole volume inside this cylinder is evacuated. All coils are insulated with aerogel from the room-temperature. There are no windage losses as the rotor operates in a vacuum space – required for a high speed machine.

Fig. 2.32 shows overall configuration of the machine, including relative positions of stator and rotor components. Except for the superconducting coils, all stator and rotor components are at room-temperature. Superconducting coils are cooled to a temperature necessary for selected superconductor material. As shown in Fig. 2.33, each coil has axially running G10 (or equivalent) support for transferring torque to the support pins. The epoxy impregnated monolithic armature structure (similar to Fig. 9) is supported off the stator frame using Kevlar straps shown in Fig. 2.34. The strap loops

around the support pins located at ends of the armature assembly as shown. On the basis of allowable stress of 13.3 MN in a 78 mm diameter rope (data from internet), the needed strap (rope) cross-section is 20 mm<sup>2</sup>. This strap supports the superconducting armature mechanically at its intended location and transfer torque to the stator frame. One end of the strap is at room-temperature and the other at the armature operating temperature. Thermal conduction from ambient to cryogenic temperature is expected to be low.

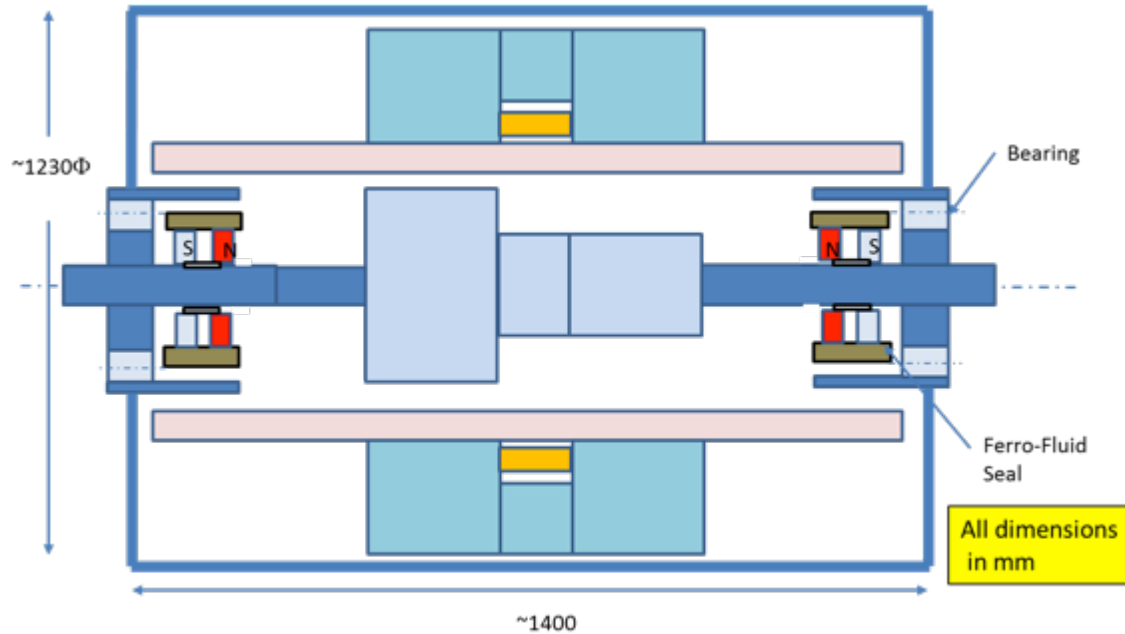


Fig. 2.32: Cross-section of the machine showing stator and rotor components along with ferro-fluid seals and bearings

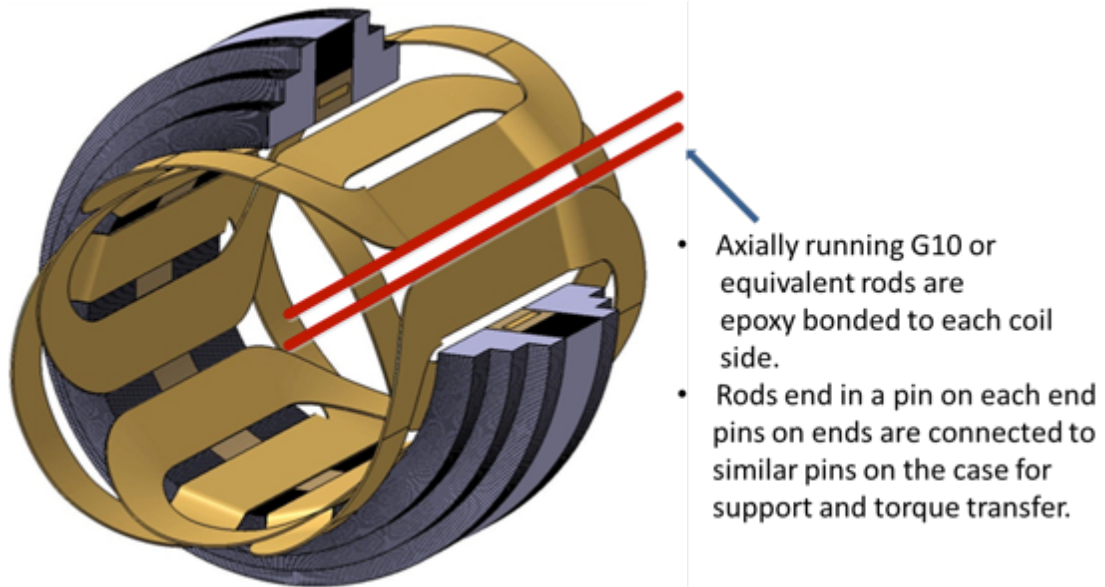


Fig. 2.33: Individual armature coil supported by axially running G10 (or equivalent) support rod

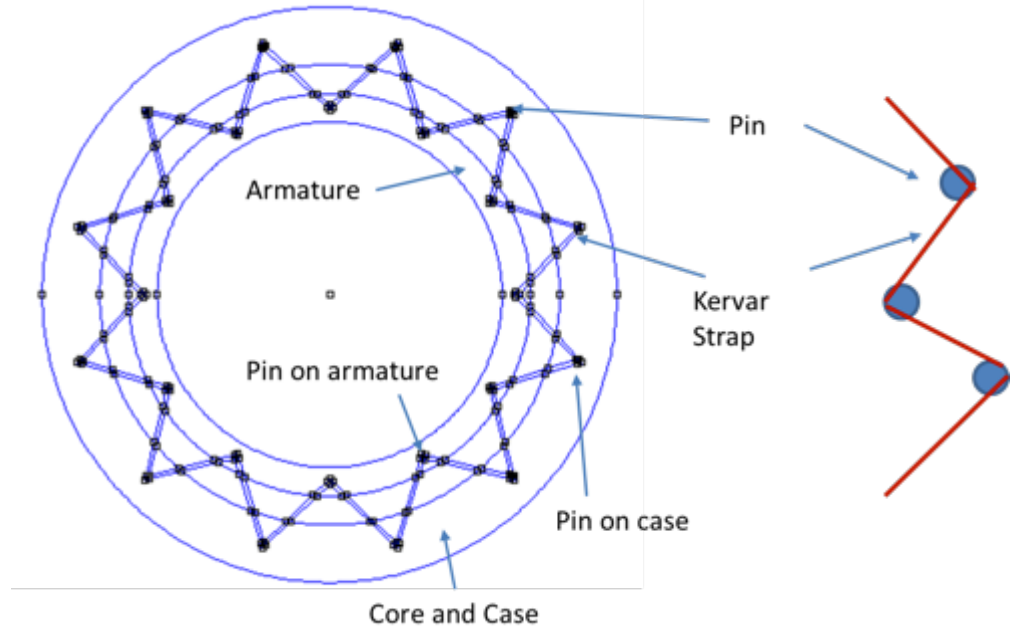


Fig. 2.34: Superconducting armature support is supported off the stator frame using Kevlar straps

Fig. 2.35 shows detailed arrangement of stator components. All components of stator, except the superconducting coils, operate at room temperature. The ReBCO armature coils, radially 12 mm thick (includes cooling tubes Fig. 2.36), are surrounded in an aerogel layer (15 mm thick) and are operated at 35 K. The field coil is also surrounded with 15 mm thick layer of aerogel for insulating it from the room temperature iron core.

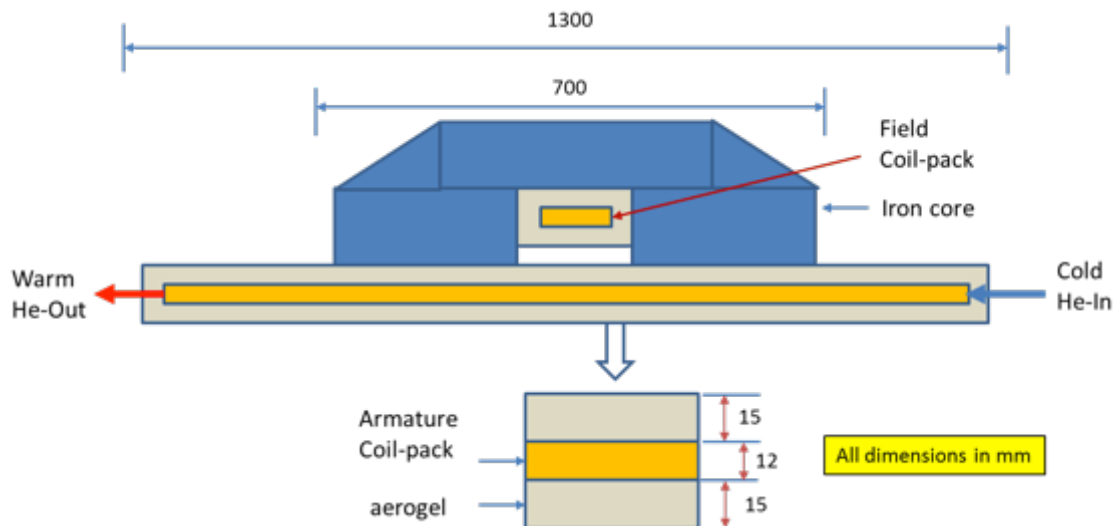


Fig. 2.35: Cross-section of the machine showing armature and field coils

Fig. 2.36 shows an armature coil with its dedicated cooling tubes attached to its both sides. Cold helium is circulated through them for keeping the coils at intended 35 K operating temperature. The pancake coil build is also shown in the picture – width of each coil is about 60 mm for coils employing with Roebel cables built from ReBCO. Each pancake coil is about 7 mm thick and has 2.5 mm tall

rectangular stainless steel cooling tubes. A thin sheet of Alumina (or equivalent) sheet is inserted between the cooling tubes and the pancake. The Alumina sheet acts as a thermal shunt among all coil turns as well as an interface between the pancake and the cooling tubes. The cooling tubes are made in U-shape for preventing net voltage difference between its inlet and outlet ports. In order to obtain the best coil performance, it would be necessary to impregnate the pancake and cooling tubes together using a thermally conductive but electrically non-conductive epoxy (TBD). For ReBCO coils, each cooling tube is 20 mm wide and 2.5 mm tall and has 0.1 mm thick wall. Eddy-current loss (25 W) in these tubes (made of stainless steel) is negligible as compared to AC losses in the superconducting coils. Consider a race track coil with horizontal build of 60 mm (top sketch). Cooling tubes are placed on each leg of the racetrack. Bottom sketch shows vertical build of the coil sandwiched between the cooling tubes.

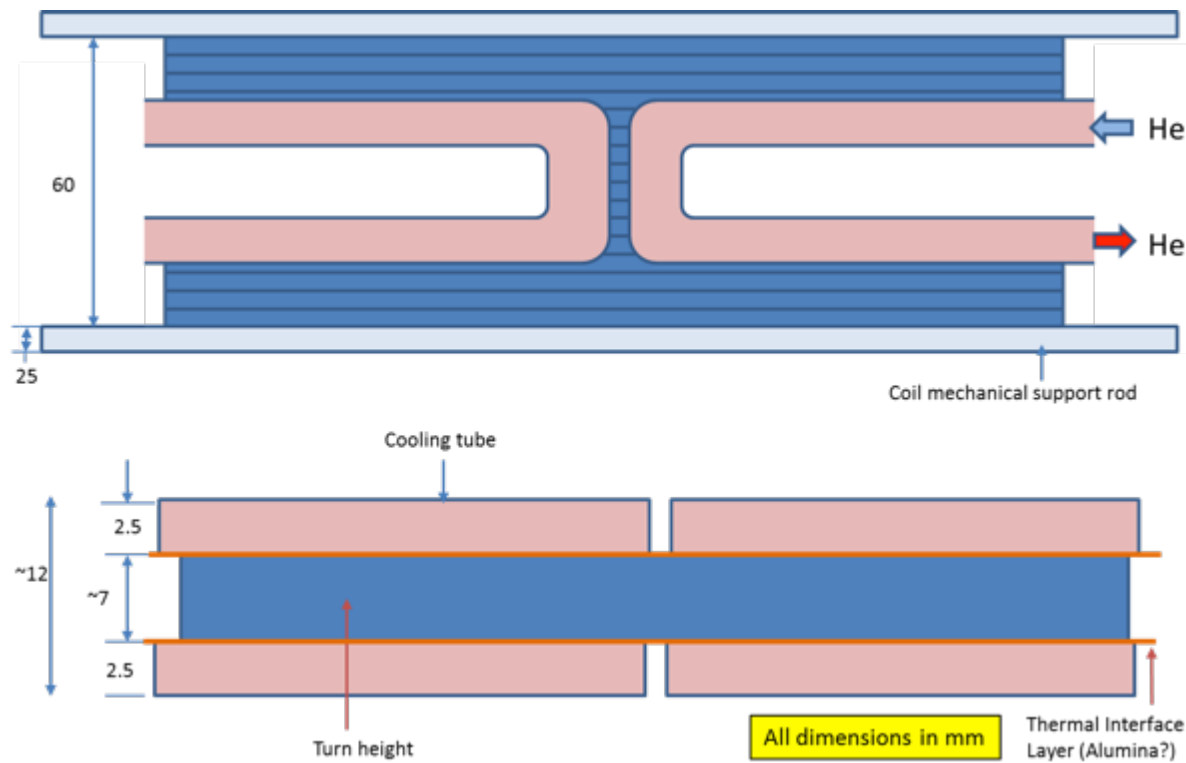


Fig. 2.36: Arrangement for cooling individual armature coils with cooling tubes attached to their sides

High temperature superconductor (HTS) ReBCO is employed for both armature and field windings. The solid iron rotor generates 4 poles, which are excited with a single circular coil made of 2 mm wide ReBCO conductor. The armature winding employs Roebel cable consisting 3 mm wide strands. However, a good analysis for calculating these losses is not currently available. The armature winding consisting of 6 coils is constructed using the single layer concept. Each coil has a single pancake and operates at 35 K.

The overall machine configuration is shown in Fig. 2.37 along with possible arrangements for the coolant manifolds. More details will be developed later if this concept is selected for detailed design. In order to reduce windage losses at the rotor surface, G10 pieces could be bolted to fill non-iron spaces. This concept is shown in Fig. 2.38.

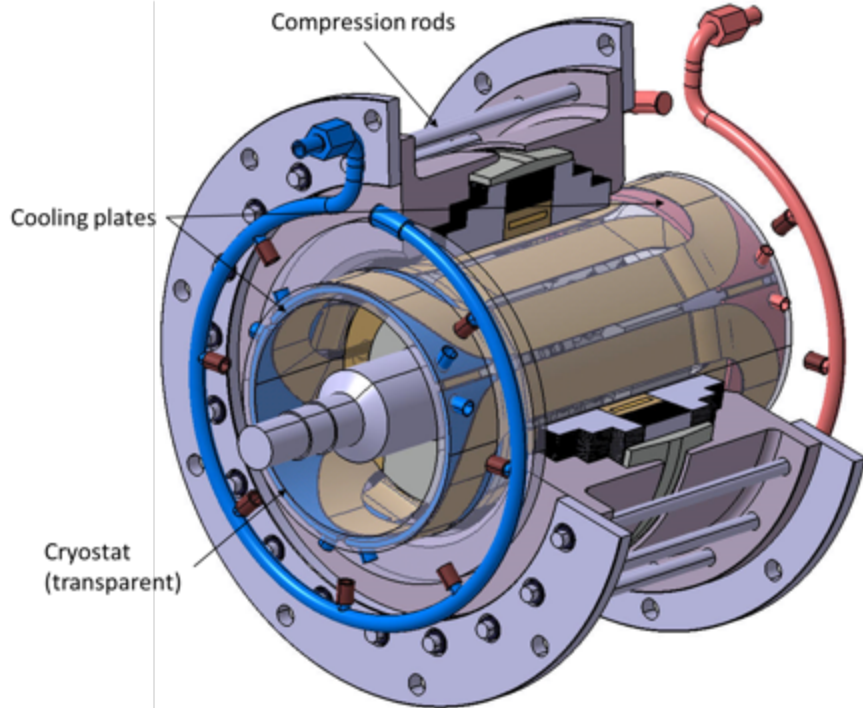


Fig. 2.37: Overall configuration of the Homopolar generator with a possible stator cooling arrangement

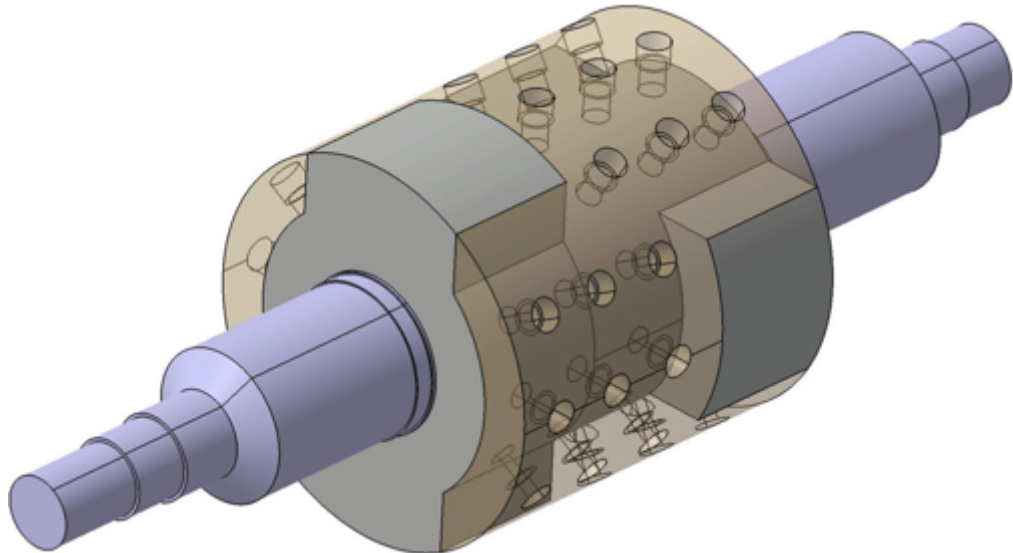


Fig. 2.38 G10 block are attached to the non-iron areas to make the rotor a smooth cylinder

## 2.6.2 MAGNETIC ANALYSIS

Before proceeding further, the magnetic analysis for such a machine is discussed. Analysis below is based on Finite Element Analysis (FEA) software using both 2-D model and 3-D model.

The configuration of Fig. 2.28 is used for calculating the air-gap magnetic field due to excitation current in the field winding. Magnetic field is calculated by exciting the field coil with 50 kA-turns. In the 6 coil single layer armature winding concept, each phase of the 3-phase winding consists of 2 coils connected in series – the two coils are placed on diametrically opposite locations. The magnetic field under each pole is unidirectional; it oscillates between maximum and minimum values at a

frequency fixed by rotor speed. The difference between the maximum and minimum field is utilized for inducing voltage in the armature coils. The magnitude of the oscillating field is estimated with the 2-D FEA model using the arrangement shown in Fig. 2.39. Fig. 2.40 shows a model (left) and results of fields at the midplane of the machine, used to assure the accuracy of the 2D model. It should be noted that this figure shows both North and South poles aligned but in a real situation they are 180 degrees apart. Flux lines travel from North to South azimuthally in both rotor and stator bodies. Assuming ampere-turn expended for flux travel in azimuthal direction to be negligible, the 2-D FEA magnetic model seems to be acceptable – as calibrated with the 3-D FEA model.

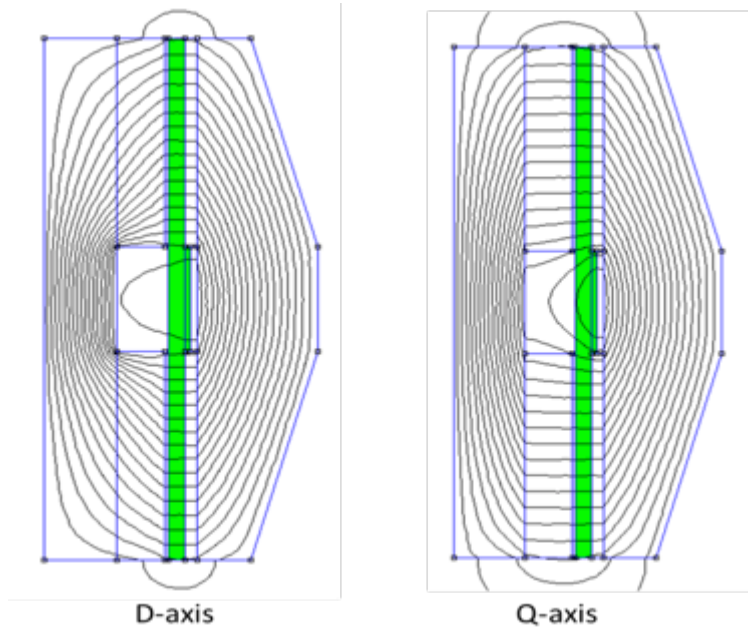


Fig. 2.39: 2-D FEA model for calculating magnetic field in phase-A for d-axis and q-axis locations

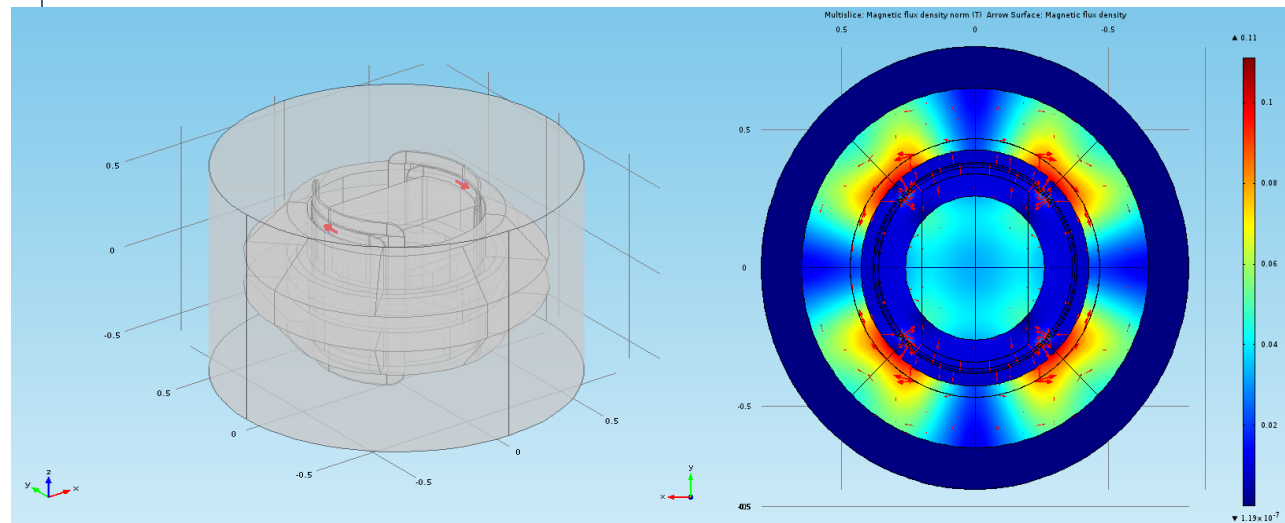


Fig. 2.40 3D FEA model for calculating fields and fluxes for in phase A for d axis and q axis.

The magnetic flux distribution is shown for two cases; 1) d-axis, where rotor salient poles are aligned

with phase-A coil, and 2) where the rotor is aligned with q-axis (45 degree rotation from the d-axis here.) The process for calculating mutual coupling between field excitation and armature phase-A windings is summarized in Table 2.3 and described below. Under the d-axis, the rotor pole body is magnetic steel and under the q-axis it is just air. The magnetic fields at mid-point of a pole for d-axis and q-axis are 0.60 T and 0.21 T, respectively. Thus, the amplitude of the oscillating field is the difference between the two; i.e. 0.39 T (= 0.60-0.21). To account for field variation in axial and azimuthal directions, a correction factor of 0.74 is used for calculating an average field (B<sub>ave</sub> = 0.29 T). The flux per pole (0.039 Wb) is obtained by multiplying together the average field, pole-pitch and axial active length of a pole. This flux divided by the field excitation ampere-turns (50 kA-turns) yields mutual inductance of 0.75 micro-H/turn between the field winding and an armature coil. This inductance value matches that calculated by 3-D FEA analysis (this justifies the correction factor 0.74 used above.) Each stator coil has 48 turns for generating an open-circuit phase voltage of 3.8 kV or line voltage of 6.7 kV

Table 2.3: Calculation of mutual inductance between field and armature phase-A windings

Parameter	Value
Field coil ampere-turn, kA	50
Maximum field under d-axis, T	0.60
Maximum field under q-axis, T	0.21
Maximum pulsating field under a pole, T	0.39
Correction factor for axial and azimuthal field variations (FEA)	0.74
Average field under a pole, T	0.289
Active length of each pole, mm	250
Pole pitch at air-gap, mm	534
Flux/pole (B.L.pp), Wb	0.039
Number of coils in series/phase	2
Flux/phase, Wb	0.077
Mutual inductance between field and an armature coil, mH	0.0008
Frequency of AC coils, Hz	233
Induced (rms) voltage/turn in armature coils, V	40
Chosen number of turns in an armature coil	48
Voltage induced per phase, kV	3.8
Line voltage, kV	6.7

Next step is to calculate synchronous reactance that represents armature reaction. The process for calculating synchronous reactance is explained below:

1. Excite field coil with open-circuit ampere-turns ( 50 kA-turn here)
2. Calculate flux linkages with a phase-A armature coil when it is aligned with a salient pole (d-axis)
3. Excite a phase-A armature coil (along with equivalent currents in other phases) with suitable current that produces the same flux linkages as in the step 2 above
4. Calculate per-unit value of the armature current in step 3 above (= Current in step 3/pu-armature current)
5. In per-unit, when armature is shorted at its terminals, voltage drop in synchronous reactance is equal to the induced voltage;  $V = x_d * I$  or  $x_d = V/I$ ; where I is pu current from step 4 and V is 1 pu.

In order to calculate equivalence between field and armature currents (required in step 3), model shown

in Fig. 2-41 is used. In this model, field winding is excited with 10 kA-turns to generate flux linkages of 0.00028 Wb over a pole-pitch. An armature phase-A is excited with 10.5 kA-turn for creating the same flux linkages. The ratio between armature current and field current is  $10.5/10 = 1.05$ . In the machine under discussion, field excitation of 50 kA-turn is needed to generate rated voltage on open-circuit. The phase-A armature coil would need  $1.05*50 = 52.5$  kA-turns to create the same flux. At the rated load, phase-A carries 86 kA-turns (= 1 pu current.) Thus, the value of current needed in phase-A coils to equate the field excitation is  $52.5/86 = 0.61$  pu. Using the formula in the step 5 above, d-axis synchronous reactance,  $x_d = 1/0.61 = 1.64$  pu.

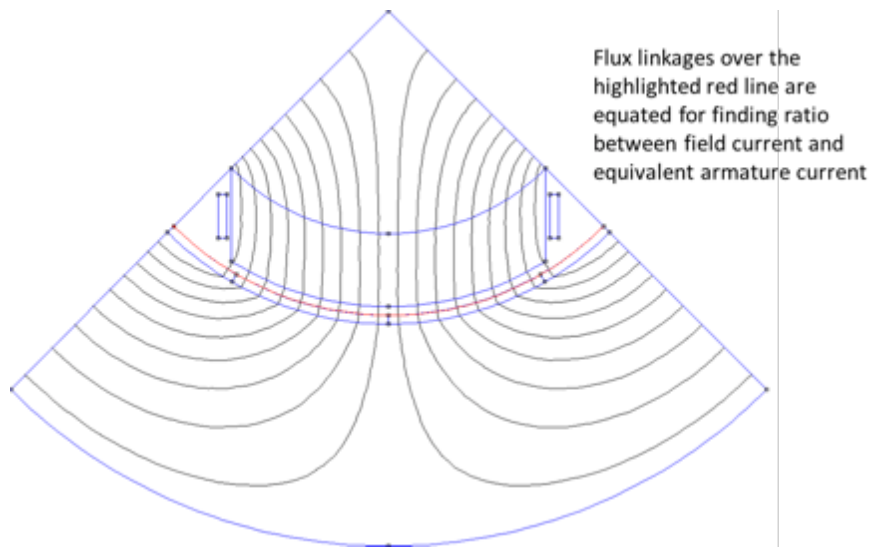


Fig. 41: Model employed for calculating ratio between field and armature ampere-turns for creating identical flux linkages over a pole-pitch [on the highlighted (red) line]

Next, it is necessary to determine extent of saliency in this machine; i.e. determine ratio of synchronous reactances on d-axis and q-axis. In order to determine this, another 2-D model (shown in Fig. 2.42) is created. Rotor is aligned on d-axis and q-axis locations with phase-A coils excited with 2 kA. Phase-A inductance is calculated in both cases. The ratio between d-axis and q-axis reactances is determined to be  $12/11.6 = 1.03$ . Almost unity ratio indicates that the saliency effect is small and it could be ignored. However, the value of  $x_q = x_d/1.03 = 1.59$  pu. These  $x_d$  and  $x_q$  values match with those calculated using the 3-D FEA model.

At rated unity power factor load, the induced voltage will be  $E_o = (V_t^2 + (x_d^2 I_a^2)0.5)0.5 = 1.9$  pu. The corresponding field excitation ampere-turns will be  $1.9*50$  kA-turns = 96 kA-turns. Power generated ( $P_g$ ) in the machines is given as  $P_g = (V_t^2 E_o / x_d) \sin(\delta)$ , where  $\delta$  is the load angle. The load angle for this machine at the rated load is 58.6°. Fig. 2.43 shows relationship among terminal voltage ( $V_t$ ), phase current ( $I_a$ ) for unity-power factor and induced voltage  $E_o$ .

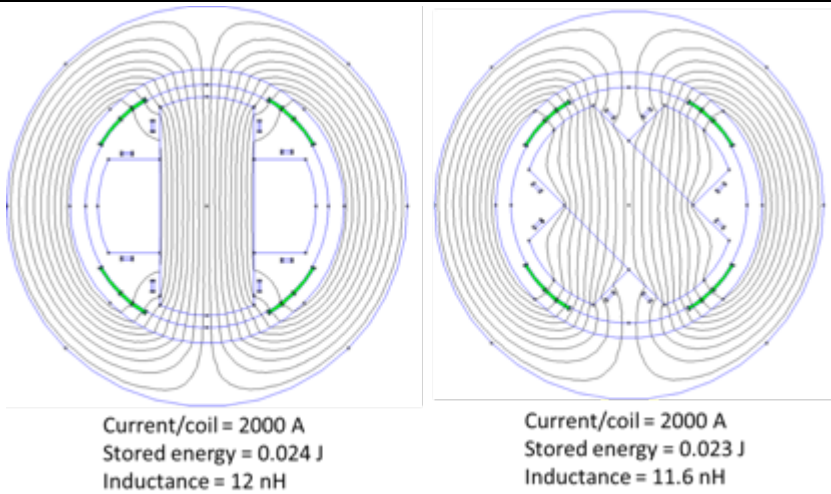


Fig. 2.42: Flux plots for d-axis and q-axis with phase-A excitation

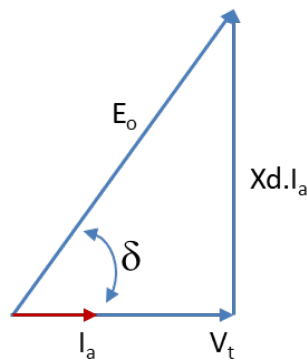


Fig. 2.43: Vector diagram showing relationship among terminal voltage, armature current and induced voltage during full-load operation

### 2.6.3 EFFECT OF ARMATURE MAGNETIC FIELD ON THE EXCITATION COIL

Fig. 2.28 includes a radial gap of 80 mm between the armature winding and field winding, though both operate at the same temperature. This is done for reducing losses in the field winding due to AC magnetic field created by the current in the armature winding. Fig. 2.44 shows magnetic flux plot due to armature current, radially directed magnetic field experienced by the field winding, and harmonic analysis of this field. As shown in the figure, fundamental field is the dominant component and most harmonics are essentially absent. The peak AC field experienced by the field winding is 0.22 T. Since this field is radially directed, significant eddy-current heating will be experienced by any metallic component interacting with it. For this reason, it would be necessary to enclose the field winding in a non-metallic enclosure.

Losses in superconducting coils are calculated with the analysis described in section 6. ReBCO field winding employs a 2 mm wide tape that has 20 micron copper layer surrounding it. Usually the two most important loss components are due to magnetization and transport current. In absence of a credible magnetization loss formulation, this loss component is replaced with eddy-currents in the copper layer. The loss due to DC transport current is 138 W. The eddy-current loss due to armature reaction field (0.2 T at 233 Hz) is 361 W. Additionally 22 W is conducted through the current leads.

Total field winding loss is 521 W, which is used for refrigeration sizing and efficiency calculations. These loss calculations could be revised once an acceptable AC loss analysis becomes available for the ReBCO conductors.

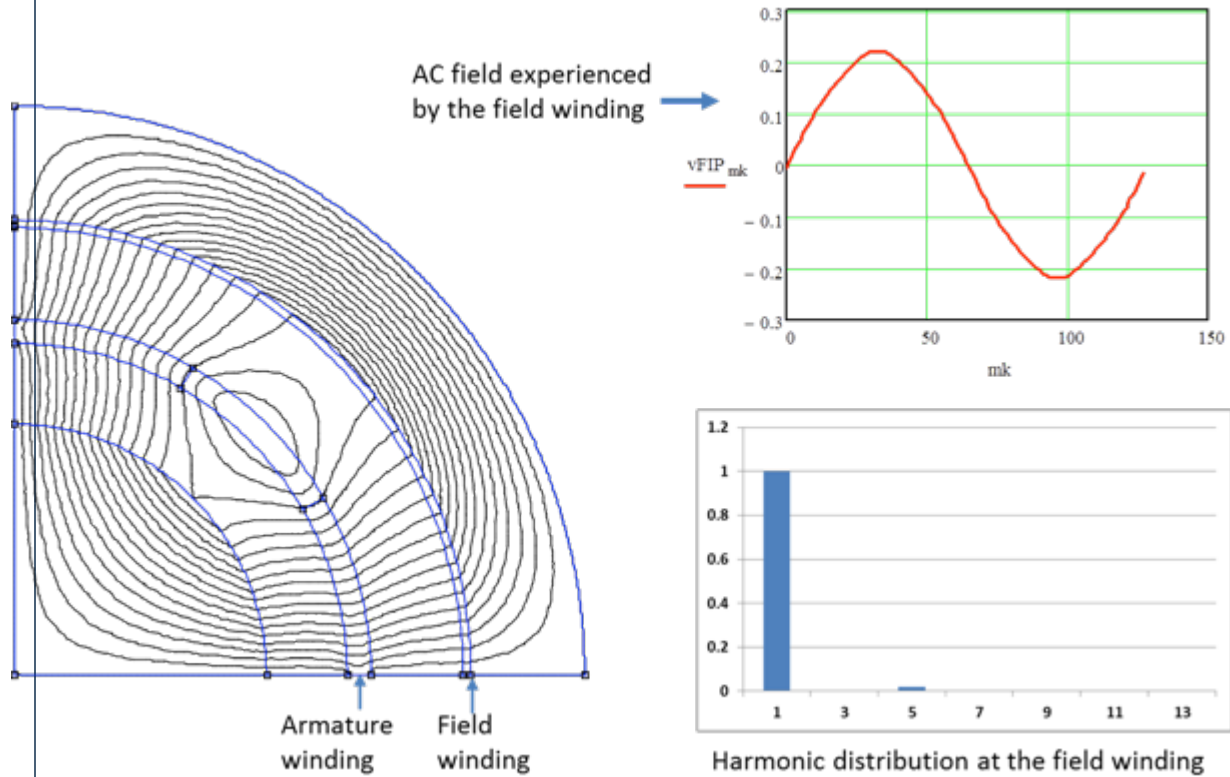


Fig. 2.44: AC magnetic field experienced by the field winding due to armature current (note: most harmonics are absent)

#### 2.6.4 SUMMARY OF REBCO MACHINE

Now the salient features of this machine employing ReBCO for field and armature could be summarized. Main parameters of the machine are listed in Table 2. This machine generates 14.6 MW at 233 Hz while operating at 7,000 RPM. The overall efficiency of the machine is expected to be 98.6%, which is above 98% ONR requirement. Table 3 provides distribution of losses in the armature and overall efficiency calculations. Total ampere-turns of the field coil are 96,000 during full-rated load of unity power factor. Each phase of armature coils (2 coils together) has 172 kA-turns. The overall diameter and axial active length are 1.23 m and 1.4 m, respectively. The mass of the machine alone is 7,700 kg that translates to a power density of 1.9 kW/kg. The mass of the cryogenic cooling system is expected to be 4,320 kg. Thus the total system mass is 12,000 kg.

Table 2.4: AC Homopolar machine employing ReBCO windings

Parameter	Value
Power, MW	14.6
Rated speed, RPM	7,000
Number of poles	4
Frequency, Hz	233
Efficiency at full-load, %	98.6
Field winding current at full-load, kA-turns	96
Armature current/phase, kA-turns	172
Overall diameter, m	1.22
Active length, m	0.7
Overall axial length, m	1.4
Machine weight, kkg	7.7
- shaft	0.05
- rotor yoke	2.38
- poles	0.24
- stator iron yoke	2.02
- stator case	3.00
Total machine weight	7.7
Cryogenic cooling system weight, kkg	4.3
Total machine system weight, kkg	12.0

This machine design employs the advanced ReBCO conductor being developed at the University of Houston. The field winding uses 2 mm wide conductor with a critical current of 240 A at 77 K and self-field. Fig. 2.45 shows the critical current as a function of magnetic field (perpendicular to the broad face of the conductor) at different temperature. It is also assumed that this wire is 0.1 mm thick and has additional 0.05 mm thickness of copper substrate.

Key characteristic parameters of the field winding are summarized in Table 2.6. A 2 mm wide conductor is operated at 48% of its critical current at the operating temperature of 35 K.

The field winding consists of 226 turns of 2 mm wide and 0.15 mm thick conductor. At the 35 K operating temperature, the critical current at the maximum field (0.4 T) experienced by the conductor is 886 A - it carries 425 A during full-load. The mean radius of the coil is 446 mm and has a radial build of 5 mm. Axial length of the field coil is 160 mm and uses 630 m length of the 2 mm wide conductor.

The armature winding consists of 6 race track coils. Each coil employs Roebel cable made of 3 mm wide strands cut out of a 7 mm wide tape. Key details of the armature winding are summarized in Table 2.7.

Table 2.5: Summary of losses and Efficiency Calculations

Parameter	Loss
Loss components at operating temperature, W	
- armature coil thermal conduction	564
- field coil thermal conduction	110
- field coil current lead conduction	22
- AC loss in ReBCO Field coils	499
- AC loss in ReBCO Armature coils	3369
- armature current lead loss	270
Total load at operating temperature, W	4834
Operating temperature of armature, K	35
Refrigerator Coefficient of performance (COP)*	40
Refrigeration compressor power needed, kW	193
Core loss, kW	13
Total power loss at rated load, kW	196.0
Total power generated, MW	14.6
Efficiency at rated load, %	98.6
Weight of refrigeration system*, kg	4.3
* Ref: MIT	

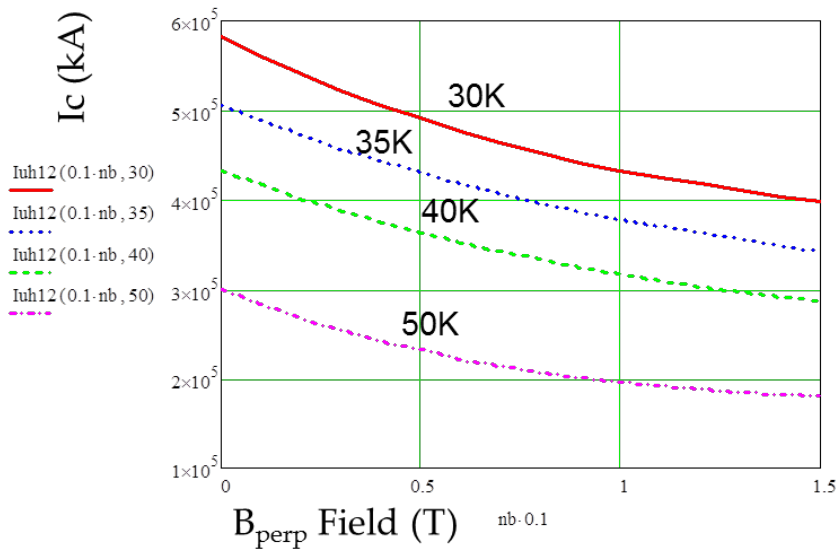


Fig. 2.45: Critical current (A/m width) of ReBCO conductor as a function of magnetic field (perpendicular to the broad face of conductor) at different temperatures (Source: University of Houston)

Table 2.6: ReBCO field winding details

Parameter	Value
University of Houston ReBCO wire	
Wire width, mm	2
Wire thickness, mm	0.15
Total field kA-turns at full load	96
Maximum perpendicular field, T	0.4
Selected operating temp., K	35
Critical current at operating temp., A	886
No-load current, A	221
Full-load operating current, A	425
Number of turns in the field coil	226
Coil cross-section area, mm <sup>2</sup>	45
Radial build of field coil, mm	5
Axial length of field coil, mm	160
Length of wire used, m	630

Armature coils are manufactured with Roebel cable. Each Roebel cable is 7 mm wide and uses 3 mm wide strands. Each cable has 15 strands and is 0.8 mm thick. With insulation, each Roebel cable is ~7 mm wide and 1.2 mm thick. The critical current of the 15 strand Roebel cable is 19.9 kA and is operated at 1800 A peak (9% of I<sub>c</sub>). The operating current is selected as a small fraction of the critical current for two reasons; 1) limiting AC losses in the 35 K operating temperature environment, and 2) withstanding larger current during a short-circuit fault near the machine terminals. Each coil has 48 turns and total length of Roebel cable used in the armature is 705 m.

Table 2.7: Key details of the armature winding

Parameter	Value
Roebel cable made from ReBCO	
Strand width, mm	3
Number of strands in cable	15
Width of bare cable, mm	7.0
Thickness of bare cable, mm	0.8
Width of insulated cable, mm	7.4
Thickness of insulated cable, mm	1.2
Critical current of cable at 35 K, kA	19.9
Operating current of cable at 35 K, A	1800
Number of turns in an armature coil	48
Length of cable used, km	705

The machine generates 14.6 MW at phase voltage of 3.8 kV (6.6 kV line-line) and current of 1,270 A rms. AC field experienced by each coil is 0.40 T (peak-peak). This is the difference between the unidirectional pulsating field under each pole (B<sub>max</sub> = 0.6 T and B<sub>min</sub> = 0.2 T). Total active length of the armature coils is 0.7 m. However, when a rotor pole aligns with a stator coil, 0.25 m length of coil experiences an average radial field of 0.6 T and the other 0.25 m experiences 0.2 T. Thus the net radial field experienced by a coil is difference between these two values (0.40 T). A 0.2 m long (axially) mid-section of the coil experiences (theoretically) no radial field.

Both armature and field coils are insulated with Aeogel (15 mm thick). Its thermal conductivity is 5 mW/m-K and total conduction into the cryogenic region is 564 W for the armature coils. Aerogel thermal barrier is expected to be simpler to build than the MLI/Vacuum system, because it does not employ metallic parts for operation in the AC magnetic field environment of the air gap of the machine.

As shown in Table 2.5, the total thermal load at the low temperature is 4,830 W, which is made of 14% thermal conduction through Aerogel, 70% AC losses in the armature coils and 10% loss in the field winding. On the basis of a COP ratio of 40 for removing losses from the 35 K environment, 193 KW of compressor power would be required. Additionally, 6 kW loss is generated in the iron core. Thus, the total 196 kW loss for 14.6 MW generated power yields an overall efficiency of 98.6%.

The ReBCO conductor is quite expensive. It is possible to operate windings at even lower temperature for minimizing use of superconductor at expense of larger cooling system. An optimization study would be necessary to find a sweet spot that balances superconductor quantity and cooling system size for minimizing matrices of cost, size and weight.

Machine component mass distribution is provided in Table 2.7. The machine frame is assumed to be a 50 mm thick cylinder applied at the outside diameter of the iron core and has 50 mm thick end covers. Total machine weight is 7,700 kg and system weight is 12,000 kg - including 4,300 kg for the cryogenic cooling system.

Table 2.7: Summary of ReBCO machine component mass

Component	Mass (kg)
Rotor	2,660
<i>Stator iron</i>	2,020
Stator case (frame)	3,000
Cryogenic system	4,300
Total machine	12,000

The conclusions of the ReBCO Homopolar machine are summarized below;

- AC Homopolar machines employing ReBCO field and armature windings are expected to yield the most compact and light weight generators
- Expected efficiency ~98.6% appears to be attractive
- Rotor, made of solid magnetic steel, requires no active cooling (other than small losses in the rotor pole faces due to armature generated harmonics)
- ReBCO Roebel cable is commercially available from General Cable Superconductor of New Zealand
- ReBCO could be operated at 50 K but will require longer length of conductor
- More detailed design and optimization is needed for a better assessment of potential of such machines

## 2.6.5 MGB2 IN THE ROTOR AND ARMATURE WINDINGS

The configuration of the AC Homopolar machine employing MgB2 superconductor windings is the same as discussed above for the ReBCO machine. Both armature and field coils employ MgB2 superconductor operating at 20 K. All other features and parameters remain unchanged.

Key features of the machine build with MgB2 are summarized in Table 2.8. This machine generates 14.6 MW at 233 Hz while operating at 7,000 RPM. The overall efficiency of the machine is expected

to be 98%, which meets the 98% ONR requirement. Total ampere-turns of the field coil (at full-load) are 96,000. Each phase of armature coils (2 coils together) has 172 kA-turns. The overall diameter and axial active length are 1.22 m and 0.7 m, respectively. The mass of the machine alone is 7,700 kg that translates to a power density of 1.9 kW/kg. The mass of the cryogenic cooling system is expected to be 6,100 kg. Thus the total system mass is 13,800 kg, which also is well within the ONR requirements.

Table 2.8: AC Homopolar machine employing MgB2 superconducting windings

Parameter	Value
Power, MW	14.6
Rated speed, RPM	7,000
Number of poles	4
Frequency, Hz	233
Efficiency at full-load, %	98
Field winding current at full-load, kA-turns	96
Armature current/phase, kA-turns	172
Overall diameter, m	1.22
Active length, m	0.7
Overall axial length, m	1.4
Machine weight, kkg	7.7
- shaft	0.05
- rotor yoke	2.38
- poles	0.24
- stator iron yoke	2.02
- stator case	3.00
Total machine weight	7.7
Cryogenic cooling system weight, kkg	6.1
Total machine system weight, kkg	13.8

The machine is designed using the MgB2 conductor available from Hypertech Research. The standard wire diameter is 0.85 mm. The field winding employs this wire with a critical current of 465 A at 20 K and 0.3 T. The critical current as a function of magnetic field at different temperature is shown in Fig. 2.46.

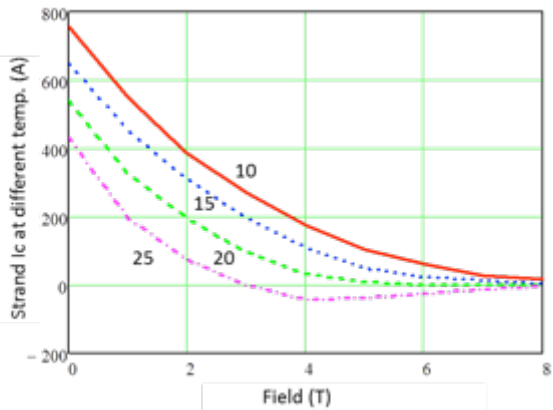


Fig. 2.46: Critical current of a 0.85 mm diameter wire as a function of field at different temperatures

Key characteristic parameters of the field winding are summarized in Table 2.9. A 0.85 mm diameter conductor is operated at ~30% of its critical current at the operating temperature of 20 K. The coil is thermally insulated with 18 mm thick layers of Aerogel. The field winding has 1035 turns. Field current is 135 A (full-load) at the operating temperature of 20 K. The coil cross-section is 5 mm (radial) x 164 mm (axial). Total length of wire used is ~2900 m.

Table 2.9: MgB2 field winding details

Parameter	Value
HyperTech 2G MgB2 wire	
Wire diameter, mm	0.85
Total field kA-turns at full load	96
Maximum perpendicular field, T	0.3
Selected operating temp., K	20
Critical current at operating temp., A	465
Full-load operating current, A	93
Number of turns in the field coil	1035
Coil cross-section area, mm <sup>2</sup>	748
Radial build of field coil, mm	5
Axial length of field coil, mm	170
Length of wire used, km	2.9

Armature winding has the same race track coil configuration as for the ReBCO design discussed earlier. However, a 15-strand cable of MgB2 replaces the ReBCO Roebel cable. More details of this cable are summarized in Table 2.10 and Fig. 2.47. The cable is rectangular in shape with bare width and height of 2.7 mm and 3.9 mm, respectively. Insulated cable dimensions are also shown in the table. The strand bundle is wrapped with 1-mil thick stainless steel tape with a small gap between adjacent tape turns.

The coil pack shown in Fig. 2.47 is sandwiched between adjacent stainless steel tubes (similar to those in Fig. 2.36). Each cooling tube is 50 mm wide and 2.5 mm tall and has a wall thickness of 0.1 mm. Cold helium is circulated in these tubes for maintaining the coils at the desired operating temperature.

It is assumed that the whole coil assembly, including winding pack and cooling tubes, will be impregnated with a thermally conductive but electrically non-conductive epoxy (TBD). Total eddy-current loss in the cooling tubes is 430 W, which is a small fraction of total AC losses.

DC critical current of the cable is 7.0 kA and is operated at 1.8 kA. The ratio between the operating current and critical current is kept low for minimizing AC losses during the normal operation. AC losses in the armature coils were calculated using analysis described in section 6.c. The analysis equations were incorporated in the design code.

Table 2.10: MgB2 cable details

Parameter	Value
MgB2 cable	
Strand diameter, mm	0.85
Number of strands in cable	15
Number of strands in cable width	3
Number of strands in cable height	5
Width of bare cable, mm	2.6
Height of bare cable, mm	4.3
Width of insulated cable, mm	3.0
Heighth of insulated cable, mm	4.7
Critical current of cable at 20 K, kA	7.0
Full-load operating current of cable at 20 K, kA	1.8
Number of turns in an armature coil	48
Length of MgB2 cable used, m	723

The machine generates 14.6 MW at phase voltage of 3.8 kV (6.6 kV line-line) and current of 1,260 A-  
rms. AC field experienced by each coil is 0.30 T (peak-peak), as explained previously. It would be easier to build saddle shaped race-track coils with MgB2 cable as it is amiable to bending in both x-y directions.

Both armature and field coils are insulated with Aerogel (15 mm thick). Its thermal conductivity is 5 mW/m-K. Total thermal load at 20 K is 3.52 kW, which includes AC loss of 2.8 kW (39 W in field winding, and 2.77 kW in armature winding), a thermal conduction load of 712W in transmitted through the aerogel insulation, and current lead conduction of 270 W. The compressor power with a COP of 80 is 282 kW. Additionally, 6 kW loss is generated in the iron core. Thus, there is a total loss of 288 kW for 14.6 MW generated power which yields an overall efficiency of 98%.

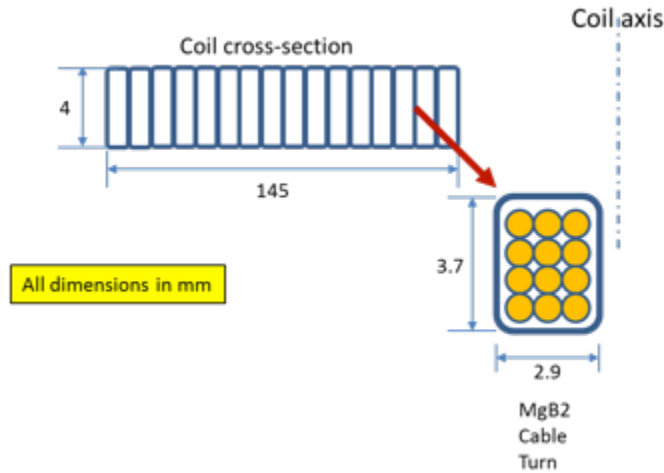


Fig. 2.47: An armature coil cross-section with turn details – (MgB2 strands in a cable)

Machine component mass distribution is provided in Table 9. The machine frame is assumed to be a 50 mm thick cylinder applied at the outside diameter of the iron core and has 50 mm thick end covers. Total machine weight is 7,700 kg and system weight is 13,800kg - including 6,100 kg for the cryogenic cooling system.

Table 2.11: Summary of MgB2 machine component mass

Component	Mass (kg)
Rotor	2,660
Stator iron	2,020
Stator case (frame)	3,000
Cryogenic system	6,100
<b>Total machine</b>	<b>13,800</b>

The conclusions of the MgB2 Homopolar machine are summarized below:

- AC Homopolar machines employing MgB2 field and armature windings are expected to yield compact and light weight generators
- Expected efficiency ~98% equals to the ONR guideline
- Rotor, made of solid magnetic steel, requires no active cooling (other than small losses in the rotor pole faces due to armature generated harmonics)
- MgB2 cable is commercially available from Hypertech, Columbus, OH
- MgB2 machine is expected to cost less than ReBCO machine due to lower cost of MgB2.
- More detailed design and optimization is needed for a better assessment of potential of such machines

#### COMPARISON AMONG MACHINES WITHOUT SC IN THE ROTOR

All machines designed in this report are compared in Table 2.12 – the highlighted components exceed the ONR requirements. With the exception of the switched reluctance machine, all other machines are comparable in size, mass and efficiency. On the basis of this study, it difficult to justify that superconducting stator will have significant advantage over copper stator (employing air-gap winding). Moreover, the copper stator is likely to be less costly and risky than the superconducting stators. Summarized below are key features of each type of machine;

- SRM generators is too heavy, large and inefficient and does not satisfy many ONR requirements

- ACHP employing MgB2 field winding and normal copper armature winding meets all ONR requirements; its mass is merely 700 kg (6%) more than the ONR requirement.
- ACHP with all MgB2 windings meets all requirements except the mass, which is 1,800 kg (15%) more than the requirement. The machine alone is 7,700 kg but the cooling system mass makes the system mass exceed the ONR requirements.
- Only the ACHP with ReBCO windings meets all requirements.

All key parameters for MgB2 and ReBCO machines are strong functions of superconductor characteristics; such as critical current, operating temperature, and AC losses. Improved performance of superconducting materials could have positive impact on the attractiveness of superconducting stators.

Nevertheless, it should be recognized that this report describes design approach, assumptions and results using the current state-of-the-art of various technologies. Designs presented are essentially first pass and are not optimum in any sense. However, on the basis of this study, all AC Homopolar machines appear to be acceptable within a margin of (+/- 10%) with respect to the ONR requirements.

Table 2.12: Comparison of machines without SC in the rotor

Parameter	SR	ReBCO	MgB2	Cu/MgB2
Power rating, MW	14.0	14.6	14.6	14.6
Output power at full-load, MW	13.3	14.4	14.3	14.4
Overall axial length, m	3.5	1.4	1.4	1.7
Total mass, kkg	22	12.0	13.8	12.7
Mass of machine alone, kkg		7.7	7.7	12.4
Mass of cooling system, kkg		4.3	6.1	0.7
Efficiency at full-load, %	95.0	98.6	98.0	98.7
Core loss, kW	2,000	6.1	6.1	10.1
Cryocooler load, kW	1,500	193	282	10.9
Copper coil loss, kW				158
Armature cooling power, kW				15.8
Superconductor operating temp.,	20	35	20	20

## 2.7 MACHINE CONFIGURATIONS OPTIMIZATION AND COMPARISON

After performing the analysis of the subcomponents, we revisited the main designs and worked out the parametric analysis, to determined sweep spots for future work. Two designs were performed, one for REBCO and the second one for MgB2. The designs were based upon the toroidal stator configuration. The designs constrains was a rotor diameter of less than 70 cm, operationg at 7000 rpm. The iar gap is 7 cm, out of which 5 cm is for mechanical containments and 2 cm is for the cryostat and physical gap. The magnetic flux is limited so that the iron core is not saturated, so  $B_{max} \sim 1.6$  T. Finally for the case of MgB2 it is assumed that there is a 10 cm gap between the stator core and the stator coil outer legs. Figure 2.48 shows the schematics for the two generators assumed for the designs.

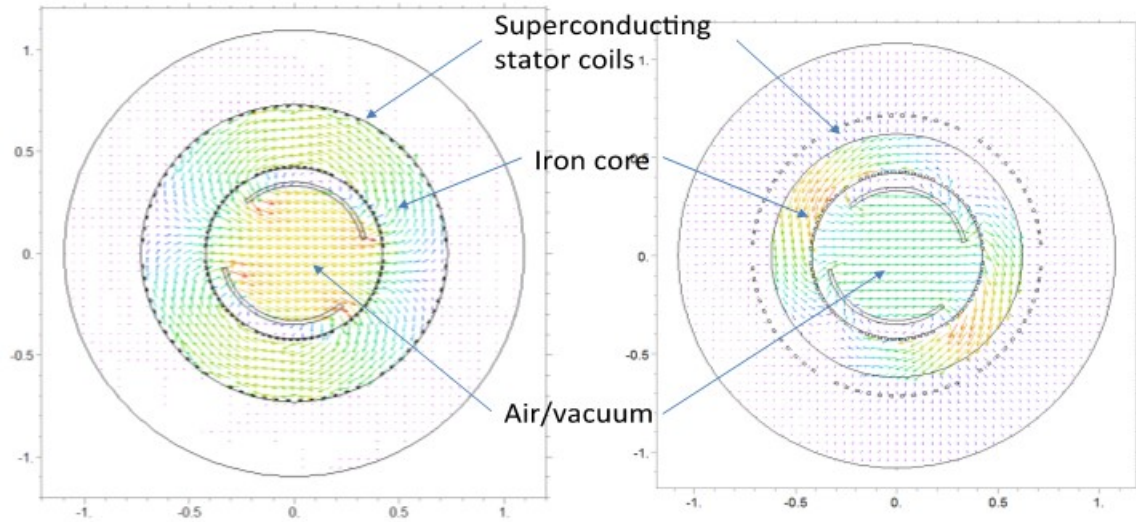


Figure 2.48 Toroidal stator configurations for post-study evaluation, with air core rotor. In the case of the YBCO armature, the windings are in slots both in the inner leg as well as the outer leg. In the case of MgB<sub>2</sub>, the inner leg is in slots, but the outer leg return is in air (in order to enable assembly, as shown in Section 5).

In the case of MgB<sub>2</sub>, we performed parametrics in two cases, without iron rotor and with it. In the case of the iron rotor, we employed both a smooth iron rotor and a cut iron rotor. Figure 2.49 shows the iron rotor configurations.

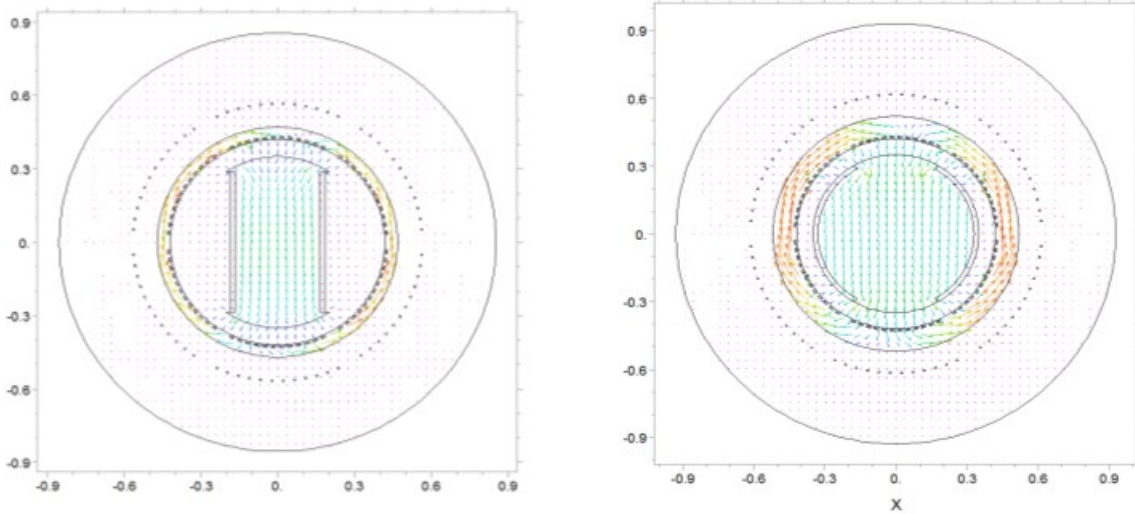


Figure 2.49 MgB<sub>2</sub> stator winding configurations, with iron rotor (cut rotor in the left, smooth rotor in the right).

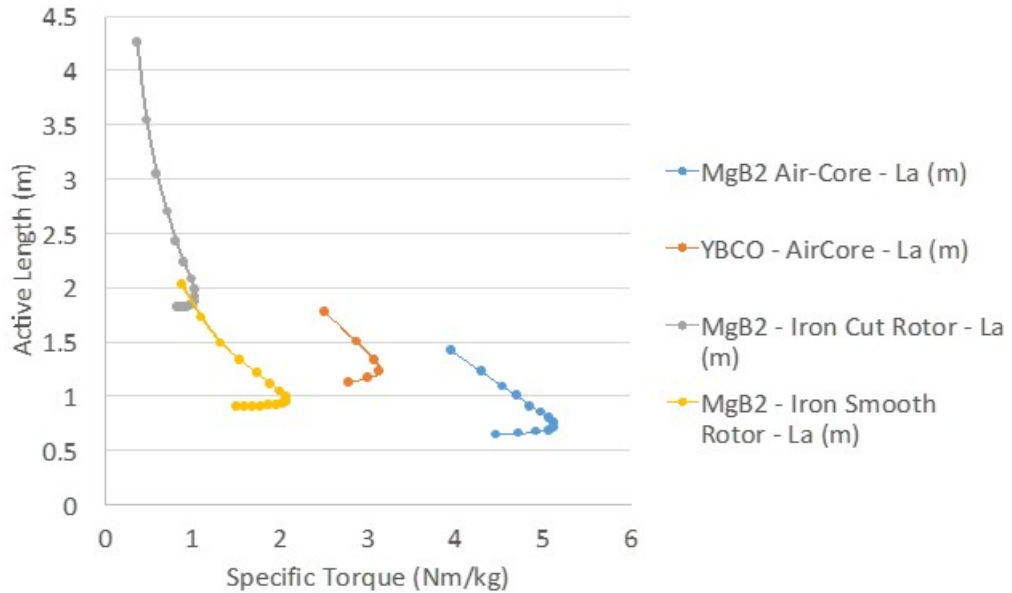


Figure 2.50 Comparison of designs, for YBCO and MgB2. Shown is the active length vs the specific torque.

Figure 2.50 and 2.51 show the results from the optimization. The active length of the machine, as a function of the specific torque, is shown in Figure 2.50. The specific torque includes a crude estimation of the power and weight of the cryogenic system, including the refrigerators. Clearly the design with an MgB2 air core has substantially better specific torque, and active lengths, than then others investigated. It is possible to have a machine with a specific torque of about 5 Nm/kg, which corresponds to about 3.5 kW/kg. This metric is substantially higher than the Navy goal, which is about 1.5-2 kW/kg in the medium term [Kuseian]. The active length is decreased from the baseline machine to about 60-70 cm, making the generator also shorter. By comparison, the design with the closest specific torque to air core MgB2 design is the YBCO, with about 2/3 of the specific torque, with about twice the length. The iron rotor machines with MgB2 are substantially worse, and do not even meet the desired metrics in the neat term.

Figure 2.51 shows the corresponding AC losses for the 4 designs. The values are the actual losses, not the power required by the refrigerator (which is sensitive to the temperature of operation and the size of the unit. In section 9 there is a discussion of the AC losses. Although the AC losses in the MgB2 air core designs are higher than those of the MgB2 with iron rotor, the losses are only about twice those of the minimum for the iron cut rotor. Thus, even with somewhat larger losses, the MgB2 air core machine is superior to the MgB2 iron rotor designs, when including the issues illustrated in Figure 2.50.

The YBCO designs have higher losses, but because of the higher temperature of operation (about 50 K), then electrical load for the refrigerator is actually smaller. The problem with YBCO is that it is not clear how to remove the heat from the superconductor. Some potential approaches were described in the section fro the homopolar generator, Section 2.6, Figure 2.36.

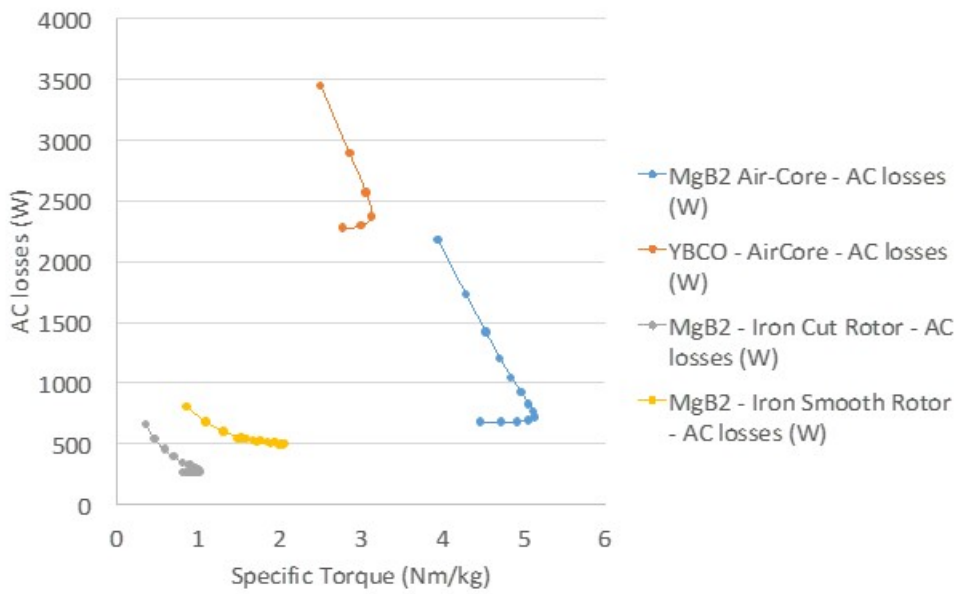


Figure 2.51 Comparison of designs, for YBCO and MgB2. Shown is the AC losses vs the specific torque.

The optimized design is shown in Figure 2.52. The features are 14 MW at 7000 rpm, 3 phases at 4.5 kV, an outer diameter of 1.6m and a length of 0.8 m. The specific torque is 5.1 Nm/kg and a mass, including the cryostat, of 3.9 tons. The cable in conduit conductor (CICC) operates at one third of the critical current.

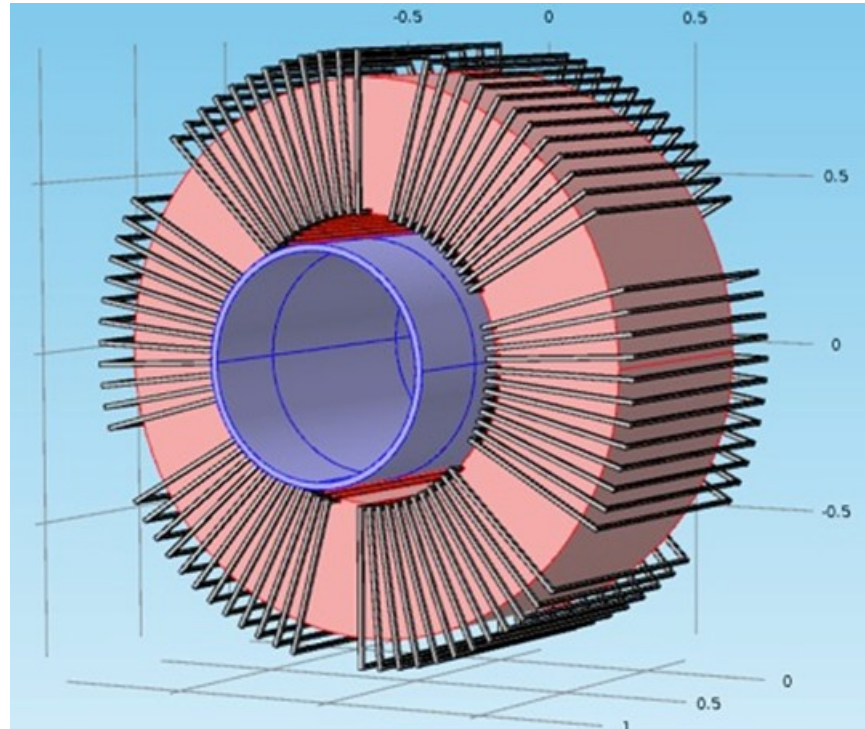


Figure 2.52 Machine specifications of a potentially attractive design with MgB2, with air core rotor.

## 2.8 REFERENCES

[Calfo] Ray M. Calfo, Matt B. Smith, and John E. Tessaro, High-Speed Generators for Power-Dense, Medium-Power, Gas Turbine Generator Sets, American Society of Naval Engineers DOI: 10.1111/j.0028-1425.2007.00020.x (2007)

[Kuseian] J. Kuseian, Naval Power Systems, Technology Development Roadmap, APM Technology Transition PMW320/NSWCCD-SSES 982 Electric Ships Office (2013)

[Miller] T. J. E. Miller, “Optimal Design of Switched Reluctance Motors”, IEEE Trans. On Industrial Electronics, Vol.49, No.1, February 2002, pp. 15-27

[Lawrenson] P. J. Lawrenson, et al., “Variable-speed switched reluctance motors”, IEE Proc., Vol. 127, Pt. B, No. 4, July 1980, pp. 253-265

[Sivasubramaniam] K. Sivasubramaniam, T. Zhang, M. Lokhanwalla, E. T. Laskaris, J. W. Bray, G. Gerstler, M. R. Shah, and J. P. Alexander, “Development of a High Speed HTS Generator for Airborne Applications”, IEEE Trans. On Applied Superconductivity, Vol. 19, No. 3, June 2009, pp. 1656-61

[Kalsi] S. S. Kalsi, ‘Applications of High Temperature Superconductors to Electric Power Equipment’, Wiley/IEEE Press, 2011, ISBN: 978-0-470-16768-7

W. T. Norris, “Calculation of hysteresis losses in hard superconductors carrying ac: isolated conductors and edges of thin sheets”, J. Phys. D: APPL. PHYS., 1930, Vol. 3, pp.489-507

[Kalsi1] S. S. Kalsi, ‘Superconducting Wind Turbine Generator Employing MgB2 Windings Both on Rotor and Stator’, IEEE Trans. on Applied Superconductivity, Vol. 24, No. 1, February 2014, 5201907

[Kalsi2] S. S. Kalsi, ‘Chapter 3.19 Ship Propulsion Motor Employing Bi-2223 and MgB2 Superconductors’ in Research, Fabrication and Applications of Bi-2223 HTS Wires; Sato K. Editor; World Scientific Publishers/Imperial College Press, In Press

[EPRI] ‘Superconducting Generator Design’, Final Report Prepared by GE, EPRI EL-663 Project 429-2, March 1978, page 2-141.

### 3. WEIGHT REDUCTION BY IRON ELIMINATION

The weight of the machine is dominated by the iron that is used as an environmental shield, that is, the backiron. The iron used in the rotor is a small fraction of that iron. As shown in the previous section, the lightest generator occurs with systems that do not have either a back iron or teeth. However, the overall weight (including the refrigerator) makes for a overall larger machine, unless light refrigerators (as being developed using Turbomachinery, such as Reverse Turbo-Brayton systems) are used.

Figure 3.1 shows a concept with a stator with both teeth and back iron (Figure 3.1 a) and one that does not use iron (Figure 3.1 b), but instead uses a image-current shield (or resistive shield). Substantial weight reduction occur, although the generator requires higher magnetic drive because of the increased reluctance, as well as less-than optimum use of the magnetic field produced.

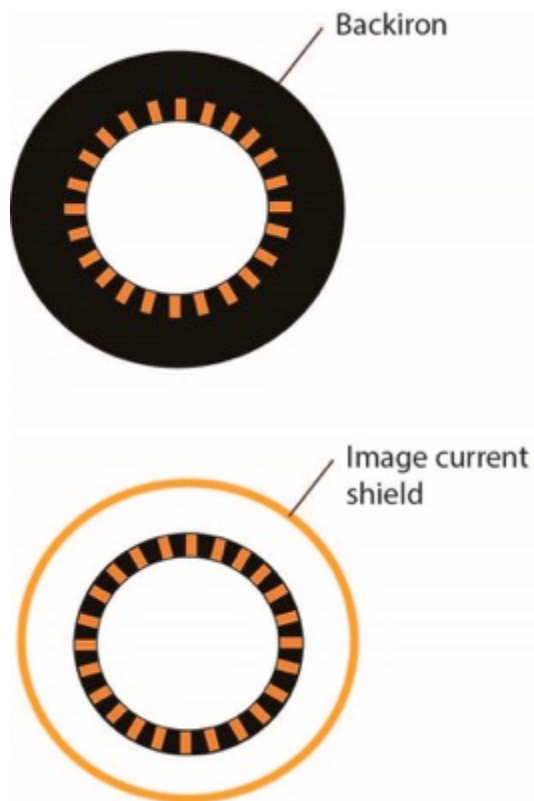


Figure 3.1 Magnetic vs resistive shield stators

For Navy applications, there is the requirement of shielding, as magnetic signature is used for location of the ship over open waters. Thus, it is needed to replace the iron used for shielding with other type of shielding. We have considered the use of resistive shields, where the magnetic iron is replaced with conducting elements that generate eddy-induced currents used for shielding.

#### 3.1 SOLID SHIELD.

The frequency of the induced current for our machines (operating at 7000 rpm with 2-poles) is about 120 Hz. At that frequency, the skin depth is short, on the order of 5 mm. In aluminum, a preferred material because of the conductivity to weight ratio, the skin depth is slightly larger. The skin depth is

calculated as shown in Table 2.1

Table 2.1 Skin depth calculations

$$\delta = \sqrt{\frac{2\rho}{2\pi f \mu_R \mu_0}} \text{ (meters)}$$

$\rho$  = resistivity (ohm - meters)

$f$  = frequency (Hz)

However, because of the small skin depth, the power density of the induced currents in a solid material would be very large, with losses on the order of 300 kW in a 1-m machine, with power density on the order of 5 W/cm<sup>3</sup>. It is difficult to remove all this heat, which also decreases the efficiency of the machine by about 2 percentage points.

## 3.2 LITZ-WIRE SHIELD.

We have considered a design that uses the equivalent of Litz wire used in high frequency electrical machine operation

Figure 3.2 shows the concept. Instead of a solid conductor, the conductor is made from strands that are twisted or twisted and transposed. By twisting, the current over the conductor radial thickness can be made uniform (as any element is equivalent to its neighbor. The current is thus distributed over the radial thickness, decreasing both the total power as well as the power density. With a radial thickness of 10 cm, the power can be decreased by about a factor of 10, to 30 kW, comparable to the iron losses in the case of a generator with back-iron (magnetic losses of those systems are typically about .3% of the power of the machine).

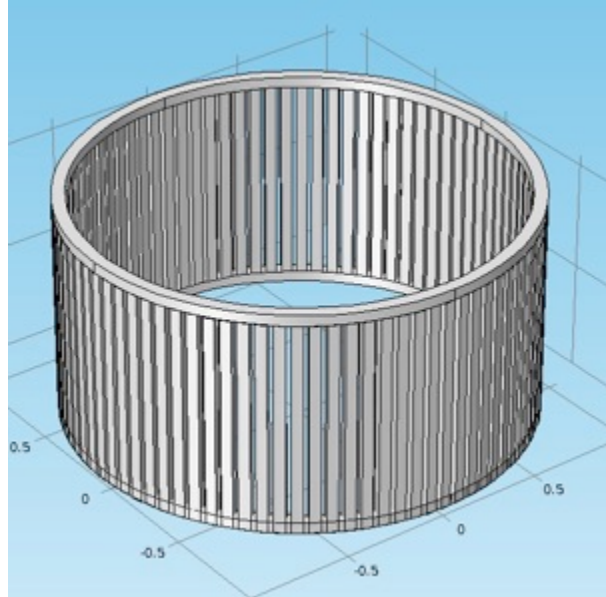


Figure 3.2 Squirrel-cage resistive shield

In order to gain with weight reduction, the resistive shield is made from aluminum. If each conductors are made from less than 64 strands, a simple twisting process is all that is needed to produce uniform current density (that is, transposition is not needed). Transposition is a method of making the conductor such that they are stochastically moved with respect to each other, resulting in a system where each conductor is the same as any other conductor. In the case of twisting, for example, the relationship

between neighbors is maintained. However, it has been shown that for less than 64 conductors, twisting is all that is needed. [Sullivan]

With 1 cm strands, and a depth of 10 cm and a width of 8 cm, we can fit about 64 strands. Thus, each conductor shown in Figure 3.2 would be 10 by 6 cm, made from 64 1 cm aluminum strands. Cooling the system would be substantially easier than cooling the back iron, as the squirrel cage is relatively porous.

It would be possible to decrease the signature of the system by making a hybrid shield. Figure 3.3 shows such a configuration, where the squirrel cage shield reduces the bulk of the signature, but a solid shield outside of the squirrel cage further reduces it. The additional shield could either be a magnetic shield (i.e., a solid thin hollow cylinder made from iron or other magnet material), or it could be a resistive shield.

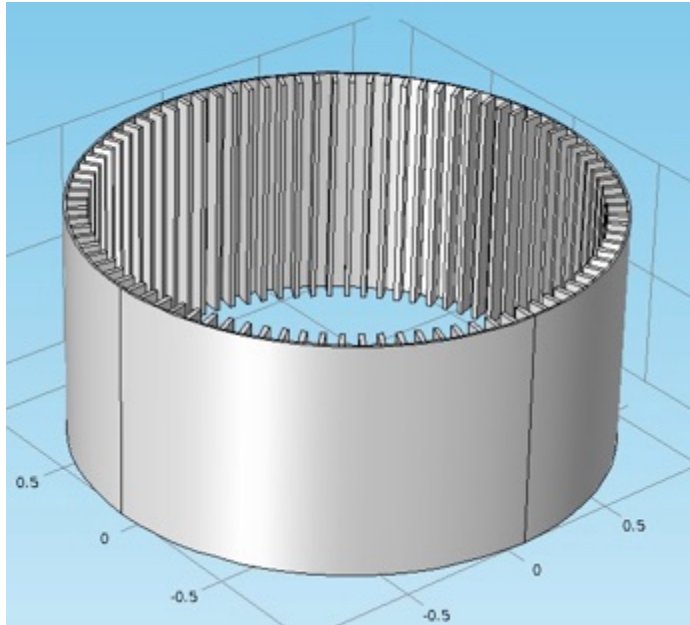


Figure 3.3 Combination of squirrel cage resistive shield and solid shield (either magnetic or resistive).

The end effects are critical in order to provide an uniform current density through the length of the shielding wires. It is important to determine whether the conductors are arranged in loops or are terminated in an element, as shown in Figure 3.1, that homogenizes the conductors (that is, all of them are shorted out). It is necessary to make all the elements relatively similar to each other, and thus, at the ends, if they are just shorted out to a ring element, currents could flow preferentially in those that are in the inner region of the cable.

We have evaluated the impact of the required terminations. One possibility, if there are issues with shorting the elements at the ends, is to make loops of the conductors. This process would make the winding somewhat more complicated and reduce some of the efficiency of the shield, but that could be addressed by using a hybrid system, as shown in Figure 3.3.

**The second option, more attractive, is to make the connection at the ends of the axial wires, small in cross section, to match the skin depth. If this is the case, it would be possible to short the cables to the ring conductor without deviating from an uniform current density. Dissipation will be higher at the ends, but since they are relatively small, the contribution to the total losses is decreased.**

### 3.3 RADIAL FLUX MACHINES WITH ELECTRICALLY CONDUCTING SHIELD

Figures 3.4 and 3.5, show the flux plots for designs with resistive shields. Figure 3.4 shows the case that includes iron teeth, while Figure 3.5 does not have iron teeth. In both cases there is a perfectly conducting wall that contains the magnetic field in the region of the generator, shielding the outside. In the case of iron teeth, there is large shortening the of the magnetic field lines in the region of the conductor, reducing the effectiveness of the generated flux, and requiring substantially higher peak fields for generating the required electromotive force.

In the case without iron teeth, shown in Figure 3.5, there is substantially less shortening of the field, resulting in substantially decreased peak fields. .

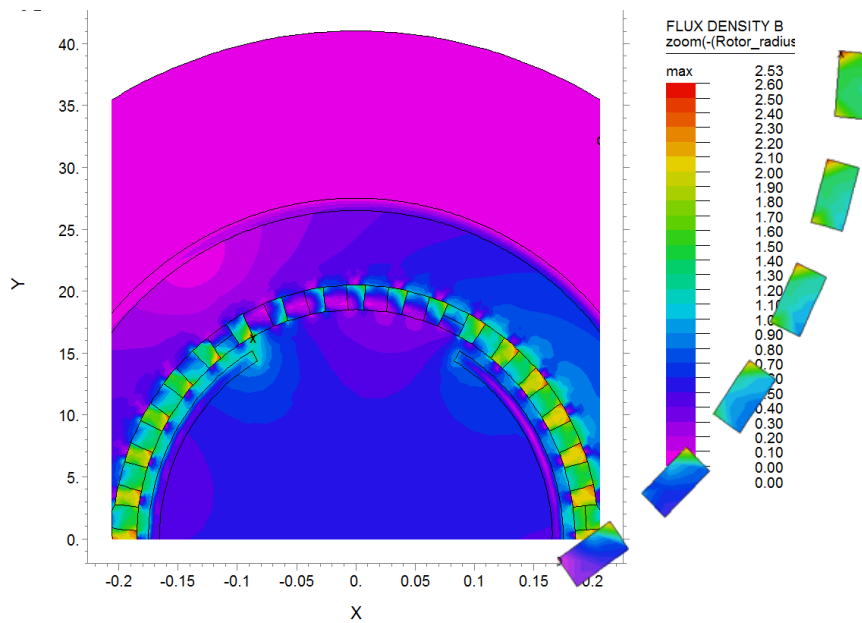


Figure 3.4 Flux density with iron teeth, no back iron, resistive shield

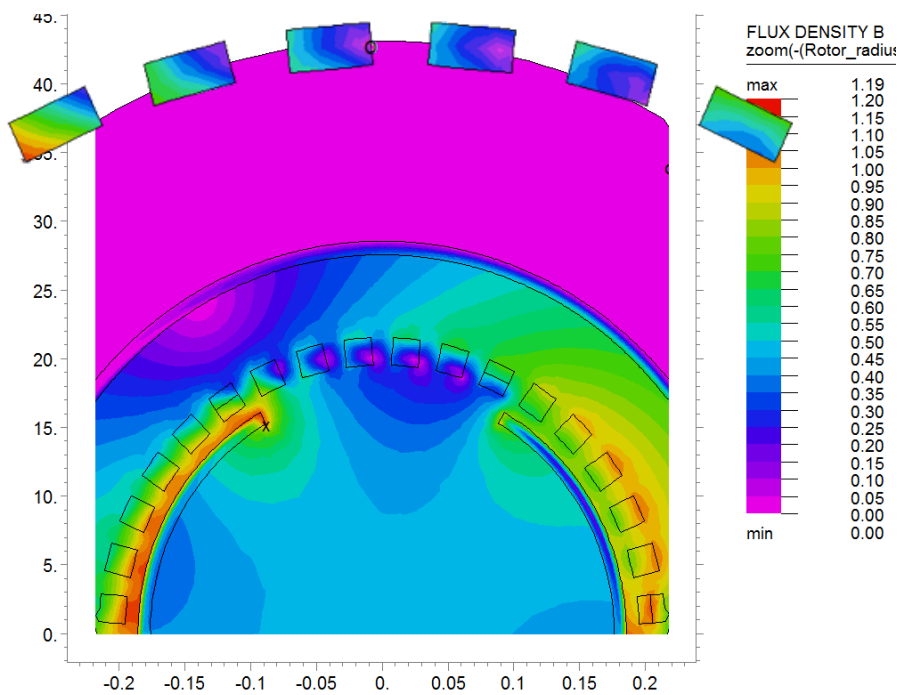


Figure 3.5 Flux density without iron teeth, no back iron, resistive shield.

**It should be noted that the machine without iron teeth and with resistive shield was the lightest machine of those scoped in Section 2.1. Those concepts have conventional stators. We did not evaluate the resistive shield concept for the case of toroidal stators. It may be interesting to do that in the future.**

The Navy and ONR have previously supported superconducting shielding. It is possible to use such a shielding in this case. However, since it is possible to reduce the weight of the system substantially by using aluminum conductors, the use of a superconducting shielding is not necessary. It could be useful, as there is already a substantial cryogenic environment.

### 3.3 REFERENCES

[Sullivan] Sullivan, C.R., Zhang, R.Y., *Simplified design method for Litz wire*, presented at the 2014 IEEE Applied Power Electronics Conference and Exposition (APEC), p 2667-74, 2014

## 4. INVESTIGATION OF LOCAL FIELD MODIFICATION TO CONTROL AC LOSSES

One possibility for decreasing the AC losses in any type of superconductor is by reducing the field magnitude in the region of the superconductor. The loops in the stator need to link field, but the field at the location of the superconductor can be 0 and still generate an EMF.

We have investigated both ferromagnetic elements to try to reduce the field, as well as conducting elements. In a brief summary, the idea proved not to work, at least as to the minimization of the field. Below we summarize the effort to minimize the fields at the superconductor using ferromagnetic and/or electrically conducting elements.

### 4.1 MAGNETIC ELEMENTS

We have evaluated the impact of the pole number by performing calculations to investigate the impact of using magnetic elements to guide the magnetic field away from the superconductor. As mentioned above, one of the goals is to minimize the use of iron, as iron dominates the weight of the machine. Instead, we use an image shield (electrically conducting elements).

The results from our initial studies are shown in Figures 4.1-4.3. Figure 4.1 show results for our baseline superconducting machine, which contains both iron teeth and back iron. The field at the stator is mostly radial, with relatively minor fields in the slots for the armature winding.

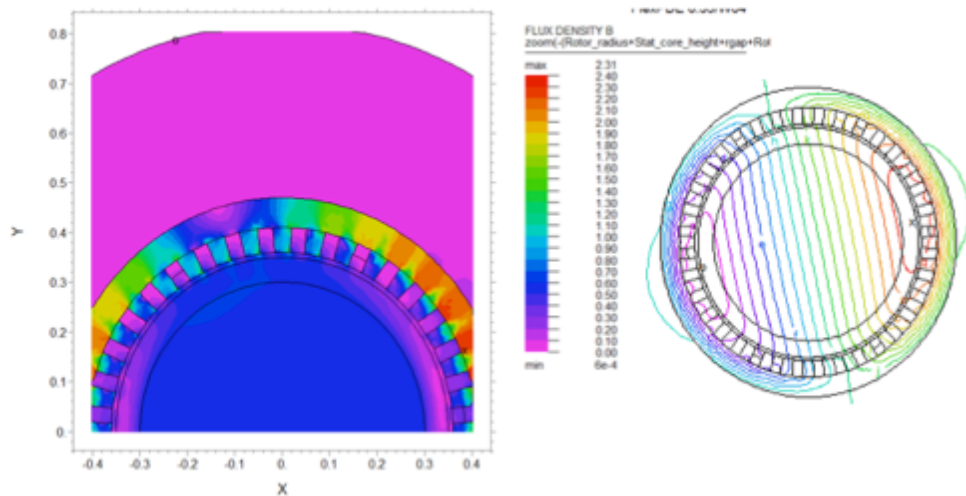


Fig 4.1 Field profile and amplitude in the presence of back iron

In the case of no back iron, with iron teeth and an image shield, the field profiles are illustrated in Figure 4.2. The field direction is in the azimuthal direction, resulting in little EMF generation. The case in Figure 4.2 has about 1/4 the torque from that in Figure 4.1. Part of the decrease is the reduced reluctance of the magnetic circuit, with a lot of iron replaced by air. And part is due to the field generated being much less effective in generating torque.

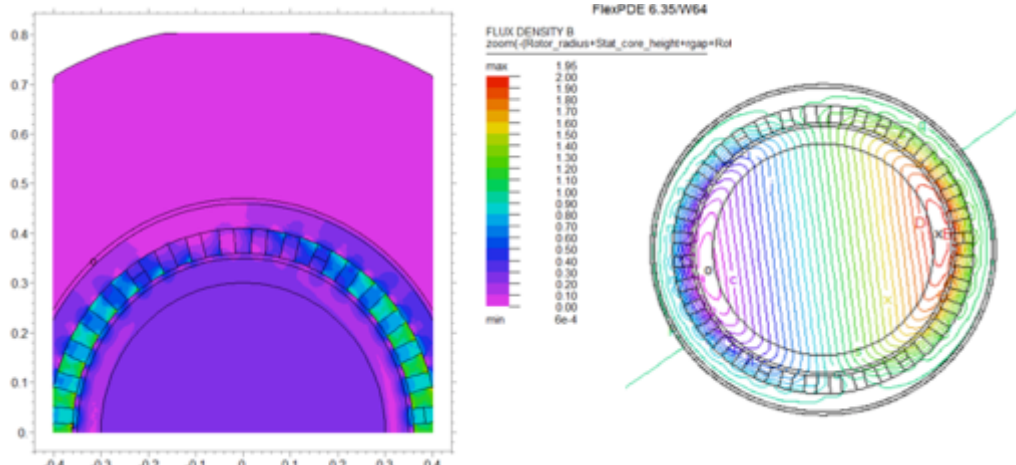


Figure 4.2. Field profiles and field lines for the case with iron teeth but no back-iron, with a small gap between the back-iron and the stator.

The image shield in Figure 4.2 is placed very close to the stator. The impact of moving the image shield away from the stator is illustrated in Figure 4.3. Although less of the field is in the azimuthal direction in the region of the stator, there is still a lot of field there. The azimuthal field not only decreases the torque of the machine, but it increases the AC losses in the stator.

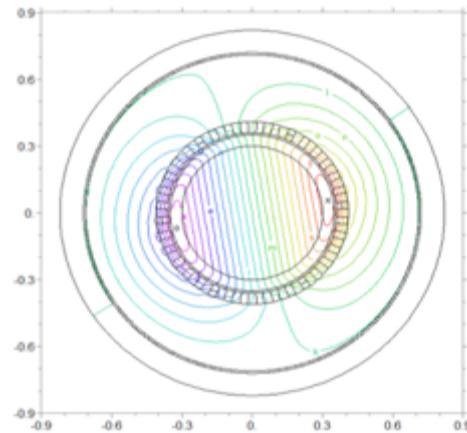


Figure 4.3. Same as Figure 4.2 but with a larger gap between the stator and image shield.

The case with larger number of poles shows similar effects. Figure 4.4 shows the base case, assuming the presence of back iron. The flux is nicely guided by the iron away from the slots in between teeth.

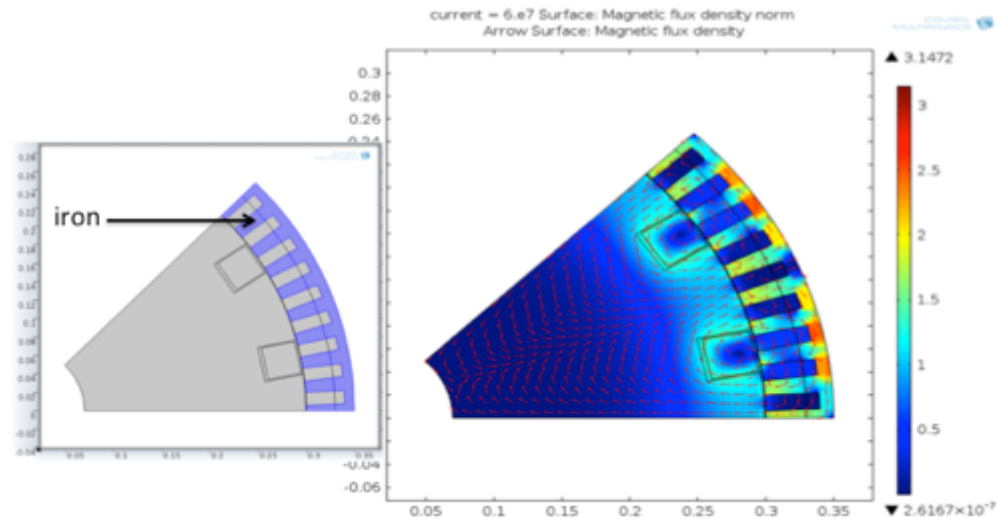


Figure 4.4. Baseline configuration for an 8 pole machine. The iron region is shown in light blue.

Figure 4.5 shows the case without the back iron. The field in the slots increases substantially, with some region going into saturation. What is happening is that the iron is actually short-circuiting the field in the azimuthal direction.

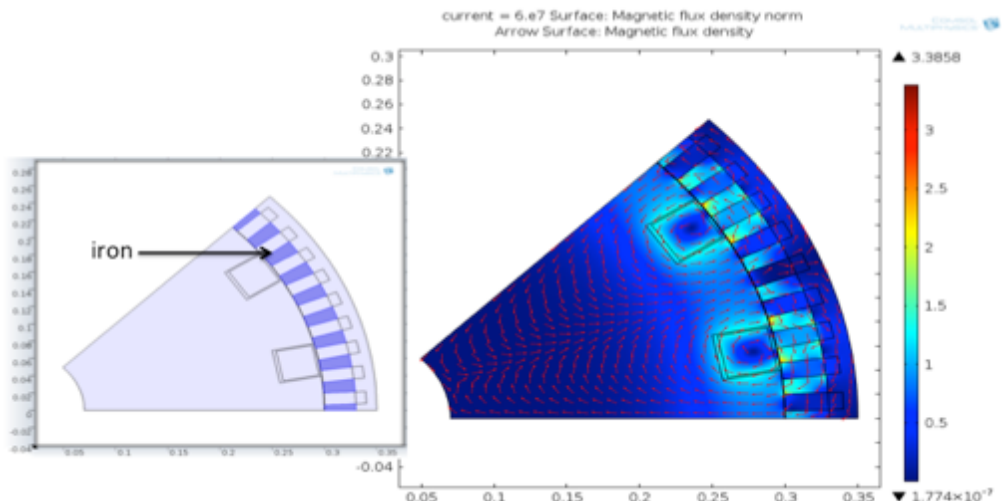


Figure 4.5. Impact of the use of iron teeth but no back-iron. Iron is shown in light blue.

To eliminate the azimuthal fields in the stator, we have investigated the option of a split rotor. In this case, the rotor on one side pushes the field while the rotor on the other side pulls on the field. We describe this option later in this report.

## 4.2 ELECTRICALLY CONDUCTING ELEMENTS

As the magnetic shielding elements were ineffective for controlling the field in the armature, we explored the possibility of using electrically conducting elements. The electrically conducting elements were assumed to have high conductivity, using the conductivity of copper at room temperature.

The concept assumes that there is a conducting element, located away from the cryogenic environment, where currents can flow to eliminate the externally produced field at the superconductor. It is clear that the concept will not remove the self shield, but it is assumed that the losses due to the self shield will be small. The goal of this part of the program is to calculate the required amount of conductor to shield the field, and then to calculate the losses.

We determined that in order to calculate the effect, it could not be performed in 2D. We built a 3D model, shown in Figure 4.6. We assume an axial extent of the conductor of 10 cm, sufficient to make the end effects small.

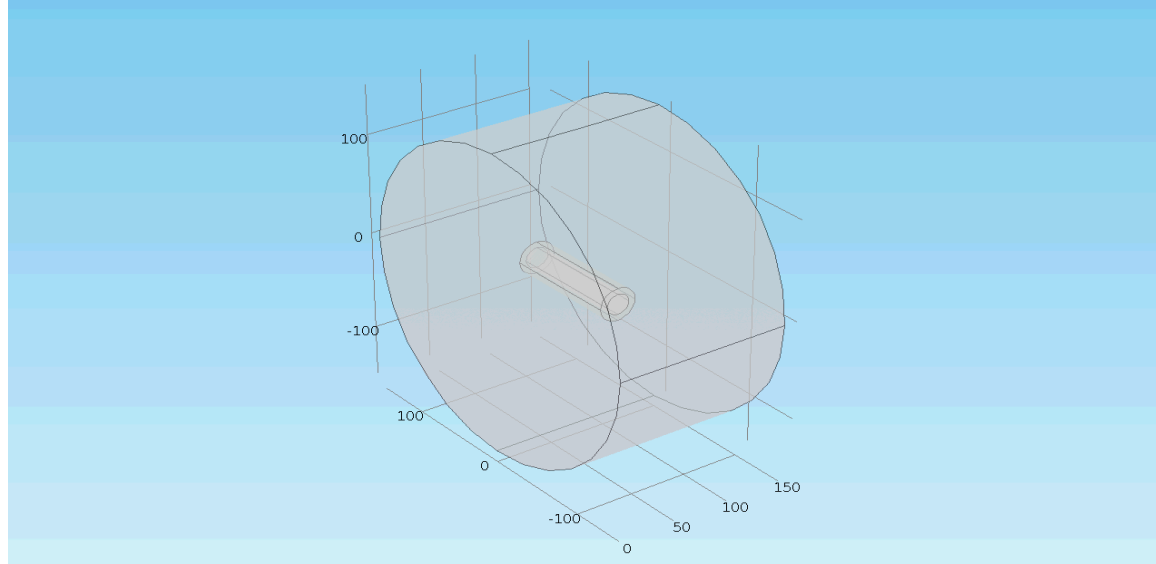


Figure 4.6 3-D model of the electrical conductive shielding of the superconductor. As mentioned in the text, the electrically conducting shield is at room temperature.

As shown in Section 2, the typical field in the superconductor is about 0.1 T. We have fixed the AC field in the system to 0.1, homogeneous (in the absence of currents in the electrical conducting sheaths).

Typical results for an inner diameter of 20 mm and shield thickness of 2 and 6 mm are shown in Figure 4.7. Shown in the Figures are contours of magnetic fields. For 2 mm thickness (left plot), the field inside the electrically conducting sheath is about 0.09 T, that is, the field has been decreased by about 10%. On the other hand, on the right, with a wall thickness of 6 mm, the field has been decreased by about 50%. Thus, the shielding is somewhat successful, but at 117 Hz (7000 rpm), for substantially more efficient shielding, the thickness will have to be about 1 cm.

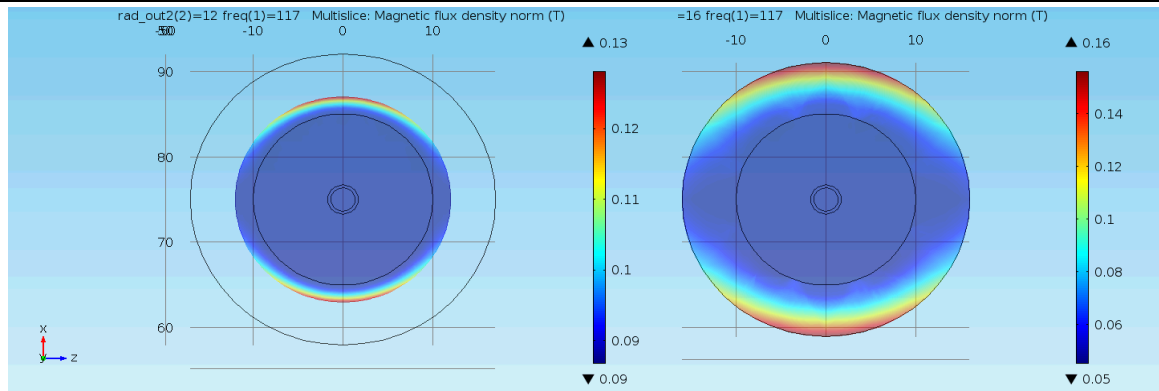


Figure 4.7 Efficiency of electrically conducting shielding for 2 mm (left) and 6 mm (right) wall thickness. Background field is 0.1 T.

The corresponding plots with current density are shown in Figure 4.8 for the same cases as Figure 4.7. As expected, the total current density is 0, being positive on one side of the shield and negative on the opposite side. The peak current density for 2 mm thickness is about  $2.1 \times 10^7$  A/m<sup>2</sup> while for 6 mm it is  $2.6 \times 10^7$  A/m<sup>2</sup>. Both the current density is higher in the case of the thicker wall, but also it is thickness, meaning that the total current in one polarity increases substantially for the case of 6 mm, by about a factor of 4, contributing the substantial shielding of the magnetic field in the core.

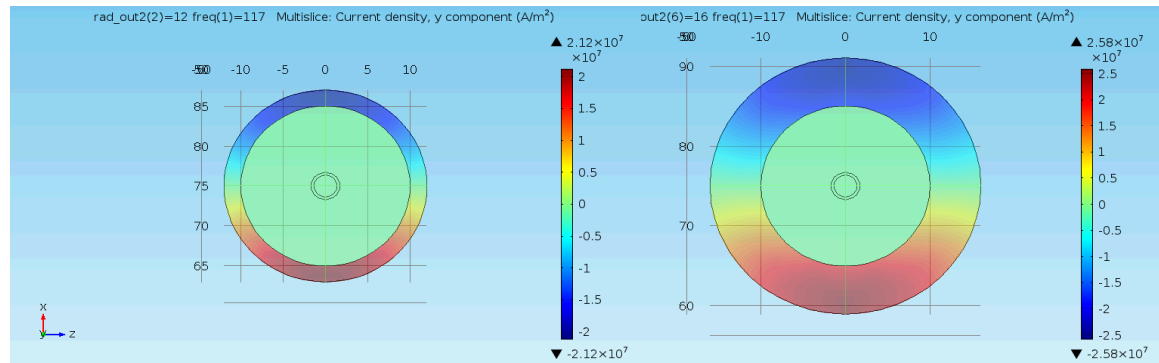


Figure 4.8 Current density (flowing in the axial direction) for the cases shown in Figure 4.7

We have calculated the losses in the electrically conducting shield. The resistive losses, per unit length, as well as the field in the core of the electrically conducting shield, are shown in Figure 4.9.

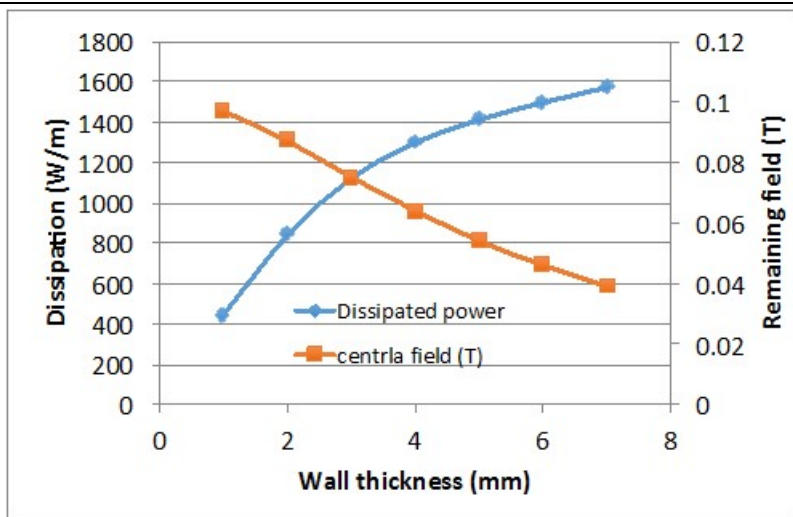


Figure 4.9 Resistive losses and remaining magnetic field for the electrically conducting shield. 177 Hz and 0.1 T applied background magnetic field.

Thus, the electrically conducting shield can be effective. However, at the high frequencies of the Navy operation, it results in high power dissipation. It should be noted that only shielding is needed in the inner leg of the toroidal stator. There are 144 turns in this region, with a length of about 0.6 m, for a total length of 100 m. The resistive losses are then about 150 kW, which decreases the efficiency of the generator by about 1%. However, more importantly, is the need for aggressively cooling the shield. This is the challenging issues

## 5. STATOR WINDING AND ASSEMBLY

For superconducting stator coil, manufacturability of the stator assembly and stator coil is one of the main factors to determine coil shape. The main goal is to minimize potential risk of damaging coils during fabrication and assembly while controlling cryogenic heat load to the overall cooling system. Here is a breakdown of different coil configurations investigated during the project.

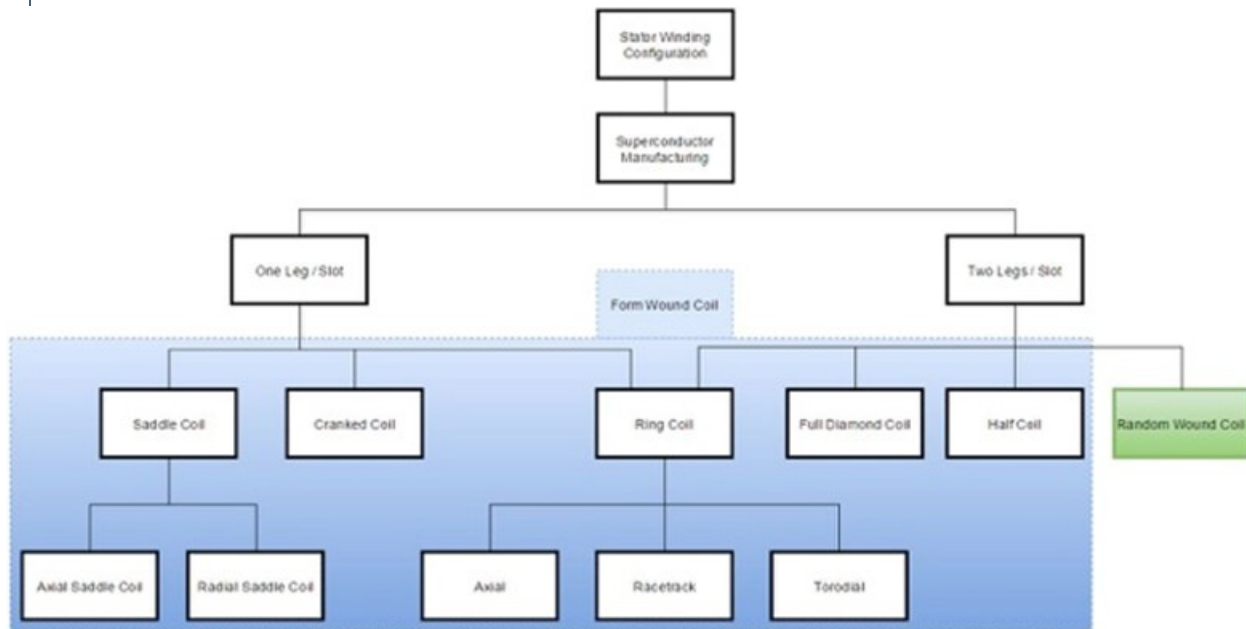


Figure 5.1 Breakdown of different potential coil configurations

### 5.1 SUPERCONDUCTOR MANUFACTURING METHOD

The main superconductors considered for this section are YBCO and MgB<sub>2</sub>. YBCO tape conductor can be used directly during the winding process without additional process. The tape form lends itself to more of racetrack geometry. MgB<sub>2</sub> comes in stranded form, so it is not as limited to coil geometry as YBCO. However, how MgB<sub>2</sub> is manufactured can limit the coil forming process. There are two methods to process MgB<sub>2</sub>: ex situ and in situ. An ex situ technique uses pre-reacted MgB<sub>2</sub> powder, while an in situ technique uses precursors of MgB<sub>2</sub> that requires a reaction temperature up to 650+°C to form MgB<sub>2</sub>. Even though MgB<sub>2</sub> using in situ technique tends to have better current carrying capability, it is more brittle compared to the ex situ technique. This high temperature requirement prevents certain manufacturing process, such as, winding and reacting superconducting coils around stator teeth, because stator lamination and coil insulation cannot survive such temperature. React the superconductor first and wind it into a coil can be challenging because of the lack of ductility.

### 5.2 NUMBER OF LEGS PER SLOT

Slot filled ratio is the area percentage of conductor inside the slot over the slot area. One leg per slot has higher slot fill ratio because it has less insulation compared to two legs per slot configuration, and this usually allows one leg per slot configuration to have higher current and flux level inside the machine. However, this parameter affects the coil shape and how coils are inserted into the slot.

## 5.3 COIL MANUFACTURING

Besides the number of legs per slot, methods to form a coil have an effect on coil configuration. For traditional electric machinery, coils are divided into two categories: form wound and random wound.

Form wound coil represents a coil that is wound and formed on an outside fixture and wrapped with insulation. Form wound coil has a well-defined geometry where not only the cross section of the coil is constant along the core, but the position of each conductor/turn is fixed. After fully formed, each coil is laid into the proper location inside the machine. Random wound coil can be wound directly inside the machine or on an outside fixture but the position of each conductor is not fixed along the length of the core, hence “random”, and relies mostly on the insulation of each individual strand. Figure 5.2 shows a comparison between random wound and form wound stator.

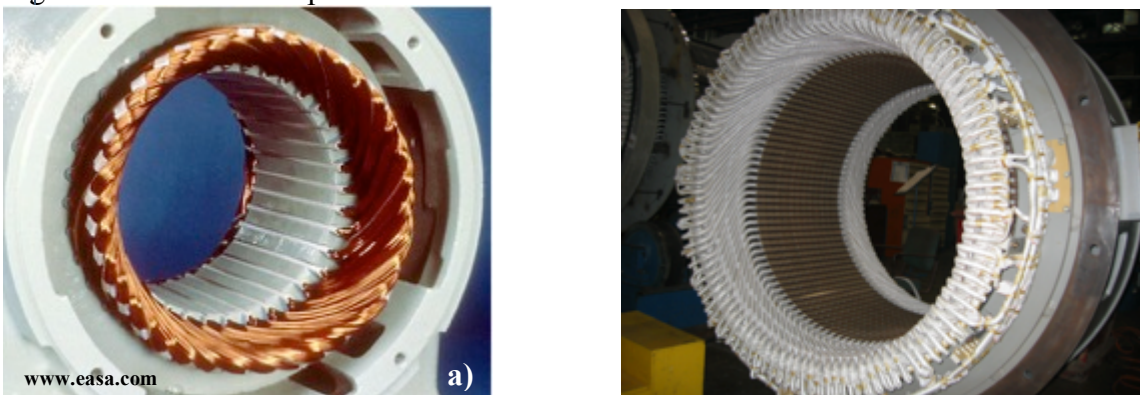


Figure 5.2 Comparison between a) random wound and b) form wound stator

### 5.3.1 RANDOM WOUND COIL

Random wound coils are used traditionally for low HP and low voltage machines. Bundles of small magnetic wires are formed and pressed into final coil shape after inserting into the slot, so the coil shape tends to be less defined. Since MgB<sub>2</sub> comes in the stranded form, random wound was considered as a potential configuration for the stator coil. Figure 5.3 shows a conceptual model of random wound stator.

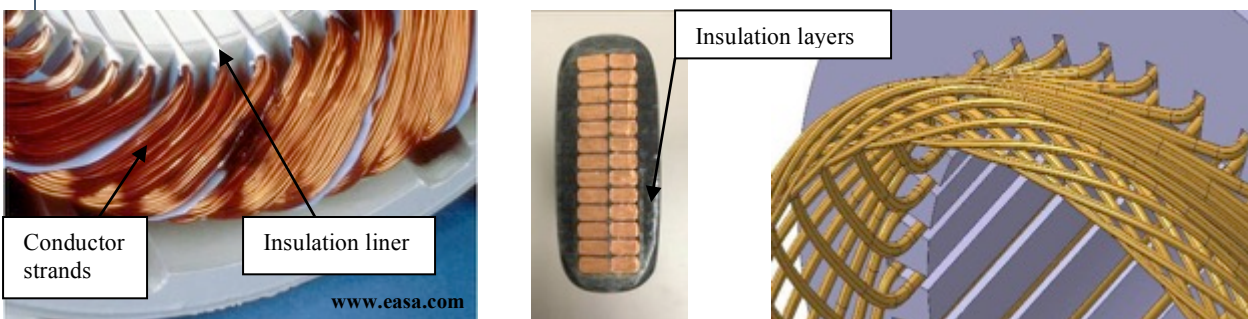


Figure 5.3: Partial stator view for a random wound stator (left), cross section of a form wound coil (center) and illustration for random wound configuration using superconductor (right)

One drawback for the random wound machine is poor insulation protection, which leads to early machine failure, especially for high voltage machines. As seen in figure 5.3, a random wound stator

uses only slot liner compared to many layers of insulation used in form wound coil. The insulation protection is the reason why most high voltage large motors use form wound coils even though the manufacturing process is more labor intensive and expensive. Another concern for this configuration is the complex bending geometry. The nesting pattern near the end turn shows the intricate weaving between strands. Traditional conductor material, copper, is very malleable, but unfortunately, superconductor may not be able to survive such complex bends while maintaining its current carrying capability. If the coil is formed using the CIC method, another potential concern is the bending radius of the stainless steel jacket and the cooling tube inside.

### 5.3.2 FORM WOUND COIL

The rest of the section will discuss several different types of form wound coil configurations.

#### 5.3.2.1 FULL DIAMOND AND HALF COIL

Full diamond coil is the most common form wound coil used in large electric machinery. Because all the coils are the same, once the setup is in place, coils can be built from a single setup. One potential challenge to use diamond coil configuration with superconductor is the knuckle region, shown in Figure 5.4. Around the knuckle bend, a generous bending radius is needed to prevent damage to the superconductor and the cooling tube for CIC configuration. One way to circumvent the issue is to use two half coils joined by a special connector. This method is used for traditional coils with embedded cooling tubes. The connector serves both as an electrical and hydraulic connector.

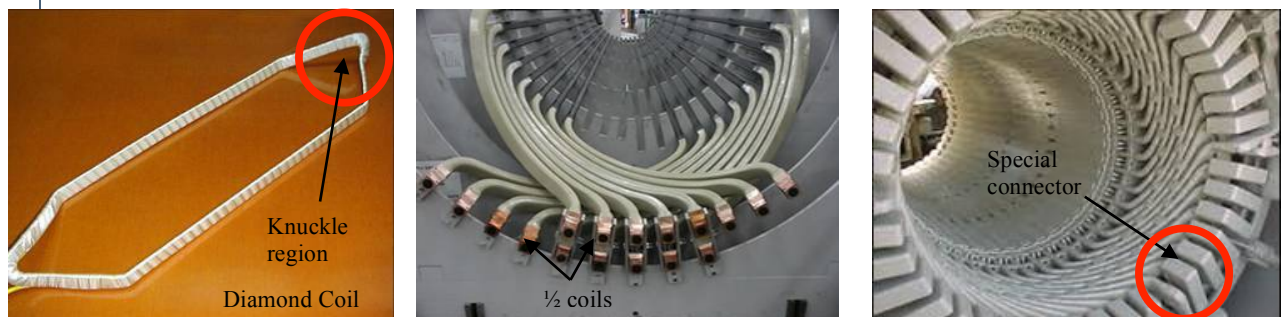


Figure 5.4: Diamond coil (left), half coil (center) and special connector for half coil (right)

Even though half coil configuration can sidestep the knuckle problem, it does introduce additional joint per coil. For the entire stator, this doubles the number of joints, which are potential quench and heat leak locations. The additional heat leaks will raise the cryogenic cooling requirement and lower the overall system efficiency.

#### 5.3.2.2 SADDLE COIL

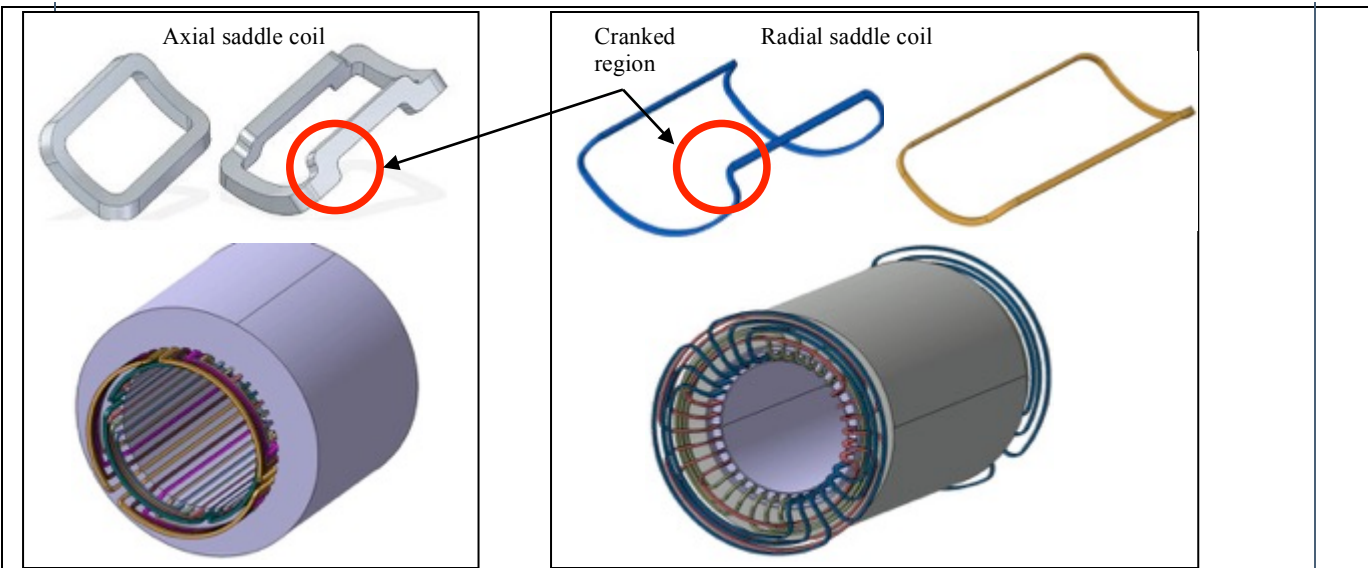


Figure 5.5: Axial saddle coil (left) and radial saddle coil (right)

For saddle coil seen in figure 5.5, the sharpest bending angle is  $90^\circ$  at the cranked region. The one leg per slot design is the reason for the cranking; it allows one coil leg to cross over other coil legs. For superconducting tape, the cranked region may require special attention because of the edge bending around the tape. The difference between the two configurations is the end region. Axial saddle coil occupies more axial space in the end region while radial saddle coil requires more space radially. To insert the coil into the slot, radial saddle coil will require a much more complicated split core assembly, which will be discussed in later section. Unlike diamond coil, saddle coil configuration requires more tooling to adjust for different coil shapes and sizes. Lastly, because of the coil pattern, the lowest pole count for this configuration is 4 pole.

#### 5.3.2.3 CRANKED COIL

Cranked coil (figure 5.6) is a hybrid design between the diamond and the saddle coil. It has both the cranked and the knuckle region, so the challenge is the bending radius. Like the diamond coils, all the coils are the same, so a single setup can be used to build every coil.

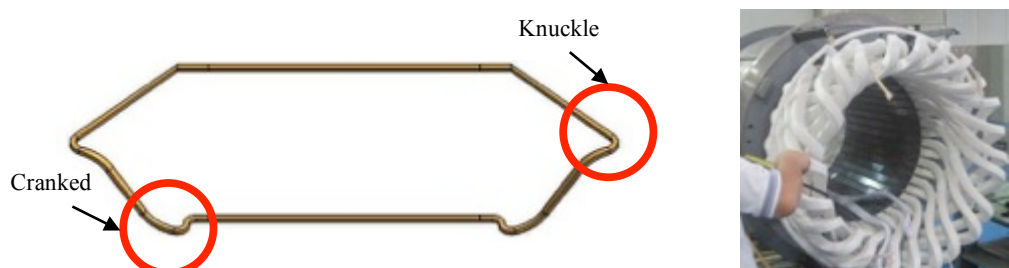


Figure 5.6: Cranked coil configuration

#### 5.3.2.4 RING COIL

Comparing with other coil configurations, ring coil is probably the least complicated and the most appealing from the manufacturing point of view because of the familiarity with this design used on

superconducting rotor field coil. This configuration is especially suitable for any tape conductors. There are 3 main configurations: racetrack, axial and toroidal (figure 5.7).



Figure 5.7: Ring configurations: racetrack (left), axial (center) and toroidal (right)

Another advantage for ring coil is the possibility of individual coil cryostat. Because the simplicity of the coil shape, it is possible to build a cryostat around the coil. Even though designing and manufacturing individual cryostats can be a challenge compared to building a cryostat for the entire stator, individual cryostats can isolate losses and lower cryocooler requirements significantly.

Normally, if the entire stator is in cryogenic temperature, a massive cooling power from the cryocooler is needed to remove superconductor losses as well as core losses (kW range) from the stator. By separating core losses from losses in the superconductor, individual cryostat can lower the cooling requirement, raise overall system efficiency and minimize cryocooler footprint. Core losses can be removed by other more efficient cooling methods.

For axial and racetrack configuration, it is possible to have two legs per slot. For axial configuration, one of the limitations is the bending radius in the ID region. The space constraint in the ID region controls the maximum bending radius possible in that region. For racetrack configuration, the space in between the teeth limits the size of the coil. This concept was evaluated in the SRM design, but excessive loss and inherent high torque ripple make this design not feasible for large motors.

As mentioned in previous section, electromagnetically, the toroidal configuration has a great potential for superconducting stator, but one of the major challenges with toroidal design using individual cryostats is the stator assembly. For the toroidal stator with regular copper coils, winding is wound directly onto the stacked stator. Unfortunately, the process is very complicated with form wound coils in individual cryostats. In the next section, several potential options are offered on how to build a toroidal stator with individual cryostats.

Below is a summary of different configurations.

Table 5.1: Summary of different coil configurations

Ring/Racetrack Coil								
	Full Diamond	Half Coil	Random Wound	Cranked Coil	Radial/Axial Saddle Coil	Axial Flux Stator	SRM Stator	Toroidal Stator
Pros	<ul style="list-style-type: none"> <li>• Manufg. familiarity</li> <li>• Single setup</li> </ul>	<ul style="list-style-type: none"> <li>• No knuckle bend</li> </ul>	<ul style="list-style-type: none"> <li>• Strand pattern like MgB<sub>2</sub></li> </ul>	<ul style="list-style-type: none"> <li>• Single setup</li> </ul>	<ul style="list-style-type: none"> <li>• 1 leg/slot</li> <li>• Simple 90° bend</li> </ul>	<ul style="list-style-type: none"> <li>• Manufg. familiarity</li> <li>• Individual cryostat</li> <li>• Single setup</li> </ul>	<ul style="list-style-type: none"> <li>• Manufg. familiarity</li> <li>• Individual cryostat</li> <li>• Single setup</li> </ul>	<ul style="list-style-type: none"> <li>• Manufg. familiarity</li> <li>• Individual cryostat</li> <li>• Single setup</li> </ul>
Cons	<ul style="list-style-type: none"> <li>• Knuckle bend</li> </ul>	<ul style="list-style-type: none"> <li>• Increase joints</li> </ul>	<ul style="list-style-type: none"> <li>• Complex bends</li> <li>• Poor insulation protection</li> </ul>	<ul style="list-style-type: none"> <li>• Knuckle bend</li> </ul>	<ul style="list-style-type: none"> <li>• Possible complex assembly</li> <li>• Cannot use for 2 pole</li> </ul>	<ul style="list-style-type: none"> <li>• ID space constraint</li> </ul>	<ul style="list-style-type: none"> <li>• High losses</li> <li>• High torque ripple</li> </ul>	<ul style="list-style-type: none"> <li>• Complex Assembly</li> </ul>

## 5.4 STATOR ASSEMBLY

Certain winding configurations require special assembly processes. The process is strongly influenced by the cryostat design and its location in the stator. As mentioned before, it is important to limit the heat load into the cryocooler because of the large core losses. This means it is critical for the cryostat to intercept heat loads from certain components while relying on other cooling methods to remove heat elsewhere.

### 5.4.1 RADIAL SADDLE COIL STATOR ASSEMBLY

Typically, the stator is stacked and pressed before inserting coils through stator ID. It is not possible for radial cranked coil configuration because of the coil's long end turns. Since it is still too complicated to build a cryostat around each coil, cryostat can be built to separate (stator teeth + coils) and (stator backiron). Instead of absorbing all the stator losses, cryostat only has to absorb the losses from stator teeth and coils. The losses are still significant, but not unmanageable.

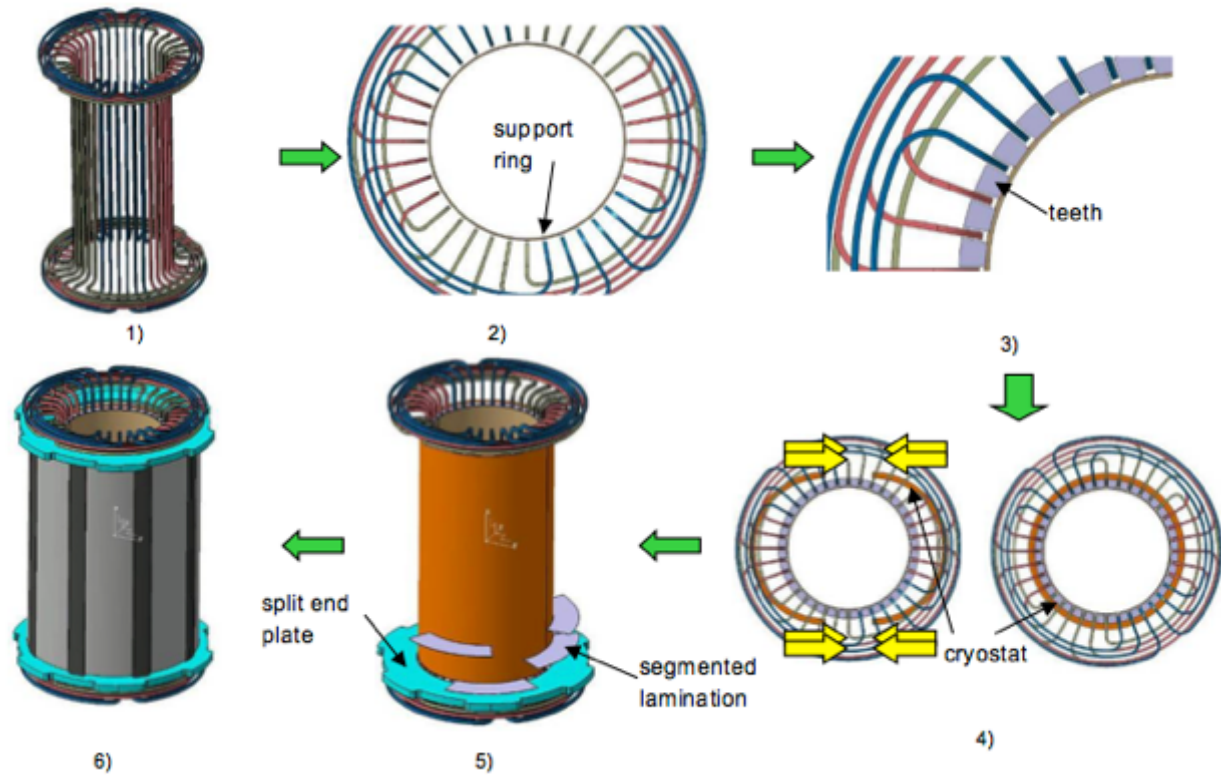


Figure 5.8: Stator construction for radial saddle coil configuration

Here is the simplified process (figure 5.8)

- 1) Form coils and position coils in designated locations
- 2) Add inner support ring
- 3) Insert stator teeth onto the support ring
- 4) Attach the cryostat. Cryostat has to be in 2 pieces to fit over the coils and the teeth.
- 5) Lay out segmented lamination around the cryostat
- 6) Stack and compress the stator core.

#### 5.4.2 RACETRACK COIL

From the manufacturing (coil and stator) perspective, racetrack configuration is the easiest. As shown in figure 5.9, the stator backiron can be stacked like the traditional machine, and the stator teeth and the racetrack coil can be assembled similar to a traditional synchronous field pole and mounted onto the backiron.

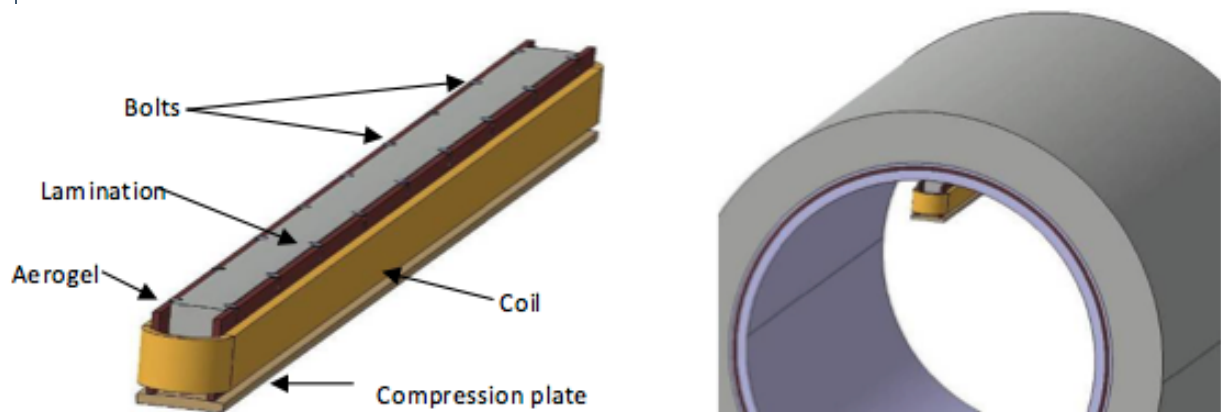


Figure 5.9: Preliminary concept for racetrack coil with bolt on stator teeth

#### 5.4.3 TOROIDAL COIL

The methods described below show 3 ways of assembling a stator with form wound toroidal coil.

Method 1 (figure 5.10):

- 1) Setup segmented end plates with built-in supports
- 2) Each coil is slide in between the plates and moved to the side
- 3) Lamination segment is inserted sideway. This will require a little fitness to fit the lamination inside the coils.
- 4) Need to use locating rods on the OD to location the lamination's radial and tangential position.
- 5) Alternate the lamination so the seam in between the laminations does not overlap each other.

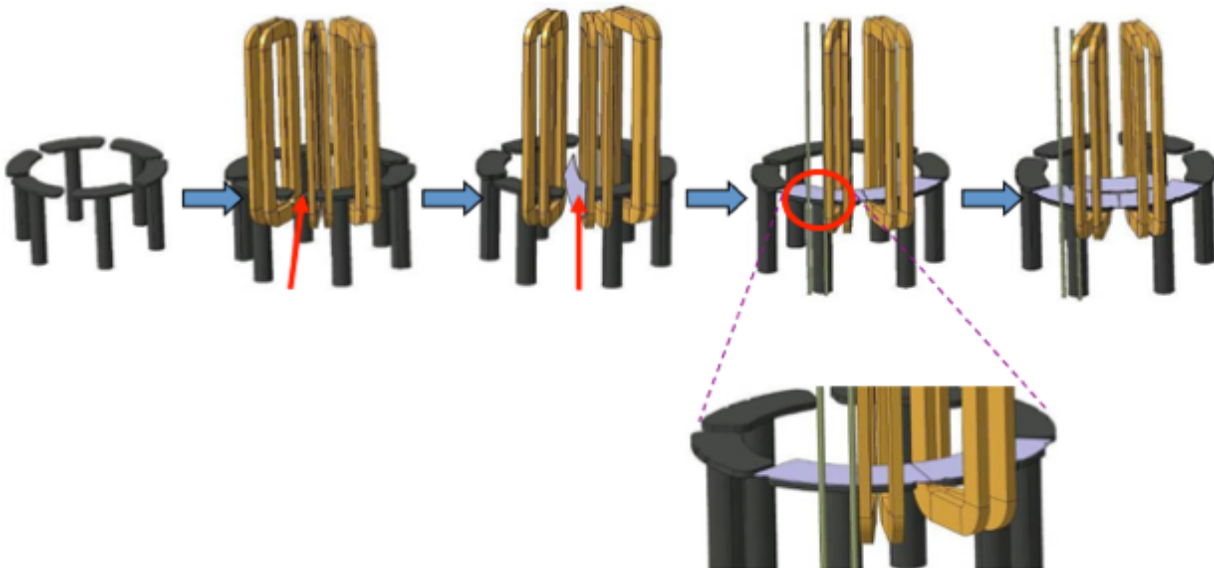


Figure 5.10: Method 1 to assemble the toroidal stator

Method 2 and 3 (figure 5.11) are very similar:

- 1) Setup supports and an end plate with an opening
- 2) Slide in all the coils
- 3) Add another support and continue to shift original supports and the coils until they reach proper position.

- 4) Close up the end plate opening
- 5a) Install gauges to locate the segmental lamination
- 5b) Rotate the supports and coils around the circle to install lamination.
- 6) Instead of using segmented lamination, it is a full circle lamination with a slit. The lamination can be installed like a keychain due to the flexibility of the lamination and the slit.

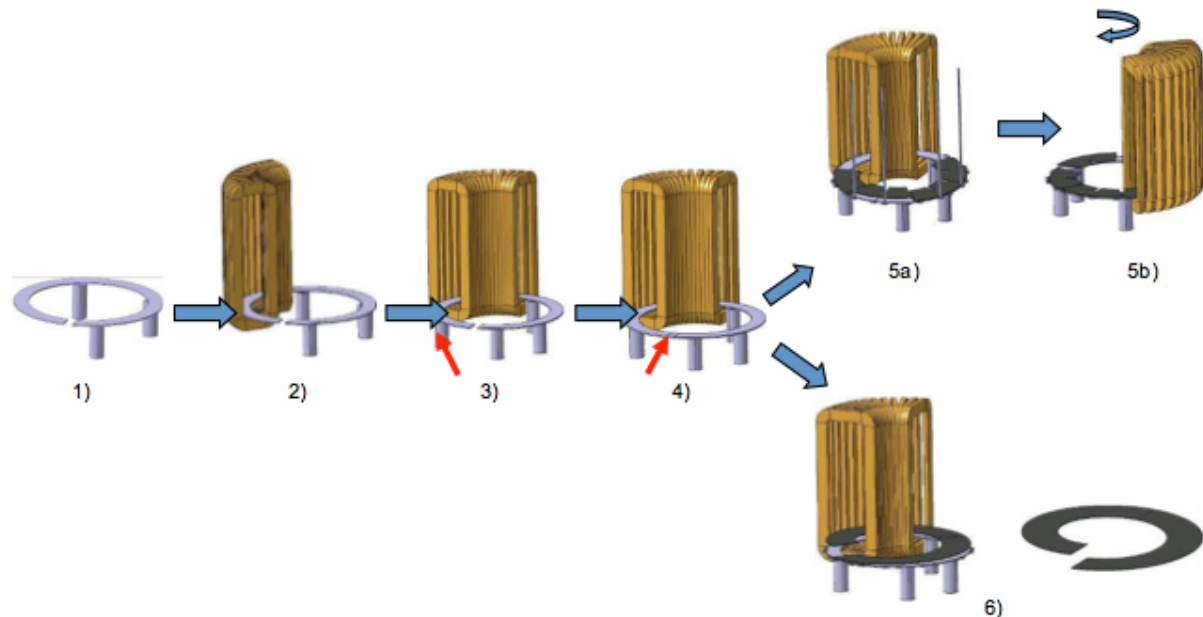


Figure 5.11: Method 2 and 3 to assemble toroidal stator

One concern for this configuration is stator backiron cooling. Normally, the stator backiron can be cooled through waterjacket cooling. Waterjacket, a built in water-air heat exchanger, is shrunk onto or wrapped around the backiron, and the losses generated in the stator is removed through direct contact conduction cooling. With this toroidal configuration, it is challenging to implement this type of cooling scheme since the space around the stator OD is taken up by half of the coils. To remove the heat from stator core, it can use air cooling or water cooling with sophisticated piping.

#### 5.4.4 AC HOMOPOLAR STATOR

For AC Homopolar stator, because, at different parts of the stator, the magnetic field can travel axially, azimuthally and/or radially (figure 5.12), the stator lamination has to be divided into different sections to channel the magnetic field.

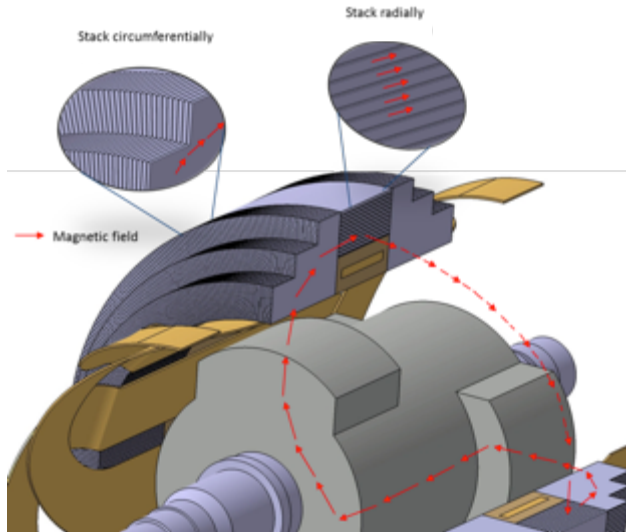


Figure 5.12: magnetic field path and lamination stacking direction for AC Homopolar stator

For this special design, there are multiple stacking sequences. Both ends of the stator core are stacked circumferentially while the middle of the core is stacked radially. For the middle of the core, lamination can be stacked in the form of a steel roll. As for both ends, the main challenge is to apply stacking pressure circumferentially. As the lamination stacked in a circle, gaps in the OD are much larger than gaps in the ID (figure 5.13). One method is to exert pressure using wedges driven in between laminations. Even though figure 5.13 shows a single teeth plate with tooth acting as a wedge, it can also be several segmental teeth plates. Radial pressure is applied on segmental teeth plates, which, in turn, apply circumferential pressure to the lamination. Once sufficient pressure is achieved, the remaining gaps in between laminations can be filled with epoxy.

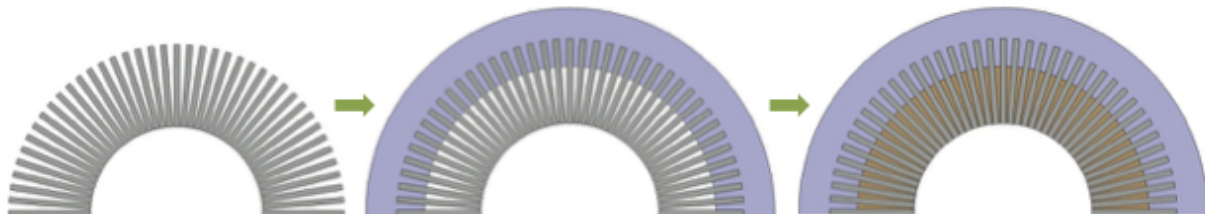


Figure 5.13: Proposed method to stack circumferential laminations

After each section is stacked and pressed, all three sections are pressed against each other axially to form the complete core. Since sections are pressed against each other, there will be a discontinuity magnetically between the seams. The reluctance in those regions needs to be considered during the design.

Another concern for this design is the heat transfer through or across the lamination. For materials, like Metglas®, thermal conductivity is 9W/mK parallel to the plane and 0.625 W/mK normal to the plane. Since stacking direction varies in the core, it is important to properly design the heat transfer path to remove heat from the core. Also, since this design has three cores pressed together, contact resistance will play an important role for the heat transfer.

## 5.5 JOINTS

Joints inside the stator are used to connect coils in different configurations. Figure 5.14 is an example of 2 pole, 3 phase, Wye connection, 1 parallel, 72 coils.

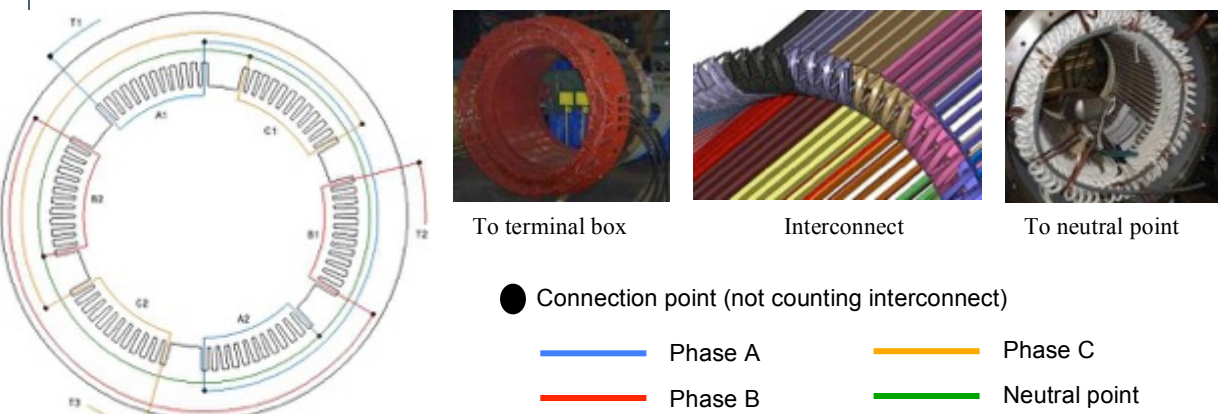


Figure 5.14: Connection diagram and the type of connection

This diagram does not show the number of interconnect (connection in between the coils in the same phase group). The number of connections is 78 total (66 - interconnections, 6 - within phase, 3 - neutral point connection, 3 - to terminal box). For 14MW, 6.6kV, 1 parallel,  $I = 1224.68A$ , so the loss due to connection is  $I^2R \times 78$ , and  $R$  is the joint resistance. If  $R = 5e-6W$ , the loss is 585W. In order to control the heat load into the cryocooler, less number of coils or the resistance value  $< 1e-7W$  is recommended.

For traditional machines, making joints involve brazing copper wires or cables in between the leads. To make superconducting joints, space constraint inside the stator and bending radius are some of the limiting factors to consider. The space for interconnect connection in between the coils is very small because the coils are next to each other. Without a special connector, superconductors, such as MgB<sub>2</sub>, may present challenge to connect each strand in a tight location. An alternative to making joints inside the stator is to pull all the cables into a terminal box and make the connections inside. One drawback is the cryogenic requirement for the entire length of the cable as well as inside the terminal box.

## 5.4 CONCLUSION

In conclusion, each winding configuration has advantages/disadvantages and is influenced by many factors (superconductors, stator assembly, bending radius...etc.). At the same time, each configuration produces different electromagnetic results, so, to down-select the best configuration, it is a balance between manufacturability and performance. Risk assessment has to be made to address the potential damage to the superconductor during manufacturing.

## 6. SUPERCONDUCTOR OPTIONS

There are several choices for the type of superconductor to use in the stator winding, and several means to make cables out of them. Figure 6.1 shows the variation between critical magnetic field and temperature for all major technical superconductors. A technical superconductor is one that can be produced with consistent properties over long enough length and has high enough critical current density to be usable in a high current density device. The processing characteristic for each superconductor determine the form of the composite wire that can be manufactured using that material. Some conductors are available as fine filaments in round wire, while others are applied as coatings on flat tapes. The form of the wire in turn determines the available cabling technique.

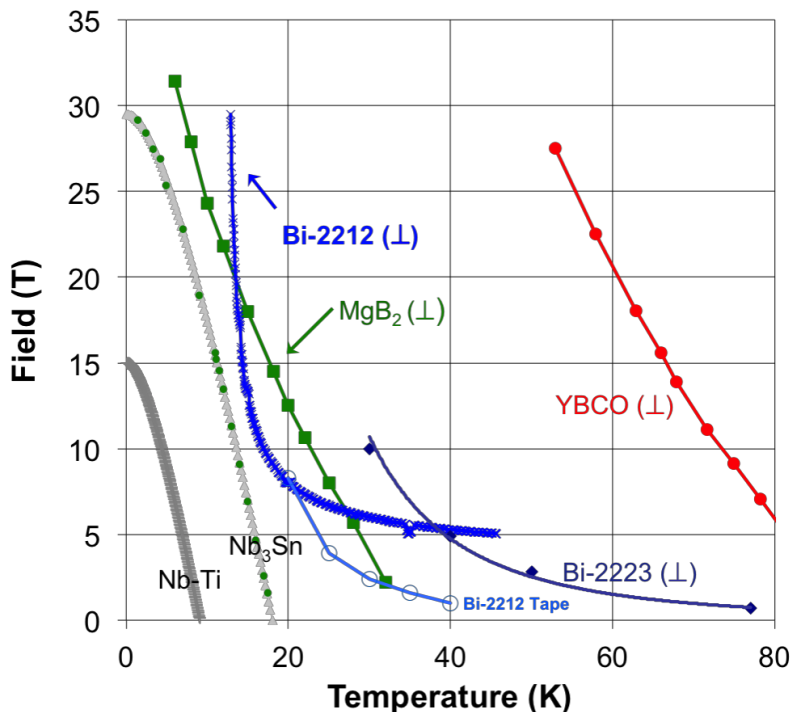


Figure 6.1. Critical magnetic field vs temperature for technically useful superconductors.

### 6.1 HIGH TEMPERATURE SUPERCONDUCTOR SELECTION

For the high speed stator application we are most interested in superconductors that can operate at low fields at temperatures above roughly 15~20 K. We are interested in this operating temperature range because it offers the possibility to significantly reduce the refrigeration cost associated with the use of superconducting materials. The overall efficiency of a cryogenic cooling system,  $\eta_{ov}$ , is typically represented as the product of two components. The first is the Carnot efficiency,  $\eta_{Carnot}$ , which is the maximum efficiency that can be achieved for an ideal refrigerator that absorbs energy at low temperature,  $T_L$ , and rejects it at high temperature,  $T_H$ . The second is the coefficient of performance,  $COP$ , which is the ratio of the achieved refrigerator efficiency to the Carnot efficiency. For comparison purposes, the heat rejection temperature,  $T_H$ , for a cryogenic cooling system is generally taken as 300 K.

$$\eta_{ov} = COP \cdot \eta_{Carnot}$$

$$\eta_{Carnot} = \frac{T_L}{T_H - T_L}$$

The overall refrigerator efficiency determines the electrical input power,  $P$ , needed to produce low temperature cooling power,  $Q$ .  $P = \frac{Q}{\eta_{Carnot}}$ .

Four types of superconducting materials have undergone significant commercial development since the discovery high temperature superconductivity (HTS) more than three decades ago. All four are capable of operating in the low field stator environment at temperatures above 20 K. The candidate materials for potential use in a high-speed stator include:

- *BSCCO – 2223*: This is the first HTS material to be extensively commercialized. The conductors are in the form of highly compacted ceramic filaments embedded in a large aspect ratio, silver matrix tape. The compaction is used to achieve high current density in the filaments, while the tape structure is an artifact of the rolling process used to obtain the desired crystallographic orientation of the superconductor. These tapes are typically on order of 0.2 mm thick and 4 mm wide.
- *BSCCO – 2212*: These conductors generally consist of multiple ceramic filaments in a round silver matrix. Recent efforts to increase the current density in these conductors have focused on high pressure processing during heat treatment as a means to compact the filaments to high density.
- *YBCO*: These conductors consist of continuous superconducting ceramic films deposited on specially textured, high aspect ratio metallic substrates. YBCO tapes are typically on order of 0.1 mm thick and between 4 mm and 12 mm wide. YBCO tapes presently exhibit the highest effective critical current density of all commercial HTS. Recent development efforts have investigated the use of continuous striation along the length of the coating layer as a means to reduce ac losses in YBCO tapes in the presence of time varying magnetic field.
- *MgB<sub>2</sub>*: This is actually a medium temperature superconductor, with a critical superconducting temperature of 39K. MgB<sub>2</sub> is a simple ionic binary compound, which is expected to be cost competitive for moderate temperature applications because it is fabricated using readily available, common materials. Multifilamentary MgB<sub>2</sub> round wires generally include a small amount of copper to improve thermal stability in an otherwise highly resistive metal matrix.

Because of their generally small cross-sectional areas, the critical currents for all four high temperature superconductors are typically no more than a few hundred amperes. To achieve the 1.4 kA<sub>rms</sub> specified in our 14 MW reference design we need to consider cabled conductors built up from several HTS strands acting in parallel. The production of a superconductor in tape form generally produces a directional dependence in the critical current vs. magnetic field dependence of the conductor; the critical current for given field is typically lower when the field is directed perpendicular to the broad face of the tape. By comparison, superconductors that can be processed into round wires are generally free of this effect.

## 6.2 Bi-2212

During the past few years there has been renewed interest in the particle accelerator community to develop Bi-2212 based superconductor for use in high-field magnets. Figure 6.1 shows a tremendous increase in the high-field capability of Bi-2212 at temperatures below roughly 15 K. The critical current performance for more modern strands has improved considerably due to the introduction of advanced processing techniques like over pressure processing [Labalestier] and mechanical compaction [Huang] that increase the density of material in the superconducting filaments. Magnet

designers are also interested in Bi-2212 because it can be processed as a multi-filamentary round conductor, with relatively low anisotropy in the critical current with magnetic field orientation. AC loss for this type of conductor should be reasonable low, depending on achieved filament diameter and matrix resistivity. We became interested in Bi-2212 for possible use in our superconducting stator because of the observed cross-over in magnetic field capability with MgB<sub>2</sub> at temperatures above roughly 30 K in Figure 6.1. Although the minimum achievable, uncoupled filament diameter in Bi-2212 is likely to be significantly larger than that for MgB<sub>2</sub> [Otto], resulting in higher loss, the ability to operate at higher temperature, where Carnot efficiency is proportionally greater may result in net gain in overall system performance. The anticipated minimum filament diameter achievable in Bi-2212 strands is roughly 30  $\mu\text{m}$ , which is three times larger than what has been demonstrated for MgB<sub>2</sub> developmental wires.

Figure 6.2 shows the projected critical current performance for Bi-2212 strand over a range of magnetic fields and operating temperatures. This plot is based on simple rescaling of historic data, using recently measured 4.2 K performance data as a guide. This rescaling assumes that the performance gains are based solely on increase in filament density rather than any inherent change to superconductor behavior.

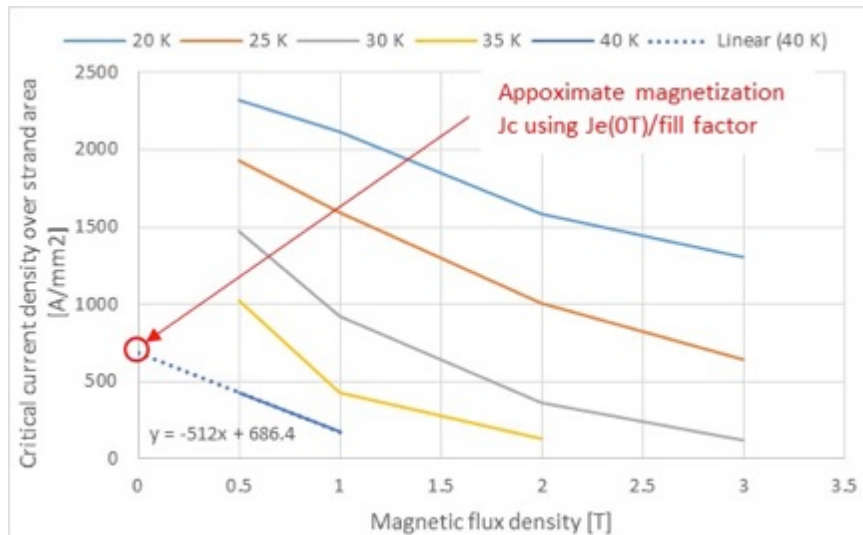


Figure 6.2 Projected performance data for Bi-2212 strands with improved filament density.

Table 6.1 compares the expected total loss power for an MgB<sub>2</sub>-based superconducting stator operating at a nominal temperature of 20 K, with that for a Bi-2212 based stator operating at a nominal temperature of 40 K. For simplicity only the magnetization hysteresis and coupling current losses were considered for this study. The hysteresis loss power in the stator conductor,  $P_h$ , was calculated using the relation:

$$P_h = \frac{8}{3\pi} f J_c B_m d_f \lambda V_s$$

where  $f$  is the electrical frequency of the generator,  $J_c$  is the magnetization critical current density,  $B_m$  is the magnetic field amplitude,  $d_f$  is the filament diameter,  $\lambda$  is the filament fraction in the strand, and  $V_s$  is the active strand volume in the stator winding. The coupling current loss power in the strands was calculated using the relation:

$$P_c = \frac{1}{2\rho} (f L_p B_m)^2 V_s$$

where  $\rho$  is the resistivity of the matrix material between the superconductor filaments, and  $L_p$  is the twist pitch of the strand.

By 40 K operating temperature, the critical current density of the Bi-2212 has decreased to a point where significantly more strand area is needed to achieve the generator's rated current output, compared to the 20 K operating temperature MgB<sub>2</sub>-based CIC shown in Figure 7.2. The combination of large filament diameter and total filament volume markedly increases the loss power for the Bi-2212 based stator.

Table 6.2 compares the cryogenic performance of MgB<sub>2</sub> and Bi-2212. **We have decided not to do more work on Bi-2212, as it does not seem to offer substantially advantages for rotating machinery over those of MgB<sub>2</sub> (indeed, it seems that the losses are higher for Bi-2212). Furthermore, MgB<sub>2</sub> for high frequency operation is much more developed than Bi-2212.**

Table 6.1. Estimated loss powers for MgB<sub>2</sub> and Bi-2212 based superconducting stators.

	MgB <sub>2</sub> @ 20 K	Bi-2212 @ 40 K
Electrical frequency, $f$ [Hz]	117	117
Magnetic field amplitude [T]	0.5	0.5
Magnetization critical current density, $J_c$ [A/mm <sup>2</sup> ]	8000	2740
Filament diameter, $d_f$ [μm]	10	30
Twist pitch, $L_p$ [mm]	10	15
Engineering critical current density at 0.5 T [A/mm <sup>2</sup> ]	750	430
Filament fraction	15%	25%
Total strand area to produce 2 kA operating current at 60% of cable critical current [mm <sup>2</sup> ]	4.5	7.9
Matrix resistivity, $\rho$ [Ohm-m]	10 <sup>-6</sup>	10 <sup>-5</sup>
Estimated hysteresis loss power [W]	342	1022 (3x)
Estimated coupling loss power [W]	98	39
Total loss power [W]	440	1061 (2.4x)

Table 6.2. Compares the relative cryogenic efficiencies at different conductor operating temperatures

	MgB <sub>2</sub> @ 15 K	MgB <sub>2</sub> @ 20 K	Bi-2212 @ 40 K
Cold temperature, $T_L$ [K]	15	20	40
High temperature, $T_H$ [K]	300	300	300
Carnot efficiency, $\eta_{Carnot}$	0.053	.071	0.154
Coefficient of performance, $COP$	0.2	0.2	0.2
Estimated total stator loss power, $Q$ [W]		440	1061
Estimated electrical power to drive cryogenic cooling system, $P$ [kW]		31	34.5

## 6.3 STRAIN EFFECTS

The critical current in all four of the HTS conductors remains reasonably constant at tensile axial

strains below roughly 0.3% to 0.4%. At larger strains, the critical current decreases sharply and often irreversibly. The operating strain in the conductor depends on the entire strain history, from manufacture, through cabling, winding and assembly operations, cool-down to the cryogenic use temperature, and from electromagnetic and centrifugal loads during operation. Depending on the proposed fabrication route for stator coils and type of conductor under consideration, we occasionally needed either to devise manufacturing strategies to minimize the conductor's strain excursion throughout the process history, or to exclude some topologies from consideration all together.

YBCO coated conductors are particularly sensitive to peeling loads applied normal to the surface of the conductor, which can result in delamination. Tensile differential strains that can develop within a superconducting winding during cool-down from room temperature to the cryogenic operating temperature, or between the surface of the winding and a winding former, are often of sufficient magnitude to separate the YBCO coating from the substrate, thus rendering the conductor useless. This is an active area of investigation and coil fabrication techniques, such as the use of compliant coatings to relieve the peeling loads, have been developed to mitigate these effects. As yet no method has been demonstrated to be universally applicable to the manufacture of superconducting coils.

Manufacturing and cool down strains are of concern for all superconducting windings. By comparison, centrifugal loads are important for the rotor windings, while the cyclic electromagnetic loading applied to the stator is of concern for estimating its fatigue resistance and fatigue life. Shock loads during off normal operating conditions need to be accommodated within the winding support structures.

## 6.4 AC LOSSES

AC losses: Superconductors are capable of the lossless transmission of electric power only under DC conditions. The application of time-varying magnetic field or current to a superconductor produces losses due to:

- The penetration of magnetic flux density into the conductor caused by an externally varying magnetic field. This mechanism is known as hysteresis loss.
- The penetration of magnetic flux density into the conductor caused by changes to the conductor's self-magnetic field due to changes to the conductor current. This mechanism is known as transport current loss.
- The inducement of eddy currents in the conductor matrix due to time variation in the magnetic field. This mechanism is known as eddy current, or alternatively as coupling current loss. Coupling currents can also be induced between adjacent conductors in a cabled conductor in the presence of time-varying external magnetic field.

One approach to minimize the losses in a superconducting winding are to use conductors with fine superconductive filaments embedded in moderately resistive matrices. The fine filaments help to limit hysteresis and transport current losses, while the resistive matrix helps to limit eddy current losses. The viability of the HTS stator needed for a fully superconducting generator will depend fairly strongly on our ability to minimize ac losses in the stator winding. The filament diameters in today's HTS conductors are fairly large compared to what can be achieved to limit loss in a LTS material, for instance NbTi, which is why ac loss minimization in the stator is of such concern to us.

The scaling laws for each ac loss mechanism are generally well known for each type of conductor. Determination of the conductor AC loss is an essential part of the evaluation process for each proposed stator configuration. The combination of loss power and operating temperature has significant impact on overall system efficiency and both gravimetric and volumetric power density.

#### 6.4.1 AC LOSS CALCULATIONS FOR YBCO

The losses in YBCO are difficult to estimate, because of the cross section of the superconductor, which is made in very thin, wide plates. For stacked cables (where the tapes are placed on top of each other, without twisting), only the transverse field (field along the c-axis of the superconductor) will lead to significant losses.

We have built two models for HTS tapes. The first model is for a stack of 12 tapes, 3 mm wide tapes. The tapes all magnetically coupled, resulting in field penetration issues. The second model is a Roebel cable, with 3 mm and 2 mm tapes. In this case, all tapes are magnetically decoupled.

The model is FEA based on H-formulation. It is assumed that the critical current of the tapes is 200 A at 0.2 T, with an index  $n = 30$ . Thus, the cables are carrying about 2000 A, in an external magnetic field of 0.2 T.

The model for the HTS stacked cable is shown in Figure 6.3

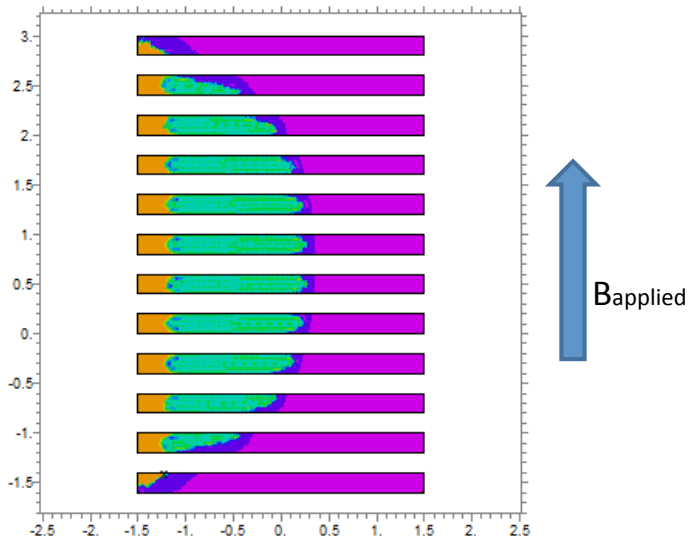


Figure 6.3 Model of stacked cable, with 12, 3 mm wide tapes.

The results are shown in Figure 6.4, for a frequency of 117 Hz, and 2000 A transport current. As mentioned before, the losses are due to the c-axis component, with tapes that are magnetically coupled.

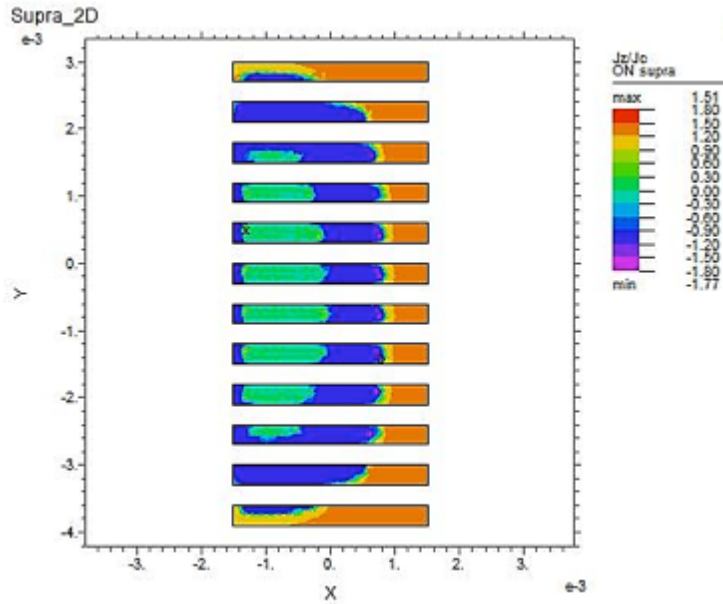


Figure 6.4 current in HTS cable, as a fraction of critical.

It should be noted that the current reverses direction in the innermost region. There is substantial heating, as the current exceeds the critical current ( $J/J_{\text{crit}} > 1$ ). It is assumed that the voltage is due to the power law,

$$\vec{E} = \frac{E_c}{J_c} \left( \frac{|\vec{J}|}{J_c} \right)^{n-1} \vec{J} \quad \text{where} \quad \begin{aligned} J_c &= 100 \text{ A/mm}^2 \\ E_c &= 100 \mu\text{V/m} \\ n & \end{aligned}$$

The transport current, as well as the losses, for a transient that starts at 0 current, are shown in Figure 6.5 (left). The corresponding losses are shown in Figure 6.5 (right).

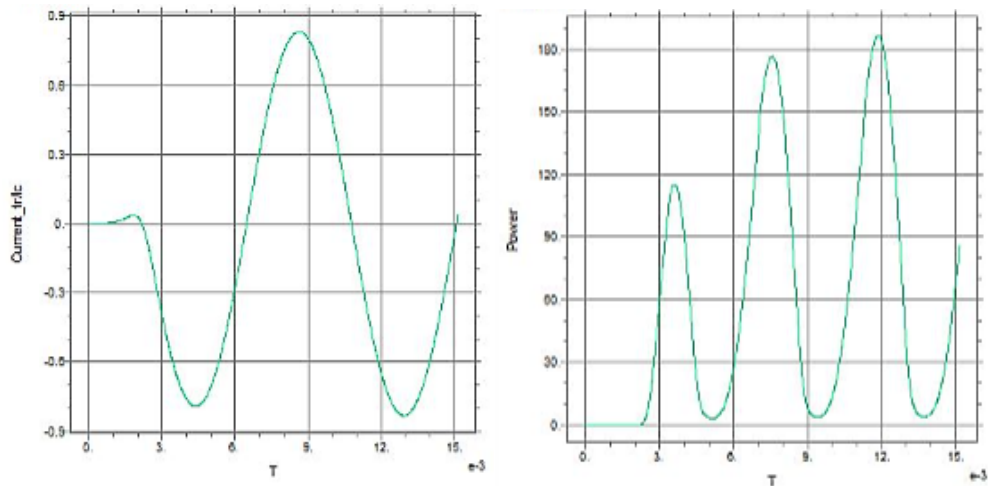


Figure 6.5 (left) Transport current ( $I/I_c$ ); Instantaneous losses ( $\text{W/m}$ )

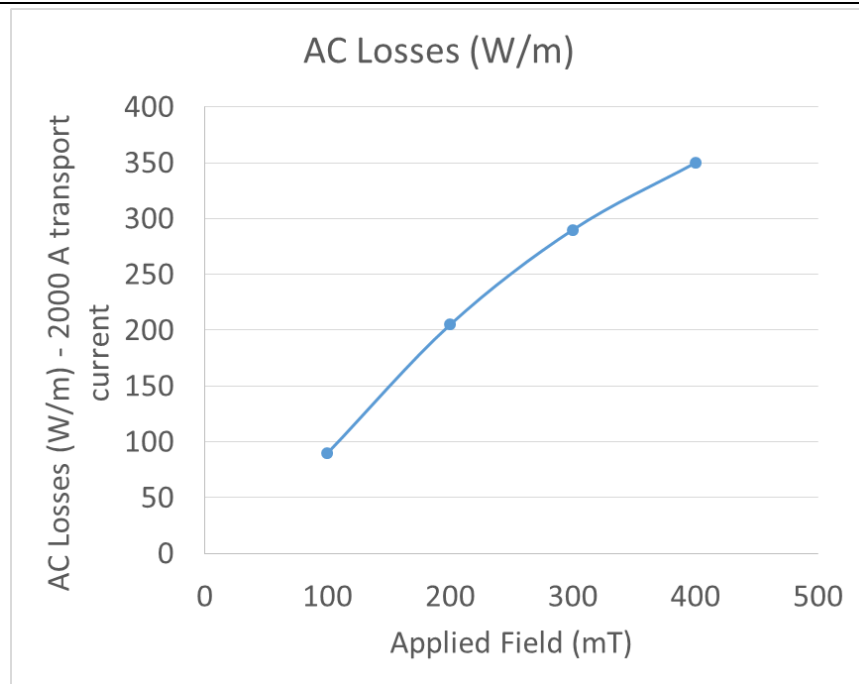


Figure 6.6 Dissipation in HTS cable as a function of the applied magnetic field.

The loss procedure shown above has been used in the latter optimization of the toroidal stator generator, described in Section 2.7.

We have also investigated Roebel cables. The critical current is 200 A at 0.2 T, with an index of  $n = 30$ . The cable current is 2000 A, with 12 tapes. The Roebel cable is shown in Figure 6.7. Because the cables are magnetically decoupled, it is only necessary to model a single tape.

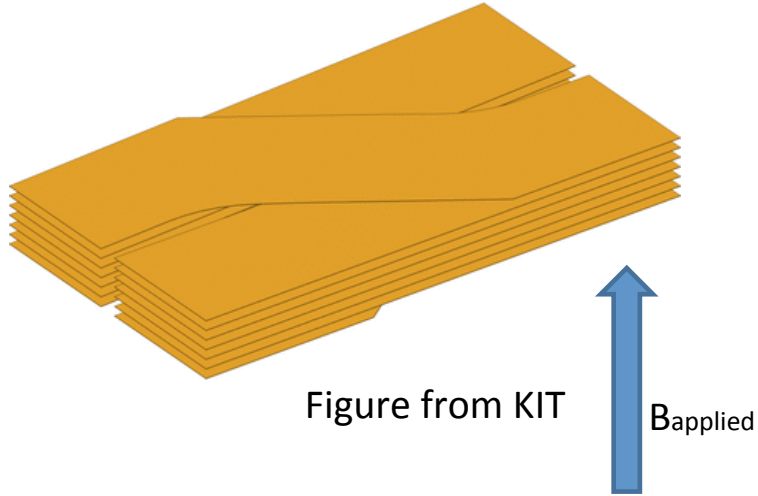


Figure 6.7 Roebel cable geometry. Figure provided by KIT.

The results from the model of the Roebel cables are shown in Figures 6.8 and 6.9. Figure 6.8 shows the current distribution along the cross section of the tape (the cross section has been arbitrarily increased in thickness in order to facilitate meshing of the model).

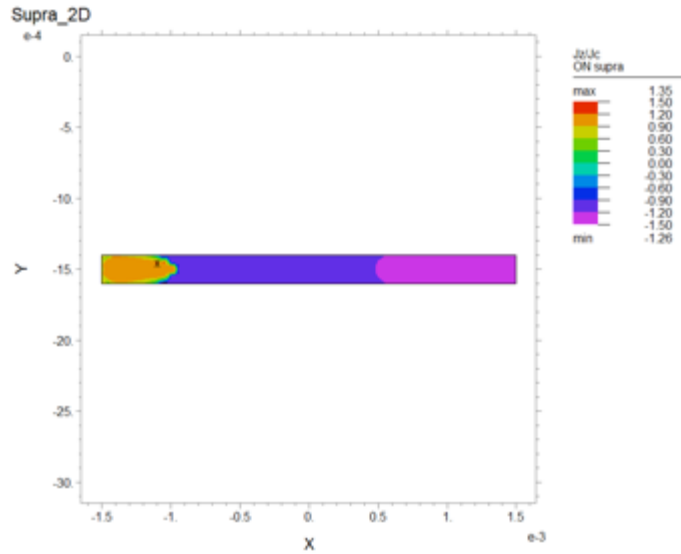


Figure 6.8 Current density over the cross section of the tape. The height of the tapes has been arbitrarily increased in order to provide better meshing.

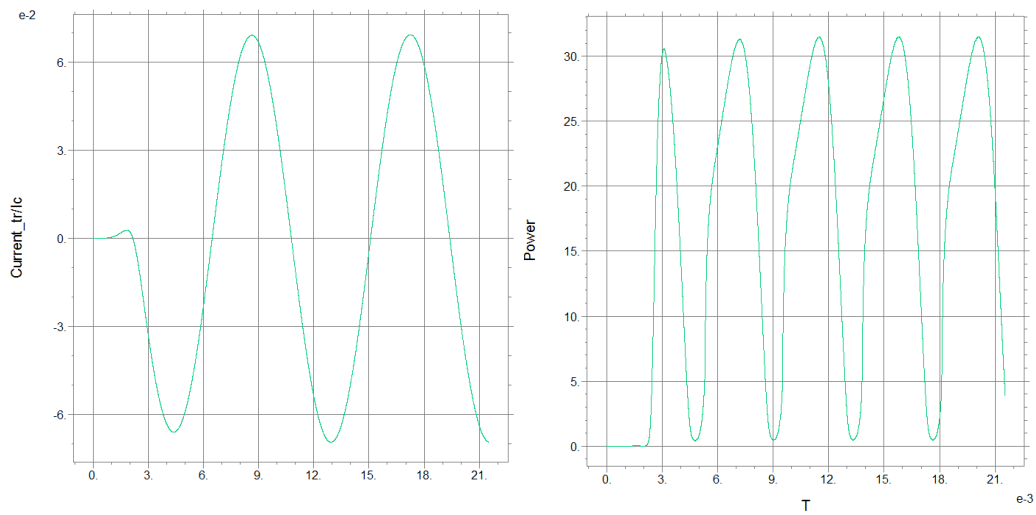


Figure 6.9 Transport current  $I/I_c$  (left) and dissipation (W/m) for Roebel cables.

The losses for a 2000 A cable are summarized in Figure 6.10. Two Roebel cables are shown, one with 12, 3 mm wide tapes, and one with 18, 2 mm tapes. The losses for all three cables are comparable, although the Roebel cables show slightly reduced losses. In the case of the stacked tape, the cable is not fully penetrated, resulting in different field dependence from the Roebel cables.

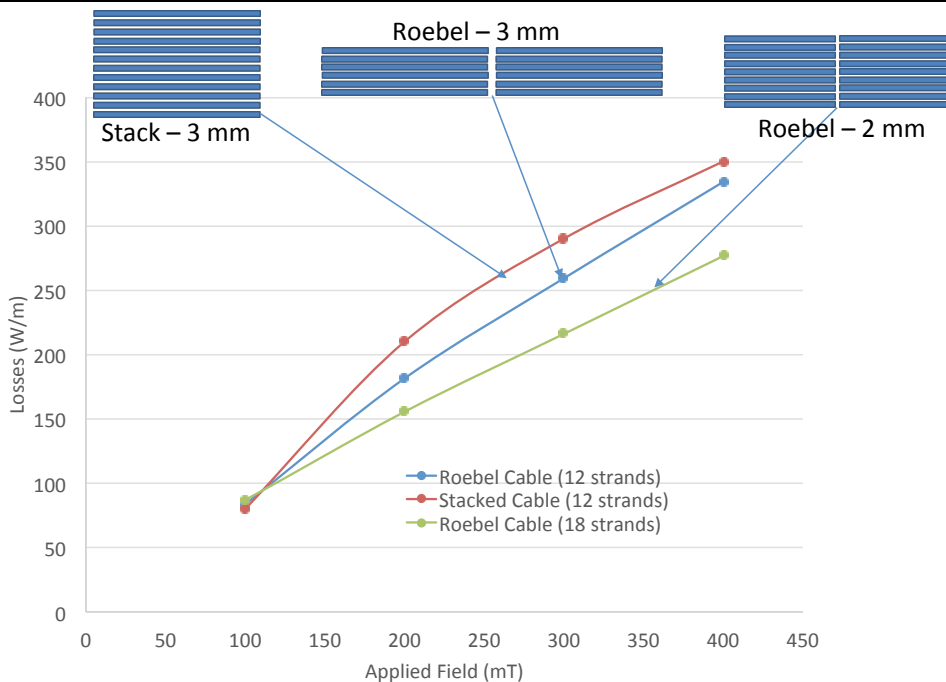


Figure 6.10 Comparison between Roebel and stacked cables.

#### 6.4.2 AC LOSS CALCULATIONS FOR MGB2 (233 Hz OPERATION)

There are several challenges to analytical estimate of loss. One of the more significant approximations regards the interaction between transport current loss and magnetization/coupling loss. This interaction depends on the phase relation between the transport current and field variation on the winding, which is not precisely known from the available information. The total loss also depends on the fraction of the armature winding exposed to the rotor field and the ratio between peak operating current and conductor critical current.

Despite its significantly higher critical current performance, HyperTech does not foresee a means to fabricate 2nd generation conductors fine enough filaments needed for low ac loss. During previous discussions with HyperTech they recommended that we retain the 1st generation strand critical current characteristics for our armature conductor designs. A summary of the critical current density vs. field variation for both 1st and 2nd generation strands at 20 K is shown in Figure 2.48. Note that the critical current density is referenced to the filament area within the strand. For most HyperTech strands the filament area is roughly 15% of the total strand area. Because the armature conductor for most of our designs operate at fields below 1 T (for which no measured reference data is included in the plot), we simply extrapolated the low field tendency for the 1st generation strand towards zero field to generate the approximate fit overlaid on the plot.

At 0.6 T peak field, the 20 K critical current density for a 1st generation strand should be roughly 492 kA/cm<sup>2</sup>, based on the fit shown in Figure 6.11. This yields a 20 K critical current for a 0.85 mm diameter strand, with 15% superconductor fill fraction, of roughly 420 A. The peak cable current from Table 2.10 is 2030 A. The total number of strands needed for the armature conductor depends on the assumed ratio of the cable critical current divided by the peak operating current. The minimum achievable loss in the armature depends in part on this ratio, which affects both loss power per unit volume of conductor as well as the total volume of conductor needed for the armature.

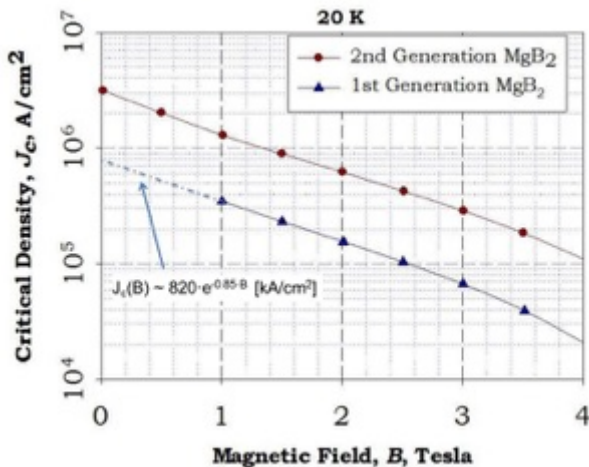


Figure 6.11: Critical current density vs. field for 1st and 2nd generation HyperTech strands at 20 K.

The conductor loss has been divided in to three components – hysteresis loss due to field penetration into the superconductor filaments, coupling loss in the strand matrix, and losses due to transport current in the conductor.

*Magnetization loss:* For simplicity we have been using the modified Bean equation shows in Equation 1 to estimate the magnetization hysteresis loss in superconductors for various recent programs at MIT. This equation assumes that the super currents during a change in field, from  $B_i$  to  $B_f$ , always penetrate to the center of each filament.

$$e_h(B_f - B_i) = \frac{2}{3\pi} d_f \int_{B_i}^{B_f} J_c(B) dB \quad (1)$$

For the present arrangement, the penetration field,  $B_p = \mu_0 \pi \cdot J_c (0.6T) \cdot d_f$ , is approximately 0.02 T and the assumption of full penetration throughout the cycle produces negligible error in the estimate. The finest filament diameters,  $d_f$ , that HyperTech has achieved during limited production runs is roughly 10  $\mu$ m, which is the value that will be used for the loss calculations. For the half cycle ac loss calculations,  $B_i$  will be set to 0.2 T, while  $B_f$  will be set to 0.6T. The  $J_c(B)$  fit from Figure 6.11 is also used. For a half field cycle the estimated magnetization hysteresis loss per unit volume is roughly 5 kJ/m<sup>3</sup>, while the estimated magnetization loss per unit volume is 10 kJ/m<sup>3</sup> for a full cycle. The volumetric loss power density due to magnetization hysteresis is simply the loss energy per volume times the excitation frequency. For 233 Hz (for example, for the AC homopolar machine in Section 2.6),  $p_h = e_h = 2.32 \text{ MW/m}^3$ .

*Transport current loss:* Hysteresis loss in applied field and self-field loss due to transport current operate via similar mechanisms, that is, they result due to penetration of magnetic flux into the interior of the superconducting filaments. Estimation of the self-field transport current loss power per unit length for single, isolated strand can be performed using the Norris equation included in Equation 2.

$$\frac{p_t}{L} = \frac{\mu_0}{\pi} f i_c^2 \left[ \left( 1 - \frac{i_{op}}{i_c} \right) \ln \left( 1 - \frac{i_{op}}{i_c} \right) + \frac{i_{op}}{i_c} - \frac{1}{2} \left( \frac{i_{op}}{i_c} \right)^2 \right] \quad (2)$$

where  $i_{op}/i_c$  is the ratio of the conductor's operating current to its critical current. Calculation of transport current loss in a cabled superconductor is significantly more complicated and depends significantly on the cabling pattern, which influences the distribution of self-field through the cable volume. For simplicity we will calculate the transport current loss on a single strand basis ( $i_{op}$  and  $i_c = 420 \text{ A}$ ) and then multiply this value by the total number of strands in the cable,  $n_s$ , to estimate the

total transport current loss power per cable length. That is,  $P_t/L \sim n_s \cdot p_t/L$ . The number of strands in the cable is equal to the reciprocal of the fraction of critical current operation times the peak operating current,  $I_{op}$ , divided by the strand critical current,  $I_c$ . That is,  $n_s = I_c/I_c$ .

*Coupling current loss:* In addition to magnetization and transport current loss in the superconductor, coupling currents between the twisted superconducting filaments in the strands also generates a volumetric loss power,  $p_c$ , that can be estimated using Equation 3.

$$p_c = \frac{1}{2 \cdot \rho_m} (f \cdot t_p \cdot \Delta B)^2 \quad (3)$$

where  $\rho_m$  is the resistivity of the strand matrix (roughly  $10^{-6}$  Ohm·m),  $t_p$  is the twist pitch of the strand (approximately 10 mm), and  $\Delta B$  is the amplitude of magnetic field variation (0.2 T). These values yield an estimated coupling loss power density of about 0.21 MW/m<sup>3</sup>, which acts on the matrix fraction of the strand volume.

*Loss power dependence on strand number:* The variation in total loss power with numbers of strands in the cable is summarized in Table 6.3, based on a total length of 720 m for all MgB<sub>2</sub> armature windings (from Table 2.10), a single strand cross-section area of  $5.67 \times 10^{-7}$  m<sup>2</sup>, filament fill fraction of 0.15, matrix fill fraction of 0.85, with an assumed value of approximately 60% for the portion of the armature exposed to the rotor field variation. The minimum loss power appears to occur near a fraction of critical current operation of roughly 0.3.

Table 6.3: Variation in estimated armature ac loss vs. numbers of strands in cable, at 233 Hz

Fraction of critical	Number of strands	Hysteresis loss [W]	Transport current loss [W]	Coupling loss [W]	Total loss [W]
0.05	97	8263	24	2192	10.479
0.1	48	4131	100	1096	5327
0.2	24	2065	424	548	3037
0.3	16	1377	1014	365	2756
0.4	12	1032	1927	274	3234

#### 6.4.3 AC LOSSES IN CICC FOR TOROIDAL STATORS

During preliminary design of the test sample, we performed more a detailed evaluation of anticipated AC losses for our proposed MgB<sub>2</sub> CICC; these calculations revealed that eddy current losses induced in the conductor jacket were not negligible and could actually be more than ten times higher than the expected AC losses in the MgB<sub>2</sub> strands. As this point, we decided to complete the prototype CICC using stainless strand, but to redesign our AC loss sample for the CAPS calorimeter using triplet conductors only. This does not mean that we abandoned the CICC configuration. Rather, we believe that the CICC configuration is still viable, but would require the use of a dielectric jacket, such as glass wrap, followed by epoxy impregnation following the reaction heat treatment cycle, to limit AC losses to acceptable values.

#### EDDY CURRENT LOSSES IN CICC JACKET

Figure 6.12 shows a cross-section sketch of the conductor proposed for the technology demonstration, while Table 6.4 lists pertinent dimensions for this conductor. The conductor dimensions were driven by the 0.31 mm diameter of the strand procured from Hyper Tech.

By this stage of the program we had begun to investigate the Gramme ring stator configuration, which

permits attainment of the rated 14 MW generator output with a peak field amplitude of roughly 0.1 T at the conductor. The conductor contains eighteen MgB<sub>2</sub> triplets (54 strands total) and has an anticipated critical current of roughly 4 kA (twice the peak phase current of 2 kA) when energized in 0.1 T field at 20 K. The outer diameter of the central cooling tube and inner diameter of the outer jacket were chosen to achieve roughly 40~45% void fraction in the annular cable space. This void fraction should permit the strands to be loosely held in place without excessive deformation of the strand cross-sections during compaction of the conductor jacket. In the event that strand motion has negative impact on MgB<sub>2</sub> cable performance at these high void fractions, we analytically investigated the possibility to introduce a liquid or gaseous cryogen in the cable space, which when cooled and frozen would provide the required strand constraint [Voccio].

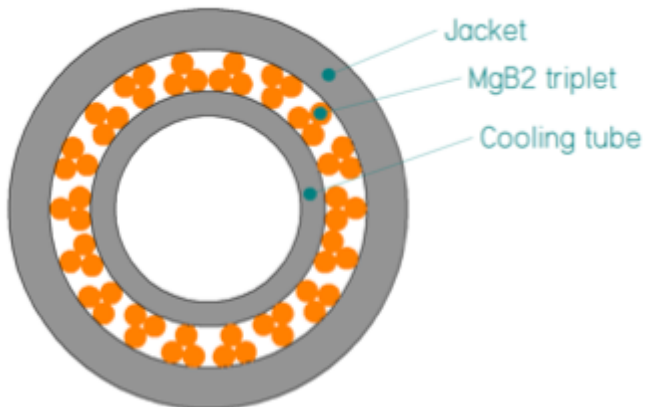


Figure 6.12 Section view of design for the CICC fabrication trial.

Table 6.4 Target dimensions for the CICC fabrication trial.

<b>Cooling tube inner diameter [mm]</b>	<b>2.69</b>
<b>Cooling tube outer diameter [mm]</b>	3.40
<b>Strand diameter [mm]</b>	0.31
<b>Strand twist pitch length [mm]</b>	5
<b>Triplet twist pitch length [mm]</b>	10
<b>Twist pitch for 2<sup>nd</sup> cable stage [mm]</b>	100
<b>Estimated void space in cable volume [%]</b>	~45.5
<b>Jacket inner diameter [mm]</b>	4.59
<b>Jacket outer diameter [mm]</b>	5.78

Figure 6.13 shows the arrangement of a finite-element model implemented in COMSOL to evaluate the distribution of AC losses in the CICC when it was exposed to a uni-directional, sinusoidally varying external magnetic field,  $B_{ext}$ . The model considered: magnetization hysteresis loss in the MgB<sub>2</sub> filaments; eddy current losses in the strand matrix, coupling losses in the matrix between the filaments, magnetization loss in the strand matrix, and eddy current loss in the cooling tube and conductor jacket; table 6.5 and Figure 6.14 are calculated assuming a copper tube and sheath, which result in very high eddy current losses in the tube/sheath. The computed loss power for a 0.2 m long sample (similar to that used in the experiment, described in Section 6.5) for each mechanism is summarized in Table 6.5 for frequencies between 5 Hz and 400 Hz, field amplitude of 0.1 T, and operating temperature of 20 K. The same results are shown in graphical form in Figure 6.14.

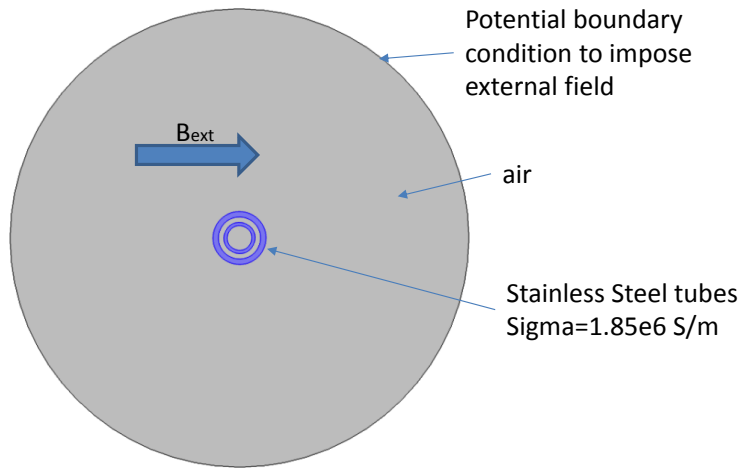


Figure 6.13. COMSOL model to compute AC loss in the CICC when exposed to oscillating background field.

Table 6.5. Distribution of AC loss power among mechanisms for a 0.2 m length of the proposed MgB<sub>2</sub> CICC.

100 mT field amplitude							
f (Hz)	Filament magnetization loss [W]	Strand eddy current loss [W]	Strand coupling current loss [W]	Strand matrix loss [W]	Tube-jacket eddy current loss [W]	Total Loss (W)	% Loss in Tube-jacket
5	4.1E-3	9.09E-08	9.48E-06	9.55E-05	0.01	<b>0.01</b>	57
25	22.E-3	2.27E-06	2.37E-04	4.77E-04	0.14	<b>0.16</b>	86
50	45.4E-3	9.09E-06	9.48E-04	9.55E-04	0.54	<b>0.59</b>	92
100	93.9E-3	3.64E-05	3.79E-03	1.91E-03	2.16	<b>2.26</b>	96
200	193.6E-3	1.46E-04	1.52E-02	3.82E-03	8.65	<b>8.87</b>	98
300	295.5E-3	3.27E-04	3.41E-02	5.73E-03	19.47	<b>19.80</b>	98
400	398.9E-3	5.82E-04	6.07E-02	7.64E-03	34.60	<b>35.07</b>	99

The slopes of the loss curves in Figure 6.14 vary, indicating that different mechanisms are more important in some regions than others. The loss component due to magnetic hysteresis, namely filament and matrix magnetization vary linearly with frequency, while those due to induced currents, such as eddy currents in the matrix, coupling currents between filaments and eddy currents in the cooling tube and jacket vary with the square of frequency. At very low frequency (around 5 Hz) the filament magnetization loss is roughly comparable to the eddy current loss in the cooling tube and jacket, whereas at frequencies above roughly 100 Hz the eddy current losses in cooling tube and jacket clearly dominate the total.

The COMSOL model indicates that up to 99% of the loss power in the proposed CICC sample could be generated by eddy currents induced in the copper cooling tube and conductor jacket, depending on the magnetic field amplitude and frequency (Table 6.5), in the case of copper as the material of the tubes, with a resistivity that is reduced by a factor of 7 from room temperature. We have made similar calculations for the case with stainless steel tubes. The results are shown in Table 6.6. Both the dissipated power per unit length, as well as the power dissipated in 20 cm long fixtures, have been

shown in Table 5.5. Due to its significantly larger diameter and greater wall thickness, the outer jacket contributes significantly more to the total. It is clear that the tubes can not be made from copper, but that with steel there are small losses, about 0.15 W/m for 117 Hz.

Table 6.6 Sheath losses as a function of frequency and sheath resistivity, for the same parameters as Table 6.5

Conductivity (S/m)	1.86E+06		4.20E+08	
	W/m	W	W/m	W
Frequency (Hz)	20 cm		20 cm	
5	3.25E-04	6.49E-05	0.074	0.015
25	8.11E-03	1.62E-03	1.833	0.367
50	0.033	0.007	7.230	1.446
100	0.130	0.026	27.4	5.5
200	0.519	0.104	90.9	18.2
300	1.168	0.234	159.4	31.9
400	2.077	0.415	217.4	43.5

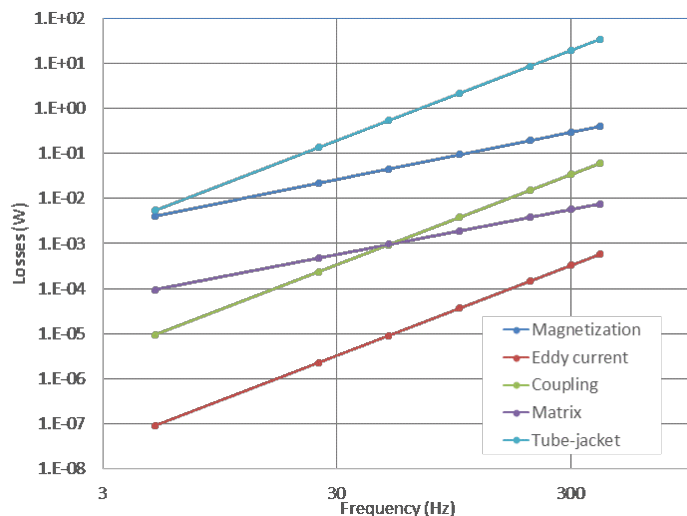


Figure 6.14. Variation in CICC AC loss components with frequency at 0.1 T magnetic field amplitude. Note that the tube jacket losses are calculated for a copper tube and sheath.

## 6.5 EXPERIMENTAL LOSSES IN MGB2 CICC TOPOLOGIES

We arranged with the Center for Advanced Power Systems (CAPS) at FSU to test an MgB2 conductor sample for us using their 20 K, helium gas flow calorimeter [Kvitovich, Pamidi1, Pamidi2]. However, due to the high anticipated eddy current loss in a CICC sample reported in section 6.4.3, we decided to examine the loss characteristics for a sample containing multiple, first-stage MgB2 triplets. The choice of triplets, rather than single strand samples for the AC loss measurements was to permit us to also examine the cabling characteristics of the strand and to examine the magnitude of coupling losses between strands that could occur at the sub-cable level.

### 6.5.1 SAMPLE PREPARATION

In preparation for the triplet cabling, a 65 m length of the 0.31 mm diameter MgB2 strand was

transferred to each of three pay-off spools using the re-spooling machine shown in Figure 7.6. During the re-spooling process, the strands were lightly coated with Mobil 1™ oil. Mobil 1™ was employed as an anti-sinter agent during the development of early Nb<sub>3</sub>Sn-based superconductor cables. During heat treatment reaction, the oil burns away leaving a relatively high resistance coating on the strands that effectively limits the magnitude of strand-to-strand coupling currents for cables exposed to time-varying external magnetic field [Pamidi2].

The pay-off spools were then transferred to the spinner of our cabling machine (Figure 7.5). Despite our previous experiment with triplet cabling of the stainless steel prototype, several small issues were encountered when working the MgB<sub>2</sub> strand. First, the MgB<sub>2</sub> was significantly stiffer than the annealed stainless steel that we used for the prototype. Second, the Mobil 1 coating lead to occasional slippage of the pay-off cable against the capstan, which tended to worsen as the run progressed. We encountered a few strand breaks before noticing this slippage. The principal mitigation was to increase the torque on the take-up spool and to use lightly soaked rag to remove oil build-up from the capstan surface on an occasional basis during the cabling run. Strand breakage significantly declined once we noticed these issues and only one break occurred during the second half of the run. A 65 m cable length should have yielded at least 100, 0.2 m long triplet samples. However due to the strand breaks, we only managed 96 pieces following reaction. 90 of these triplets were used in the AC loss test specimen while six were retained for critical current measurement, assuming a suitable test facility could be identified.

Although the un-reacted strand is robust and can accommodate moderate deformation without significant impact on ultimate performance, reacted strands and triplets need to be carefully protected against unintended deformation during handling after reaction. Hyper Tech reports that the axial strain limit of one of their multifilament wires is ~ 0.3% after heat treatment [Rindfleisch]. In preparation for the sample's reaction heat treatment, we installed un-reacted triplet cables into 230 mm long, 1 mm inner diameter, by 1 mm wall thickness quartz glass tubes. The quartz tubes had sufficient stiffness to prevent bending during routine handling, and had high enough softening temperature to follow the triplets through the reaction treatment.

Also, according to Hyper Tech, without proper preparation it is possible that some of the magnesium to leak out of the ends of un-reacted filaments during heat treatment, leading to a loss in superconducting performance. Three steps were taken to minimize this possibility during processing of our MgB<sub>2</sub> triplets. First, multiple samples were mounted together using a single, roughly 3 m length of triplet conductor as shown in Figure 6.15. The triplet conductor was passed in sequence through each of 10 quartz tubes, which were then folded into a compact meander for installation into our heat treatment furnace. Second, the final ~0.5 m length of conductor protruding past each of the final quartz tubes in the sequence was brought from the high temperature zone in the furnace to within a few inches of the furnace end flange to keep the ends of all strand well below the filament melting point. Finally, as recommended by Hyper Tech, we crimped flat the final 8~12 mm of each strand as shown in Figure 6.16 [Rindfleisch].

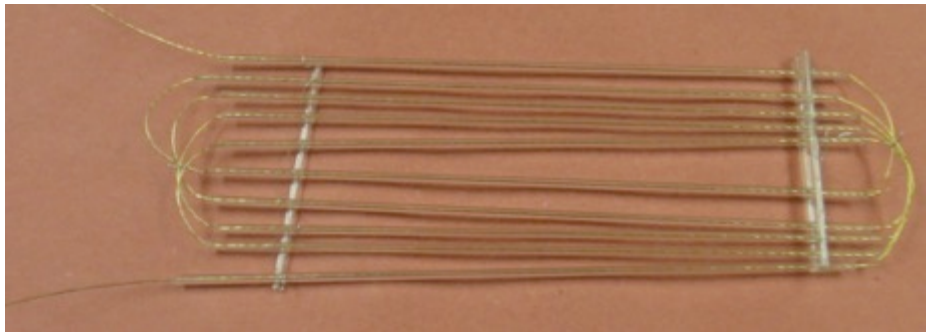


Figure 6.15. 3 m length of cabled triplet inserted into ten 1 mm ID quartz tubes in preparation for heat treatment reaction.



Figure 6.16. Each strand end was crimped flat to prevent magnesium leakage from the filaments.

### 6.5.2 HEAT TREATMENT

The MgB<sub>2</sub> triplets were heat treated in two batches to minimize risk due to possible errors in the controller or programming. Six single strand MgB<sub>2</sub> “witness” samples were included in each heat treatment batch. The critical currents for a few of these reacted strands were measured to verify the success of the heat treatment. Results from the single strand critical current measurements are reported in section 6.5.3.

The heat treatment reaction was performed using the three zone furnace shown in Figure 6.17. For our strand configuration Hyper Tech recommended a heat treatment temperature of 650°C for a hold time of one hour [Rindfleisch]. An example heat treatment schedule based on their in-house furnace is shown in Figure 6.18. Hyper Tech also indicates that the heat treatment duration above 600°C is as important as the heat treatment temperature and hold (dwell) duration. In other words the recommended reaction time and temperature is a combination of heating from around 600°C up to 650°C plus hold time and cooling 650°C to 600°C. For their heat treatment scenario (Figure 6.18) the duration that the sample was above 600°C was 90 minutes. Hyper Tech also acknowledged that period of time above 600 degrees C may need to change slightly depending on the particular furnace used for the strand heat treatment. The recommended heat treatment atmosphere was argon gas.



Figure 6.17. Furnace room setup showing three zone furnace, furnace controller, argon gas flow system and data acquisition computer.

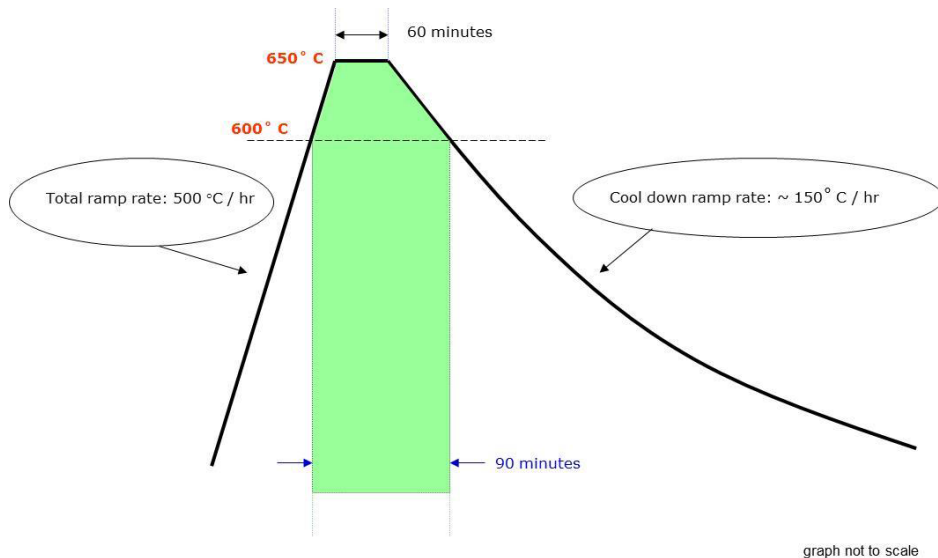


Figure 6.18. Typical heat-treat profile of an MgB<sub>2</sub> sample.

Figure 6.19 shows the heat treatment temperature vs. time profiles achieved for each batch of triplets. The temperature profile for batch 1 is shown in Figure 6.19a, while that for batch 2 is shown in Figure 6.19b. A much more gradual temperature rise of roughly 150 degrees C/hr was used below 200 degrees C to accommodate the rather high thermal inertia of our furnace and to ensure that all three furnace zones remained within 5 degrees C of each other up to and through the 650 degrees C plateau. Although we qualified the temperature control program using a batch of thirty stainless steel triplets prior to the first batch of MgB<sub>2</sub> triplets the actual flat top duration at 650 degrees C fell about 5 min. short of the intended 60 minute hold time. We modified the heat treatment control slightly between batches in attempt to increase the duration of the 650 degrees C hold; in this case we overshot the intended 60 minute hold time by about 5 minutes.

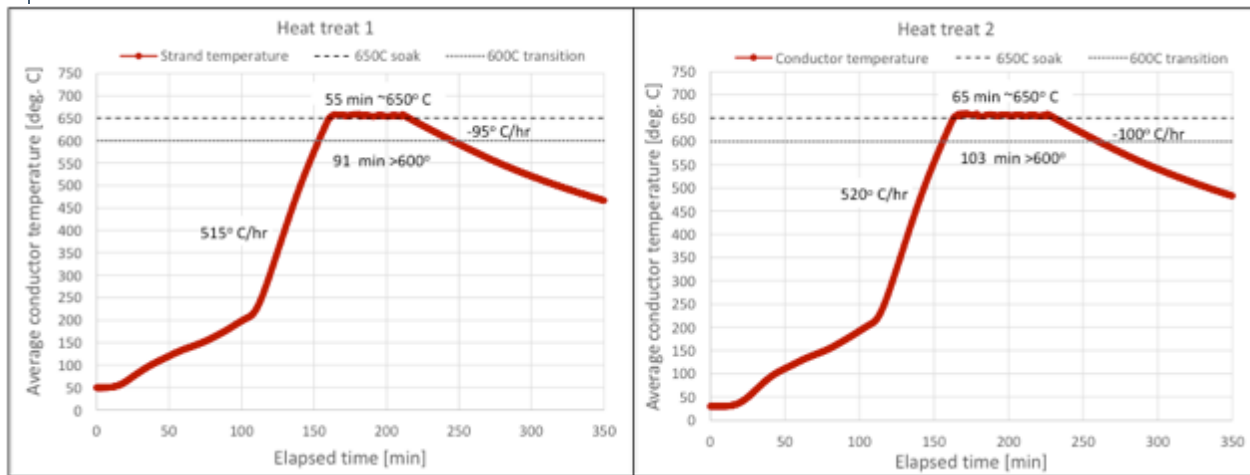


Figure 6.19. Heat treatment profiles achieved during reaction of our samples.

Following the completion of the heat treatment cycle, ninety of the reacted MgB<sub>2</sub> triplets were carefully removed in sequence from their quartz tubes and mounted in grooves machined along the length of a 0.2 m long by 0.05 m outer diameter hollow G-10 cylinder and transferred to CAPS for installation in their 20 K helium flow calorimeter. A photo of the test sample just prior to installation in the calorimeter is shown in Figure 6.20. Both ends and the midpoint off each triplet were secured to the G-10 cylinder using GE varnish, while intermediate locations along the sample length were secured using dental floss.

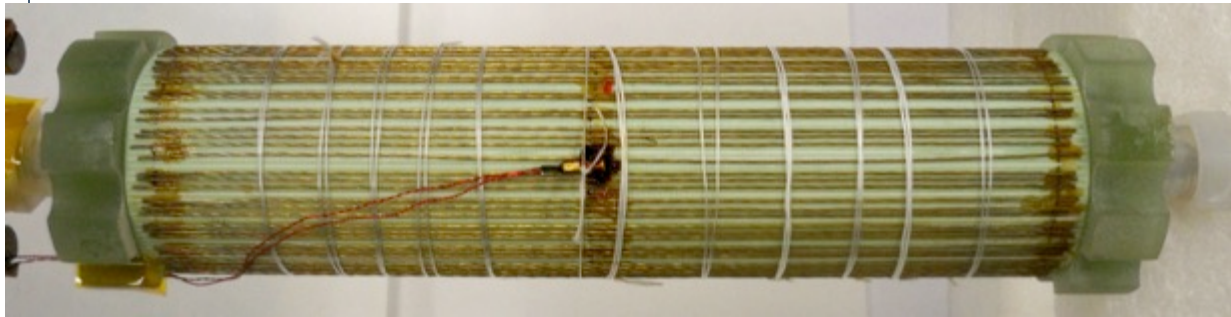


Figure 6.20. Ninety, reacted MgB<sub>2</sub> triplets mounted to the outer surface of a G-10 cylinder in preparation for calorimetric AC loss measurement.

### 6.5.3. CRITICAL CURRENT CHARACTERIZATION OF THE MGB<sub>2</sub> STRANDS AND TRIPLETS

As part of its quality assurance process, Hyper Tech Research reacted a length of strand from our billet on an ITER-type J<sub>c</sub> barrel [Bruzone]. The critical current vs. background magnetic induction for this strand was measured by Mike Sumption's group at the Ohio State University. Figure 6.21 shows results from these measurements along with those performed using straight, 0.2 m long witness samples co-reacted with the MgB<sub>2</sub> triplets at MIT. Two single strand witness samples from each of the heat treatment batches performed at MIT were sent in the same quartz tubes in which they were reacted to Hyper Tech Research. These strand samples were subsequently transferred to OSU for the critical current characterization.

The low-field critical current for the first batch of strands reacted at MIT was about 20% below those

reacted by Hyper Tech, while that for the second batch was about 2% lower. The improved performance for the second batch of strands probably reflect the effect of the changes to the furnace control program for the second batch of triplets, to better match the recommended reaction cycle. The critical currents for all strands show roughly exponential variation with the background magnetic induction. This is evidenced by the linear variation in  $I_c$  vs  $B$  when presented on a semi-log plot. Extrapolation of these exponential fits yields a zero field critical current of 339 A for the strand reacted at Hyper Tech and an average critical current of 298 A for the strands reacted at MIT. A single strand sample and a triplet from each heat treatment batch was also sent in the same quartz tubes in which they were reacted to Philippe Masson's group at the University of Houston (UH) for critical current characterization in their conduction cooled test rig. The UH rig also uses straight test samples and can attain a measurement base temperature in the range between 20K and 22K. As yet we have not received any data for these samples.

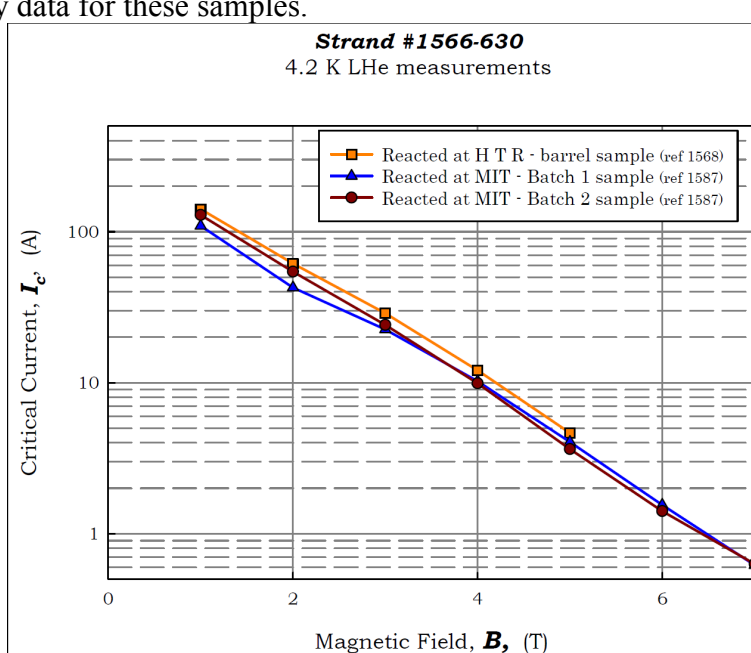


Figure 6.21 Critical currents vs. background magnetic induction for strands reacted at Hyper Tech and at MIT, respectively.

#### 6.5.4. ESTIMATION OF ZERO FIELD, 20K CRITICAL CURRENT

In the absence of direct measurement of the strand critical currents at 20K, we previously published results, shown in Figure 6.22, to estimate the desired value [Doll]. Figure 6.22 shows typical critical current density vs field measurements for Hyper Tech MgB<sub>2</sub> strands at several temperatures. The dashed black line shows the extrapolated, zero-field critical current at 4.2 K, while the dashed yellow line shows the extrapolated, zero-field critical current at 20 K. The extrapolated values show that the zero-field critical current is reduced by a factor of about 2 when the operating temperature is increased from 4.2 K to 20 K. Applying this same ratio to our strand yields an estimated zero-field, 20 K critical current of roughly 149 A. Based on this value, we obtained a critical current density of roughly  $1.6 \times 10^{10}$  A/m<sup>2</sup> by dividing the critical current by the total filament area. The filament area was computed using the 54 filament, 15 micro-m filament diameter values listed in Table 5.2.

##### 5.3.5. AC loss characterization of MgB<sub>2</sub> triplets

A test sample containing ninety, MgB<sub>2</sub> triplet (shown in Figure 6.20) was sent to the Center for Advanced Power Systems (CAPS) at the Florida State University (FSU) for AC loss measurement using their 20 K helium gas flow calorimeter [Kvitkovic Pamidi1, Pamidi2]. Figure 6.23 shows a schematic of the arrangement, while Figure 6.24 shows a photograph. The calorimeter consists of two main parts. The first part, shown with grey shading towards the left side of Figure 6.23, contains a cooling module for cooling and circulating the helium gas. The second part, shown with light green shading towards the right side of Figure 6.23, contains an experiment module that surrounds the test sample (T9) and contains two sets of liquid-nitrogen-cooled, racetrack-wound, copper magnets to produce variable frequency AC magnetic field. The cooling module and experiment module are connected via vacuum jacketed helium transfer lines. The racetrack magnet sets are arranged to produce orthogonal field components at the sample location. The phase between the field components can be varied to produce either a net oscillating, or net rotating field at the sample. The AC loss measurements were performed without transport current in the sample.

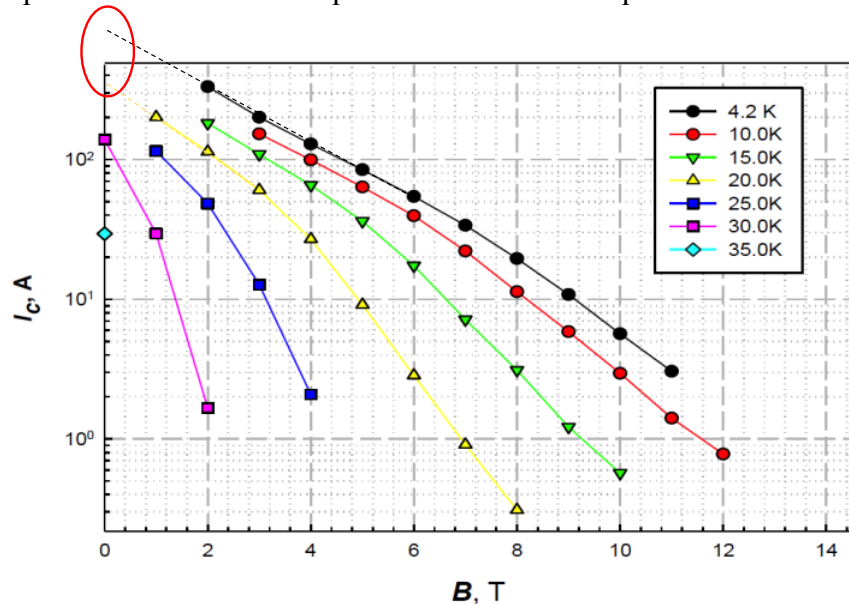


Figure 6.22. Previously published MgB<sub>2</sub> critical current data, used to estimate the 20 K zero-field critical current for our strand.

The cooling module contains a pair of Cryomech model AL-325 cold heads, a CryoZone model AD2000 M cryocirculator, and a helium mass flow meter. Each AL-325 cold head has a design cooling power of 100 W at 25 K and a base temperature of 12 K. Each cold head is equipped with a heat exchanger installed in series with the cryocirculator. The inlet temperature to the experiment module is controlled using a trim heater installed on the cryoline exiting the cooling module. The AC losses,  $Q_{AC}$ , were calculated based on the helium mass flow,  $\dot{m}$ , the nominal heat capacity of the gas,  $C_p(T_s)$ , at the sample temperature,  $T_s$ , and the temperature rise through the experiment module,  $\Delta T$ :

$$Q_{AC} = \dot{m} C_p(T_s) \Delta T.$$

The accuracy of the calorimetric AC loss measurements reported here have recently been called into question. Until the issue is resolved we will process to process the data as if they were accurate.

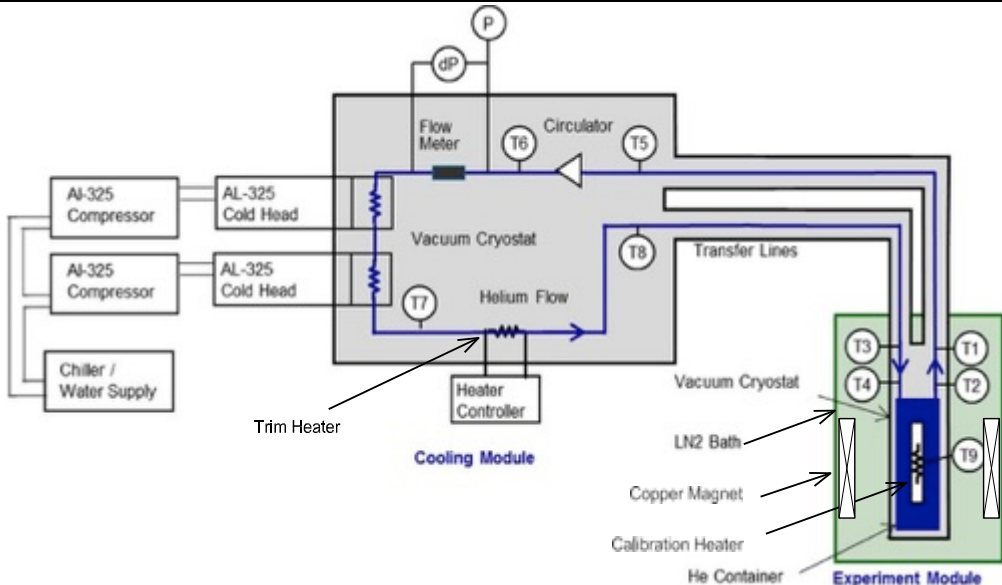


Figure 6.23. Schematic arrangement of the CAPS 20 K helium flow calorimeter.

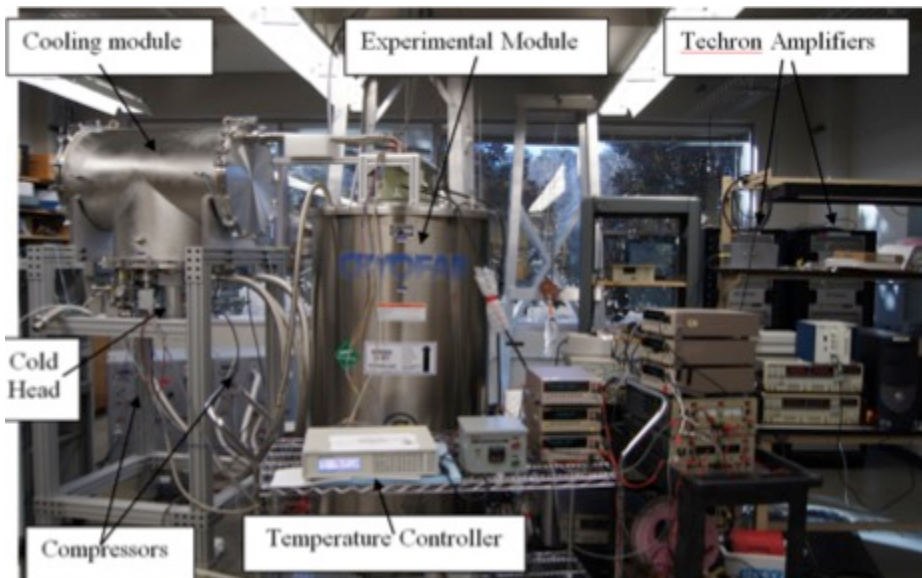


Figure 6.24. Digital photo of the CAPS calorimeter.

Figure 6.25 shows the measured AC loss per cycle at 20 K vs. the peak-peak amplitude of applied magnetic field at frequencies of 50 Hz, 110 Hz, and 300 Hz for the 90 MgB<sub>2</sub> triplets. For this set of measurements, the background field magnet sets in the CAPS facility were operated in-phase and with the same magnetic field amplitude. For this field configuration, the axis of the combined magnetic field is oriented at 45 degrees relative to both coil axes, while the magnitude of the field variation is greater than that for either coil by a factor of the square root of 2.

The loss energy per cycle values plotted in Figure 6.25 were obtained by dividing the asymptotic value of the measured loss power by the excitation frequency. The black dashed line, with slope of 2 on the log-log plot, suggests that the losses in the triplets was dominated by inter-filamentary coupling current losses. This is especially true for the higher amplitude results obtained at 50 Hz. The AC loss per

cycle measurements obtained during lower field excitation at 300 Hz show noticeably less than quadratic dependence on the magnetic field amplitude; this suggests that proportionally more of the total loss under these low field conditions occur as a result of magnetic hysteresis, which often shows closer to linear dependence on the applied field amplitude.

To permit rescaling of the measured results to other operating conditions we attempted to divide the measured AC loss in Figure 5.22,  $Q_t$ , in two components, the first attributed to magnetic hysteresis,  $Q_h$ , and the second to losses due to coupling currents between the filaments,  $Q_c$ . The hysteresis loss component depends solely on the magnetic field amplitude,  $\Delta B$ , while the coupling loss component depends on both field amplitude and frequency,  $\omega$ :

$$Q_t(\Delta B, \omega) = Q_h(\Delta B) + Q_c(\Delta B, \omega).$$

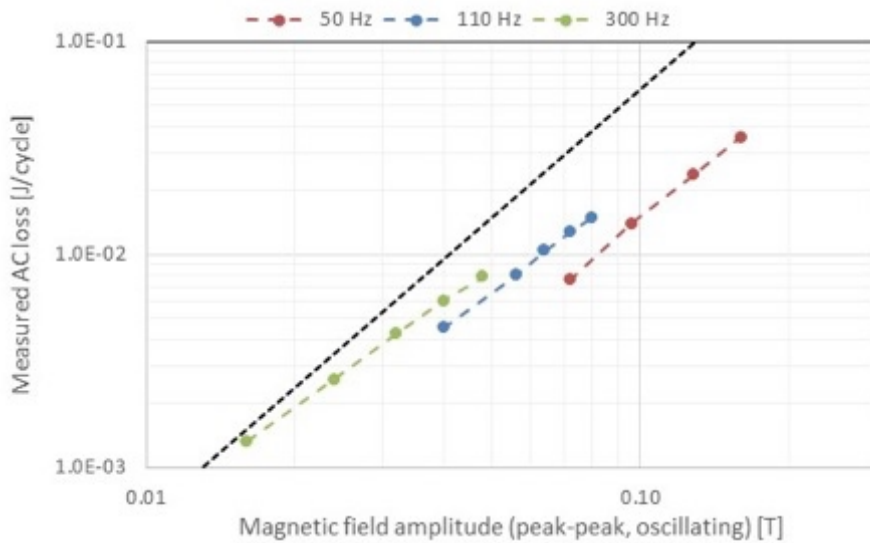


Figure 6.25. Measured AC loss per cycle vs magnetic field amplitude.

#### 6.5.4.1 HYSTERESIS LOSS COMPONENT

There are at least two ways to estimate the hysteresis loss component for a superconducting strand, experimentally and computationally. In cases where an extensive experimental database is available, covering a wide range of magnetic field amplitudes and frequencies, the hysteresis loss component for a given field amplitude can be obtained by extrapolating the low frequency portion for the measured AC loss vs. frequency curve at that field amplitude to zero frequency. In this case, the y-axis intercept corresponds to the experimentally determined hysteresis loss. In the absence of an experimental database, it also is possible to rely on analytical models which depict the magnetic behavior of superconducting filaments when subjected to external magnetic field variation. The specific form of the hysteresis loss equation due to magnetization of the superconducting filaments depends on the orientation of the background field relative to the filament axis and the ratio of the applied magnetic field amplitude,  $\Delta B$ , to the filament's magnetic penetration field,  $B_p$ , which is expressed in terms of the zero-field critical current density,  $J_{c,0}$ , and filament diameter,  $d_f$  [Kobayashi].

$$B_p = \frac{\mu_0 J_{c,0} d_f}{\pi}$$

When the applied transverse magnetic field amplitude is less than or equal to twice the penetration field, the hysteresis loss per volume due to filament magnetization,  $q_{fh}$ , can be calculated using:

$$q_{fh} = \frac{\Delta B^3}{3 \mu_0 B_p} \left(1 - \frac{\Delta B}{4 B_p}\right), \quad \Delta B \leq 2 B_p,$$

whereas when the applied field amplitude is slightly larger than twice the penetration field, the hysteresis loss per filament volume can be calculated using:

$$q_{fh} = \frac{4 \Delta B B_p}{3 \mu_0} \left(1 - \frac{B_p}{\Delta B}\right), \quad \Delta B > 2 B_p.$$

In either case the hysteresis loss due to filament magnetization,  $Q_{fh}$ , is calculated by multiplying the loss per unit filament volume by the total filament volume in the sample:

$$Q_{fh} = q_{fh} n_s n_f \pi \left(\frac{d_f}{2}\right)^2 L_s;$$

where,  $n_s$ , is the numbers of strands in the sample,  $n_f$ , is the number of filaments in each strand,  $d_f$  is the average filament diameter, and  $L_s$  is the sample length.

Depending on the superconductor type and processing conditions, the effective filament diameter deduced from the measured AC losses can be larger than the apparent diameter determined from optical measurement. Wherever feasible it is preferable to deduce the effective filament diameter from the measured losses, before extrapolating to other operating conditions by use of the analytical loss equations.

In the case of HyperTech strands with CuNi matrix, the hysteresis loss assessment is further complicated by the existence of magnetic impurities, which tend to increase the hysteresis loss component to above that due solely to magnetization losses in the superconducting filaments.

The data set presented in Figure 6.25 contains only two field amplitudes where losses were measured at more than one frequency. Figure 6.26 shows the variation in measured AC loss vs frequency for the data points collected at 0.072 T magnetic field amplitude. These points were chosen because they were measured at lower frequency than the alternative possibility. The dotted red line in the plot shows the result of a linear fit of the data, which extrapolates to a zero frequency yield an estimated hysteresis loss,  $Q_h$ , of 0.0033 J/cycle.

Based on our estimated 20 K, zero field critical current density of  $1.6 \times 10^{10} \text{ A/m}^2$  and the strand parameters listed in Table 7.3, the penetration field for our strand should be roughly 0.094 T. This results in an estimated loss per unit volume at 0.072 T field amplitude of 850 J/m<sup>3</sup>. Multiplying through by the total filament volume in the sample yields a total sample loss of 0.00046 J/cycle, which is about 1/7<sup>th</sup> of the experimentally determined value. This suggests that the bulk of the low-field hysteresis loss in the sample was due to the magnetic impurities rather than to filament magnetization.

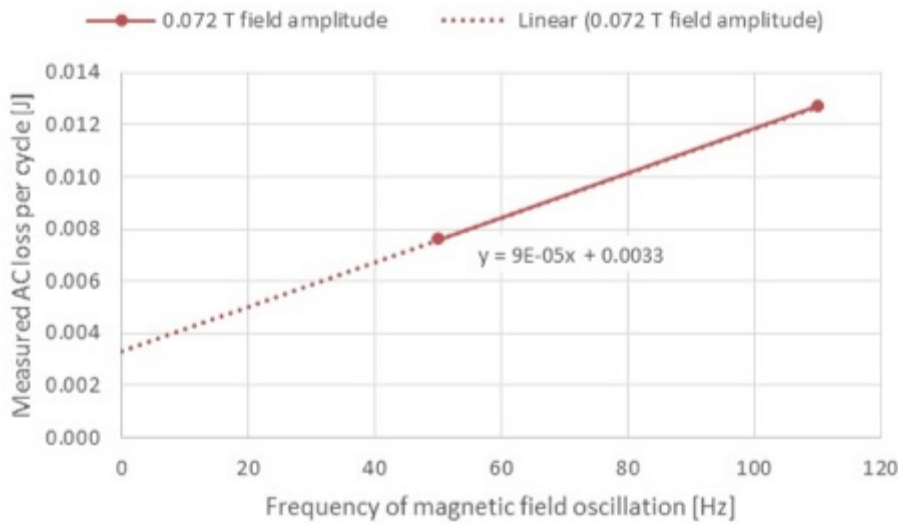


Fig. 6.26. Extrapolation to estimate hysteresis loss component at 0.072 T field amplitude.

The magnetization loss for materials that contain distributed magnetic impurities generally shows a fairly weak, power-law dependence with respect to the amplitude of the applied magnetic field [Kobayashi], [Smith]. Observed values of the power-law exponent range from roughly 0.5 to 1.5. Due to the limited numbers of measurements at the same magnetic field amplitude, we cannot determine an exact fit for our sample. To account for its existence, we assumed that the hysteresis loss component in the measured data varied linearly with field amplitude, that is:

$$Q_h = k_Q \Delta B ;$$

where  $k_Q = 0.0458 \text{ J/cycle/T}$  is the hysteresis loss coefficient deduced from the extrapolated hysteresis loss for the measurements performed using 0.072 T magnetic field amplitude. The assumed linear dependence seem reasonable based on subsequent evaluation of the remaining coupling loss components. The magnitude of the hysteresis loss component is expected to saturate at some value of applied field amplitude, but based on the observed results that field level had not been achieved during the course of the test program reported here. Figure 6.27 shows the computed filament magnetization loss and deduced strand magnetization loss vs. magnetic field amplitude. The extrapolated value of the strand magnetization loss at 0.072 T amplitude is highlighted in this plot.

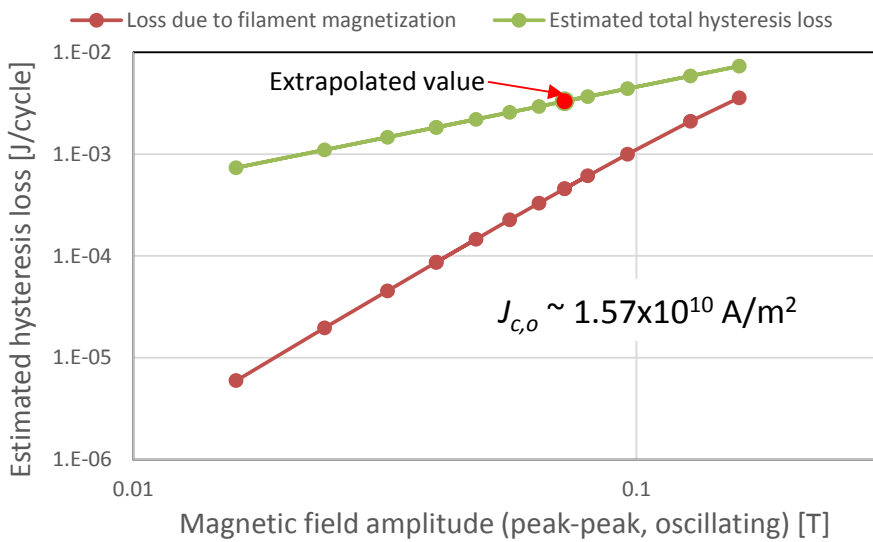


Fig. 6.27. Estimated hysteresis loss and computed filament magnetization loss vs. magnetic field amplitude.

### 5.3.5.2 COUPLING LOSS COMPONENT

The coupling current losses in our sample can occur at both the strand and within triplet level. However, because the electrical contact between filaments within each strand is typically several orders of magnitude higher than that between the strands in a triplet, our initial analysis will focus on the evaluation of the single strand coupling losses. This approach is consistent with the sample preparation method, where each strand was coated with Mobil 1 prior to cabling. Based on historic trends, the Mobil 1™ coating produces an insulating residue as it burns away during the heat treatment reaction and effectively decouples the strands from one another in terms of their AC loss behavior [Bruzone].

When a multi-filamentary superconductor is subjected to a time-varying transverse magnetic field, the magnetic flux captured between the filaments induces a small current flow between them. The time-varying magnetic flux creates current loops that circulate among the filaments in an attempt to “buck out” the external field variation. Although the current in these coupling loops generally follow the superconducting filaments, a portion of the current does pass through the resistive matrix between filaments, giving rise to losses that depend on the magnitude of the field variation and the excitation frequency. Superconducting strands are twisted to limit the magnetic flux linked between the filaments. Reducing the twist pitch length of a strand generally reduces the magnitude of the induced coupling currents and by extension the coupling current loss.

A portion of the magnetic energy induced in the coupling current loops during each external magnetic field cycle is dissipated in the matrix between the filaments due to resistive decay of the induced currents. The energy dissipation is governed by time constant,  $\tau$ , which can be interpreted as the ratio of the inductance of the coupling loop to its resistance:

$$\tau = \frac{\mu_0 l_s^2}{8\pi^2 \rho_m} ;$$

where  $l_s$  is the strand's twist pitch length, and  $\rho_m$  is the resistivity of the resistive matrix between the filaments.

Figure 6.28 shows the estimated coupling current loss for our sample vs. the magnetic field amplitude and frequency. The estimated coupling current loss was obtained by subtracting the computed hysteresis loss (Figure 6.27) from the measured AC data (Figure 6.25). As before, the dashed black line overlaid on the plot shows the quadratic dependence with magnetic field amplitude anticipated for the coupling loss component. The reprocessed data now shows much closer correspondence to the expected behavior at all frequencies.

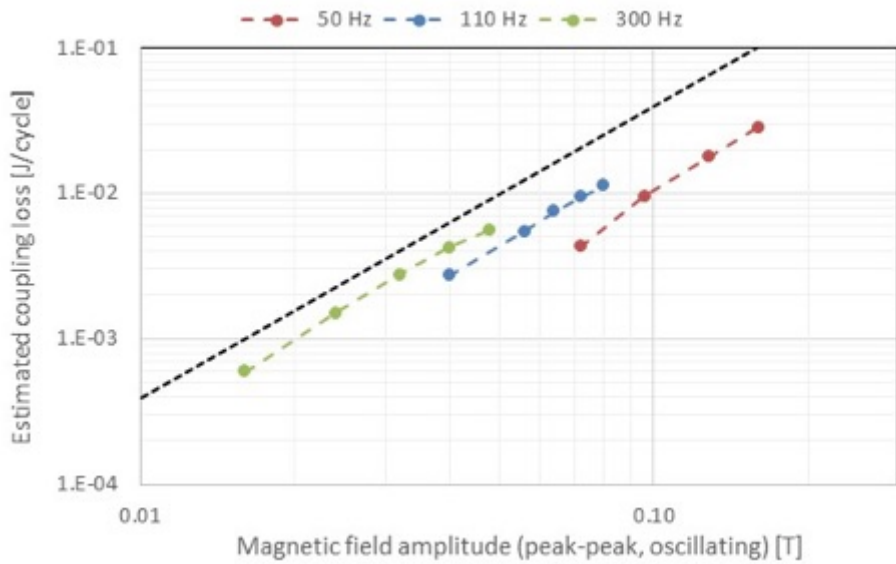


Figure 6.28. Estimated coupling loss vs. magnetic field amplitude and frequency.

The coupling loss per unit volume during sinusoidal excitation,  $q_c$ , is determined by the geometric shape of the strand, characterized by the parameter,  $n$ , the amplitude of the applied transverse magnetic field,  $\Delta B$ , the excitation frequency,  $f$ , and the strand's coupling loss time constant,  $\tau$ :

$$q_c = \frac{\pi n \tau \Delta B^2 (2 \pi f)^2}{4 \mu_0 (1 + (2 \pi f)^2 \tau^2)}$$

For cylindrical strands,  $n$ , is usually equal to 2. The coupling loss for the complete sample is equal to the volumetric loss times the fraction of filament matrix material in the strand,  $f_{fm}$ , numbers of strands in the sample,  $n_s$ , strand diameter,  $ds$ , and sample length,  $L_s$ .

$$Q_c = q_c f_{fm} n_s \pi \left(\frac{ds}{2}\right)^2 L_s .$$

Figure 6.29 shows the result of a data fitting exercise to determine values of matrix resistivity and the filament fraction in the filament zone to match the estimated coupling current loss for our sample. Overall the results look quite reasonable. The data fit required a matrix resistivity on order of  $6 \times 10^{-10}$  Ohm-m and filament fraction,  $f_{fm}$ , of roughly 20% to match our estimated coupling loss. The resistivity is consistent with the use of high purity niobium in the filament barriers, which the estimated filament fraction corresponds to the fractional percentage of the Nb barriers in the strand. The data fit result in Figure 6.29 suggests that the coupling loss in our strand was dominated by the Nb barriers which occupy a large fraction of the interfilament space as shown in Figure 7.4, rather than by the much more resistive CuNi matrix that fills out the remainder of the strand.

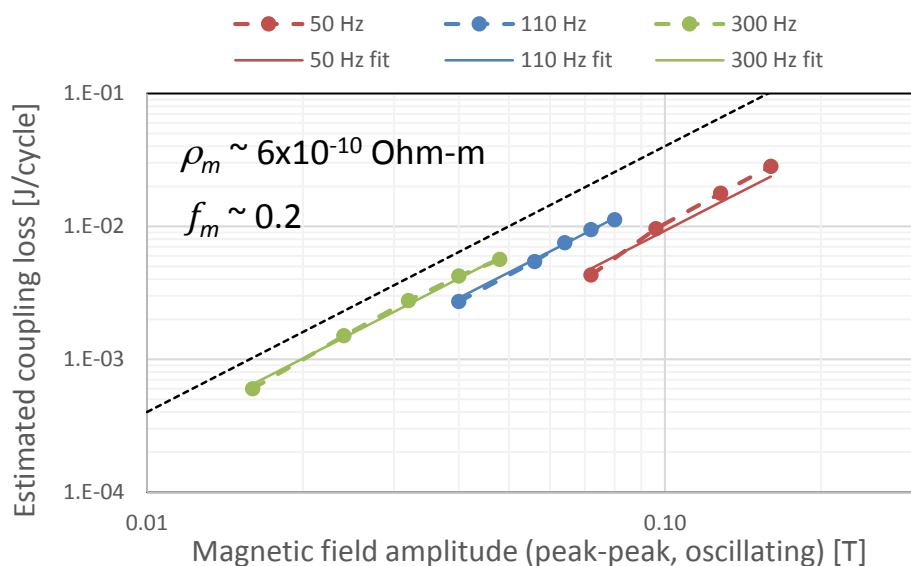


Figure 6.29. Estimated coupling loss vs. magnetic field amplitude and frequency.

## 6.6 SUMMARY

As part of our ONR funded high-speed, armature investigation, we performed a technology demonstration program to examine near term feasibility of MgB<sub>2</sub> cable-in-conduit conductors (CICC) for the production of low AC loss armature windings for high-speed turbo-generators. Production of a 1 m CICC prototype using surrogate stainless steel strand was performed out as a low risk means to examine manufacturability. AC loss calculations performed in support of planned calorimetric measurement of the proposed MgB<sub>2</sub> CICC revealed that eddy current losses in the stainless steel jacket were not negligible as initially assumed; eddy current losses in the jacket could easily exceed losses in the MgB<sub>2</sub> strands by a factor of ten or more. This observation does not invalidate the CICC concept, rather it indicate that the jacket would need to be a low loss dielectric such as epoxy glass. The glass wrap could accompany the triplet wound cooling tube through the heat treatment, before being epoxy impregnated following clean-up from the reaction heat treatment.

The cooling tube can be made from stainless steel. The outer jacket can be made from either stainless steel or dielectric material that can also serve for as the turn-turn insulation.

The AC loss measurements were performed in the CAPS 20 K helium flow calorimeter using ninety MgB<sub>2</sub> triplets mounted on a 50 mm diameter G-10 tube. The measured AC losses were significantly higher than anticipated by pre-test calculations, but could be reconciled with physical characteristics of the strands.

## 6.7 REFERENCES

[Labalestier] D.C. Larbalestier, J. Jiang, U.P. Trociewitz, F. Kametani, C. Scheuerlein, M. Dalban-Canassy, M. Matras, P. Chen, N.C. Crain, P.J. Lee, and E.E. Hellstrom, “Isotropic round-wire multifilament cuprate superconductor for generation of magnetic fields above 30 T,” *Nature Materials* 13 (2014) 375-381.

[Huang] Y. Huang, H. Miao, S. Hong, and J.A. Parrell, “Bi-2212 round wire development for high field applications,” *IEEE Trans. Appl. Superconductivity* 24 (2014) 6400205.

[Otto] A. Otto, personal correspondence, Feb. 2015.

[Voccio] J.P. Voccio, P.C. Michael, L. Bromberg, and S Hahn 2015 Solid-cryogen-stabilized, cable-in-conduit (CIC) superconducting cables *IOP Conf. Ser.: Mater. Sci. Eng.* **101** Art. 012120.

Lienhard J H 1981 Turbulent pipe flow section 8.3 in A Heat Transfer Textbook (Englewood Cliffs: Prentice-Hall)

[Lemon] Lemmon E W, Huber M L and McLinden M O 2013 NIST Standard Reference Database 23: Reference Fluid Thermodynamic and Transport Properties-REFPROP, Version 9.1 (Gaithersburg: National Institute of Standards and Technology, Standard Reference Data Program)

[NASA] Fine filament MgB2 superconductor wire, <http://ntrs.nasa.gov/archive/nasa/casi.ntrs.nasa.gov/20160005362.pdf>

[Voccio] J.P. Voccio, P.C. Michael, L. Bromberg, and S Hahn 2015 Solid-cryogen-stabilized, cable-in-conduit (CIC) superconducting cables *IOP Conf. Ser.: Mater. Sci. Eng.* 101 Art. 012120.

[Rindfleisch] M. Rindfleisch 2015 personal correspondence Dec. 9, 2015.

[Bhatia] M. Bhatia, M.D. Sumption, M. Tomsic, and E.W. Collings 2004 Influence of heat-treatment schedules on the transport current densities of long and short segments of superconducting MgB2 wires *Physica C* 407 153-159.

[Kvitkovic] Kvitkovic, R. Hatwar, and S. Pamidi, "Simultaneous magnetic shielding and magnetization loss measurements of YBCO cylinders at variable temperatures under cryogenic helium gas circulation," *IEEE Trans. Appl. Supercond.* 26(3) (2016) Art. 9000505.

[Pamidi1] S. Pamidi, C.H. Kim, J.H. Kim, D. Crook, and S. Dale, "Cryogenic helium gas circulation system for advanced characterization of superconducting cables and other devices," *Cryogenics* 52 (2012) 315-320.

[Pamidi2] S.Pamidi, J. Kvitkovic, U. Trociewitz, S. Ishmael, R. Meinke, and G. Stelzer, "A novel magnet for AC loss measurements on 2G superconductor rings and coils in axial and radial magnetic fields," *IEEE Trans. Appl. Supercond.* 22(3) (2012) Art. 9003004.

[Bruzone] P. Bruzone 1999 Hysteresis and coupling losses in superconductors in *Wiley Encyclopedia of Electrical and Electronic Engineering*, Suppl. 1 J. Webster ed. John Wiley and Sons, pp. 233-248.

[Kobayashi1] S. Kobayashi 2011 Magnetic hysteresis scaling behavior in terbium and holmium *Phys. Rev. B* 84 Art. 224418.

[Kobayashi2] S. Kobayashi, N. Kikuchi, S. Takahashi, Y. Kamada, and H. Kikuchi 2010 Magnetic properties of  $\alpha'$  martensite and austenitic stainless steel studied by a minor-loop scaling law *J. Appl. Phys.* 108 Art. 043904.

[Smith] B.A. Smith, P.C. Michael, J.V. MInervini, M. Takayasu, J.H. Schultz, E. Gregory, T. Pyon, W.B. Sampson, A. Ghosh, and R. Scanlan 2001 Design, fabrication and test of the react and wind, Nb3Sn LDX Floating Coil conductor *IEEE Trans. Appl. Supercond.* 11(1) 1869-1872.

## 7. CABLE DESIGN

Because the configuration and overall efficiency for a high-speed, fully-superconducting generator depends critically on the ac loss power generated in the stator windings, we decided to concentrate our preliminary work on the more recently developed MgB<sub>2</sub> conductors. By virtue of their structure, MgB<sub>2</sub>-based superconductors appear reasonably well suited to high frequency electro-magnetic excitation. There is significant on-going effort to reduce the filament diameter and shorten the twist pitch length for MgB<sub>2</sub> round wires. Also, the critical current of MgB<sub>2</sub> wires does not depend on the direction of the local magnetic field, which simplifies the evaluation of both its superconducting performance and ac loss characteristics.

### 7.1 MgB<sub>2</sub> CABLE-IN-CONDUIT CONDUCTOR

Cable-in-conduit (CIC) superconductors have been used since 1975, when they were developed for large, high-current plasma fusion magnets [Hoenig, Ciazinski, Besette]. Figure 7.1a shows a Nb<sub>3</sub>Sn based CIC with two partially separated channels; the outer channel contains a multi-stage superconducting cable, while the inner channel provides a low-pressure-drop flow path for the supercritical helium coolant [Lienhard]. Sub-division of the composite superconductor strands in the CIC cable volume significantly increases the wetted perimeter of the conductor for given cross-sectional area, which enhances its cooling characteristics. The side length of the square conductor shown in Figure 7.1a is 51 mm. A spiral, or perforated, tube is often used for LTS-based CIC to facilitate coolant exchange between the cable space and central cooling channel.

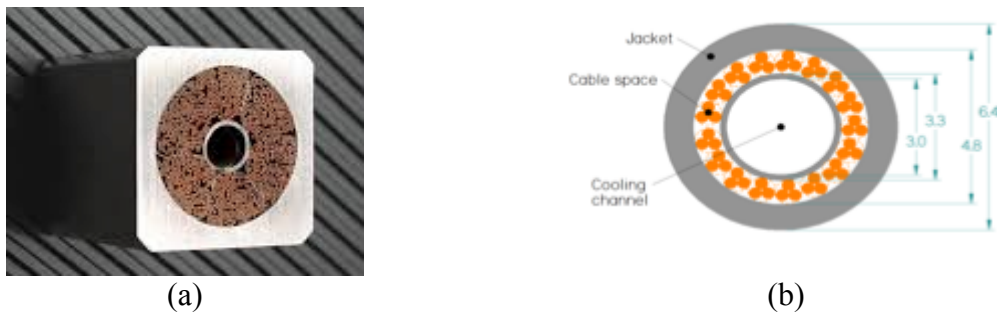


Figure 7.1. Cable-in-conduit superconductors: (a) conventional LTS design for the ITER central solenoid; (b) proposed two-stage MgB<sub>2</sub> cable design. (All dimensions in mm.)

More recently, the CIC concept has been adapted to lower current, single-stage cable applications such as fast-ramped particle accelerator magnets [Lemmons, NASA]. These previous, miniature CICs were designed to be cooled with supercritical helium cooling; the central cooling channel is retained in these designs to provide adequate coolant flow to manage the high anticipated ac loss during fast-ramped operation. The outer jacket of the CIC also provides significant structural support throughout the magnet volume.

For this study, we adopted the CIC configuration for the MgB<sub>2</sub>-based conductor shown in Figure 5.1b to accommodate the relatively high AC conductor loss anticipated in the superconducting stator. Of necessity, the conductor layout and stator configuration need to be designed iteratively. The space allocated for the stator windings affects the magnitude of magnetic field on the conductor. The amplitude and time-dependent variation in magnetic field on the conductor influences both its current carrying capacity and ac loss power production. The current carrying capacity determined the total

required cross-section of superconductor, while the ac loss power influences the required diameter of the center cooling channel. Due to the relatively low mass density of the 20 K helium gas coolant the diameter of the central cooling channel comprises a significantly larger fraction of the CIC conductor cross-section compared to liquid helium cooled conductors operating near 4.2 K.

## 7.2 CONDUCTOR OVERVIEW

Nearly all of the machine topologies investigated in this program assumed the use of MgB<sub>2</sub>-based cable in conduit conductor (CICC) for the stator design. There were several reasons for this selection. First, MgB<sub>2</sub> retains acceptable engineering current density at temperatures in the range from 20 K to 25 K. Second, MgB<sub>2</sub> can be manufactured as tightly twisted, fine filamentary round strands with isotropic critical current properties. Third, the CICC configuration integrates conductor cooling in intimate contact with all cable strands and provides structural support for the strain-sensitive conductor throughout the winding pack.

Stator operation near 20 K permits significant reduction in the size and cost of the cryogenic plant needed to cool the stator, compared to conductors operating near 4 K. The use of high current density isotropic conductor minimizes the conductor requirement, compared to conductors with anisotropic critical currents like REBCO. The fine filament diameter in the strands minimizes hysteresis losses, while the tight twist pitch helps to minimize coupling current losses.

Figure 7.2 shows a cross-section for one of our MgB<sub>2</sub> CICC conductor designs, while Table 7.1 lists characteristics for this conductor. The conductor in Figure 7.2 consists of a central, stainless steel cooling tube, surrounded for thirty MgB<sub>2</sub> triplets, enclosed in an outer stainless steel jacket. The CICC dimensions varied significantly through the course of the program, based largely by the computed loss in the conductor and the length of conductor for each stator winding, which determine the minimum cooling path length. The conductor configuration shown in Figure 7.2 was for a 14 MW, 6.6 kV, two-pole turbo-generator operating at 7000 RPM. For this design the amplitude of the field variation at the conductor typically ranged from 0.5 T to roughly 1.0 T. Under these conditions, the calculated AC loss per conductor length range from roughly 2 W/m to 4 W/m.

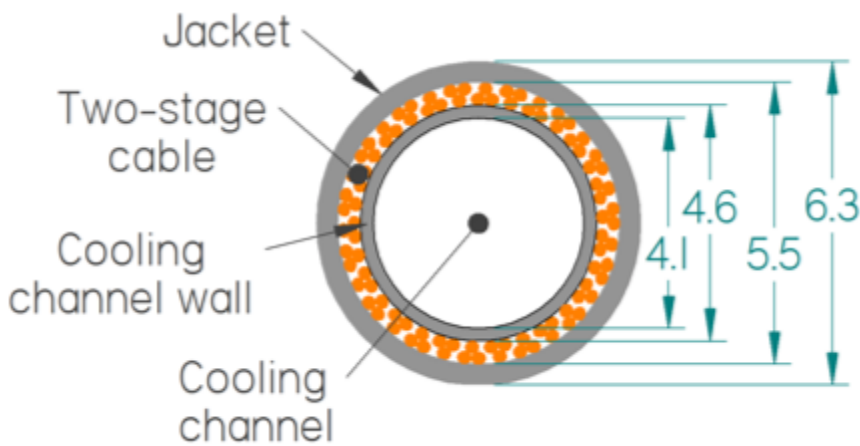


Figure 7.2. Cross-section of a typical MgB<sub>2</sub> cable-in-conduit conductor.

The CICC configuration for each machine topology was designed iteratively. The required strand area was determined using the peak magnetic field on the conductor, the critical current density vs. local magnetic flux density plot shown in Figure 7.3, and an assumed superconductor fill factor of

15% [Doll] to limit the peak phase current of roughly 2kA to 60% of the conductor critical current. The assumed strand parameters of 10  $\mu\text{m}$  filament diameter, 10 mm twist pitch, and  $10^{-6}$  Ohm-m matrix resistivity have been achieved in prototype 1st generation Hyper Tech strand development, but have not yet made it into routine production [Tomsic]. The anticipated AC loss in the conductor was calculated based on magnetization hysteresis, coupling current, and transport current losses in the superconductor strands [Tixador]. Eddy current losses in the cooling channel walls and outer jacket were neglected during the machine topology studies.

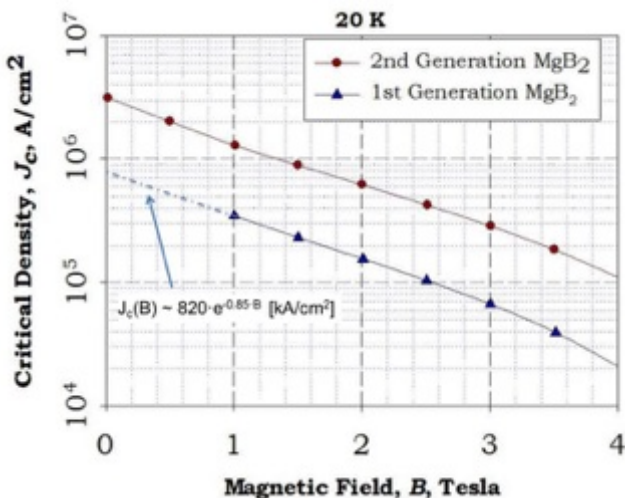


Figure 7.3. Critical current density vs. local magnetic flux density used in the 20 K conductor design. Figure from [Rindfleisch].

Table 7.1. MgB<sub>2</sub> strand, cable and conductor design parameters.

Item	Value	Item	Value
Strand diameter (mm)	0.256	Strands per Cable	90
Filament diameter ( $\mu\text{m}$ )	10	Cable pattern	30 x 3
Strand twist pitch (mm)	10	Cooling channel ID/OD (mm)	4.1 / 4.6
Matrix resistivity (Ohm-m)	$10^{-6}$	Jacket ID/OD (mm)	5.5 / 6.3
Fraction of critical current	0.6	Peak operating temperature (K)	25
Peak strand current (A)	22		

The central cooling channel diameter for the CICC in Figure 7.2 was determined based on thermohydraulic considerations. The conductor cooling design assumes inlet conditions of 20 atm, 20 K helium gas, 0.5 atm pressure drop, and 3 K temperature rise along the 16 m conductor length. Preliminary cooling channel design was performed using standard analytic solutions and average value of the inlet and outlet helium gas properties [Lienhard], and confirmed by subsequent CFD (FLUENT) analysis. The helium properties needed for this analysis were obtained from the software package REFPROP [Nasa]. The peak temperature on the conductor of 25 K in Table 7.1 includes roughly 2 K temperature drop across the radial width of the cable space. Nominal cooling channel flow parameters to remove the computed 56 W heat load for the conductor include: a mass flow of 3.2 g/s, Reynolds number of  $2.2 \times 10^5$ , and average heat transfer coefficient of 3580 W/m<sup>2</sup>-K.

### 7.2.1 TECHNOLOGY DEMONSTRATION

Towards the end of our high-speed stator program, we sought to fabricate a prototype MgB<sub>2</sub> CICC to assess the feasibility of the concept using the Gramme ring stator configuration, which permits attainment of the rated 14 MW generator output with a peak field amplitude of roughly 0.1 T at the conductor. Table 7.2 shows the characteristics of the cable shown schematically in Figure 7.2. The conductor contains eighteen MgB<sub>2</sub> triplets (54 strands total) and has an anticipated critical current of roughly 4 kA (twice the peak phase current of 2 kA) when energized in 0.1 T field at 20 K. The outer diameter of the central cooling tube and inner diameter of the outer jacket were chosen to achieve roughly 40~45% void fraction in the annular cable space. This void fraction should permit the strands to be loosely held in place without excessive deformation of the strand cross-sections during compaction of the conductor jacket. In the event that strand motion has negative impact on MgB<sub>2</sub> cable performance at these high void fractions, we analytically investigated the possibility to introduce a liquid or gaseous cryogen in the cable space, which when cooled and frozen would provide the required strand constraint [Voccio].

Table 7.2. Target dimensions for the CICC fabrication trial.

<b>Cooling tube inner diameter [mm]</b>	<b>2.69</b>
<b>Cooling tube outer diameter [mm]</b>	<b>3.40</b>
<b>Strand diameter [mm]</b>	<b>0.31</b>
<b>Strand twist pitch length [mm]</b>	<b>5</b>
<b>Triplet twist pitch length [mm]</b>	<b>10</b>
<b>Twist pitch for 2<sup>nd</sup> cable stage [mm]</b>	<b>100</b>
<b>Estimated void space in cable volume [%]</b>	<b>~45.5</b>
<b>Jacket inner diameter [mm]</b>	<b>4.59</b>
<b>Jacket outer diameter [mm]</b>	<b>5.78</b>

We procured a 300 m length of un-reacted, tightly twisted (5 mm twist pitch length), fine filament (15 micro-m diameter) MgB<sub>2</sub> strand from Hyper Tech Research of Columbus OH for this purpose. Un-reacted strand was chosen due to the high strain sensitivity of the MgB<sub>2</sub> in the reacted state and our desire to fabricate a tightly-twisted, multiple-stage cable using the strand. Table 7.3 summarizes parameters for our 54 filament, 0.31 mm diameter strand, while the photomicrograph in Figure 7.4 shows a cross-section micrograph of a similar strand manufactured by Hyper Tech as part of a NASA SBIR [Tomsic]. The strand was manufactured using Hyper Tech's power-in-tube (Type 1) processing technology. The strand in Figure 7.4 also contains 54 MgB<sub>2</sub> filaments with niobium barriers embedded in a CuNi matrix. The micrograph shows the strand cross-section at a strand diameter of 0.35mm, which is just slightly above the 0.31 mm strand diameter used for our strand.

Table 7.3: Parameters of MgB<sub>2</sub> strand obtained from Hyper Tech Research

<b>Id #</b>	<b># Mono Filament</b>	<b>Filament Barrier</b>	<b>Mono sheath</b>	<b>Multi sheath</b>	<b>Strand diam. (mm)</b>	<b>Fill factor %</b>	<b>Effective filament diameter (μm)</b>	<b>Twist pitch (mm)</b>	<b>Insulation</b>	<b>Heat treatment</b>	<b>Length (m)</b>
·630	54	Nb	CuNi	CuNi	0.31	13	15	5	n/a	n/a	300

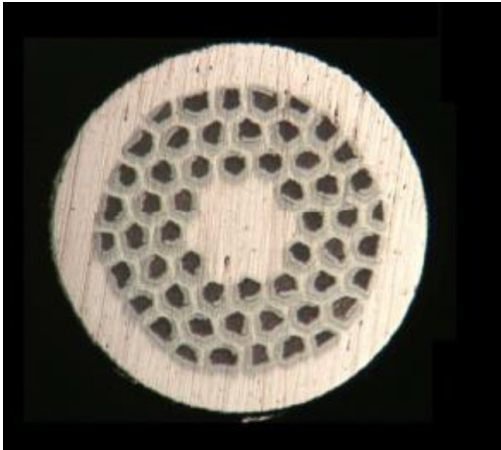


Figure 7.4. Cross-section of a 54 filament MgB2 strand with Nb filament barriers and CuNi matrix at 0.35mm diameter.

The CICC fabrication effort began using surrogate, 0.31 mm diameter stainless steel wire as a substitute for the MgB2 strand, to minimize risk while the manufacturing procedures were developed. The goal of the cable fabrication effort was to characterize the MgB2 CICC to the extent possible using existing facilities to benchmark our stator design codes. The test plan emphasized AC loss measurement because this is the least well demonstrated aspect of MgB2 conductor performance. Because it provides a reasonable match to the stator's design operating conditions, we arranged with the Center for Advanced Power Systems (CAPS) at FSU to test an MgB2 conductor sample for us using their 20 K, helium gas flow calorimeter. We would prepare the sample using the strand described in Table 7.3, while CAPS would perform calorimetric evaluation of the losses in time-varying background field.

During preliminary design of the test sample, we performed more a detailed evaluation of anticipated AC losses for our proposed MgB2 CICC; these calculations revealed that eddy current losses induced in the conductor jacket were not negligible and could actually be more than ten times higher than the expected AC losses in the MgB2 strands.

## 7.3 PROTOTYPE SAMPLE FABRICATION

As part of the technology demonstration program, we manufactured 1 m long CICC prototype using 0.31 mm (actually 0.012") diameter stainless steel strand to qualify all manufacturing steps before implementing them on the most expensive MgB2 strand procured from Hyper Tech. The manufacturing steps included fabrication of a 65 m long triplet cable, selection of the cooling tube and jacket from commercially available sizes, fabrication of the 2nd stage cable by winding 18 triplets around the chosen cooling tube, drawing the 2nd stage cable into the chosen conductor jacket, and compacting the jacket to its nominal, design void fraction.

### 7.3.1 TRIPLET CABLING

The 1st stage triplets for the prototype sample were twisted using the planetary cabling machine installed in our laboratory (shown in Figure 7.5). The cabling machine can accommodate up to six pay-off spools, each with 3/4" (1.9 cm) shaft diameter, 4" (10 cm) drum width, and up to 6" (15 cm) flange diameter. Our cabling machine is a two motor machine; separate motors are used to power the spinner and the drive capstan. The operation of these motors is synchronized electronically. The "speed

control" in Figure 7.5 sets the spinner rotational speed, while the "ratio control" sets the capstan drive speed as fraction of spinner speed.

Data collected during prior cabling runs is cataloged in a logbook near the machine. These data establish an approximate set of parameters to begin the practice cable run. The target twist pitch for the prototype triplet was 10 mm. The parameters need to achieve the desired twist pitch were fine-tuned by repeatedly running off a length of the triplet cable (typically 2 m), stopping the machine to measure the pitch, and adjusting the speed or ratio control as needed.

The payoff force on the strands is controlled by adjustable, spring-loaded friction brakes applied to the shaft for each payoff spool. A payoff force in the 20~30 N range is typically for cabling single strand samples. The nominal, 0.67 mm diameter of the triplet cable was set by the diameter of a Delrin® cabling die, which is machine a few tens of microns larger than the computed diameter of the cable stage. A separate control sets the torque on the take-up spool; the torque needs to be large enough to smoothly feed the cable through the die when the machine is running, but not so great as to pull the cable through the die when the machine is idling.

In preparation for cabling, 65 m lengths of stainless steel strand were respooled from a delivery spool onto each of three cabling machine take-up spools using the respooling machine shown in Figure 7.6. An overview of the setup looking along the length of the respooling machine is shown in Figure 7.6a, while Figure 7.6b emphasizes the take-up end of the machine. The strand is directed over and under a pair of guide wheels, one of which is connected to a rotary counter to measure the length of strand applied to the take-up spool. The rotational speed of the take-up spool and lateral speed of the guide wheel traverser were controlled separately to achieve well-ordered packing of the strand onto the spools.

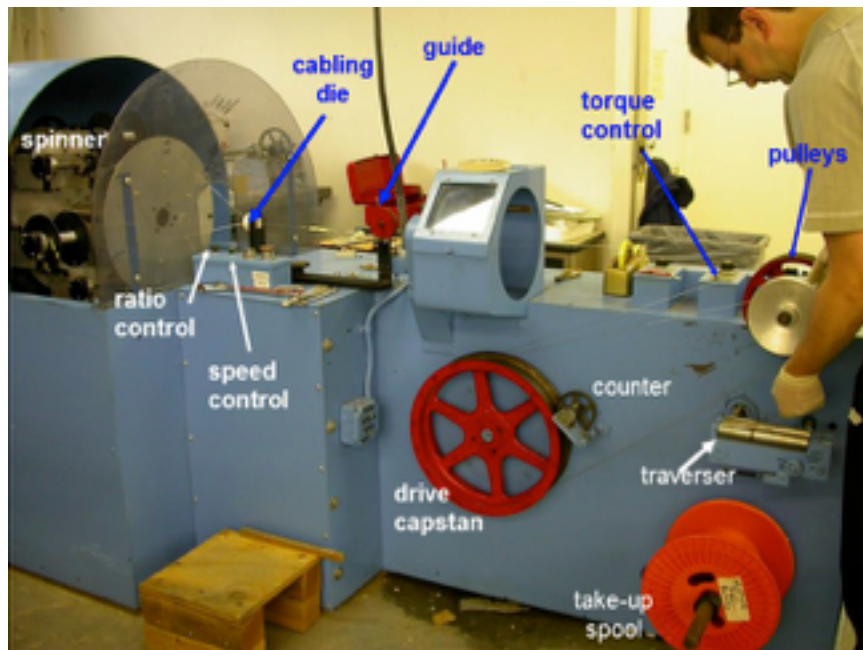


Figure 7.5 Planetary cabling machine used to fabricate the 1st stage triplets.

### 7.3.2. JACKET COMPACTION TRIALS

With the exception of the MgB2 strands, both the prototype and the demonstration CICCs were both to have been made using off-the-shelf items. For a low-temperature superconductor-based CICC, where

moderate strand deformation can be accommodated, the void fraction in the cable space is often in the range from 0.28~0.35. This is done largely to minimize strand motions within the cable which might generate sufficient local energy dissipation to drive the conductor from the superconducting state. For cable based on Nb<sub>3</sub>Sn strands, these void fractions are also used to minimize damage due to cyclic motion of the cable within the conductor.

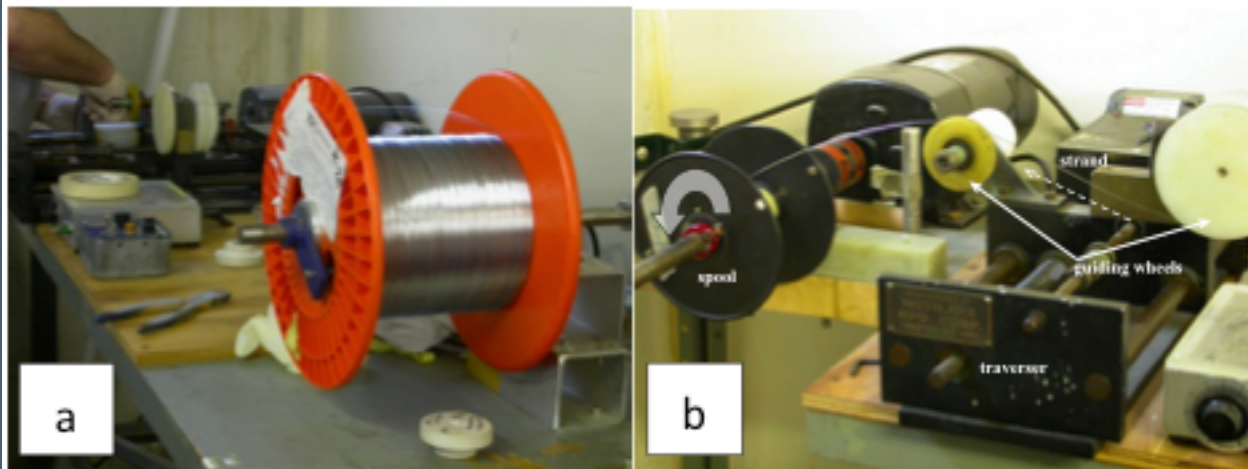


Figure 7.6. Respooling of stainless steel strand from a delivery spool onto smaller, pay-off spools to fit the cabling machine spinner.

Because the effect of transverse compaction on the performance of MgB<sub>2</sub> strands has not yet been thoroughly investigated, we targeted a slightly higher void fraction for our samples, in the range from ~0.35 to 0.45. Because the diameter of our strands was set at 0.31 mm, the void fraction in the finished cable depends on the outer diameter of the cooling tube, the numbers of triplets in the finished cable, and the inner diameter of the compacted conductor jacket. Because our CICC was to be made using the “draw through” process, in which the finished cable is first drawn into an uncompacted jacket before the jacket is compacted to its final dimensions, the inner diameter of the uncompacted jacket needs to be large enough to permit the cable to draw through without exceeding interference. Table 7.4 lists commercially available tubes whose dimensions are in the range to serve respectively as either the cooling tube or conductor jacket.

Table 7.4. Candidate, commercially available tubes for cooling channel and jacket.

Candidate location in CICC	Nominal, uncompacted inner diameter [mm]	Nominal, uncompacted outer diameter [mm]
Cooling tube	2.67 (0.105")	3.18 (0.125")
Cooling tube	2.69 (0.106")	3.40 (0.134")
Cooling tube	3.00 (0.118")	3.76 (0.165")
Cooling tube	3.43 (0.135")	4.19 (0.165")
Jacket	5.33 (0.210")	6.35 (0.250")
Jacket	5.71 (0.225")	7.21 (0.283")
Jacket	6.17 (0.243")	7.95 (0.313")
Jacket	6.53 (0.257")	7.95 (0.313")

The specific combination of cooling tube, numbers of triplets, and jacket used for the prototype CICC was determined based on compaction trial performed using candidate jacket specimens. Because the jacket is significantly stiffer than the rest of the conductor, compaction trials on empty jacket sections provide nearly the same result as compaction of the entire CICC. The compaction trials were performed using a commercial swaging machine (shown in Figure 7.7) located at Supercon, Inc. Use of this machine was arranged by a former colleague who has frequent dealings with Supercon. The swaging dies available for these trials were designed to achieve compacted diameters of: 0.210", 0.230", 0.250", and 0.280". Table 7.5 summarizes the results of the compaction trials. Two dies were used for each of the candidate jackets listed in Table 7.4. Table 7.5 lists both nominal and measured outer diameters (OD) for each combination of tube size and die diameter. The outer diameter for each tube was measured using digital caliper. The value reported in Table 7.5 is the average value obtained from orthogonal measurements performed at seven locations along each ~1 m long tube. The inner diameters (ID) for the tubes were calculated using the weight for each tube, the density for stainless steel (8000 kg/m<sup>3</sup>), and the tubes measured OD and length. Based on the result of these compaction trials, a tube with nominal ID of 2.69, nominal OD of 3.40 mm was selected for the cooling tube. A tube with nominal ID of 5.33 mm and nominal OD of 6.18 mm was selected for the jacket, while the cable space was filled with eighteen triplet sub-cables at a nominal void fraction of 45%.



Figure 7.7. Swaging machine at Supercon, Inc. used for the compaction trials and completion of the CICC prototype sample.

Table 7.4. Results from compaction trials performed at Supercon, Inc.

Nominal tube OD [mm]	Uncompacted OD [mm]	Uncompacted ID [mm]	Compaction die size [mm]	Compacted OD [mm]	Compacted ID [mm]
7.95 (0.313")	7.92	6.10		6.43	4.30
7.95 (0.313")	7.87	6.06		7.07	5.10
7.95 (0.313")	7.85	6.46		7.07	5.57
7.95 (0.313")	7.75	6.31		6.40	4.76
7.21 (0.283")	7.09	5.70		6.36	4.88
7.21 (0.283")	7.06	5.66		5.81	4.22
6.35 (0.250")	6.36	5.28		5.36	4.13
<b>6.35 (0.250")</b>	<b>6.30</b>	<b>5.19</b>		<b>5.78</b>	<b>4.59</b>

### 7.3.3 SECOND-STAGE CABLING

The 2nd cable stage was fabricated by hand using the 6 mm thick by 50 mm diameter Delrin® die shown in Figure 7.8. The Delrin die was equipped with a 3.58 mm diameter center hole to provide a light slip fit over the cooling tube, and eighteen 0.79 mm diameter holes equally spaced on a 4.5 mm radius about the center of the die.

The 2nd-stage cable was fabricated using eighteen, 1.3 m lengths of the stainless triplet and a 1 m length of the 3.4 mm OD cooling tube listed in Table 7.4. To start the fabrication, the triplets were tightly secured near the center of the cooling tube using stainless steel wire. The ends of the triplets near one end of the cable were also temporarily secured and the tube was upright and secured vertically using a lab stand, so that the free end of the triplets hung down vertically. The cabling die was installed onto the cooling tube and the triplets were inserted in sequence into the circular hole pattern. The die was then slid up towards the secured, center section of the triplets so that cabling could

proceed from the sample center to the free end. The radial black mark was used to indicate each full revolution of the die as it was simultaneously rotated and translated along the length of the cooling tube. A meter stick (not shown in Figure 7.8) was mounted vertically next to the cabling stand to measure the ~75 mm twist pitch for each rotation of the die. The twisted 2nd stage cable was secured every two twist pitches using stainless steel wire.



Figure 7.8. Hand-held die to cable the eighteen triplets around the central cooling tube.

Once the first end of the cable was complete, the sample was removed from the lab stand and inverted so that the cabling process could be repeated starting from the secured center section of the triplets and working towards the opposite end of the sample. We believe that cable fabrication can be readily scaled to long length using commercial cabling equipment. For the superconducting armatures examined in this study, the maximum cable length was about 16 m (corresponding to 4 turns around the stator yoke).

#### 7.3.4 CABLE DRAW-THROUGH AND COMPACTION

The CICC sample fabrication was completed by first pulling the triplet wrapped cooling tube into the uncompacted jacket using a length of stainless steel wire as a guide. To minimize the chance of the cable expanding during this process the stainless steel ties holding the triplets against the cooling tube were left in place until the corresponding section was about to enter into the jacket. Additionally, the cable was passed through a 5.30 mm diameter Delrin cabling die mounted at the leading edge of the jacket as shown in Figure 7.9 to ensure that it entered smoothly into the jacket.



Figure 7.9. Cabling die to guide the cable into slightly larger, un-compacted jacket.

Once the cable was pulled completely into the jacket, the jacket with cable installed was passed through the swaging machine shown in Figure 7.7 to complete the fabrication of our prototype CICC. A photo of the completed CICC prototype is shown in Figure 7.10. The loop at the end of the cable to the right of the photo was attached to a stainless steel lead wire used to draw the cable through the jacket. We believe that it is technically feasible to fabricate demonstration cables that are about 10 m long using the process described above. Longer length cables would most likely need to be made

using a commercial cabling line.



Figure 7.10. Stainless steel CICC prototype following jacket compaction.

### 7.3.5 THERMOHYDRAULIC CONSIDERATIONS

The central cooling channel diameter in the CIC was determined based on thermohydraulic considerations. The conductor cooling design assumes inlet conditions of 20 atm, 20 K helium gas, 0.5 atm pressure drop, and 3 K temperature rise along the conductor length. Because of the low mass density of helium gas at 20 K, there is virtually no flow through the cable space for the chosen pressure drop, if the cable space were connected to the flow channel. The 3.0 mm cooling channel i.d. listed in Table 7.4 is based on an average AC loss heat load of 28 W. Preliminary cooling channel design was performed using standard analytic solutions and average value of the inlet and outlet helium gas properties [Lienhard], and confirmed by subsequent CFD (FLUENT) analysis. The helium properties needed for this analysis were obtained from the software package REFPROP [NIST]. Nominal cooling channel flow parameters include: a mass flow of 3.2 g/s, Reynolds number of  $2.2 \times 10^5$ , and average heat transfer coefficient of 3580 W/m<sup>2</sup>-K.

To complete the CIC design, the diameter of the MgB<sub>2</sub> strand was freely varied to best fill the annular gap between the outer diameter of the cooling channel and inner diameter of the conductor jacket. The 33% void fraction in the cable space minimizes the free space between strands while minimizing strand deformation. A two-stage cable design was used, based on 1<sup>st</sup> stage triplets that were helically wrapped around the cooling channel to form the 2<sup>nd</sup> cable stage. A solid wall tube was used for the cooling channel. The wall thickness for both cooling channel and jacket were chosen to permit pressurization of the cable space to at least 100 atm, without risk of either cooling channel collapse or jacket rupture.

## 7.4 TWO-LAYER CORC

Figure 5.4 illustrates the two layer CORC envisioned for our high-speed stator. The cable is designed to operate at approximately 50 K in presence a nominal field of field of 0.5 T. Under these conditions, the expected lift factor is approximately 3. Assuming 100 A, 77 K, self-field critical current, a peak operating current of 2.04 kA and fraction of critical current operation of roughly 60%, we will require roughly 12 tapes in all, divided equally into six tapes per layer. To distinguish between layers, the inner layer of REBCO tape is shown in orange, while the outer layer is shown in violet.

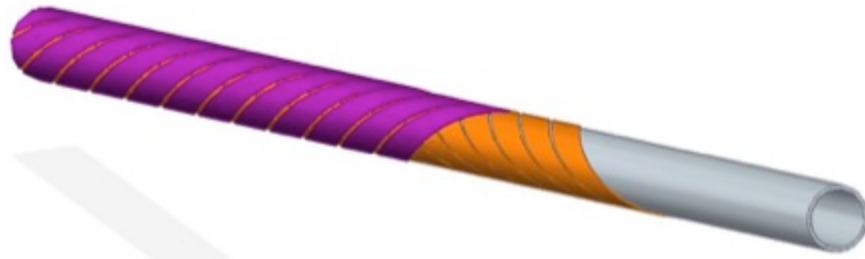


Figure 5.4. Illustration of 2-layer, 12-tape cable-on-round-core conductor for the stator windings.

- Two-layer cable wound on 11 mm OD tube
  - Six tapes in each layer
  - 4 mm wide tape with 0.5 mm gap between tapes
- Straight cable inductances
  - Inductance from axial component of current flow, plus
  - Inductance from azimuthal component of current flow
  - Layer pitch direction changes handedness, increasing coupling between layers
- Time-stepping current calculation using applied voltage and inductance inverse matrix
  - Includes effect of layer self-field in critical current (fit needs updating)
  - Includes effect of layer to terminal resistances
  - Neglects background field and probable shielding current in the layers

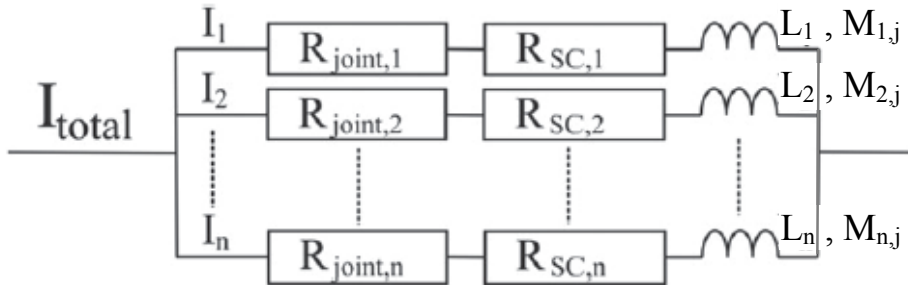


Figure 5.5 Electrical circuit model used for the 2-layer CORC.

$$[M_{i,j}] \left\{ \frac{dI_i}{dt} \right\} = \{V_t - I_i(R_{joint,i} + R_{SC,i})\}.$$

$$\left\{ \frac{\Delta I_i(t_k)}{\Delta t} \right\} = [M_{i,j}]^{-1} \left\{ V_t(t_k) - I_i(t_{k-1}) (R_{joint,i} + R_{SC,i}(t_{k-1})) \right\},$$

$$\{I_i(t_k)\} = \left\{ \sum_{l=0}^k \frac{\Delta I_i(t_l)}{\Delta t} \right\}$$

$$I_{total}(t_k) = \sum_{i=1}^n I_i(t_k)$$

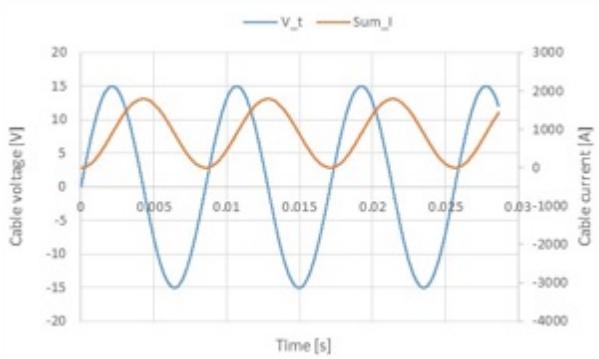


Figure 5.6a. Computed variation in phase current for given inductive input voltage

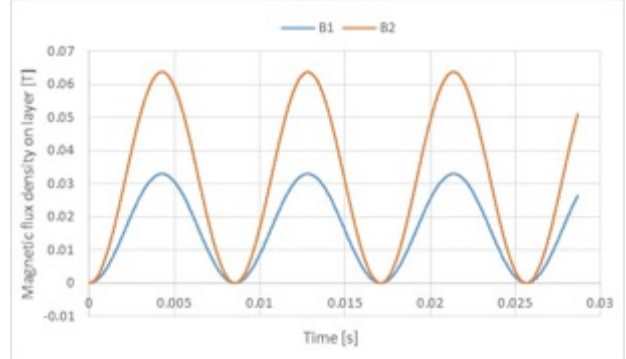


Figure 5.6b. Self-magnetic field is higher on outer conductor layer.

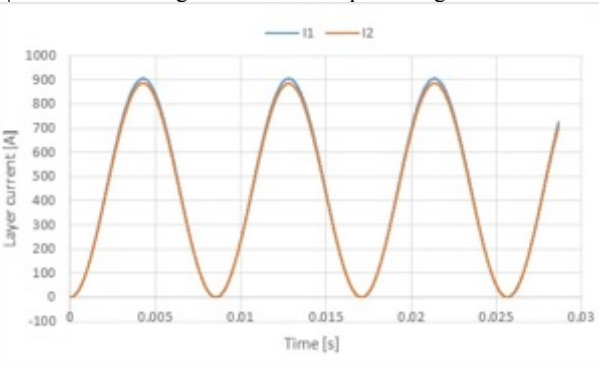


Figure 5.6c. Computed layer currents are equal when phase current is far from computed critical current.

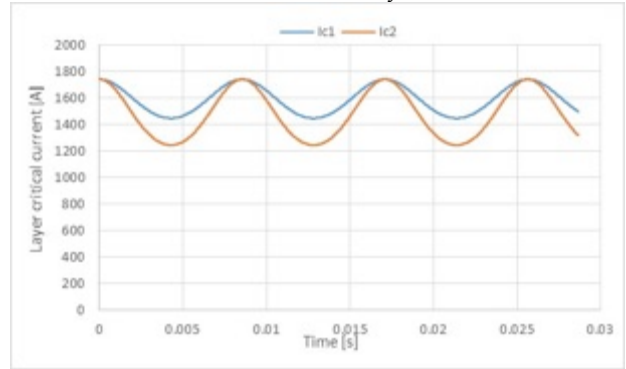


Figure 5.6d. Computed critical current shows larger variation in outer layer due to field effects.

## 7.5 REFERENCES

- [Hoenig] Hoenig, M.O. et al, "Supercritical helium cooled bundle conductors and their applications to large superconducting magnets," Proc. 5<sup>th</sup> Conf. on Magnet Tech., Roma (1975), p. 519.
- [Ciazynski] Ciazynski, D., et. al, "Large Superconducting Conductors and Joints for Fusion Magnets: from Conceptual Design to Test at Full Size Scale.
- [Bessette] Bessette, D, "Design of a Nb3Sn Cable-in-Conduit Conductor to Withstand the 60,000 Electromagnetic Cycles of the ITER Central Solenoid, Applied SC IEEE, Vol. 24(3).
- [Tsuji] Tsuji, H. et al, "Progress of the ITER Central Solenoid Model Coil Program," *Nuc. Fus.* **41** (2001) p. 645-651.
- [Soika] R. Soika, N. Diacenko, T. Elliott, W. Henchel, E. Hill, G. Liang, P. McIntyre, L. Motowidlo, and M. Yavuz, "Fabrication and prototype testing of a strain-tolerant Bi-2212 cable," *IEEE Trans. Appl. Superconductivity* **11** (2001) 2142-2145.
- [Sytnikov] V.E. Sytnikov, V.S. Vysotsky, A.V. Rychagov, A.V. Taran, G. Moritz, M. Kauschke, E. Fischer, S.A. Egorov, I.Y. Rodin, V.E. Korsunsky, L. Bottura, and M.N. Wilson, "Development and test of a miniature novel cable-in-conduit-conductor for use in fast ramping accelerators with superconducting magnets, *IEEE Trans. Appl. Superconductivity* **16** (2006) 1176-1179.
- [Doll] Doll D, Rindfleisch M, Tomsic M, Yue J, Thong C J, and Peng X 2013 The markets that are opening for MgB<sub>2</sub> superconductors and related applications Presentation 1M-WT-I1 at the 11th European Conference on Applied Superconductivity Genova, July 16, 2013
- [Tomsic] Tomsic, M., *personal correspondence*, Oct. 31, 2014.
- [Tixador] Tixador, G., "Fully superconducting generators," chapter H2.3 in *Handbook of Applied*

*Superconductivity Vol. 2: Applications*, B. Seeber, editor, Taylor & Francis, 1998.

[Lienhard] Lienhard, J.H., "Turbulent pipe flow," *section 8.3 in A Heat Transfer Textbook*, Prentice-Hall, Englewood Cliffs, 1981.

[NIST] Lemmon, E.W., Huber, M.L. and McLinden, M.O., *NIST Standard Reference Database 23: Reference Fluid Thermodynamic and Transport Properties-REFPROP*, Version 9.1, National Institute of Standards and Technology, Standard Reference Data Program, Gaithersburg, 2013.

## 8. QUENCH DETECTION AND PROTECTION FOR MgB<sub>2</sub>

Loss power in the MgB<sub>2</sub> cable remains low as long as the cable remains in the superconducting state. Local power dissipation increases considerably if for some reason a portion of the cable were to transition to the normal (resistive) state. This transition might occur, for instance, due to transient disturbance to the conductor cooling system. If the transition to resistive state is quickly detected, control circuitry to block current flow in the stator windings can be activated at the zero current crossing, within a fraction of a line cycle to prevent run away heating of the conductor. Preventing current flow in the stator windings can be achieved rapidly by opening the output power connections from the generator using solid state switches. The main challenge in the electrically noisy stator environment is to reliably detect a growing normal zone in the MgB<sub>2</sub> cable before the local temperature rise threatens cable integrity.

### 8.1 HOT SPOT TEMPERATURE RISE

The MgB<sub>2</sub> stator conductor relies on use of a highly resistive matrix between the superconductor filaments to limit coupling losses during operation. This works to good advantage as long as the conductor remains fully superconducting, but leads to relatively high resistive dissipation in the case that superconductivity is lost.

Figure 6.1 shows a typical cross-section view of an MgB<sub>2</sub> strand manufactured by Hyper Tech Research. The strand contains an approximate filament area fraction of 15%, copper area fraction of 15%, matrix area fraction (the material between filaments) of about 35%, while the outer Monel sheath comprises roughly 35% of the total area fraction. The copper core is used to improve the transient thermal stability of the strands against small disturbances. Typical high resistance matrix materials include the Cu-10Ni and Cu-30Ni alloys. The alloy with lower nickel fraction is slightly easier to draw, while the higher nickel alloy has slightly higher resistivity.

Under adiabatic conditions the temperature rise in the cable following a quench (the unplanned transition from the superconducting to the normal state) depends on the cable composition and the duration of the heating period. That is,

$$\int_0^\tau I_{rms}^2 R_e(T) dt = \int_{T_0}^{T_\tau} m C_{p,e}(T) dT ,$$

where  $I_{rms}$  is the RMS phase current,  $\tau$  is the heating duration,  $R_e(T)$  is the temperature-dependent, effective electrical resistance of the cable,  $m$  is the cable mass,  $C_{p,e}(T)$  is the temperature-dependent, effective heat capacity,  $T_0$  is the initial temperature, and  $T_\tau$  is the temperature of the cable at time  $\tau$ .  $R_e(T)$  and  $C_{p,e}(T)$  are weighted averages of the temperature-dependent properties for the cable constituents. Actually some portion of the heating power dissipated in the cable is transferred to the surrounding coolant and to the cable jacket, so this relation yields a slightly conservative estimate of the temperature vs time behavior of the cable following quench. The use of RMS phase current assumes that the heating duration will extend past several line cycles, for which the use of an average heating power is computationally easier to implement.

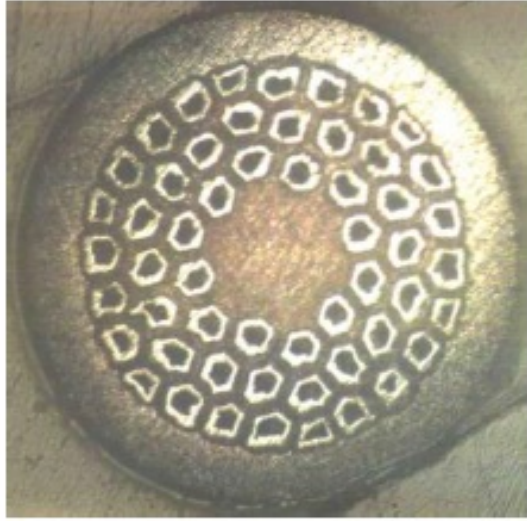


Figure 8.1. Typical cross-section view of an MgB<sub>2</sub> strand. Figure from Hyper Tech Research.

Because the initial length of the normal zone is generally not well known, the resistive heating vs temperature rise relation is typically re-written to minimize geometric dependencies. The effective cable resistance can be determined by adding all component resistances in parallel:

$$\frac{1}{R_e} = \frac{1}{R_{Cu}} + \frac{1}{R_{Monel}} + \frac{1}{R_{Cu-Ni}} + \frac{1}{R_{MgB_2}},$$

where  $R_{Cu}$  is the resistivity of the copper fraction in the cable,  $R_{Monel}$  is the resistivity of the Monel sheaths,  $R_{Cu-Ni}$  is the resistivity of the matrix material, and  $R_{MgB_2}$  is the resistivity of the filaments. The resistivity vs temperature of MgB<sub>2</sub> in the normal state is not well known and will be excluded from further calculations. The resistance of the remaining components (denoted by value “x”) depend on the area fraction of the component,  $\lambda_x$ , the cable area (excluding MgB<sub>2</sub>),  $A_c$ , its temperature dependent resistivity,  $\rho_x(T)$ , and the length of the initial resistive zone,  $l$ . The metallic area in the cable,  $A_c$ , is simply the number of strands in the cable,  $n_s$ , times the metallic area in each strand,  $A_s$ . Expressing the cable resistance in terms of the component properties yields:

$$R_e(T) = \frac{\rho_e(T) l}{A_c} = \frac{(\lambda_{Cu} \rho_{Cu}(T) \lambda_{Monel} \rho_{Monel}(T) \lambda_{Cu-Ni} \rho_{Cu-Ni}(T)) l}{(\lambda_{Monel} \rho_{Monel}(T) \lambda_{Cu-Ni} \rho_{Cu-Ni}(T) + \lambda_{Cu} \rho_{Cu}(T) \lambda_{Cu-Ni} \rho_{Cu-Ni}(T) + \lambda_{Cu} \rho_{Cu}(T) \lambda_{Monel} \rho_{Monel}(T)) A_c}.$$

The effective heat capacity of the cable is determined in similar fashion, where the density of component “x” is denoted  $D_x$  and temperature-dependent heat capacity is denoted,  $C_{p,x}$ .

$$m C_{p,e}(T) = D_e A_c l C_{p,e}(T) = D_{Cu} A_c l C_{p,Cu}(T) + D_{Monel} A_c l C_{p,Monel}(T) + D_{e,Cu-Ni} A_c l C_{p,Cu-Ni}(T).$$

The heating duration vs temperature rise equation can be rearranged to include all temperature-dependent properties inside the integral on the right hand side of the equation and then simplified to minimize the geometric dependencies as follows:

$$\int_0^\tau I_{rms}^2 dt = \int_{T_o}^{T_\tau} \frac{D_e A_c l C_{p,e}(T)}{\rho_e(T) l} dT.$$

$$\int_0^\tau \frac{I_{rms}^2}{A_c^2} dt = \int_0^\tau j_{rms}^2 dt = \int_{T_o}^{T_\tau} \frac{D_e C_{p,e}(T)}{\rho_e(T)} dT.$$

The final version of the equation relates the average current density in the metallic portion of the cable to measurable physical properties, to determine the rate of temperature rise in the cable following quench, until current flow in the cable is interrupted at time  $\tau$ .

Figure 8.2a shows the time-dependent variation in heat capacity for the metallic portions of the cable used for the calculations [6.1 - 6.5], while Figure 8.2b shows the time-dependent variation in electrical resistivity [Hampton, Copper, NIST, OTER, Kaye]. Table 8.1 summarizes the cable parameters for the MgB<sub>2</sub> CIC stator conductor shown in Figure 5.1b, for which the temperature rise vs time calculations were performed.

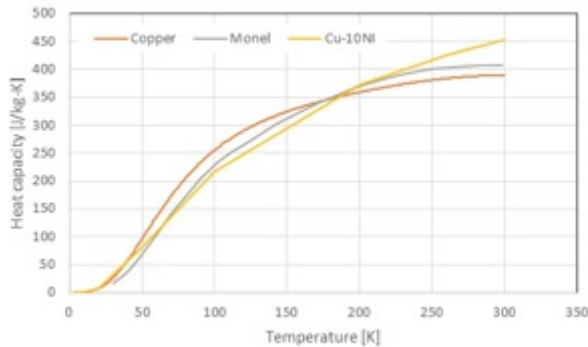


Figure 8.2a Heat capacity vs. temperature for cable constituents.

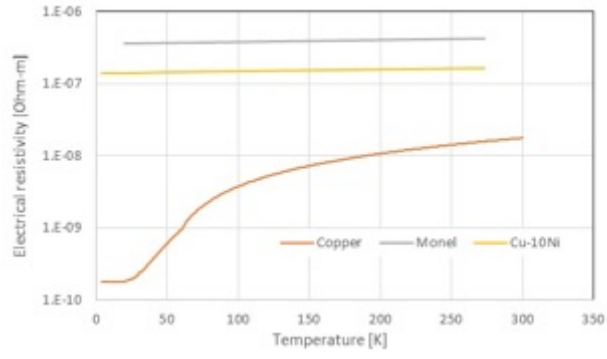


Figure 8.2b Electrical resistivity vs. temperature for cable constituents.

Table 8.1: Cable parameters used for the temperature vs time calculations.

RMS phase current [A]	1441
Strand diameter [mm]	0.35
Numbers of strands in cable	51
Total metallic area in cable, $A_c$ [m <sup>2</sup> ]	4.2x10 <sup>-6</sup>
RMS current density, $j_{rms}$ [A/m <sup>2</sup> ]	3.5x10 <sup>8</sup>
Area fraction of copper in metallic cable area, $\lambda_{Cu}$	17.6%
Area fraction of Monel in metallic cable area, $\lambda_{Monel}$	41.2%
Area fraction of Cu-Ni in metallic cable area, $\lambda_{Cu-Ni}$	41.2%
Density of copper, $D_{Cu}$ [kg/m <sup>3</sup> ]	8920
Density of Monel, $D_{Monel}$ [kg/m <sup>3</sup> ]	8800
Density of Cu-Ni, $D_{Cu-Ni}$ [kg/m <sup>3</sup> ]	8900

Figure 8.3 shows the computed temperature rise vs elapsed time following initiation of a normal zone in the MgB<sub>2</sub> cable. The maximum allowed temperature in the cable depends on several factors, but

most typically it is limited to below 200~300 K based on concerns over mechanical damage due to differential thermal expansion of the conductor relative to its surroundings. Figure 8.3 indicates that these peak temperature occurs for the MgB<sub>2</sub> CIC conductor within roughly 0.17s to 0.22s of a quench event.

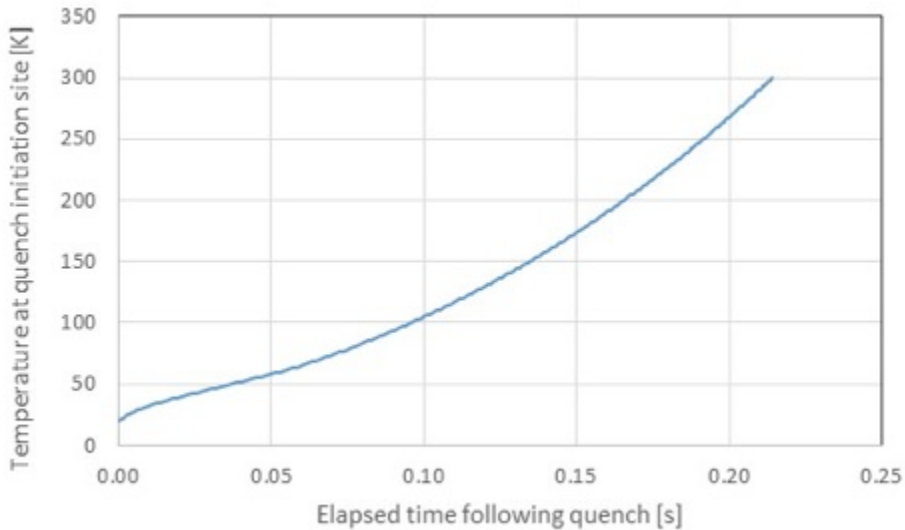


Figure 6.3. Temperature at quench initiation location vs. elapsed time following the quench.

## 8.2 ADDED COPPER STRANDS

The ability to detect a quench in an electrically noisy environment depends in part on how quickly the normal zone grows. The resistive voltage drop needs to increase rapidly enough so that it can be unambiguously detected above the level of background noise in the quench detection signal before the conductor is damaged by excessive temperature increase at the quench initiation location. A commonly used method to limit the temperature rise in a conductor following quench is to increase its copper fraction. Figure 8.2b shows that the electrical resistivity for pure copper is several orders of magnitude below that for either the Monel sheath or Cu-Ni matrix material, while Figure 8.2a shows that the heat capacities for all three materials are nearly the same. That is, significant increase in the copper fraction in the MgB<sub>2</sub> CIC can significantly reduce the rate of temperature rise at the hot spot. Rather than alter the MgB<sub>2</sub> strand configuration, which is already optimized for reliable strand manufacture, the increase in copper fraction in the cable is most commonly achieved by adding pure copper strands to the cable pattern. To limit coupling losses in the cable which might result from the addition of pure copper, the strands are typically coated with a highly resistive material like nickel plate to limit current transfer between strands during routine operation.

Table 8.2 summarized the increase in copper area fraction resulting from the addition of 23 pure copper strands (with 0.35mm diameter) to the cable layout shown in Figure 7.2 and described in table 7.1, while Figure 8.4 shows the effect of the added copper strands on the computed temperature rise vs elapsed time following a cable quench. The time to reach 200K to 300K has increased to slightly over 1s, which should allow sufficient time to reliably detect a stator winding quench before any damage is done. The added copper strand reduce heat generation in the cable by both reducing the effective cable resistance, and by reducing the overall cable current density.

Table 8.2: Change in cable copper fraction following addition of 23 pure copper strands

RMS phase current [A]	1441
Strand diameter [mm]	0.35
Numbers of MgB <sub>2</sub> composite strands in cable	51
Number of pure copper strands in cable	23
Metallic area in original cable, $A_c$ [m <sup>2</sup> ]	4.2x10 <sup>-6</sup>
Metallic area in cable with added copper strands, [m <sup>2</sup> ]	6.4x10 <sup>-6</sup>
RMS current density in cable with copper strands [A/m <sup>2</sup> ]	2.3x10 <sup>8</sup>
Area fraction of copper in metallic cable area, $\lambda_{Cu}$	46.2%
Area fraction of Monel in metallic cable area, $\lambda_{Monel}$	26.9%
Area fraction of Cu-Ni in metallic cable area, $\lambda_{Cu-Ni}$	26.9%

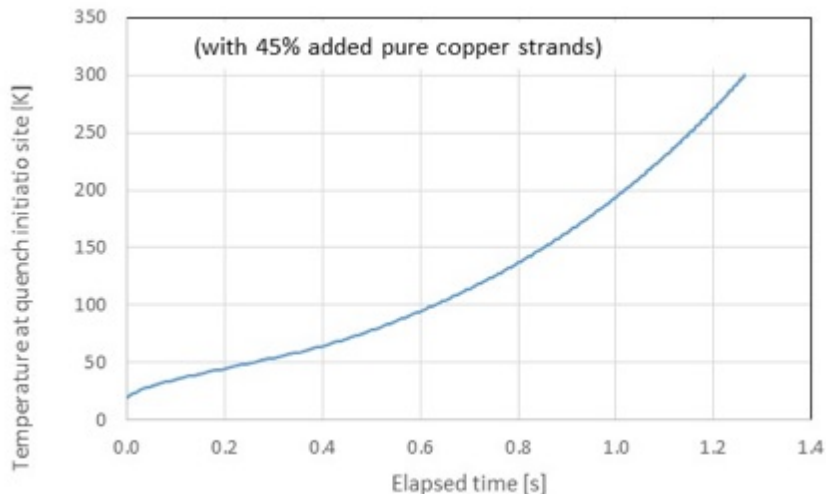


Figure 8.4. Temperature at quench initiation location vs. elapsed time following the quench for an MgB<sub>2</sub> cable with added pure copper strands.

### 8.3 SOLID CRYOGEN STABILIZED MgB<sub>2</sub> CABLE

We have examined the possible use of a solid cryogen installed within the MgB<sub>2</sub> cable space as a means to reduce the radial temperature gradient across the cable, to provide localized heat capacity (as a means to reduce the likelihood of quench), and to help reduce the rate of temperature rise at the quench initiation site in the unlikely event that the conductor could quench. The center channel in the dual channel CIC would of course remain clear to facilitate the circulation of cryogen coolant through the stator winding. In addition to its thermal properties, a solid cryogen filler can also help to mechanically stabilize the strands in the MgB<sub>2</sub> CIC by freezing them in place as the cryogen solidifies. We considered several options for the solid cryogen, such as nitrogen, hydrocarbons and other chlorofluorocarbons (CFCs) that have a range of melting temperatures and volumetric expansions (from solid at operating temperature to fixed volume at room temperature). We have examined implications for the quench protection and conductor stability, enhanced through direct contact with the solid cryogen, which has high heat capacity and thermal conductivity (compared with helium gas). Depending on the cryogen, the stator could be filled initially either with liquid at atmospheric conditions or a gas at high pressure (~100 atm). After cooldown, the cryogen in the cable space will be

solid, essentially locking the strands, preventing strand motion and degradation due to mechanical deformation while providing enhanced thermal capacity for stability and protection.

### 8.3.1 THERMAL MODEL DURING STEADY OPERATION

Figure 8.5 shows a simple 2D thermal model used to calculate the thermal behavior of this  $MgB_2$  cable. The heat transfer coefficient to the inner cold helium gas stream was calculated by the FLUENT analysis discussed in Section 5 and is equal to  $3580 \text{ W/m}^2\text{-K}$ , whereas the outside of the cable is assumed to be insulated due to the vacuum environment.

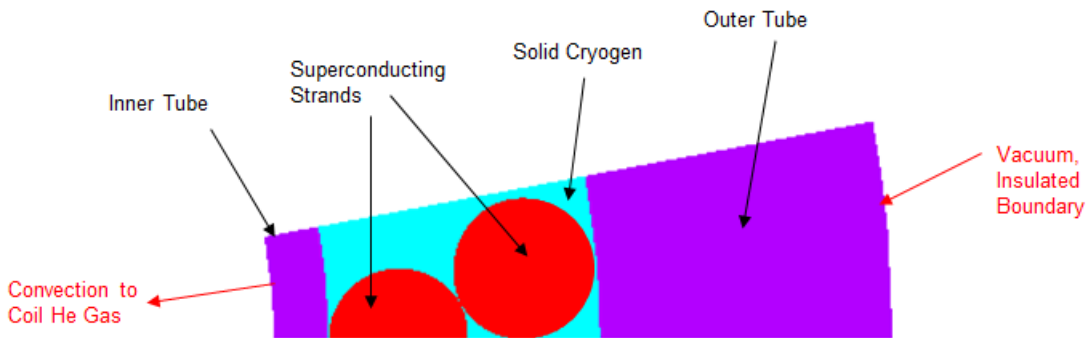


Figure 8.5. Simple model of solid-nitrogen filled cable-in-conduit cable (CICC).

We performed a simple steady-state analysis to determine the radial temperature distribution in the cable taking into account only the AC loss heat load on the conductor. Assuming a thermal conductivity of  $\sim 1 \text{ W/m-K}$  for a typical solid cryogen [Konstantinov], this model predicts a temperature rise of  $0.4 \text{ K}$  across the cable space as shown in Figure 6.6a. This indicates that the heat transfer to the cold helium gas on the inside of the cable, along with the thermal conductivity of  $\sim 1 \text{ W/m-K}$ , is sufficient to maintain an acceptable radial temperature rise of  $< 0.5 \text{ K}$  across the cable under AC loss heating.

In contrast, for the conventional case where the annular space is filled with stagnant cold helium gas with a thermal conductivity of only  $\sim 25 \text{ mW/m-K}$  [Lemmon], the temperature rise shown in Figure 6.6b becomes  $1.1 \text{ K}$ , which is high for an  $MgB_2$  cable at this nominal operating temperature, especially when the  $3 \text{ K}$  temperature rise along the conductor length is taken into account. Therefore, for this design, it is desirable to fill the annular space with a either a solid cryogen or some material with suitably high thermal conductivity. For multi-stage cables with larger radial build, the effect of solid cryogen to reduce the radial temperature gradient will be even more pronounced.

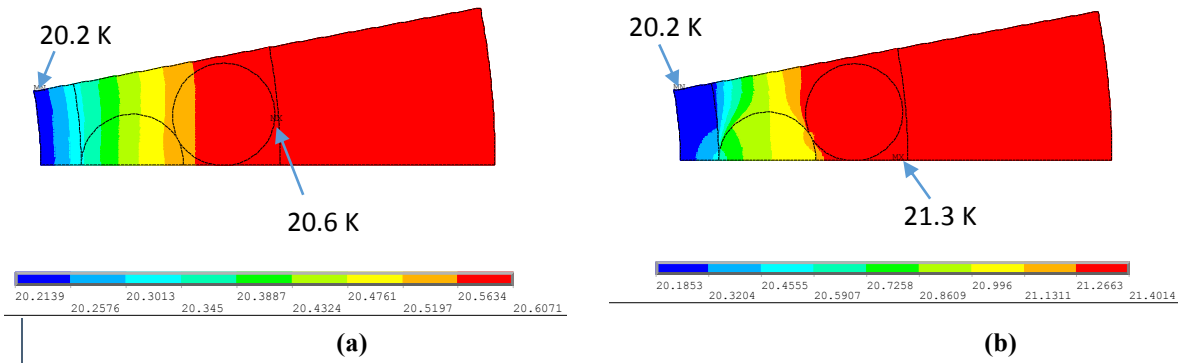


Figure 8.6. Temperature distribution (K) due to AC loss heating: (a) solid cryogen; (b) stagnant

helium gas. Scale ranges from 20.2 K (blue) to 20.6 K (red in figure a) or 21.3 K (red in figure b).

There are also 3D effects that affect the temperature as the strands are wound helically, and axial/helical heat transfer can introduce an enhanced radial heat transfer in the cable space. The ratio of the axial heat flow along the strand (from the point of contact with the jacket to the point of contact with the cooling channel) to the radial heat flow across the cable space,  $q_a/q_r$ , can be shown to be given approximately by:

$$q_a/q_r \sim 2 \Delta r^2/p^2 f (1-f) k_{solid}/k_{gas}$$

where  $\Delta r$  is the radial extent of the strand space,  $p$  is the pitch of the strands and  $k_{gas}$  and  $k_{solid}$  are the axial and radial thermal conductivities, and  $f$  is the solid fraction in the cable space. For the properties with helium gas filling, assuming a 20 mm pitch length for the strands, the ratio between the axial and radial heat flows is about 0.1. Thus, we can neglect the axial/helical heat transfer, and consider only the contribution to radial heat flow in the cable space.

### 8.3.2 TRANSIENT ANALYSIS

Next, the transient quench behavior of this cable was analyzed. The enthalpies for various select cryogens are plotted as a function of temperature in Figure 6.7 [Younglove], and a summary of some of the pertinent cryogenic data for these cryogens is provided in Table 6.3.

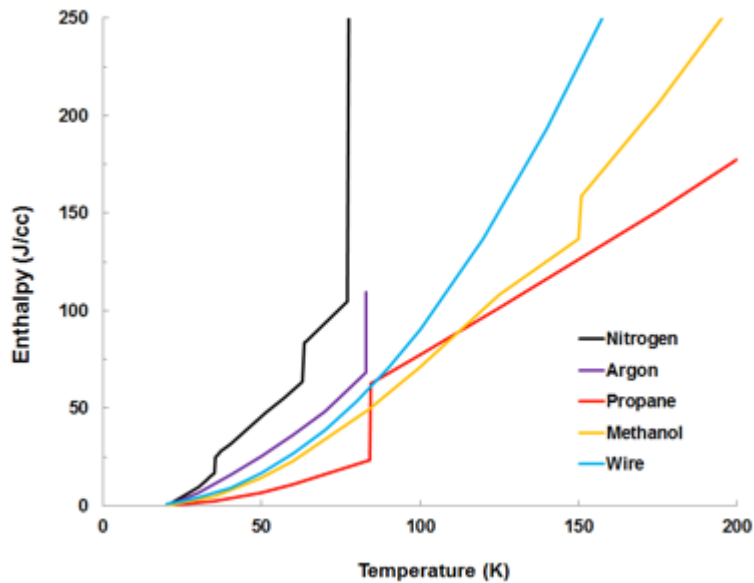


Figure 8.7. Enthalpy curves for several select solid cryogens vs temperature

During quench, the current in each strand is transferred from the  $MgB_2$  filaments to the copper stabilizer which comprises ~15% of the strand cross-sectional area. The objective of this analysis was to determine the time at which cryogen vaporization started to occur. Once vaporization occurs, there would be a corresponding localized pressure rise which could damage the cable by either rupturing the jacket or buckling the cooling channel; therefore, the goal is to determine the time before vaporization occurs, in order to avoid this condition.

Table 8.3. Data for selected cryogens.

Cryogen	Density @ 20 K [g/cc]	Thermal conductivity @ 20 K [W/m-K]	Melting point @ 1 atm [K]	Heat of Fusion [J/cc]	Boiling point @ 1 atm [K]	Density @ 298 K [g/cc]	Porosity @ 20 K [%]
Argon (Ar)	1.71 (solid)	1.8 <sup>a</sup> ~3 <sup>a</sup> (- slope)	83.8	41	87.2	0.17 (gas @ 100 atm)	90
Helium gas (He)	0.015 (@ 6.5 atm)	0.032 <sup>b</sup> (+ slope)	n.a.	n.a.	4.2	0.015 (gas @ 100 atm)	n.a.
Nitrogen (N <sub>2</sub> )	1.02 (solid)	0.4 <sup>c</sup> (- slope)	63.1	20	77.4	0.11 (gas @ 100 atm)	89
Methanol (CH <sub>3</sub> OH)	1.03 (solid)	0.12 <sup>d</sup> (+ slope)	151	10	337	0.79 (liquid @ 1 atm)	23
Propane (C <sub>3</sub> H <sub>8</sub> )	0.73 (solid)	1~1.5 <sup>e</sup> (- slope)	84.5	39	231	0.49 (liquid @ 10 atm)	30

The results of the transient thermal analysis are provided in Figure 8.8. These results take into account the increase in copper stabilizer resistivity, which increases the Joule heating, as the temperature increases. The results show only marginal improvement in time response for using argon or nitrogen, as opposed to methanol or propane. Also, both methanol or propane have much higher vaporization temperatures; therefore, the overall response time is  $\sim 3$  times longer, since the allowable final temperature can be higher.

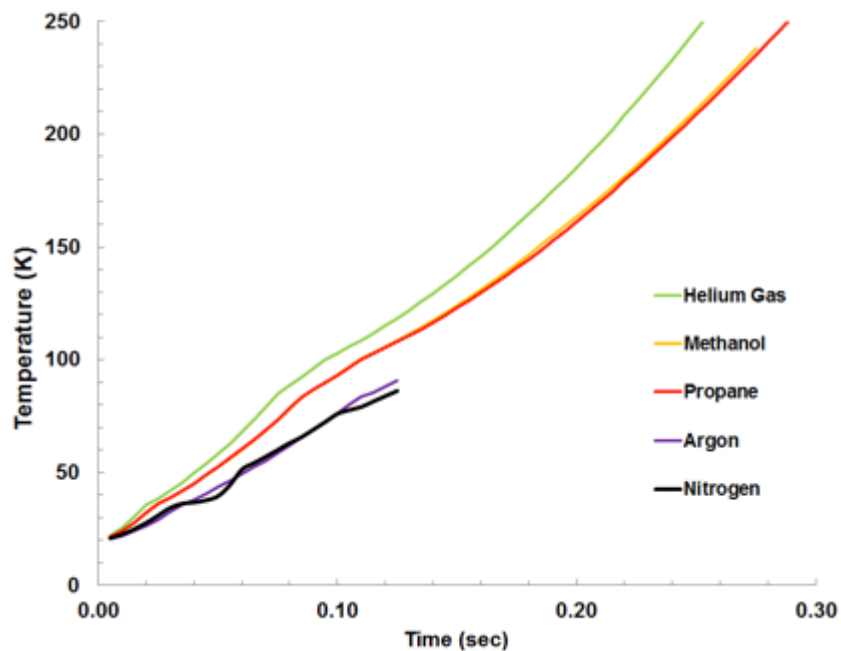


Figure 8.8. Temperature rise vs. time following quench with the cable filled with various solid cryogens.

The ideal condition, namely to use a fully dense solid cryogen is unlikely to be achieved in practice due to safety concerns, as the cryogen would need to be continually supplied during cooldown. A

safer procedure is to fill the system initially, seal it off and then cool the conductor to its 20 K operating temperature.

Nitrogen is a gas at atmospheric pressure; therefore, if nitrogen is used as the solid cyogen it would be necessary to fill the cable with high pressure nitrogen gas, in an effort to maximize the initial mass of nitrogen in the cable space. If the cable were filled with 100 atm nitrogen gas, upon cooldown to 20 K, the resulting solid nitrogen will have a porosity of > 80%. This significantly reduces the effectiveness of nitrogen; however, the overall effect on the thermal response is small (~10%) due to the relatively large heat capacity of the wires.

Conversely, if either propane or methanol were used, the system could be initially filled with liquid at atmospheric pressure in the case of methanol, or about 8-10 bar in the case of propane. Upon cooldown to 20 K, the resulting solid has a porosity of only ~25%, in which case the effect of porosity on thermal response is negligible

Assuming either propane or methanol were used, the following cooldown procedure could be used:

1. Fill stator winding with selected liquid or gas.
2. Start cooldown with cold nitrogen gas flowing through the cooling channel until reaching ~100 K,
3. Start circulating cold helium gas through system until reaching 20 K.

#### 8.3.4 CONCLUSIONS

The use of solid cryogens to improve both the thermal and mechanical stability of a cable-in-conduit cable used in the MgB<sub>2</sub> stator windings of a superconducting generator has been investigated. We have investigated nitrogen, argon, propane and methanol. Due to their higher vaporization temperature and reduced densification, and therefore lower porosity, upon cooldown to the 20 K operating temperature, either propane or methanol are preferable over nitrogen or argon.

The thermal conductivity of the solid cryogen is about 1 order of magnitude higher than gaseous helium at 20 K. Thus, it is substantially more effective at removing the power from the strands, useful in applications where there is substantial heating, such as in AC applications.

## 8.4 QUENCH DETECTION USING CO-WOUND VOLTAGE TAP IN MGB2 CICC

The most commonly used method to detect a quench in a superconducting coil is to monitor the coil voltage looking for change in the resistive component. Bridge cancellation and other techniques are used to cancel the much stronger inductive voltage components due to changing coil currents. For our stator coils the peak phase current is on order of 2kA. Sinusoidal current variation at the designed 117 Hz operating frequency yields peak current variation on order of 1.5 MA/s, resulting in pronounced inductive variation within the stator winding, which is generally out of phase with voltage pick-up due to variation in magnetic flux imposed by the rotor. Similarly, assuming roughly 0.5T peak external field on the stator conductor yields a peak field change rate on order of 370 T/s. Current transfer among strands in a cabled conductor is relatively poor, especially when the cable uses strands with inherently high electrical resistivity. Consequence, the voltage seen by external quench detection wires can vary depending on mounting location; under certain conditions this variability can lead to significant delay in the time required to reliably detect a growing normal zone in the coil, especially when several external voltage sense wires are used in a balanced bridge configuration.

A particularly sensitive technique to cancel the inductive signals in cabled conductors was developed

in the magnetic fusion community to address these concerns [Martovetsky]. The technique relies on a signal wire that is co-wound within a cabled conductor as illustrated in Figure 6.5a. The wire follow the same nominal trajectory as the average cable strand, resulting in effective cancellation of the inductive voltage component. One end of the sense wire is connected to a coil terminal at one end of the magnet, while the other is connected through a voltage meter to the terminal at the other end of the magnet. Any difference between the co-wound signal wire voltage (L2) and the magnet terminal voltage (L1) is attributed to the existence of a normal zone in the magnet. Figure 6.5b shows a possible implementation of this scheme for our MgB<sub>2</sub> CIC stator conductor using an oxide insulated coaxial conductor as the co-wound sense wire.

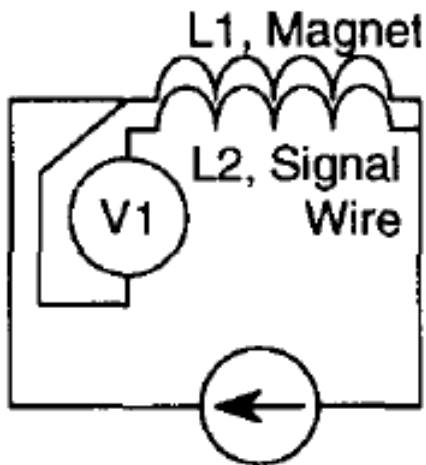


Figure 8.5a. Schematic illustration of a quench sense wire co-wound inside a cabled superconductor.

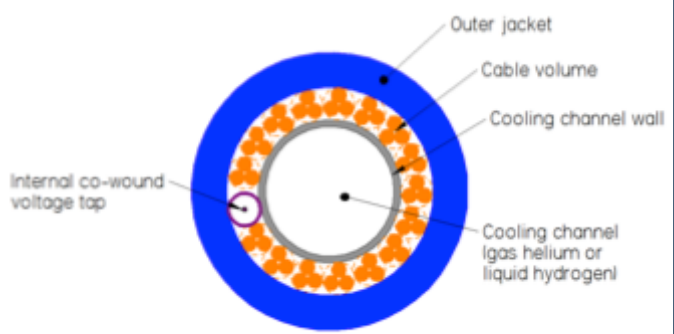


Figure 8.5b. Sketch of our MgB<sub>2</sub> cable-in-conduit conductor with an oxide insulated coaxial conductor embedded in the cable.

Despite their improved noise rejection compared to balanced bridge quench detectors, it is not possible to completely eliminate all residual inductive voltages from the co-wound wire signal. The two largest sources of residual inductive voltage imbalance in the co-wound quench detector are: a slight offset between the induced voltages on the sense wire and cable strands due to axial current flow in the cable and variations in the transverse magnetic field along the length of the conductor in the stator slots.

#### 8.4.1 AXIAL CURRENT EFFECT

Figure 6.6 shows the cross-section geometry used to estimate the residual inductive voltage in the co-wound quench detector due to axial current flow in the cable. The core for the co-wound wire is located at the mid-radius of the annual cable space,  $r_m$ , while the strands in the adjacent triplets spiral between contact with the inner radius of the cable space,  $r_i$ , and contact with the outer radius of the cable space,  $r_o$ .

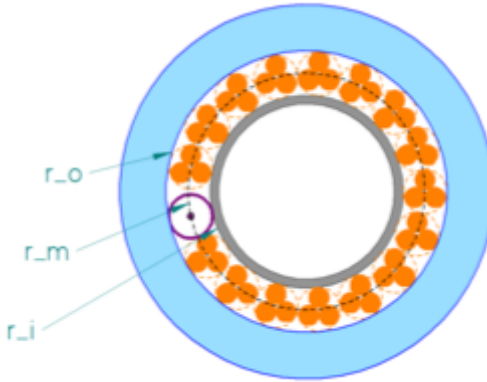


Figure 8.6. Geometry used to determine residual inductive voltage in sense wire due to axial current flow in the cable.

The axial current density is not uniform across the annual cable space; it varies from approximately zero at  $r_i$ , to a maximum value near  $r_m$ , to near zero again at  $r_o$ . For simplicity we used a cosine distribution to estimate the current density variation across the cable space,  $j(r)$ , at peak cable operating current,  $I_{pk}$ .

$$j(r) = j_{pk} \cos\left(\frac{\pi(r - r_m)}{2\delta r}\right), \text{ where } \delta r = \frac{(r_o - r_i)}{2}.$$

$$I_{pk} = \int_0^{2\pi} \int_{r_m - \delta r}^{r_m + \delta r} j(r) r dr d\theta.$$

For this assumed current density distribution, the maximum value of the induced voltage at the core of the co-wound wire,  $V_{cww}$ , is given by:

$$V_{cww} = \int_{r_i}^{r_m} \frac{\mu_o (2\pi f) I(r) L}{2\pi r} dr, \text{ with } I(r) = \int_0^{2\pi} \int_{r_i}^r j_{pk} \cos\left(\frac{\pi(r - r_m)}{2\delta r}\right) r dr d\theta,$$

where  $2\pi f I(r)$  is the maximum rate of change of current at within radius  $r$ , and  $L$  is the total conductor length in the stator winding.

By comparison, the average voltage drop along the centerline of each cable strands,  $V_{str}$ , is given by:

$$V_{str} = \frac{1}{L} \int_0^L \int_{r_i}^{r_m + (\delta r - r_s) \cos\left(\frac{2\pi n \pi}{L}\right)} \frac{\mu_o (2\pi f) I(r)}{2\pi r} dr dz,$$

where  $r_s$  is the strand radius, and  $n$  an assumed integral number of 1<sup>st</sup> stage twist pitches along the cable length. The value of  $n$  does not affect the result as long as it is an integer value. Finally, the peak residual voltage measured by the quench detector due to axial current flow in the cable,  $V_{QD,a}$ , is the difference between the strand voltage and the co-wound wire,  $V_{QD,a} = V_{str} - V_{cww}$ . For the strand and cable values listed in Table 8.3  $V_{QD,a}$  equals 30 mV.

Table 8.3. Values used to calculate residual inductive voltage in the co-wound wire quench detector due to axial current flow.

Peak cable current [A]	2040
Electrical frequency, $f$ [Hz]	117
Inner radius of cable space, $r_i$ [mm]	3.3
Mean radius of cable space, $r_m$ [mm]	4.05
Outer radius of cable space, $r_o$ [mm]	4.8

Strand diameter/radius, $d_s / r_s$ [mm]	0.35 / 0.175
2 <sup>nd</sup> stage cable twist pitch length, $p$ [mm]	300
Length of conductor in stator winding, $L$ [m]	15

#### 8.4.2 TRANSVERSE FIELD EFFECT

Figure 8.7 illustrated the trajectory of the core of the co-wound wire (CWW) as it spirals along the length of the MgB<sub>2</sub> CIC. The trajectory of the CWW is shown in red, while the centerline of the conductor is shown in dashed orange line. The dashed black lines respectively show the side walls for the central cooling channel and the conductor jacket.

In homogeneous magnetic field, the magnetic flux captured between the CWW and the conductor centerline on one side of the centerline is equal to that on the other. However, for most engineering applications, the transverse magnetic field varies across the width of the conductor. In Figure 8.7, we assume that the magnetic field above the centerline,  $B_+$ , is slightly greater than the nominal field value, while that below the centerline,  $B_-$ , is slightly less than the nominal value. In time varying magnetic field, the variation in field across the width of the conductor produces a residual inductance,  $V_{QD,t}$ , due to the transverse field variation. Both the cable strands and the co-wound wire are exposed to the same spatially varying magnetic field, however, because of the much tighter twist pitch for the first stage cable triples, the average electric field in the strands is slightly different than that for the core of the co-wound wire.

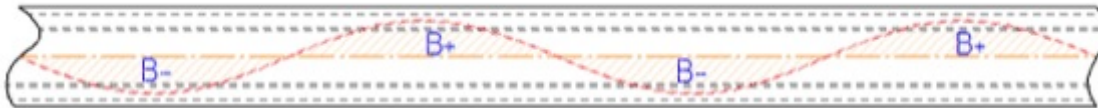


Figure 8.7. Illustration of the CWW trajectory along the length of the MgB<sub>2</sub> CIC.

For sake of simplicity, let's assume that  $B_+ = (1 + f_v) B_n$ , and  $B_- = (1 - f_v) B_n$ , where  $f_v$  is the fractional variation in seen by the co-wound fire and the average cable strand, and  $B_n$  is the average transverse magnetic field. In this case the residual quench detector voltage due to the transverse field variation can be estimated as:

$$V_{QD,t} = n \left[ \int_0^{L/2n} (1 + f_v) (2 \pi f) B_n r_m \sin \left( \frac{2 \pi n x}{L} \right) dx + \int_{L/2n}^{L/n} (1 - f_v) (2 \pi f) B_n r_m \sin \left( \frac{2 \pi n x}{L} \right) dx \right],$$

where  $n$  is equal to the integral number of twist pitch lengths of the CWW,  $p$ , divided by the conductor length,  $L$ . For an average transverse field on the conductor of  $B_n = 0.5$ T, the cable parameters listed in Table 8.3, and a fractional variation of magnetic field across the width of the conductor of  $f_v = +/-1\%$ , the residual inductive voltage due to the transverse field variation is  $V_{QD,t} = 75$ mV.

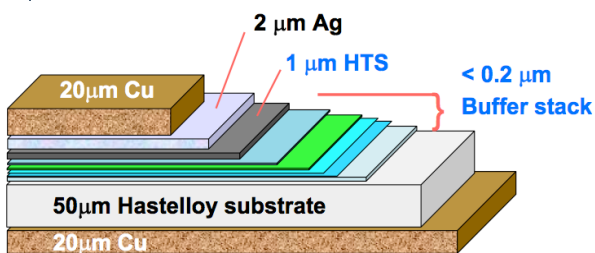
#### 8.5 YBCO-BASED THERMAL SENSOR

We have developed a quench sensor concept that uses the superconductor as the sensor. We are in the process of working with MIT's Technology Licensing Office to write up a disclosure to be turned into a patent application.

Figure 8.8 shows a copper coated HTS tape from Superpower, as well as a schematic of a stripline. In the case of the HTS tapes, if the side ends are as shown in the Figure 8(a), there is a dielectric region or “buffer stack” consisting of several oxide layers (used for alignment of the crystals in the HTS tape deposited on top). These oxides (ceria, magnesia) are insulators, and thus there is a thin dielectric (~

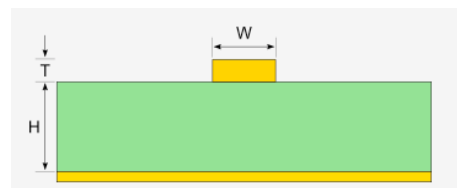
100 nm) between the conducting hastelloy (serving as ground plane in the HTS-based stripline) and the superconductor. Similarly, on the right in Figure 8(b), the stripline also has a dielectric between the top conductor and the “ground” on the opposite side. When the superconductor becomes normal, its resistivity is high and the current prefers to flow through the silver. In this case, the distance between the silver and the hastelloy increases by between 5 and 10 times, changing the impedance of the stripline. The change in impedance results in a reflected signal that can be detected with extremely low RF energy. The presence of a reflected signal (before the end of the tape) can be used to detect the quench and also the location of the quench.

## HTS coated conductor



(a)

## Stripline



(b)

Fig. 8.8. HTS coated conductor (a) Superpower's tape topology with Cu coating, (b) conventional stripline.

We have calculated the impedance of the stripline, both when superconducting and normal. Assuming that the superconductor thickness is 2 microns and the dielectric is 0.2 microns (assuming a dielectric constant for the dielectric of 10), with a tape that is 2 mm wide, the impedance of the stripline changes by an order of magnitude, from 0.0149 Ohms to 0.142 Ohms. The voltage reflection coefficient is given by:

$$\Gamma_{12} = \frac{Z_2 - Z_1}{Z_2 + Z_1}$$

where  $\Gamma_{12}$  is the reflection coefficient, and  $Z_1$  and  $Z_2$  are the impedances from the two media (in our case, the superconducting and normal regions). Because of the large differential in impedance between the normal and the superconducting regions, a substantial fraction of the signal is reflected to the source. The return signal can be used to determine the quench. It is interesting to note that there is signal that remains in the forward direction. Quenches further downstream could also be measured, although with lower sensitivity.

The time of the reflection can be used to determine the location. The time of propagation (pulse delay) of the signal in a stripline is given approximately by:

$$t_{pd}(\text{ns/ft}) = 1.017 \sqrt{0.475 \epsilon_r + 0.67}$$

where  $\epsilon_r$  is the dielectric constant of the media. The pulse delay is given above as nanosecond per foot of stripline. For the dielectric constant that we expect ( $\sim 10$ ), the delay is about 2.4 nanoseconds per

foot, or about twice that of free-space propagation. If the quench occurs 100 m into the cable, the delay is about 0.75 microseconds, resulting in a round-trip of about 1.5 microseconds. Because of the fast response multiple scans can be performed to assure that indeed there is a superconducting-to-normal transition, before initiating the active protection.

It is possible to use a network analyzer in frequency domain to implement a time delay approach. In addition, because of the quick response, it would be possible to use a single RF-quench sensor with multiple quench probes (i.e., striplines). And it may also be possible to place the RF-quench circuit in the cryogenic environment.

One advantage of the proposed approach is that it is not necessary for the normal zone in the superconducting cable to propagate. Propagation is needed in conventional voltage tap sensors in order to increase the resistance (and thus the observed voltage). Normal zone propagation can be small when using HTS material, especially when operating at intermediate temperature. A second advantage is the insensitivity to electrical noise, similar to fiber optic sensors.

### 8.5.1 STRIPLINE QUENCH DETECTOR

We have obtained two 20 m lengths of edge etched HTS tapes. The tapes had an HTS deposit that did not extend to the edges, with the insulating buffer layer intact. Thus, the superconductor and the silver coating are electrical insulated from the substrate. Figure 8.9 show the schematic of the tapes.

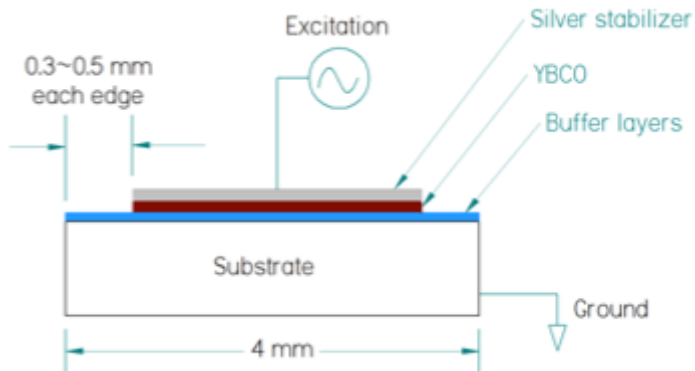


Figure 8.9 Uncoated HTS tapes with HTS and silver removed from the edges.

We have preliminarily used RF stripline reflectometry (using a network analyzer, in frequency domain). Figure 8.10 shows the setup. We coupled the cables from the network analyzer to the HTS tape and separately the ground to the substrate. We realized that there would be substantial impedance discontinuities that would give a large reflection signal. Indeed, this is what happened in the experiment. Figure 8.11 shows the signal from the network analyzer. In the test, strong reflection occur independent of the location of a short. Moving the short results in small changes to the received signal. The tests were carried out at room temperature. One problem is that the YBCO layer may be strongly absorbing at room temperature, where the tests were carried out. We will be testing the setup at lower temperatures after the end of program.

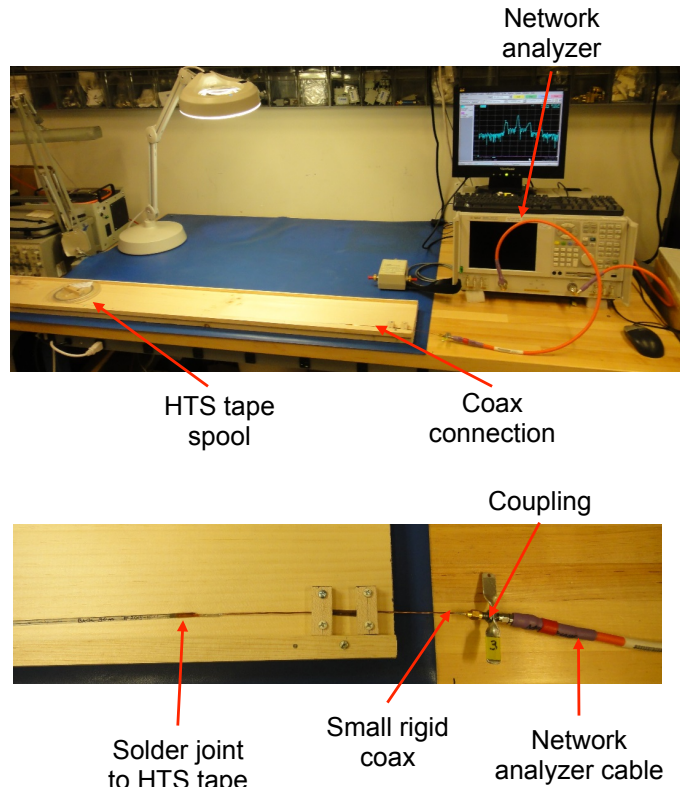
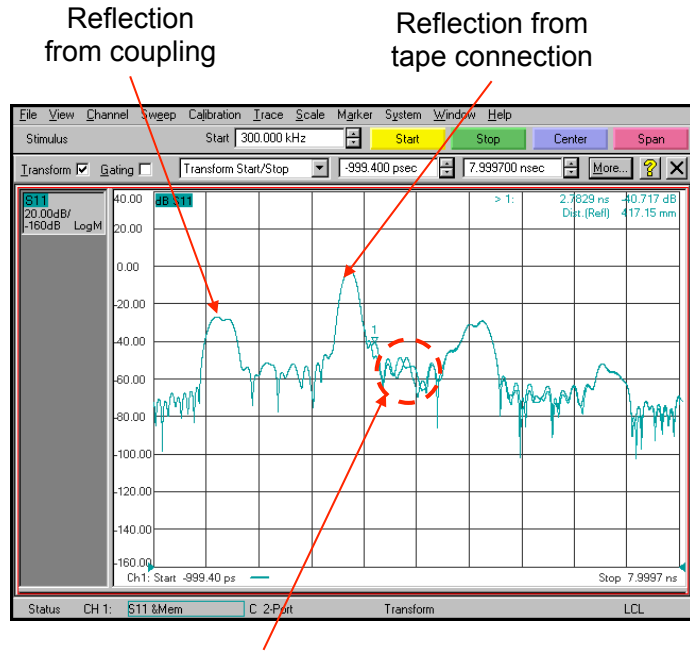


Figure 8.10 Setup of the test, including details of the coupling from the network analyzer to the HTS tape.

We will be doing a test of the method in the next one or two quarters. Thus, in the next quarterly reporting we could describe the model and the way to start to model the concept.

We will continue evaluating the concept, as we feel that quench protection and sensing is an enabling technology required for most applications of HTS. We are looking at means to improve the coupling by between matching the coax to the HTS tape. We will use high frequency transformer, among other options.



Change in reflection pattern when sliding short changed from 0.04 m to 0.1 m.

Figure 8.11 Time domain signal of setup, when there is short at 0.04 m and at 0.1 m

## 8.6 INDIRECT COOLING WITH GASEOUS HELIUM

Improved gas to gas heat exchangers can provide significant advantages for a range of applications. When the heat exchange involves gases, heat transfer is low requiring large surface area and consequently bulky heat exchangers. The design with YBCO in section 2.6.4 (Figure 2.36). Metallic foams have been proposed recently as better components for heat exchangers but present designs for their employment have substantial limitations for use in gas to gas heat exchangers. Although metallic foams have excellent performance for exchanging thermal energy between the gas and the foam (due to large surface-to-volume, and high surface heat transfer coefficient due to the small scale of the cross-elements in the foam), they have particularly low thermal conductivity. For a material with 92% porosity, the thermal conductivity is about 1/11 that of the full dense material. And because of tortuosity (tortuosity is defined as a meandering path the heat needs to take through a porous medium) of the connections the thermal conductivity decreases again by another factor of 1/3. Thus, the thermal conductivity of the material is about 1/35 that of the base metal. Substantial temperature gradients occur in the material, unless other material is used to help in the heat transfer. Thus, for proper design, the foam cannot be too thick or too far from the surface across which the heat transfers between the two heat exchanging substances (e.g. between two gases). Metallic foam heat exchangers have been discussed for removing heat in applications that do not involve gas-to –gas heat exchange. These heat exchangers are not optimized for heat transfer. Huang et al. describes a metallic foam with a heat transferring device to distribute the heat into the metallic foam. Once the thermal energy is in the foam it can be efficiently removed by the gas stream (air). The heat transferring device can be a rounded heat pipe, a loop-type heat pipe, a pulsating heat pipe, or a solid element made of thermally conductive metals. Meng et al. describe a similar approach as Huang, but the heat

transferring device is a heat pipe. Multiple holes for the heat pipes, as well as various heat pipe cross sections are described.

Mornet et al. [Mornet]describes a heat exchanger device, in which a metallic foam is used to cool a metallic element, but outside of the application in a heat exchanger. Similarly, . Ozmat describes the use of a metallic foam in contact with an electronic device, for cooling the electronic device. He does not describe a gas-to-gas heat exchanger.

The use of foams in heat exchangers is described by Kang [Kang]. It is assumed that the heat is conducted exclusively by the metallic foam, with no solid material to aid in heat transfer across the metallic foams. Kienbock et al. also describe another embodiment of a heat exchanger with porous foam. They use the porous foam only in one of their channels. They use the “high thermal conductivity” of the foam to distribute the heat through the channel.

We explored means of designing and constructing heat exchanger designs that make substantially improved use of metallic foams for gas to gas heat exchangers. These designs also improve capability for applications where the metallic foams are used for applications other than gas-to-gas heat exchange, for example, for cooling of solids.

In this section we highlight our work on the construction of heat exchangers using fins and foams.

First, we document preliminary work on the use of foams that are attached to fins with adhesives.

Secondly, we describe work on the manufacturing of foams with the use of electroforming. Finally, we describe work at MIT and elsewhere on the manufacturing of heat exchangers through the use of 3D printing.

### 8.6.1 FOAMS

There are multiple means of manufacturing the open cell structures that are used in the proposed heat exchanger. We have preferred the use of foams that are manufactured in large planar sheets. These sheets are 1 cm thick and about 0.7 m by 0.7 m in area, are inexpensively acquired commercially, in several materials.

### 8.6.2 ADHESIVE

In principle, it is possible to make the heat exchanger by applying adhesives between the foams and the fins. We have worked both with ceramic adhesives for high temperature applications, as well as with epoxies, for low temperatures.

We have designed and tested cryogenic heat exchangers that use foams-on-fins, shown in Figure 8.12. A combination of foams on fins results in an optimum choice, where the fins conduct the heat away from the highly temperature sensitive superconductor and distribute it on the foam. We have implemented cryogenic heat exchangers optimized for operation at 65 K and at 20 K. Foam-on-fins heat exchangers were used for cooling current leads for a superconducting power distribution systems. [Dietz]

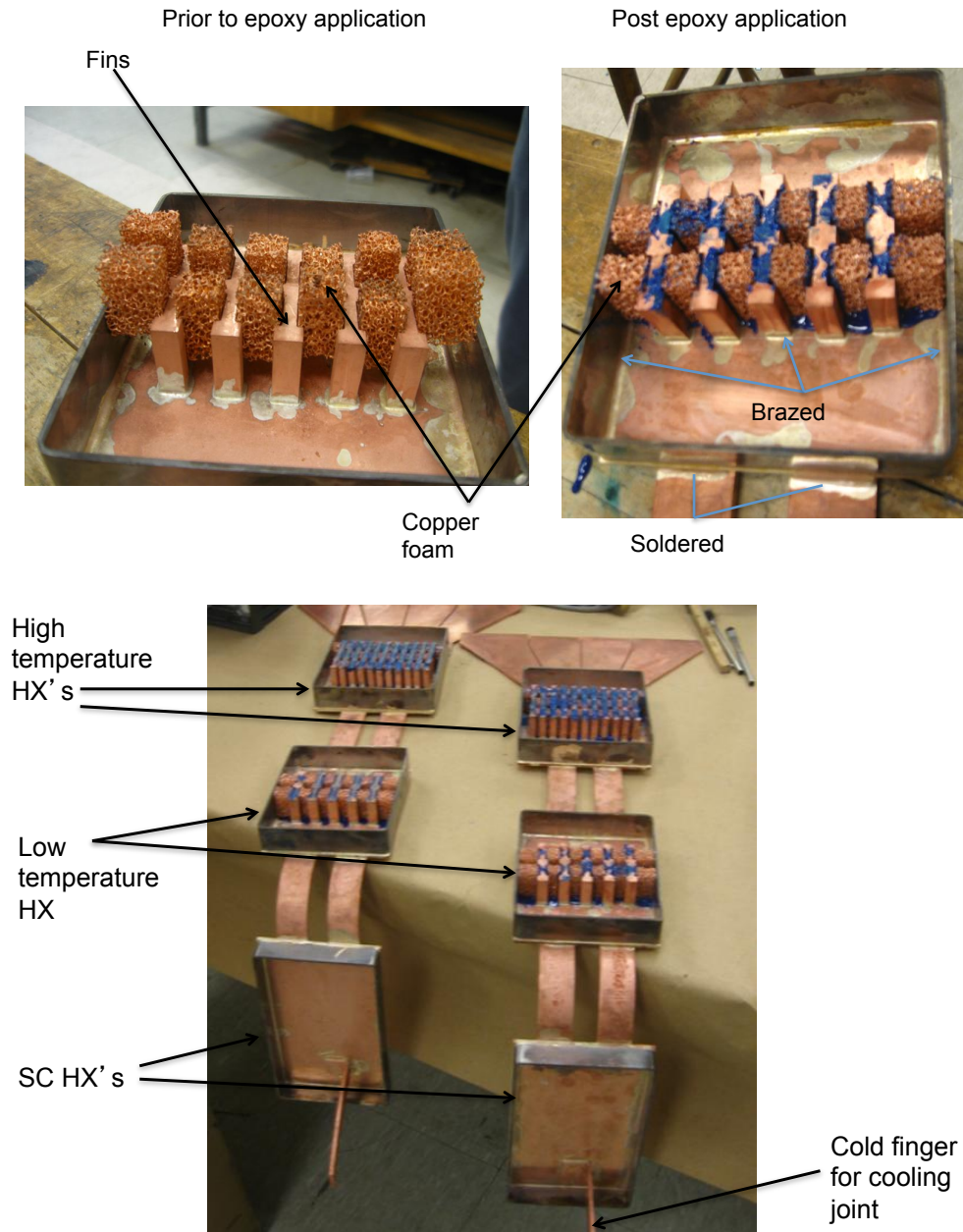


Figure 8.12. Cryogenic heat exchanger using fins-on-foams. Exchanger is made from copper, and the foams are adhered to the fins using Stycast epoxy (a low temperature epoxy).

#### Ceramic adhesives

We have used two types of ceramic adhesives, for applications at higher temperatures. The first one is CeramaBond, from Aremco. The material filler is MgO, and it should bond well between ceramic and metal, and metal to metal. Its main use is for heated, induction coils, and sensors. However, the problem with these adhesives is debonding, due to thermal stress that arises from differential thermal expansion coefficients, and from vibrations.

Table 1. Properties of ceramabond adhesive

		571
<b>Tradename</b>	Ceramabond™	
<b>Major Constituent</b>	MgO	
<b>Color</b>	Off-White	
<b>No. Components</b>	2	
<b>Viscosity, cP</b>	20,000 - 90,000 <sup>④</sup>	
<b>Specific Gravity, g/cc</b>	1.90 - 2.20	
<b>Temperature Limit, °F (°C)</b>	3200 (1760)	
<b>CTE, in/in/°F x 10<sup>-6</sup> (°C)</b>	7.0 (12.6)	
<b>Handling</b>	<b>Mix Ratio, powder:liquid</b>	1.0:1.0 - 1.5:1.0
	<b>Thinner</b>	571-T
	<b>Solvent</b>	Water
	<b>Application Temperature, °F</b>	50-90
	<b>Storage Temperature, °F</b>	40-90
	<b>Shelf Life, Months</b>	6
<b>Curing</b>	<b>Air Set, Hours</b>	1-4
	<b>Heat Cure, °F, Hrs</b>	200,2
	<b>Dielectric Strength, volts/mil @ RT (@ 1000 °F)</b>	91
	<b>Torque Strength, ft-lbs <sup>①</sup></b>	22
	<b>Moisture Resistance <sup>②</sup></b>	Excellent
	<b>Alkali Resistance <sup>②</sup></b>	Good
	<b>Acid Resistance <sup>②</sup></b>	Fair

**Footnotes**

① Tested using a torque wrench after bonding a pre-ox

② Properties were evaluated after curing at 700 °F for

③ Graphi-Bond™ 551-RN is also offered in a two-part, shipments of 1 gallon or more.

④ Graphi-Bond™ 551-RN also demonstrates a lap-shear

⑤ Ceramabond™ 571 ranges for viscosity and specific

1-to-1 to 1.5-to-1.

The material, CeramaBond 571, is preferred when used with aluminum, brass, copper, Inconel, nickel, steels (including stainless 400-series) and titanium.

We have made a few samples which look promising, but yet have to build a substantial unit. An alternative ceramic bonding that we have attempted to use is Durabond 950, from Cotronics. This aluminum-based material is useable to 1200 F (650 C). Its properties are described in Table 2. The compression strength is about 30 MPa, a thermal expansion of about  $18 \times 10^{-5}$ , and a thermal conductivity of 6 W/ m K .

Table 2. Properties of Durabond adhesives.

<b>DURABOND</b>	<b>950</b>
<b>Use Temp °F</b>	<b>1200</b>
Base	Aluminum
Color	Grey
Density (# / ft <sup>3</sup> )	120
Thermal Expansion (10 <sup>-6</sup> /°F)	10
Pot Life (Hours)	2
Cure (@ R.T.)	24
Bond Strength at 200°F (psi)	500
Bond Strength at 1200°F (psi)	1000
Components	2
Mixed Ratio (A / B)	100/60

### 8.6.3 ELECTROCHEMICALLY ATTACHING FOAMS TO FINS

An alternative to the adhesives/epoxies, is to mechanically/thermally attach the manufactured foams to the fins using an electrochemically process. It is clear that the foams shielding of the potential in the bulk of large foams, but near the surface, it is possible to add material, inexpensively, using electrodeposition.

The process is illustrated in Figure 8.13. The foams are placed in a mandrel, in this case, steel. In the real situation, the material of the mandrel would be copper, and that will be for the fins. The foams are then filled with wax, to prevent the electrolyte from penetrating in the foam. For larger application, as the electric potential would be shielded by the foam, this would not have not be used. The mandrel and the wax filled foams are then submerged in an electrolyte, and copper is deposited in the surface.

Finally, most of the wax is removed by heating and the remaining wax in the foam was oxidized (i.e., combusted). These forms were made by AJ Tuck and Co.

We have implemented the approach in the configuration illustrated in Figure 8.14 with only 6 blocks. In the implementation, the mandrel is made from aluminum. After the sheet of copper was electrodeposited on the surface, the steel and the was are removed from the component. Figure 8.15 shows a photograph of the finished component. The foam was well attached to the plate. Although the process proved successful, it was a complicated process.

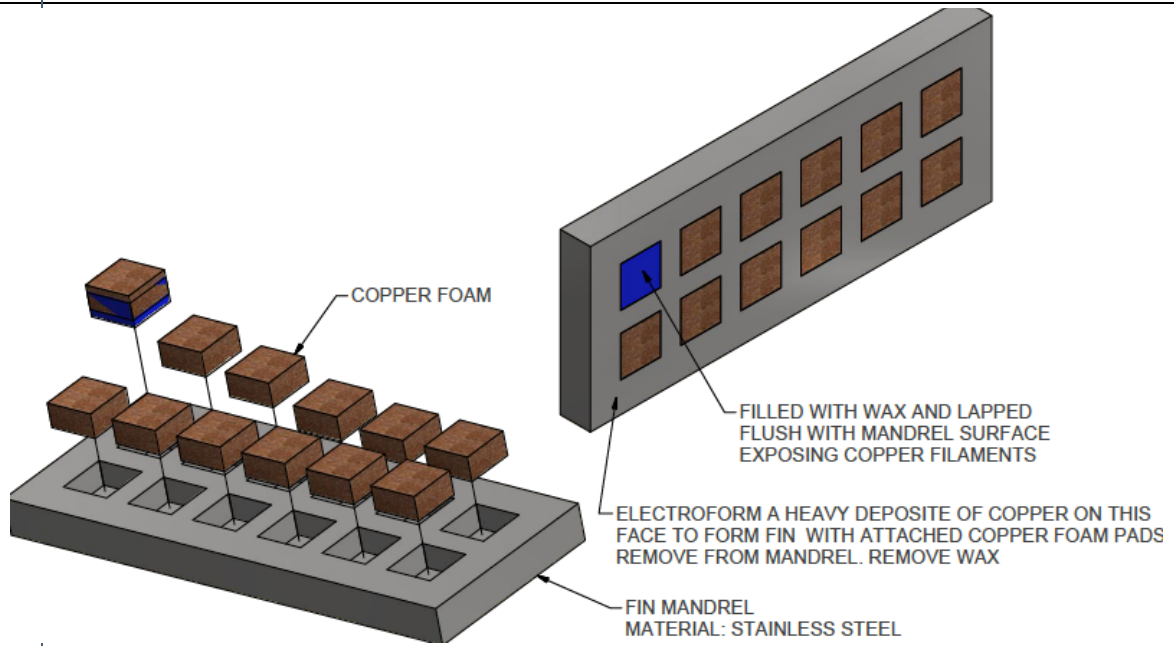


Figure 8.13. Process used to build a solid interface on the copper foam. Making of the element to be used in the electrodeposition of copper.

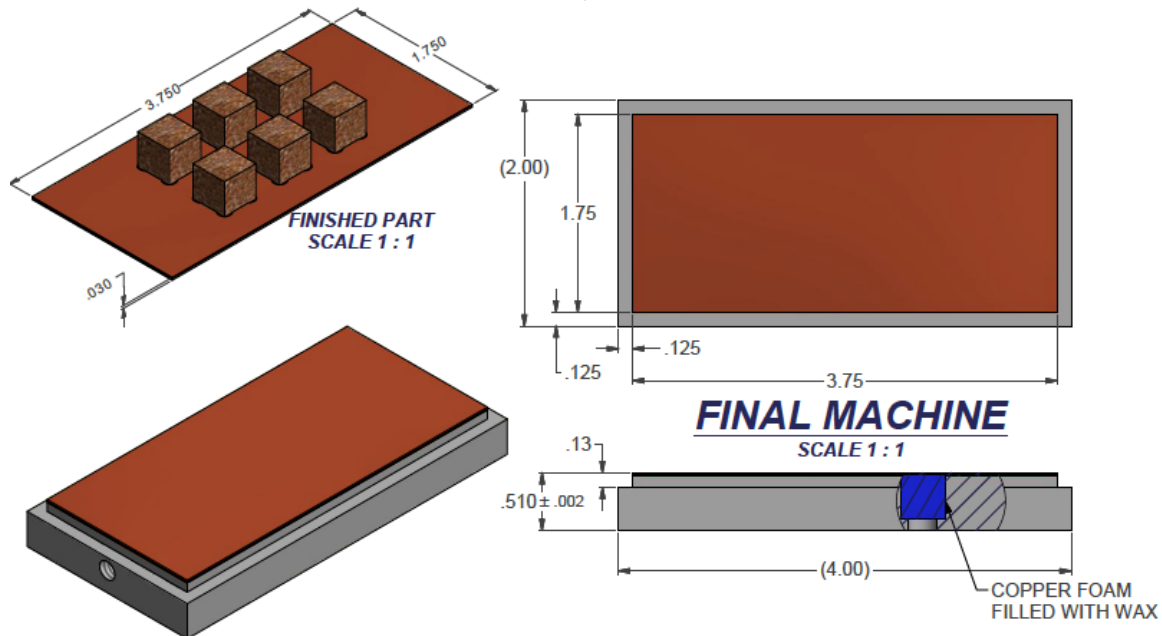


Figure 8.14. Process used to build a solid interface on the copper foam. A sheet of copper is electrodeposited on the elements.

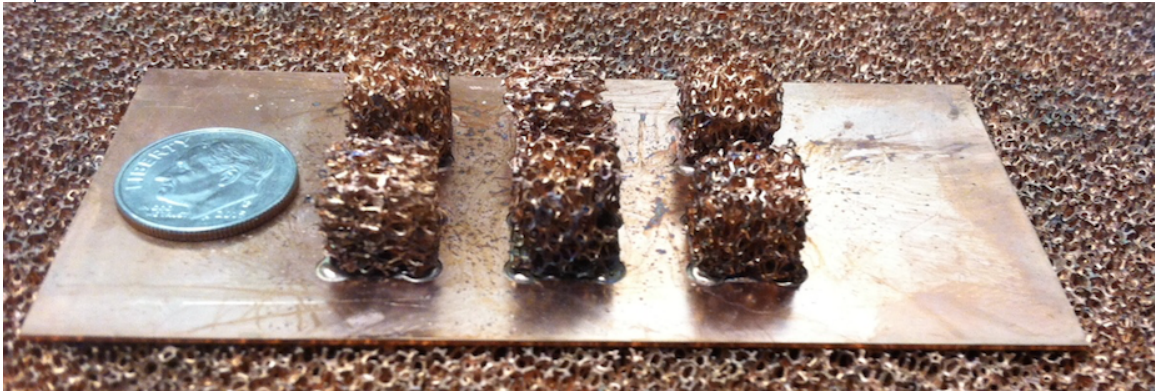


Figure 8.15. Photograph of the foams component, with the foams solidly connected to the electrodeposited copper plate.

#### 8.6.4 3D PRINTING OF HEAT EXCHANGERS AND FOAMS

Traditionally, foams are created by processes that lead to a highly non-uniform structure with significant dispersion in size, shape, thickness, connectedness and topology of its constituent cells [see, for example, Gaillard]. For the open cell structures discussed above, there is a particular pattern that approximately repeats. For the foams made from the lost-material process, the patterns are stochastic. In addition, some of the elements/struts in the foam are not very efficient for conducting the heat from the interface to the solid. Ideally, long elements from the surface would be ideal, preventing the formation of laminar layers, while avoiding the tortuosity described above, which decreases the thermal conductivity, in the direction of interest, by about a third.

Then the question is whether it would be possible to make a element that optimized the geometry. We believe that 3D printing is a very attractive option, and is described next.

We have recently demonstrated the feasibility of 3D printing of uniform foam structures in inexpensive 3D printers. We have printed 3D structures that are regular, and have rods that are perpendicular to each other. This may not be the most optimal solution, as some of the rods provide for heat transfer to the gas but do not participate in heat conduction away from the fin. Both the fins and the foam have been built using the technology. At the present, we have been limited to plastic-type material, but there is no reason why the technology can not be carried to metals and even ceramics.

Figure 8.16 and 8.17 shows drawings of the structures that we intended to build. We have used an XYZ 3D printer, with ABS as the printing material. Figure 8.16 shows an entire HX module, while Figure 8.17 shows a section, consisting of half-fins, and a region with a porous fill. 20 of these modules are used in the cross sectional area. It is our intent to make them relatively small, and then combine them axially to make a full unit.

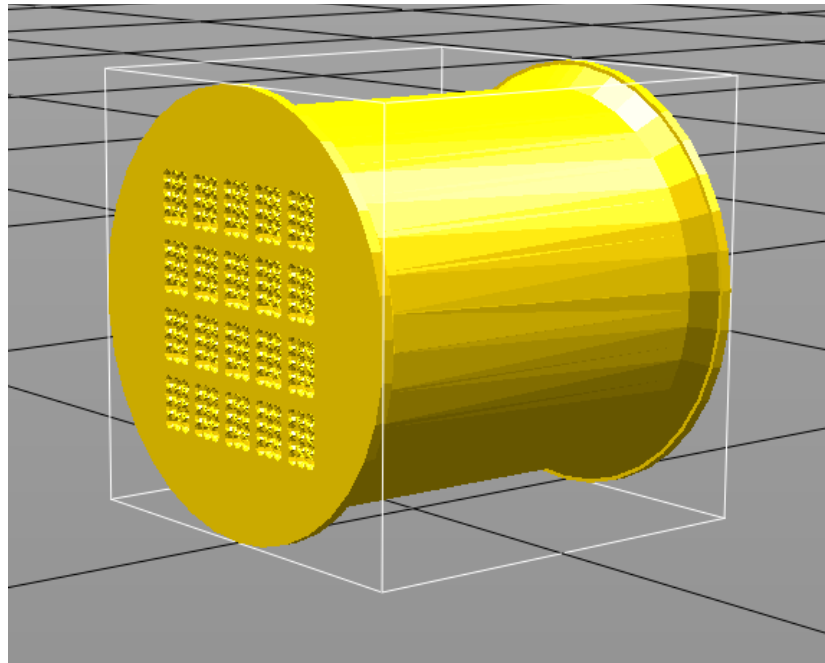


Figure 8.16. Heat exchanger design module, for 3-D printing.

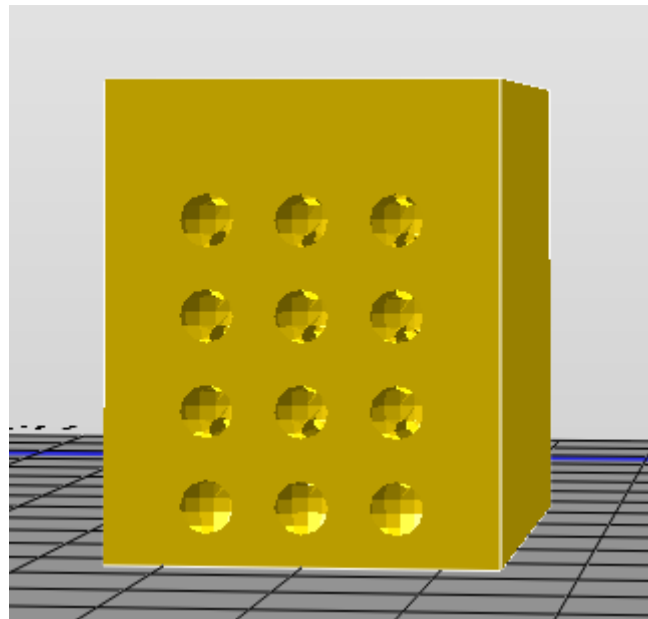


Figure 8.17. Section to be built with 3D printers.

The products, shown in Figure 8.18 with the XYZ da-Vinci printer, were disappointing, in that the fill in the porous section was poor, for the non-scaled design. The features of the rods where lost, and the material collapsed, as shown in Figure 8.18, the small yellow sample. Note that the horizontal struts are collapsed. The green small copies in Figure 8.18 have been cut to show the interior of the HX. We were able to make a better unit with this printer, by scaling up the dimensions (shown to the right of the coin in Figure 8.19). In this case, the results were adequate.

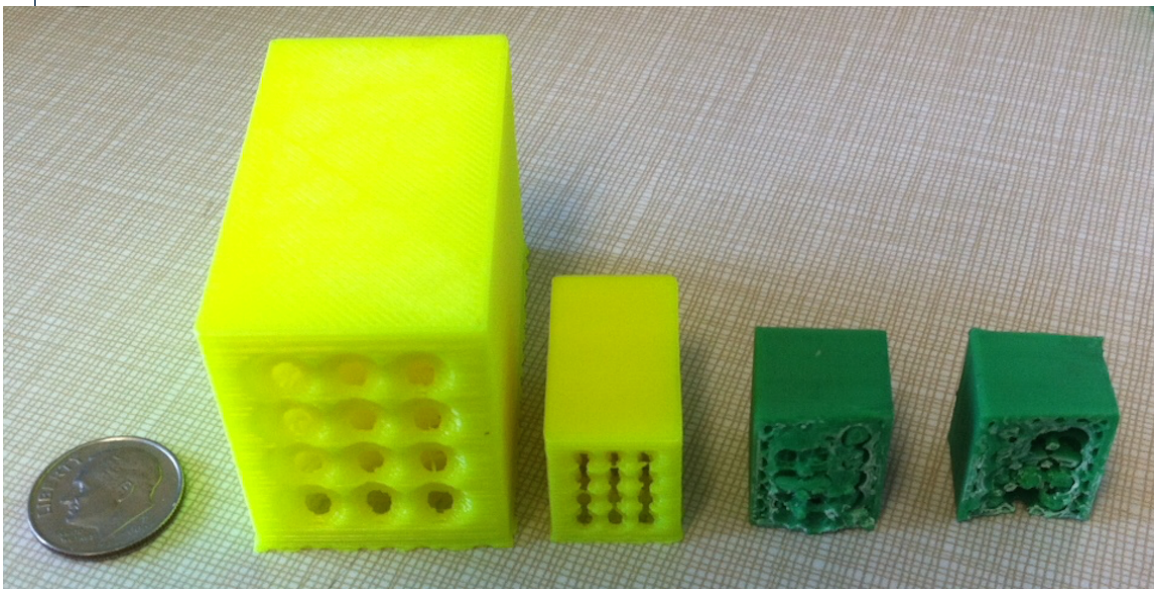


Figure 8.18. Photographs o the HXs made with the XYZ printer.

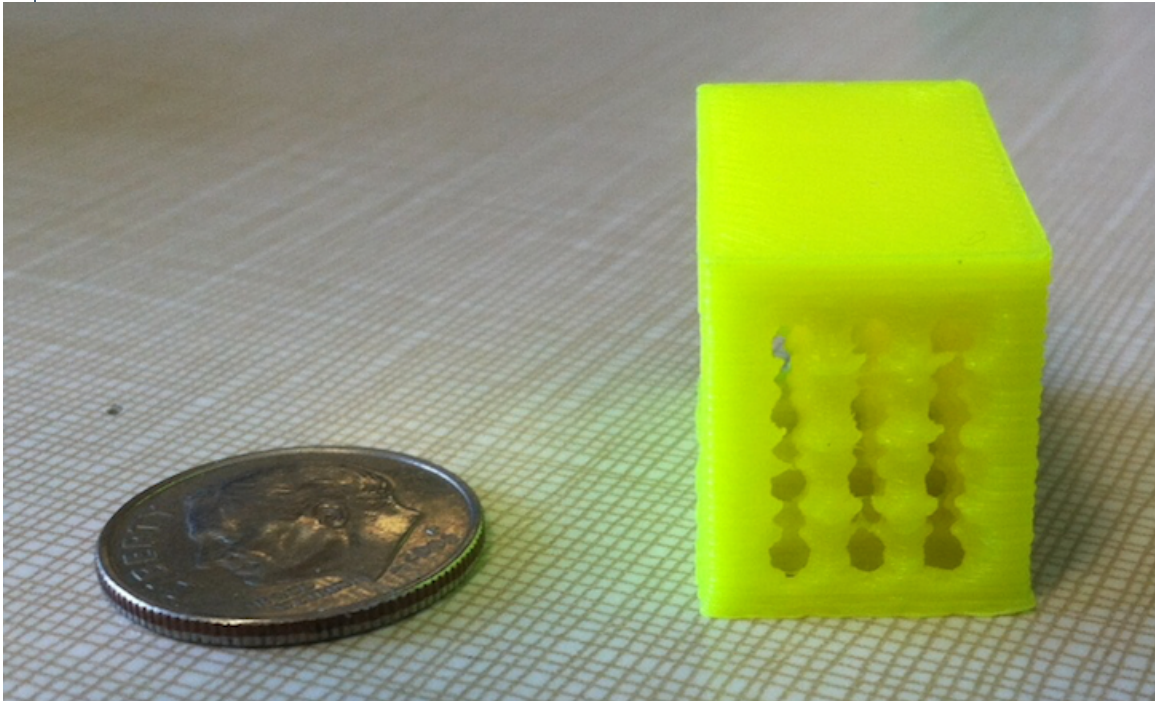


Figure 8.19. Larger figure of the right-scale of the HX. Note that the horizontal struts are missing.

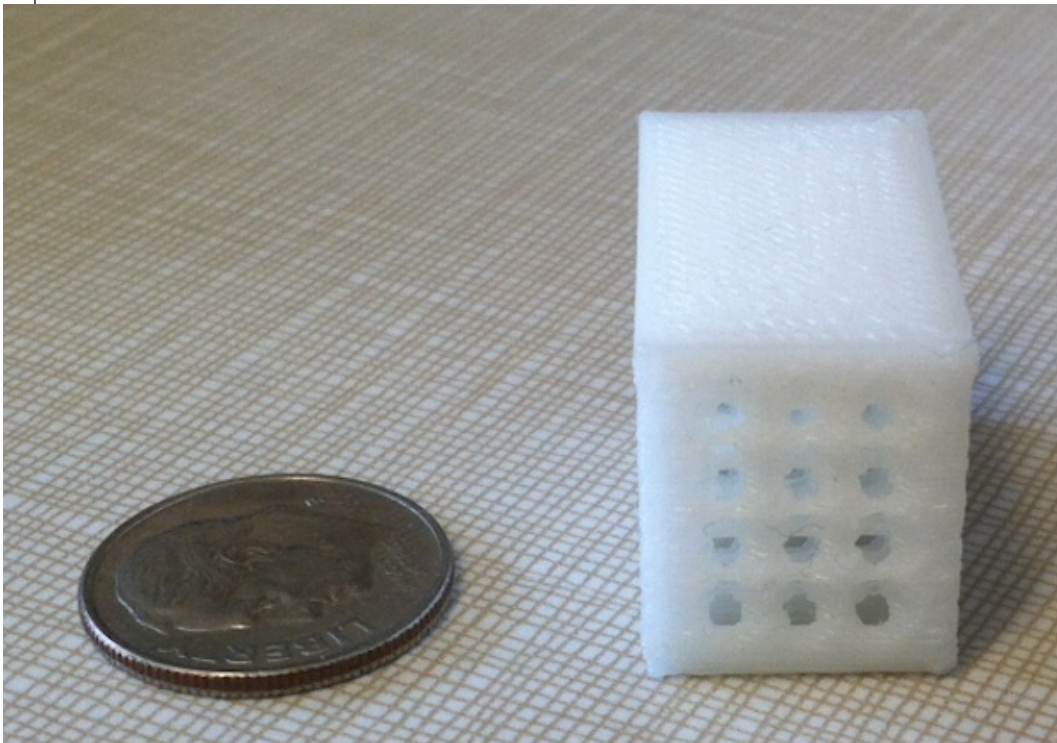


Figure 8.20. Sample a different printer, at the right scale, showing full struts, including the horizontal.

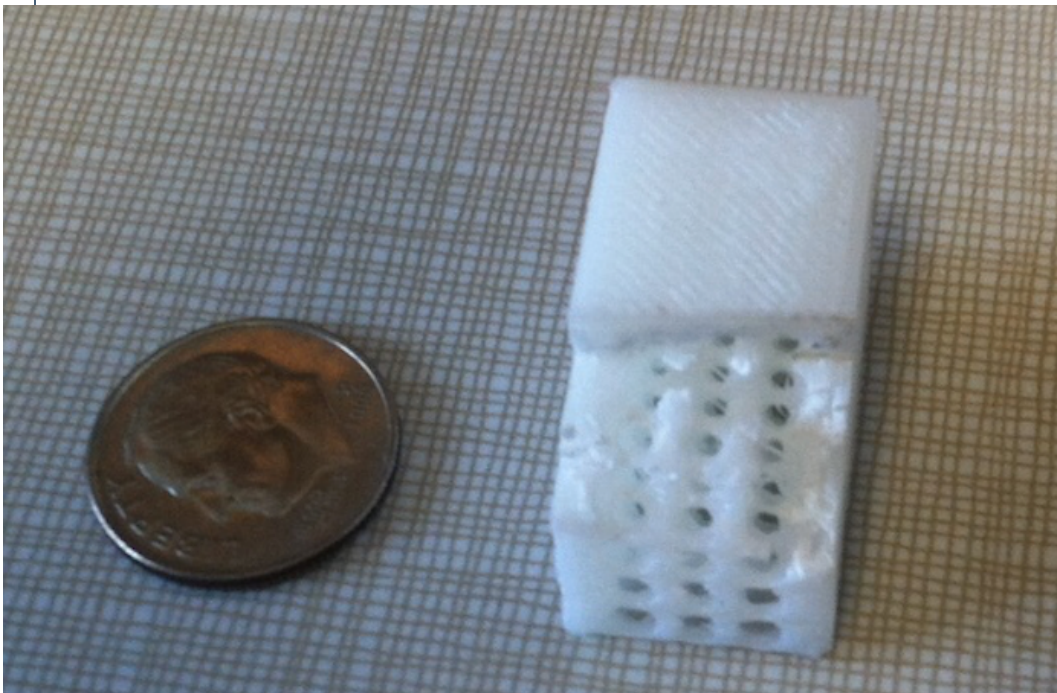


Figure 8.21-. Cut sample of the HX module made with the Portabee Go printer. Note the full struts.

We next used a Portabee Go printer. The results are shown in Figures 8.20 and 8.21. The struts are reproduced with high fidelity, including the horizontal ones. It is clear that this technology is suitable to make units, inexpensively, using plastics, which limits the temperature of operation. However, more

expensive, metal printers exist that can be used.

The above examples were made from inexpensive, polymer-based “ink.” We have also explored metallic 3D printing. An example for what can be achieved today with 3-D metal printing is shown in Figure 8.22. The sample uses a Direct Metal Laser Sintering (DMLS) system. The sample in Figure 8.22 is made from steel. [Arnold]. Arrangements of open cell and solid material can be built starting with metallic powders, as shown in Figure 8.22. The powders are sintered using a focused laser beam. The specimens are built in layers, and the powders that have not been sintered removed from the specimen. A wide range of materials can be used, including high melting temperature metals.

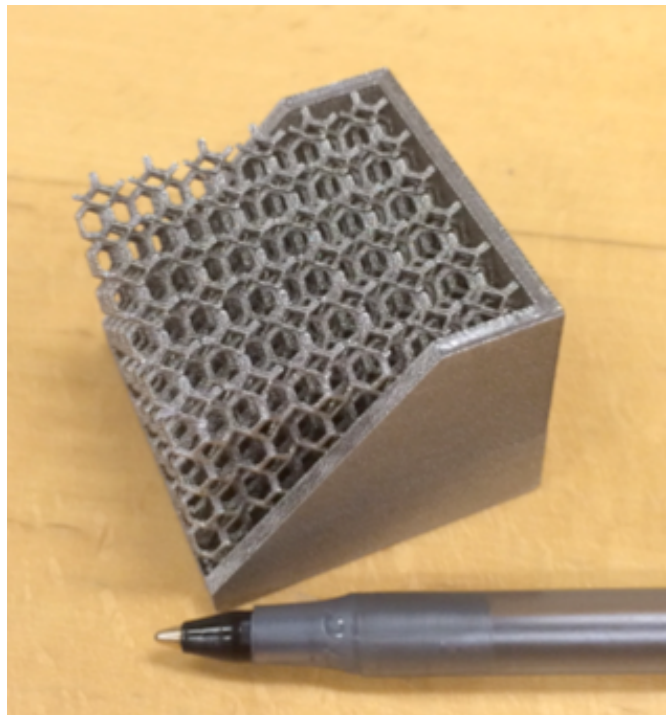


Figure 8.22. Example of metallic 3-D components manufactured by DMSL process.

#### 8.6.5 ALTERNATIVE MEANS FOR OPEN-CELL, POROUS MATERIALS

It is also possible to coat, using CVD technologies, the as printed units. Ultramet [Fortini] has been making units using CVD of many materials. First, the skeleton is built, and then metals can be deposited on the surfaces. They make a carbon foam by pyrolyzing the polymers, coating the ligaments (struts) but leaving the open space. They have made heat exchangers using this technique for the Navy and DOE.

With respect to ceramics, a group at Lawrence Livermore National Laboratory (LLNL) developed a process of manufacturing regular ceramic foams [Maiti]. LLNL scientists recently demonstrated the feasibility of 3D printing of uniform foam structures, such as that shown in Figure 8.23, through a process called directinkwrite. The material is built up layer by layer, with each layer consisting of equally spaced parallel cylinders of the same uniform diameter. LLNL material scientists demonstrated that 3D printed foam works better than standard cellular materials in terms of durability and long term mechanical performance.

Microstructures of two different foam materials. At left, a traditional open-cell stochastic open-cell structure, and at right, an additively manufactured (AM) foam with the face-centered-tetragonal (FCT) lattice structure, the diameter of each cylindrical strut being 250  $\mu$ m.

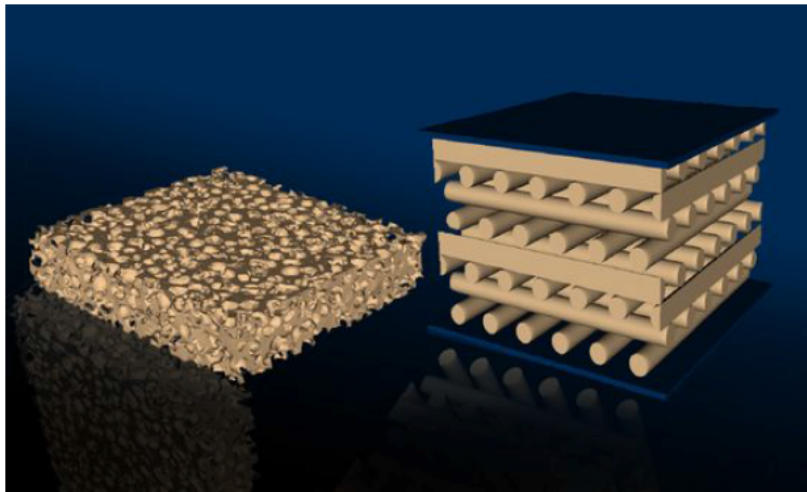


Figure 8.23. Microstructures of two different foam materials made out of filled polydimethylsiloxane (PDMS) elastomers: (a) an open-cell stochastic foam; and (b) an additively manufactured (AM) foam with the face centered-tetragonal (FCT) lattice structure, the diameter of each cylindrical strut being 250  $\mu$  m.

## 8.7 REFERENCES

[Hampton] W.F. Hampton and J.H. Mennie, “Specific heat of monel metal between -183°C and 25°C,” *Can. J. Res.* **7** (1932) 677-679.

[Copper] Copper Development Association, “Copper-Nickel 90/10 and 70/30 Alloys Technical Data,” *CDA Publication TN31* (1982).

[NIST] [http://www.cryogenics.nist.gov/MPropsMAY/OFHC%20Copper/OFHC\\_Copper\\_rev1.htm](http://www.cryogenics.nist.gov/MPropsMAY/OFHC%20Copper/OFHC_Copper_rev1.htm)

ITERITER Organization, “Annex to design requirements and guidelines Level 1 (DRG1), Superconducting materials database, Article 5. Thermal, electrical and mechanical properties of materials and cryogenic temperatures,” *N 11 FDR 42 01-07-05 R 0.1* (2001).

[Kaye] UK National Physical Laboratory – Kaye & Laby, “Table of physical and chemical constants, Section 2.6 Electricity and magnetism, 2.6.1 Electrical resistivities,” <http://www.kayelaby.npl.co.uk/>

[Konstantinov] V.A. Konstantinov, V.P. Revyakin, and V.V. Sagan, “Isochoric thermal conductivity of solid n-alkanes: propane C<sub>3</sub>H<sub>8</sub>, Low Temperature Physics, Vol. 35 (7), July 2009, pp. 735-738.

[Lemmon] E.W. Lemmon, M.L. Huber, and M.O. McLinden, *NIST Standard Reference Database 23: Reference Fluid Thermodynamic and Transport Properties-REFPROP, Version 9.1*, National Institute of Standards and Technology, Standard Reference Data Program, Gaithersburg, 2013.

[Younglove] B.A. Younglove and J.F. Ely, “Thermophysical properties of fluids II, Methane, Ethane, Propane Isobutane and normal Butane,” *J. Phys Chem Ref Data* Vol 16, Number 4, (1987) 112.

[Martovetsky] N.N. Martovetsky and M.R. Chapin, “Normal-zone detection in Tokamak superconducting magnets with co-wound voltage sensors,” *IEEE Trans. Mag.* **22** (1996) 2434-2437.

[Huang] Huang, C-B, and X-J Zhu, “Heat Dissipating Device with Metal Foam,” US patent application 2006/0137862

[Meng] Meng, J-G and C-B Hwang, “Heat Dissipation Device”, US patent 7987898

[Mornet] Mornet, E and C. Roucoules, “Heat Exchange Device, Especially for and Automotive Vehicles,” US patent application US 2011/0315342 A1

[Ozmat] Ozmat, B, “Method of Cooling and Electronic Power Module Using a High Performance Heat Exchanger Incorporating Metal Foam Therein,’ US patent 6397450

[Kang] Kang, B.H., S.Y. Kin, D.Y. Lee et al., “Plate Tube Type Heat Exchanger Having Porous Fins,” US patent 6142222

Kienbock et al., Heat Exchanger for Industrial Applications, US patent application US20050178534A1

[Tuck] Tracy Yoho, Sr. Engineer, A. J. Tuck Company, <http://www.ajtuckco.com>

[Gaillard] Gaillard , J.F. Despois, A. Mortensen, Processing of NaCl powders of controlled size and shape for the microstructural tailoring of aluminium foams, Materials Science and Engineering A 374 (2004) 250–262, doi:10.1016/j.msea.2004.03.015

[Maiti] Maiti, W. S., J. P. Lewicki, T. H. Weisgraber et al., “3D printed cellular solid outperforms traditional stochastic foam in long-term mechanical response,” Scientific Reports 6:2487; DOI: 10.1038/srep24871

[Fortini] Fortini, A.J., “Open-cell silicon foam for ultralightweight mirrors” Proc of the SPIE, SPIE Vol. 3786, page 440

[Bromberg] L. Bromberg, A. J. Dietz, P. C. Michael, C. Gold, and M. Cheadle, “Efficient and lightweight current leads,” AIP Conference Proceedings 1573, 1034 (2014); doi: 10.1063/1.4860819

[Arnold] Ben Arnold of SLM Solutions, private communication, 2016

## 9 CRYOGENIC DESIGN

The cryogenic system is key to successful implementation of a superconducting system. We consider the issues with the cryostat to be more demanding than those of the superconductor (with the exception of the AC losses, which could prevent the practical implementation of superconducting stators).

We have spent resources investigating alternative concepts that would ease the problem, or addressing the issues dealing with the cryostat. We have investigated the following alternatives:

- Single (common) cryostat configuration (for both rotor and stator)
- Separate rotor and (single) stator cryostat configurations
- Individual stator winding cryostat configurations

### 9.1 SINGLE CRYOSTAT.

The single cryostat is shown in Figure 9.1

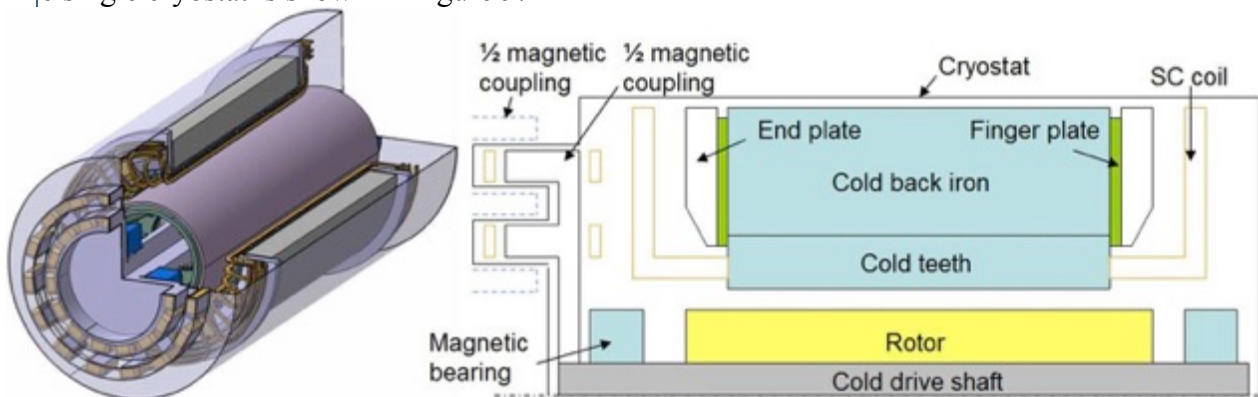


Figure 9.1 Single cryostat topology

This configuration places the rotor and the stator inside the same, non-rotating cryostat. This geometry has the following features:

- Stator is aggressively cooled.
- Rotor cooling by residual gas convection, eliminating the need for a rotating seal.
- No need for hermetic shaft seals
- Large reduction in rotating friction heat load
- Use of magnetic bearing on rotor shaft
- Due to the high AC losses in the iron, it is necessary to have the back-iron warm.
- Alternatively, a resistive shield could be used or a superconducting shield, sharing in the same cryostat, as described in Section 2.2.
- Radial magnetic coupler design

The machine is about 1 m long, 0.36 m diameter rotor, with a rotor heat load of 130 W ( $\sim 100$  W/m<sup>2</sup>). The space between the rotor and the stator is filled with  $\sim 1$  mTorr H<sub>2</sub> or He gas pressure in the cryostat for cooling where, conductivity,  $k$ , viscosity,  $\mu$ , are pressure independent. The stator is aggressively cooled to  $\sim 20$  K, with a 1 cm gap between the rotor and the stator. The rotor spins at 7000 rpm. For these conditions, we obtain a 35 K temperature difference between the stator and the rotor. Thus, at 55 K, HTS 2<sup>nd</sup> generation coated conductors could be used for the rotor.

Because of windage, there is a drag of about 0.01 N-m (out of 20,000 Nm that the machine produces).

and 10 W windage loss.

However, the load (motor weight and torque) needs to be transmitted through the cryostat, and the low radial stiffness of the system may affect the dynamic mechanical stability of the unit.

## 9.2 SEPARATE CRYOSTATS.

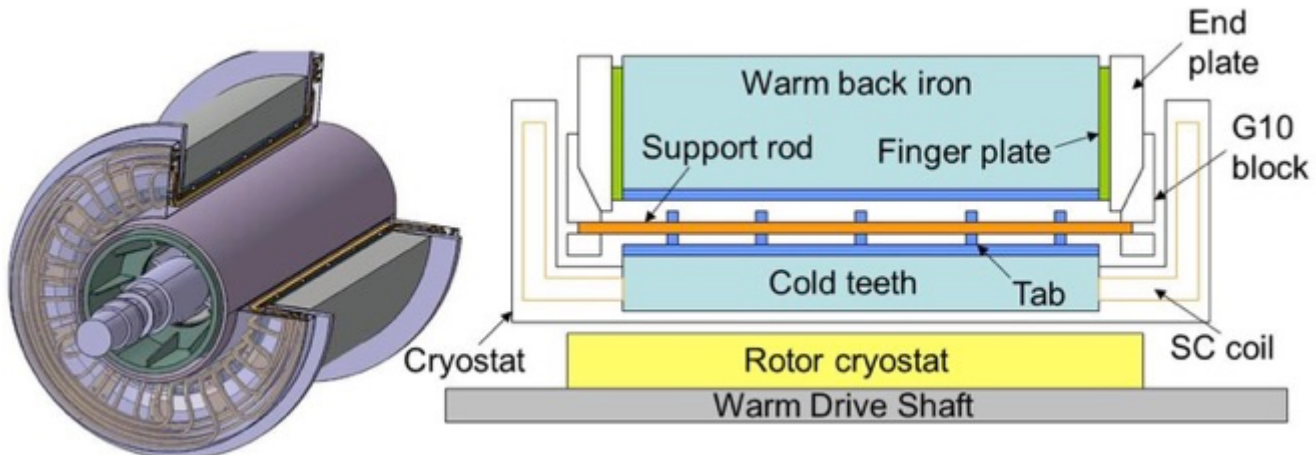


Figure 9.2 shows an illustrative design with separate rotor and stator cryostats. If iron teeth are used, they are separated from the bulk of the back iron, which is warm. This feature minimizes the magnetic losses that need to be removed at cryogenic temperatures.

This configuration has the following appeals:

- Improved mechanical support for stator windings
- More conventional cooling manifold arrangement
- Easier interconnects between coils, as all the coils are in the same cryostat.
- The use of room temperature rotor bearings.

As mentioned the back iron is removed from the cryogenic environment, needed a gap between the iron teeth (is used) and the backiron to incorporate a cryostat wall. If non-magnetic teeth are used, the additional cryogenic heat load due to the iron teeth is removed. This technology is proven, as rotating machineries with this topology have been built.

## 9.3 INDIVIDUAL CRYOSTATS SURROUNDING INDIVIDUAL STATOR WINDINGS.

The advantages of using individual cryostats around each stator winding are:

- Permits use of warm iron
- Each coil and cryostat can be tested prior to being introduced into the machine, allowing for improved assembly of machine
- Coils and associated cryostats can be replaced without having to break a single cryostat

Figure 9.3 shows an illustration of a machine that uses racetrack toroidal windings. In this case, the windings are placed in the azimuthal direction, as opposed to the toroidal stator described in sections 2.4 and 2.7.

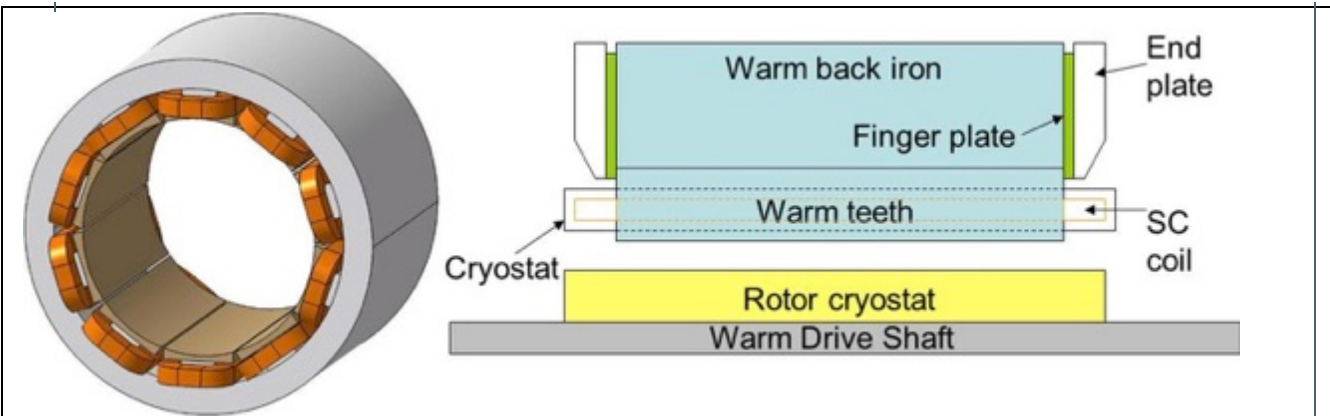


Figure 9.3 Stator with individual coil cryostats.

We have investigated two configurations:

- Radial flux machine
- Toroidal flux machine (Gramme ring)

Both machines have substantial reduction on the cryogenic loads, as all the iron, including the teeth, if used, are out of the cryostat. Also the topology allows the replacement of individual coil or individual cryostats. However, the associated cryostat and coil need to be removed at the same time. The geometry simplifies the assembly, as the coils and cryostats can be tested prior to assembly to assure operation characteristics of the machine.

However, the loads need to be transferred across the cryostat. The loads are not large, as for a 2 kA conductor in a 0.2 T field, the load is about 400 N/m, a small number. However, because of the very large number of cycles (over 7 billion cycles per year), the unit needs to be highly reliable.

## 9.4 CRYOSTAT SUMMARY

Significant challenges to the development of high-speed, HTS rotating electric machinery exist:

- Relatively high conductor ac loss, compared to equivalent LTS conductors
- Carnot efficiency gain from higher temperature (20~50 K) gas cooling, offset by low coolant density
- Use of high-speed cryo-transfer coupling for rotor cooling remains challenging

Additional cryostat topologies will be examined in effort to improve feasibility. However, we have made no significant breakthroughs yet. We are working to reduce magnetic field peaking for individual stator winding cryostat configurations in the case when the racetracks are in the azimuthal direction.

## 9.5 REFRIGERATION AND REFRIGERATOR ISSUES

In this section, the thermal loads to the stator and the refrigerator requirements are provided. We provide the total cryogenic loads below, with details of the different contributors to the cryogenic load in the following sections. We also provide weights and print surface that is required for use in stators. The conclusion from this work is that the impact of the refrigerator on the system efficiency is small, less than 1%. The weight of the refrigerator is comparable to the weight of the machine, thus reducing the specific power density of the system by a factor of 2, but still reaching the Navy roadmap goal of > 2 kW/kg. The footprint is small, about 2 m<sup>2</sup>. However, the real issue is the cost. We estimate that the cost of the refrigerator is about 500-600k\$.

Work on decreasing the cost of the refrigerator is key to making the superconducting stator practical for NAVY applications.

### 9.5.1 OVERALL CRYOGENIC LOADS/SUMMARY

The summary of the loads is shown in table 9.1 for the case of 7 kA operation of the stator. About 600 W load needs to be removed at 20 K, and about 700 W at the intermediate temperature station. The cost of the system, for 8 kA, is about 300k\$ and requires about 70 kW CW. [Brake, Stirling]

Table 9.1. Summary of thermal loads (W) (8 kA)

HEAT SOURCE (W)	8,000 A	
	To Cold mass	To int. station
Support	0.05	1.05
Radiant from thermal shield	0.55	37.79
Current leads	1.80	624.00
Residual gas Convection	1.17	1.75
Instrumentation	0.20	0.00
AC losses	650.00	0.15
<b>Total</b>	<b>653.77</b>	<b>663.69</b>
Power, electric (W)	65000	19000
Cost (k\$)	305	114

The loads are dominated, at the low temperature, by the AC losses in the superconductor. At the intermediate temperature, they are dominated by the current leads needed to bring the current from room temperature to the cryogenic temperature.

In terms of minimizing the cryogenic load to the intermediate temperature, reducing the operating current is a powerful knob (linear with current). Operating at lower current can reduce the load. It is possible to further decrease the cryogenic load by intercepting the heat at higher temperature can result in decreased net electrical power. The electrical power requirement and the estimated cost of the system can be decreased by a factor of 2 by intercepting the heat at an elevated temperature, at the expense of increased complexity.

### 9.5.2 COOLANTS

There are limited options for coolants. There are two means of cooling the unit: flowing fluids or conduction cooled. Because of the high heat load, it needs to be aggressively cooled, and the section of the cable design addresses means of removing the heat with flowing gases.

For fluids, we need a fluid at the intermediate temperature (around 65-80 K) and a second one for cooling the superconductor. The only fluid for the superconductor is flowing liquid helium, most likely supercritical. At the intermediate temperature there are several options, including liquids (i.e., liquid nitrogen, liquid air, oxygen/nitrogen blends), or gaseous (most likely, gaseous helium).

We estimate the approximate helium volume required. For the stators that we are considering, the volume of the cooling channels are about 3 liters. If totally released, assuming that the helium is at 20 K, 20 bar, the helium volume (at room temperature and pressure) is about 1 m<sup>3</sup>. Thus, it should not be a substantial safety problem if released, even if the number is somewhat higher (as the numbers indicated above include only the helium in the stator).

### 9.5.3 CRYOGENIC LOADS DUE TO LEADS.

Current leads are needed to connect electrically the superconducting stator with the external environment. Conventional leads consists of two elements, one at higher temperatures, going all the way to room temperatures, and a lower temperature section, going to the superconductor temperature.

#### LOWER TEMPERATURE LEAD SECTION

The lower temperature leads are made from superconductor, to minimize the cryogenic load. There are several manufacturers of these leads. For illustrative purposes, we highlight leads from HTS-110. The performance of the current leads is shown in Table 9.2. These leads are superconducting, with very small thermal dissipation in the lead, but with limited remaining thermal conduction. There may be better leads using different superconductor (for example, using YBCO tapes from Superpower that do not have copper coating), these numbers are conservative. Our experience with the later tapes proved to be very difficult, and the tapes were easily damaged even with careful handling.

Table 9.2. Superconducting leads specs

Standard current lead details are shown as follows:

Product	Body Diameter		Dimension		Operating Current 64K	Conductive Heat Leak at 64K-4.2K (per pair)
	A inches	mm	B inches	mm		
CS010030	0.375	9.53	.13	3.30	100A	32mW
CS025030	0.438	11.13	.25	6.35	250A	90mW
CS050030	0.563	14.30	.25	6.35	500A	130mW
CS100030	0.750	19.05	.375	9.53	1000A	250mW
CS200030	1.00	25.4	.438	11.13	2000A	450mW

For higher currents, multiple current leads would be required. Higher current operation can be managed safely if each current lead has an associated high-temperature lead section, which would assure even distribution of the currents through the superconducting current leads.

In general, it can be assumed that the heat leak per pair is about 0.25 W/kA.

#### HIGH TEMPERATURE LEAD SECTION

The lead from the warm side of the superconductor to room temperature is made from resistive materials. At MIT we have spent substantial effort to develop concepts for decreasing the power requirement for the high temperature leads, which are responsible for almost all of the cryogenic loads at the intermediate temperature. [Bromberg, Good] The conventional upper temperature stage current lead does not use an intermediate stage to intercept the heat coming from the room temperature. The current lead can be optimized in order to minimize the cryogenic loads, which consists of both thermal conduction along the lead, as well as joule dissipation along the lead. To minimize thermal conduction, the cross section of the lead needs to be decreased, while to minimize Joule dissipation, the cross section should be increased. As a consequence, there is a set of parameters where the heat load to the cryogenic environment is minimized. The relevant optimization parameter, for each element, is  $I/L/A$ , where  $I$  is the operating current,  $L$  is the length, and  $A$  is the cross sectional area (for constant cross section along the length). The heat load is insensitivity to the choice of materials, and it depends

on the upper and lower temperature of operation.

Table 9.3 shows the parameters for the optimized current leads, when the temperature range of the current lead is between 300 K and 77 K. For a pair of current leads, the minimum cryogenic load is 80 W/kA. Also indicated in Table 9.3 is the heat load in the case when the current lead is not energized (in this case, the cryogenic load is due to thermal conduction, no joule heat dissipation). The cryogenic load is reduced in the no-current case to about 50 W/kA.

Table 9.3. Characteristics of optimized current lead (copper) in the case of single stage (per lead)

$Q_{dot}/I$	W/A	0.039
$IL/A$	A/m	2.18E+06
$Q_{dot}/I$ no Current	W/A	0.024
$P_{e/I}$	W/A	1.278

It is possible to decrease the heat load due to the leads by intercepting the thermal load at higher temperature, as shown in Figure 9.4. This solution requires the complication of an additional cryocooler at higher temperature. Table 9.4 shows the results of the optimization in the case of two stages, as a function of the temperature in the intermediate stage. Two sets of numbers are provided, for the upper and lower temperature stations. Also indicated is the electrical power requirement, for a 20% Carnot efficient. When comparing Table 9.4 with Table 9.3, we conclude that the electrical power requirement can be decreased by about a factor of 1/3. When including actual Carnot efficiency as the different temperatures, it is likely to be closer to about 1/2. Substantial saving in power consumption could be achieved, at the expense of increased complexity of the current leads.

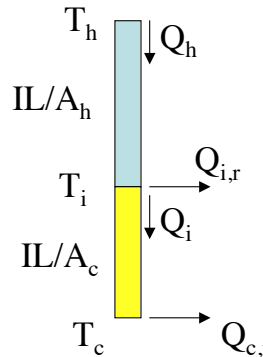


Figure 9.4. Two stage current lead

Table 9.4. Characteristics of optimized current lead (copper) in the case of two temperature stages

Intermediate temperature (K)		140	145	150	155
Upper stage					
$Q_{dot}/I$	W/A	0.036	0.035	0.035	0.035
$IL/A$	A/m	1.68E+06	1.65E+06	1.62E+06	1.59E+06
$Q_{dot}/I$ no Current	W/A	0.020	0.020	0.020	0.019
Lower Stage					
$Q_{dot}/I$	W/A	0.015	0.016	0.017	0.018
$IL/A$	A/m	1.85E+06	1.85E+06	1.85E+06	1.85E+06
$Q_{dot}/I$ no Current	W/A	0.010	0.011	0.011	0.012
$P_{e/I}$	W/A	0.869	0.867	0.867	0.868

We have studied a number of stages higher than 2, and concluded that the reduction in heat load has reduced returns and not worth the increased additional complexity.

#### 9.5.4 RADIATION.

In order to minimize radiation transport in cryogenic environments, a thermal shield is conventionally used to intercept the radiation of the high temperature (room temperature) to the low temperature (4 K). The radiation from the high temperature is usually intercepted at the same temperature as the lower temperature of the normal current leads, around 60-80 K.

It is assumed that there is a 65 K shield around the superconductor. 65 K is chosen as a convenient station for the first stage of the cryocooler. The radiation is small when appropriately designed (with the use of a thermal shield). The radiation to the high temperature is also decreased by the use of multiple thermal barriers that intercept the heat from the higher temperature and radiate to the lower temperature. The thermal barrier is conventionally made from multiple layers of insulation (MLI), form from multiple layers of a thin organic film (kapton) that is coated with a thin aluminum layer. It is usually placed between the room temperature wall of the cryostat and the thermal shield.

Table 9.5

Typical Values of Radiative Heat Flux			
Material	$T_{wm} \rightarrow T_{cl}$ [K]	$\epsilon_r$	$q_r$ [mW/m <sup>2</sup> ]
Copper as received	20 → 4	0.03	0.3
	80 → 4	0.06	140
	300 → 80	0.12	55,000
	20 → 4	0.01	0.1
	80 → 4	0.02	46
	300 → 80	0.06	27,000
Stainless steel as received	20 → 4	0.06	0.54
	80 → 4	0.12	280
	300 → 80	0.34	155,000
	20 → 4	0.04	0.4
	80 → 4	0.07	162
	300 → 80	0.12	55,000
mechanically polished	20 → 4	0.03	0.3
	80 → 4	0.06	140
	300 → 80	0.10	46,000
	20 → 4	0.04	0.4
	80 → 4	0.07	162
	300 → 80	0.12	55,000
electropolished	20 → 4	0.03	0.3
	80 → 4	0.06	140
	300 → 80	0.10	46,000
	20 → 4	0.04	0.4
	80 → 4	0.07	162
	300 → 80	0.12	55,000
Aluminum as received	20 → 4	0.04	0.4
	80 → 4	0.07	162
	300 → 80	0.49	224,000
	20 → 4	0.03	0.3
	80 → 4	0.06	140
	300 → 80	0.10	46,000
mechanically polished	20 → 4	0.02	0.2
	80 → 4	0.03	70
	300 → 80	0.08	37,000
	20 → 4	0.03	0.3
	80 → 4	0.06	140
	300 → 80	0.10	46,000
electropolished	20 → 4	0.02	0.2
	80 → 4	0.03	70
	300 → 80	0.08	37,000
Superinsulation	20 → 4	$\leq 10^*$	2†‡
	80 → 20	40*	40†
	300 → 80	60*	2,500†

Table 9.5 [Iwasa] shows the numbers for the radiation across several temperature spans and with different material finishes. The radiation is a relatively small. In the estimates with have included penetrations required for support and current leads.

### 9.5.5 CONVECTION IN THE CRYOSTAT.

There is a vacuum in the cryogenic environment, in order to minimize the thermal load due to convection/thermal conduction from the warm cryostat boundary to the cold regions. However, even under vacuum condition, there is thermal transfer between the two surface, due to presence of residual gas. The vacuum in cryostats is usually in the order of  $10^{-5}$  to  $10^{-4}$  Torr (about 1 mPa, or  $10^{-8}$  bar. The cryogenic load is a function of the pressure and the area exposed to the gas. Table 9.6, from Iwasa, provides a summary of the heat loads for several gases (helium, hydrogen) for different temperature ranges for a pressure of  $10^{-5}$  Torr. We are concerned about heat load from room temperature to the heat shield (at around 65 K) and between the heat shield and the superconductor (at 4 K). For the present estimates, we use the information from 80 K to estimate the cryogenic heat load.

Table 9.6.  
Heat Conduction by  
Residual He and H<sub>2</sub> Gases at  $P_g$  of  $10^{-5}$  Torr

Helium			Hydrogen		
$T_{wm} \rightarrow T_{cl}$ [K]	$\eta_g$ [W/m <sup>2</sup> Pa K]	$q_g$ [mW/m <sup>2</sup> ]	$T_{wm} \rightarrow T_{cl}$ [K]	$\eta_g$ [W/m <sup>2</sup> Pa K]	$q_g$ [mW/m <sup>2</sup> ]
20 → 4	1.27	27	—	—	—
80 → 4.2	0.85	86	80 → 20	2.20	176
300 → 4.2	0.64	251	300 → 20	1.32	494
300 → 80	0.44	129	300 → 80	1.02	298

## 9.6 REFRIGERATOR

There is a wide spread in types of cryocoolers. As the capacity of the cryocoolers increases, the devices get more efficient and the cost per cooling watt decrease. Although we have some numbers for actual devices, we will use first projection costs, and then give a couple of commercially available devices that could be used for the stator application. More detailed costs will be provided as the concept matures (i.e., we select a current), as the cryogenic load is a strong function (linear) with the current.

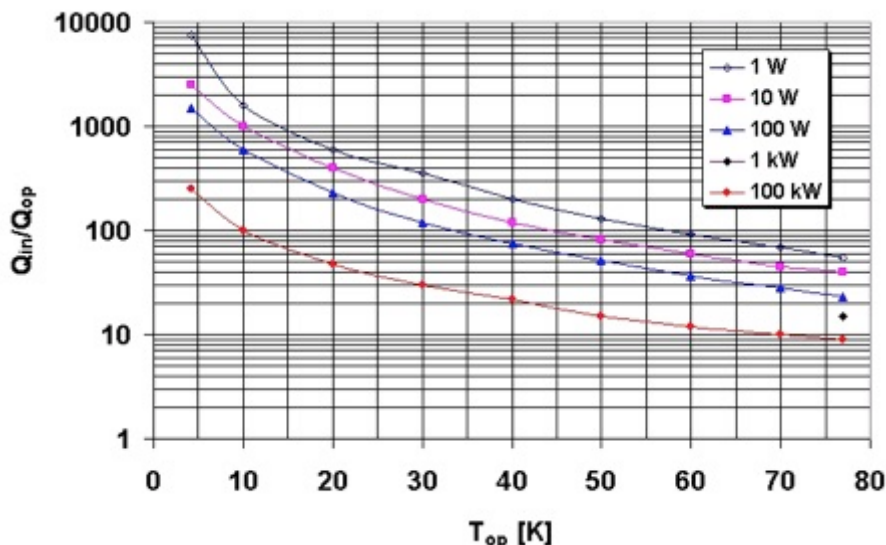


Figure 9.5. Coefficient of performance (COP) as a function of operating temperature for several cooling capacities.

Figure 9.5 shows a diagram indicating the electrical power requirement, as a function of temperature, for several cooling power [Iwasa]. For example, to remove 600 W at 20 K requires approximately 60 kW of electrical power (a COP, or coefficient of performance, of about 5000). Similarly, to remove 850 W at 65 K about 25 kW are needed (with a COP of 30). The actual number depends on the device chosen.

Higher costs are associated with higher efficiencies, and also there is the issue of maintenance. In order to provide some redundancy, it is best to have two machines with limited excess capacity, allowing for repair on one machine while the other one works harder. Actually, for N+1 redundancy, 3 refrigerators would be ideal, with two refrigerators needed for stator operation. Alternatively, it is

possible to use thermal energy storage for provided limited cooling while a single machine is being repaired. At MIT we have developed concepts for storing thermal cooling “capacity” that can be used at the intermediate temperatures.

Figure 9.6 shows an alternative summary of a wide range of refrigerators. There is a wide spread, but clearly the fraction of Carnot increases with refrigerator capacity. Thus, it may be more efficient to use a single refrigerator, rather than depend on multiple smaller units.

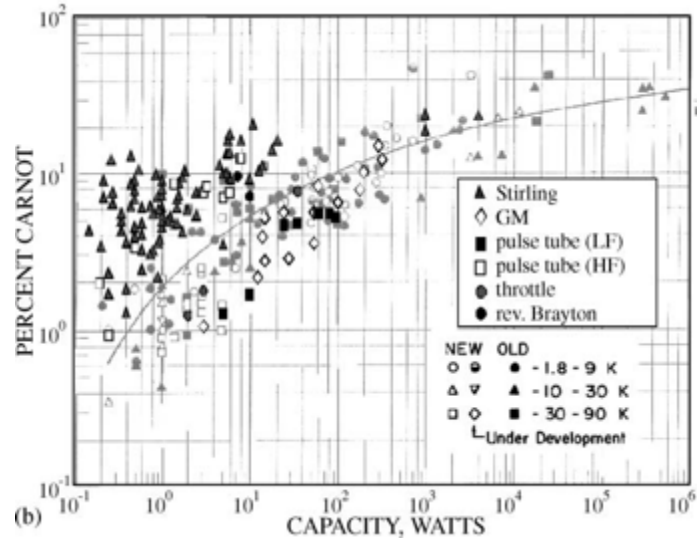


Figure 9.6. Modified Strobridge plot showing 80K refrigerators [Brake]

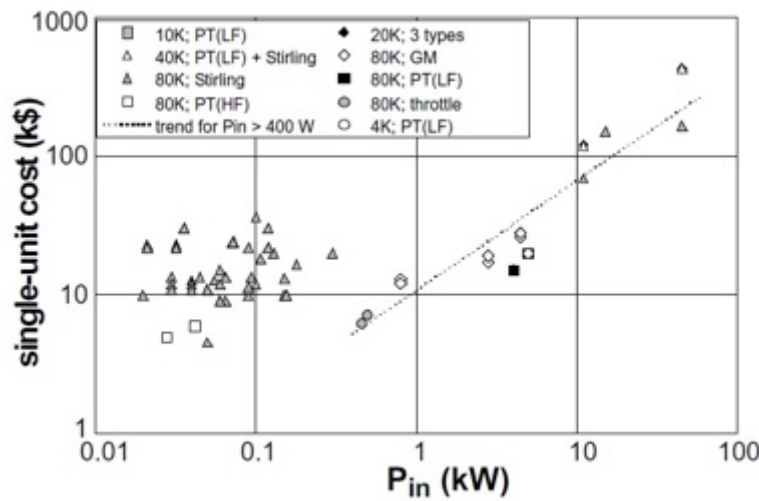


Figure 9.7. Single-unit cost versus input power. Dotted line shows the trend for  $P_{in} > 400$  W [Brake]

The costs for a range of cryocoolers, as a function of the input power, are shown in Figure 9.7, for units operating over a wide range of temperatures. For input powers  $> 400$  W, there is a relatively good fit for the cost of the units, given by:

$$\text{Cost (k\$)} = 10.8 P_{in}^{0.79}$$

where the power is in kW (the power is the electrical power needed to drive the compressor, not the

cryogenic load). We have used this costing from this fit to estimate the costs presented in Table 9.1, when combined with the COP shown in Figure 9.7.

## 9.7 SPECIFIC CRYOCOOLERS

We have checked with several suppliers about the costs and performance of cryocoolers. We have been investigating D-H-Industries Stirling machines [Stirling], and in particular, the GPC-4 unit. It has a maintenance interval of 6000 hours (about 250 days). It is shown in Figure 9.8.

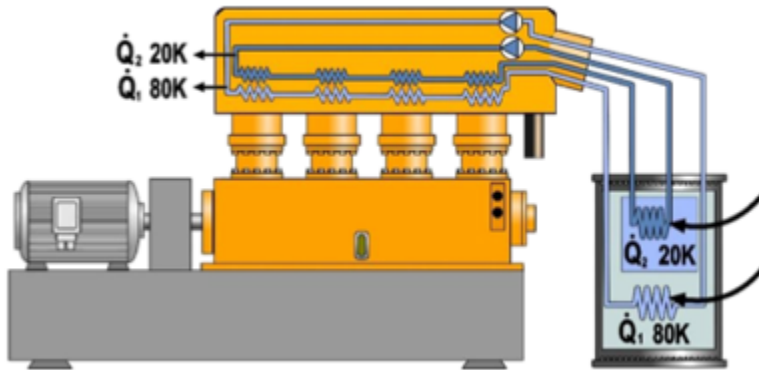


Figure 9.8 Illustration of the SPC-4C unit, with a footprint of about  $1.3 \text{ m}^2$  and a height of 1.2 m

The cooling capacity as a function of temperature is shown in Figure 9.9. Two machines are needed in order to provide the required cooling, with a total footprint of about  $2.5 \text{ m}^2$ . The cost of each machines is about 200k\$, higher than that shown in Table 9.1. The reason for the larger costs is, first, the power is smaller (larger units are cheaper for the same overall cooling capacity), and the units include a heat exchanger and a fan, for circulating the high pressure helium gas.

The Stirling machine is water cooled. There are options for air cooling, but the cost of the unit increases.

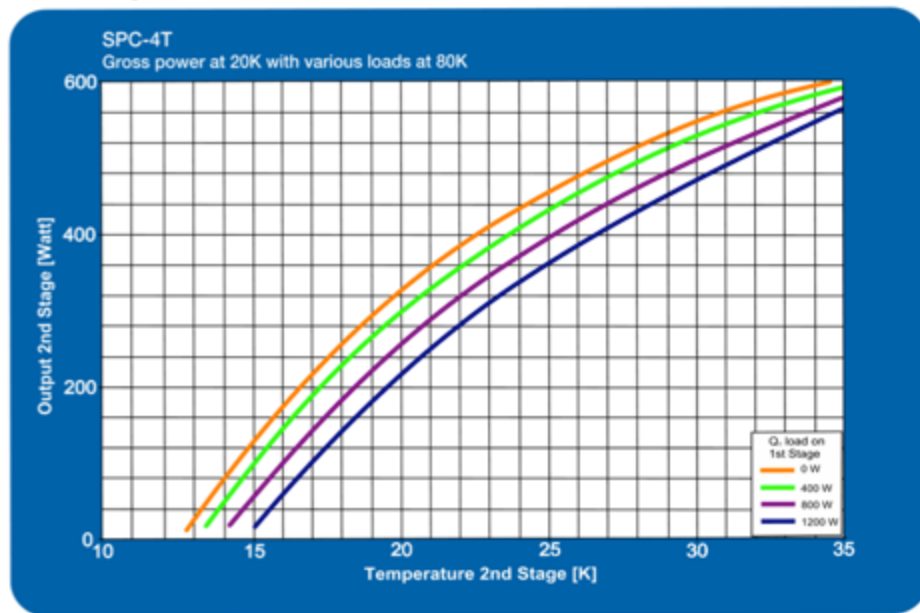


Figure 9.9 Cooling capacity of the SPC-4T Stirling refrigerator from Stirling Cryogenics

The cooling capacity of the machine is shown in Figure 9.9. It can remove 300 W at 20 K, and about 300 W at 70 K.

## 9.8 DEVELOPMENT OF SHIP-CRYOGENIC SYSTEM.

The Navy and NASA are sponsoring the development of machines that are more suitable for their applications than other commercial machines. In particular, the reverse turbo-Brayton cycle is ideally suited for this application. With lightweight, compact footprint due to the high frequency of operation, and with high efficiencies, this technology could substantially impact the development of machines with superconducting stators.

## 9.9 REFERENCES

- [Bromberg] *Current Lead Optimization for Cryogenic Operation at Intermediate Temperatures*.  
Bromberg, L., Michael, P.C., Minervini, J.V. and Miles, C. AIP Conference Proceedings 2010;1218:577-584.
- [Good] *13000 A current lead with 1.5 W heat load to 4.5 K for the large hadron collider at CERN*, J.A. Good, M.L. Allitt and L. Martini, *Physica B* **284-288** 2093-2094 (2000))
- [Seeber] *Handbook of Applied Superconductivity*, B, Seeber, Institute of Physics Publishing, Bristol 1998.
- [Iwasa] *Case Studies in Superconducting Magnets: Design and Operational Issues*, Y. Iwasa, Springer Publishing, second edition (2009)
- [Brake] *Low-power cryocooler survey*, H.J.M. ter Brake, G.F.M. Wiegerinck, *Cryogenics* **42** (2002) 705-718
- [Stirling] [www.dh-industries.com](http://www.dh-industries.com)

<b>Progress Statement</b>		
<b>Summary</b>	<ul style="list-style-type: none"> <li>• Feasible HTS generator topologies investigated: identified topologies very attractive for SC stators</li> <li>• Quench protection/detection challenging: developed several methods</li> <li>• Cable concepts using MgB2 proposed, evaluated, and tested</li> <li>• Developed alternatives to magnetic shields for reducing the weight of the machine without impacting the magnetic signature of rotating machines</li> <li>• Evaluated means of constructing armature windings from MgB2 or YBCO cables.</li> <li>• Evaluated AC losses in MgB2 (with CAPS)</li> <li>• Addressed cooling methods for removal of the dissipated energy.</li> </ul>	
<b>Refereed Journal Articles</b>		
	<p><i>Solid-cryogen-stabilized, cable-in-conduit superconductor cables</i>, J.P. Voccio, L. Bromberg, P.C. Michael and S. Hahn, presented at the 2015 CEC Conference, Tucson AZ (July 2015)</p>	
<b>Books And Chapters</b>	<ul style="list-style-type: none"> <li>•</li> </ul>	
<b>Technical Reports</b>	<ul style="list-style-type: none"> <li>•</li> </ul>	
<b>Contributed Presentations</b>	<ul style="list-style-type: none"> <li>• <i>Cooling topology options for HTS rotating electric machinery</i>, Leslie Bromberg, E. Chen, P.C. Michael, S. Hahn, J.P. Voccio and H. Karmaker, presented at the 2015 CEC Conference, Tucson AZ (July 2015)</li> <li>• <i>Solid-cryogen-stabilized, cable-in-conduit superconductor cables</i>, J.P. Voccio, L. Bromberg, P.C. Michael and S. Hahn, presented at the 2015 CEC Conference, Tucson AZ (July 2015)</li> <li>• <i>Non-contact, high-torque magnetic coupler for superconducting rotating machines</i>, P.C. Michael, S. Hensley, C. Galea and L. Bromberg, to be presented at 2015 MT Technology South Korea</li> <li>• <i>Feasibility Study of High-Speed Direct Drive Superconducting Machines in Air Separation Unit</i>, E. Chen, P. Guedes-Pinto, H. Karmaker, J. Voccio2, S. Hahn, L. Bromberg, P. Michael presented at 2015 MT Technology South Korea</li> </ul>	
<b>Patents</b>	<ul style="list-style-type: none"> <li>• <i>Frequency domain and time domain quench sensors for coated conductors</i>, L. Bromberg, P. Michael and R. Parker, MIT (2015 patent disclosure)</li> </ul>	
<b>Honors</b>	<ul style="list-style-type: none"> <li>•</li> </ul>	

#### Related Sponsored Work

- Conceptual Design of an Uninterruptible Power System Using Superconducting Magnetic Energy Storage (SMES): Conceptual Design and Analysis, sponsored by PoleMechatec
- Ironless cyclotron for variable energy proton beam therapy, DOE High Energy Physics (coil performs as a 30 MJ, 1 MW SMES):
- No-insulation winding (can be used for rotor; funded by wealthy alumni)
- Partially-slit tapes (DOE OFES; concept can be used for making field-trapped rotors for motors and generators)

#### ONR Statistics

Grad Students(total):	0
PI/Co-PI Women:	0
PI/Co-PI Minority:	0
Grad Students Women:	0
Grad Students Minority:	0
Post Docs Students:	0
Post Doc Women:	0
Post Doc Minority:	0
Under Grad Students(total:	5
Under Grad Students Women:	2
Under Grad Students Minority:	0
Degrees Granted:	0
Invention disclosures citing ONR support:	1
Other funding sources:	0